

SIMULATING THE EFFECT OF STRUCTURAL LOADS ON TURBINE BLADES IN A TIDAL TURBINE ARRAY



Mujahid Badshah

11-FET/PHDME/F14

Submitted in partial fulfillment of the requirements for the PhD degree in Mechanical
Engineering at the Department of Mechanical Engineering
Faculty of Engineering and Technology
International Islamic University,
Islamabad

Supervisor

Dr. Saeed Badshah



January, 2020



TH22347

Accession Number

PhD

621.406

MUS

Tidal turbine arrays

Tidal turbines

Copyright © 2020 by Mujahid Badshah

All rights reserved. No part of the material protected by this copyright notice may be reproduced or utilized in any form or by any means, electronic or mechanical, including photocopying, recording or by any information storage and retrieval system, without the permission from the author.

DEDICATED TO

My Kids

CERTIFICATE OF APPROVAL

Title of Thesis: Simulating the Effect of Structural Loads on Turbine Blades in a Tidal Turbine Array


Name of Student: Engr. Mujahid Badshah

Registration No: 11-FET/PhDME/F14

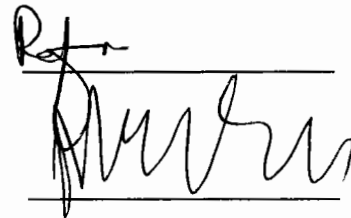
Accepted by the Department of Mechanical Engineering, Faculty of Engineering and Technology, International Islamic University, Islamabad, in partial fulfillment of the requirements for the Doctor of Philosophy degree in Mechanical Engineering.

Viva voce committee:

Dr. Syed Athar Masood (Chairman)
Associate Professor
Department of Mechanical Engineering
International Islamic University, Islamabad.



Dr. Rafi Ullah Khan (Internal Examiner)
Assistant Professor
Department of Mechanical Engineering
International Islamic University, Islamabad.



Dr. Manzoor Ahmad (External Examiner - I)
Principal Engineer
PAEC, Islamabad, Pakistan.



Dr. Muzaffar Ali (External Examiner - II)
Associate Professor
Department of Energy Engineering
UET Taxila, Pakistan



Dr. Saeed Badshah (Supervisor)
Associate Professor
Department of Mechanical Engineering
International Islamic University, Islamabad

June 11, 2020

Abstract

The development of tidal turbine arrays requires an understanding of the interaction between devices operating in array. This interaction would not only influence the power outputs but also the structural loads on turbine blades. Understanding the behavior and variations of structural loads on turbine blades operating in arrays is necessary for the development of structural design specification and improving the devices reliability against fatigue failure. Therefore, this thesis attempts to investigate the effect of upstream devices on the power output and blade structural loads of downstream devices with in co-axial and staggered arrays with different inter device spacing. These investigations are accomplished using RANS CFD simulations of the three turbines co-axial and staggered arrays of full scale SAFL RM1 turbine in the ANSYS CFX software. The RANS CFD simulation methodology is evolved successively starting from the simulation of a single scaled model SAFL RM1 rotor and extending to the full scale turbine and arrays. Additionally, the scaled model rotor and full scale turbine is also modeled in the coupled FSI simulations to establish that blades of the full scale SAFL RM1 turbine with realistic structural design would not deform to an extent to influence the performance or blade loads prediction of the RANS CFD models for the evaluated flow conditions.

Results of the single turbine RANS CFD simulations reveal that at lower TSRs, the variation of blockage ratio had almost no effect on turbine performance. However, at higher TSRs, a positive correlation exists between blockage ratio and turbine performance for the entire evaluated blockage ratio range (2–19%). The effect of blockage on performance is less pronounced at blockage ratios below 10%, but increases rapidly for blockage ratios above 10%. Maximum increase of 47 and 10% are observed in power and thrust, respectively, for the range of TSRs and blockage ratios evaluated. The presence of boundary layer resulted in an increase in the predicted thrust of between 1.6 and 2.3% and power of between 2.7 and 3.5% for the entire range of evaluated blockage ratios. These findings are significant for the future turbine arrays and reveal that the number of devices and their arrangement with in tidal arrays can alter the performance and blade loads of individual array devices.

Results from the coupled FSI simulation of full scale device shows that a $1/7$ th power velocity profile increases the thrust coefficient variation from mean cycle value of an individual blade from 2.8% to 9% and the variation in flap wise bending moment coefficient from 4.9% to 19%. Similarly, the variation from the mean cycle value for blade deformation and stress of 2.5% and 2.8% increases to 9.8% and 10.3%, respectively. Due to the effect of velocity profile, the mean stress is decreased, whereas, the range and

variation of stress are considerably increased. These findings are significant for tidal turbine designers in evaluating the fatigue life design parameters for turbine blades.

Results from the simulations of co-axial turbine arrays revealed that the moment loads curve during a single turbine rotation for the blade of downstream devices is entirely different than the upstream devices. The mean cycle values of moment loads on the blades of downstream devices are lower, while the range of moment loads is significantly higher leading to the conclusion that blades of the downstream devices would experience more variation in the moment loads and may be more susceptible to fatigue failure. The behavior of moment loads on the blades of 1st row turbines does not depend on the transverse spacing in staggered arrays. However, the moment loads behavior of blades for downstream devices is significantly influenced by this spacing. The mean cycle value of moment loads for the blades of downstream turbines is almost similar to the 1st row devices in staggered arrays with close transverse spacing between the upstream devices. However, the range and variations are considerably higher due to drop in the minimum cycle value of moment loads. Contrarily, the mean cycle value of moment loads on the downstream turbine blade is higher and the range is similar to the 1st row upstream devices for staggered array with transverse spacing between 1st row devices equal to the diameter of the downstream device. Therefore, the blades of downstream device in staggered arrays would also be more susceptible to fatigue failure due to increased loads variations or increased mean cycle value of moment loads. These findings suggest that the criterion for the design of turbines needs to be changed and the devices may be designed for the intended operation in arrays rather than as standalone turbine. Additionally, comprehensive structural design specifications may be developed for the devices operating in arrays to ensure improved reliability of the turbine blades against early failures and reduce the cost of technology.

List of Publications

- [1] S. Badshah, **M. Badshah**, N. Hafeez, S. Jan, ZU. Rehman. "CFD analysis of Tidal Current Turbine performance with different Boundary conditions". In proceedings of the 10th International Conference on Future Environment and Energy, Koyoto Japan 7-9 January, 2020.
- [2] **M. Badshah**, J. VanZwieten, S. Badshah, S. Jan. CFD study of blockage ratio and boundary proximity effects on the performance of a tidal turbine. IET Renewable Power Generation. 13 (2019) 744-9. DOI: 10.1049/iet-rpg.2018.5134. (**Category W, IF 3.605**).
- [3] **M. Badshah**, S. Badshah, J. VanZwieten, S. Jan, M. Amir, S.A. Malik. Coupled Fluid-Structure Interaction Modelling of Loads Variation and Fatigue Life of a Full-Scale Tidal Turbine under the Effect of Velocity Profile. Energies. 12 (2019) 2217. <https://doi.org/10.3390/en12112217>. (**Category W, IF 2.707**).
- [4] **M. Badshah**, S. Badshah, S. Jan. Comparison of computational fluid dynamics and fluid structure interaction models for the performance prediction of tidal current turbines. Journal of Ocean Engineering and Science. (2019). <https://doi.org/10.1016/j.joes.2019.10.001>. (**ESCI**).
- [5] **M. Badshah**, S. Badshah, K. Kadir. Fluid Structure Interaction Modelling of Tidal Turbine Performance and Structural Loads in a Velocity Shear Environment. Energies. 11 (2018) 1837. <https://doi.org/10.3390/en11071837>. (**Category W, IF 2.707**).
- [6] S. Badshah, **M. Badshah**. Performance Prediction of Tidal Current Turbine Using Coupled Fluid Structure Interaction Modelling. In proceedings of the 6th European Conference on Renewable Energy Systems, Istanbul, Turkey, 25-27 June, 2018. pp. 1139-44.
- [7] **M. Badshah**, S. Badshah, S.J. Khalil. Hydrodynamic Design of Tidal Current Turbine and the Effect of Solidity on Performance. Journal of Engineering and Applied Sciences (JEAS), Peshawar. 36 (2017). <https://doi.org/10.25211/jeas.v36i2.2068>. (**Category X**).

- [8] N. Hafeez, S. Badshah, **M. Badshah**, S.J. Khalil. Effect of velocity shear on the performance and structural response of a small-scale horizontal axis tidal turbine. *Marine Systems & Ocean Technology*. (2019) 1-8. <https://doi.org/10.1007/s40868-019-00057-0>. (**Scopus Indexed**).
- [9] **M. Badshah**, S. Badshah, M. Altaf, S. Jan, M. Amjad, N.A. Anjum. Research Progress in Tidal Energy Technology-A Review. *Technical Journal*. Vol. 22, No. 4-2017. (**Category Y**).
- [10] S. Badshah. Habibullah, **M. Badshah**, S. Khalil, M. Amjad, N. Anjum. Characterization of Tidal Current Turbine Dynamics Using Fluid Structure Interaction (FSI). *Technical Journal* Vol. 22, No. 3-2017 (**Category Y**).

Submitted papers

- [1] S. Jan, S. Badshah, **M. Badshah**, A. Javed. Effect of tower elasticity on the performance and fatigue character of monopile support tower for tidal current turbine. Submitted to *Applied Ocean Research* (4th July, 2019).

The research work presented in this dissertation is based on the published research articles from Serial No. 1 to 7.

Acknowledgements

In the Name of Allah, the Most Beneficent, the Most Merciful. Glory be to You, O Allah (SWT), and all praises are due unto You, and blessed is Your name and high is Your majesty and none is worthy of worship but You. I thank Allah for giving me the opportunity to perform this research work. Peace and blessings of Allah be upon His last Prophet Muhammad (Sallulah-o-Alaihihe-Wassalam) and all his Sahaba (Razi-Allah-o-Anhu) who are like shining stars for guiding us rightly.

I am grateful to my supervisor Dr. Saeed Badshah for supporting me to complete my higher studies. He was always very supportive and ensured availability of all the required resources for the successful completion of this research. I am also extremely grateful to Dr. James VanZwieten, Department of Civil, Environmental and Geomatics Engineering, Florida Atlantic University, Boca Raton, Florida, USA. He has been my mentor during the entire course of this research. He was always available when ever, I faced an issue during this research. Above all, his confidence in me was my real strength.

I am thankful to my dearest friends Sakhi Jan and Muhammad Amjad, who always supported me in the completion of this research as they did in other aspects of my life. I am also thankful to Sajjad Ahmad, Nida Ahsan and Dr. Imran Shahid at the Institute of Space Technology, Islamabad for their un-conditional and untiring help in the arrangements of computational facilities. I am also thankful to Dr. Naseem Iqbal at the US Pakistan Centre for Advanced Studies in Energy at the National University of Science and Technology, Islamabad for the provision of computational facilities. I acknowledge the support of Higher Education Commission of Pakistan (HEC) for providing me the scholarship and bearing all the expenses of my studies.

I am really grateful to my father (late), mother (late), brother, sister and all family members for their prayer, love and support throughout my life. I am also very thankful to my wife for her patience, encouragement and prayers during every stage of my PhD degree. Finally, I am thankful to my kids, whose love provided me the strength to complete this research.

(Mujahid Badshah)

Table of Contents

Abstract.....	v
List of Publications	vii
Acknowledgements	ix
List of Figures.....	xiii
List of Tables	xxi
1 Introduction.....	1
1.1 Motivation.....	1
1.2 Research Problem	3
1.3 Aim and Objectives.....	4
1.4 Research Methodology	4
1.5 Outline.....	6
2 Literature Review	9
2.1 Historical Background	9
2.2 Performance Prediction.....	10
2.3 Structural Loads.....	13
2.4 Wake	17
2.5 Tidal Current Turbine Arrays	19
2.6 Summary	24
3 Tidal Turbine Design.....	25
3.1 Power Output	28
3.2 Blade Shape	29
3.3 Blade Chord	29
3.4 Tip Losses	30
3.5 Blade Twist	30
3.6 Tip Speed Ratio (TSR).....	31
3.7 Number of Turbine Blades.....	31
3.8 Performance and load Parameters.....	32

3.9 Turbine design utilized for research	34
3.10 Summary	37
4 Development of RANS CFD Methodology	38
4.1 Experimental setup.....	38
4.2 Review of research on CFD Simulations of RM1 Turbine	40
4.3 Software and Governing Equations	41
4.4 Turbulence Model.....	43
4.5 RANS CFD modeling of scale model SAFL RM1 Turbine	47
4.5.1 Computational domain and boundary conditions	48
4.5.2 Mesh definition and refinement	50
4.5.3 Validation of RANS CFD methodology	54
4.5.4 Effect of blockage on turbine performance	57
4.5.5 Effect of boundary layer on turbine performance	61
4.6 RANS CFD modeling of full scale SAFL RM1 turbine.....	64
4.6.1 Numerical method.....	68
4.6.2 Computational domain and boundary conditions	69
4.6.3 Mesh definition	71
4.6.4 Verification and validation of RANS CFD methodology.....	72
4.7 Summary	76
5 Development of Fluid Structure Interaction Methodology	77
5.1 Fluid Structure Interaction (FSI) modeling.....	77
5.2 FSI simulation methodology for scale model rotor	79
5.2.1 CFD setup	81
5.2.2 FEA and system coupling setup.....	82
5.2.3 Results and discussion	84
5.3 FSI simulation methodology for full scale turbine	90
5.3.1 Simulation conditions	90
5.3.2 Numerical method.....	92
5.3.3 Verification and validation of numerical method	95
5.3.4 Results and discussion	97

5.4 Summary	110
6 Effect of array layout and inter device spacing on the performance and structural loads on the blade.....	112
6.1 Single turbine in array domain.....	112
6.1.1 RANS CFD methodology	113
6.1.2 Results and discussion	117
6.2 Tidal turbine arrays	125
6.2.1 RANS CFD methodology	126
6.2.2 Results and discussion	132
6.3 Summary	190
7 Conclusions and Recommendation for Future Work.....	191
7.1 Conclusions.....	191
7.2 Recommendations for future work	195
References.....	198

List of Figures

Figure 1.1 TRL of ocean energy technologies, according to the scale employed by European Commission Horizon 2020 [13]	2
Figure 1.2 Flow chart of research methodology	6
Figure 2.1 Schematic diagram of the discretization of rotor and resolution of the lift and drag forces [24]	11
Figure 2.2 Local loads on a TCT blade [56]	14
Figure 2.3 Variables affecting the flow field around tidal turbines [58]	15
Figure 2.4 Illustration of wake characteristics [10]	17
Figure 2.5 Tidal turbine array showing exaggerated changes in sea level [17]	20
Figure 2.6 Duct effect in a tidal array [93]	20
Figure 2.7 Axial array layout	21
Figure 2.8 Staggered array layout	21
Figure 2.9 Irregular grid arrays (a) Example of optimized 50 turbine array in large channel in the south eastern Pentland Firth (b) Example of optimized 20 turbine array in the small channel with a headland constriction [17]	24
Figure 3.1 Tidal Turbine Design (a) Horizontal Axis (b) Vertical Axis (c) Oscillating Hydrofoil (d) Enclosed Tips (e) Tidal Kite	27
Figure 3.2 Technology Readiness Level (TRL) of tidal energy devices [109]	27
Figure 3.3 Share of tidal energy technologies among all the R&D effort for technologies tested at full-scale [109]	28
Figure 3.4 Angle definition of an airfoil	30
Figure 3.5 Graphical representation of blade root bending moments [63]	33
Figure 3.6 Performance comparison of the original and modified RM1 TCT [94]	35

Figure 3.7 Performance of 1:45 lab scaled modified RM1 turbine at different flow speeds [94].....	36
Figure 4.1 Schematic of the SAFL RM1 experimental setup [26]	39
Figure 4.2 Geometric details of turbine and computational domain	49
Figure 4.3 Mesh on the rotor, rotating and stationary domains utilized in the CFD simulations.....	51
Figure 4.4 Prism layer elements around the blade surfaces for the selected mesh.....	51
Figure 4.5 Variation of blade torque with grid density at (a) TSR 9.05 (b) TSR 5.11 (c) TSR 2.23	53
Figure 4.6 Comparison of experimental and RANS CFD simulated performance curve	54
Figure 4.7 Velocity stream lines with pressure contour at selected blade sections for (a) TSR 2.23 (b) TSR 3.03 (c) TSR 5.11 (d) TSR 9.05	57
Figure 4.8 Effect of Blockage Ratio on Turbine Performance at (a) TSR 5.11 (b) TSR 9.05	60
Figure 4.9 Velocity contour through the centerline plane of turbine (a) Without Boundary Layer (b) With Boundary Layer	62
Figure 4.10 Effect of Boundary Layer on turbine (a) power coefficient (b) thrust coefficient	63
Figure 4.11 Power coefficient (C_p) vs TSR with increasing turbine diameter and velocity [64].....	67
Figure 4.12 Dimensions of the full scale simulation domain	70
Figure 4.13 Mesh used for the full scale turbine simulations	71
Figure 4.14 Variation of blade torque with grid density.....	73
Figure 4.15 Comparison of model scale experimental and full scale simulated performance curve.....	74
Figure 5.1 Flow chart of loosely coupled modular 2-way FSI solution procedure	80

Figure 5.2 Mesh on the turbine rotor for FE Analysis.....	83
Figure 5.3 Comparison of experimental and simulated performance coefficient.....	85
Figure 5.4 Pressure contour with velocity streamlines at TSR 5.11	86
Figure 5.5 Pressure contour with velocity streamlines along the blade length (a) Steady state RANS CFD (b) Coupled FSI.....	87
Figure 5.6 Velocity contour around the blade foil at 96% of the blade length.....	87
Figure 5.7 Contour plot of equivalent stress and deformation at the rotor	88
Figure 5.8 Stress and deformation at the rotor at every time step during the FSI solution process.....	89
Figure 5.9 Internal structure of the blade utilized in the FSI simulations of full scale turbine	90
Figure 5.10 Velocity profile based on $1/7^{\text{th}}$ power law (dashed lines represent turbine location)	91
Figure 5.11 Dimensions of the (a) Fluid domain; (b) Turbine	92
Figure 5.12 FEA mesh used in the coupled FSI simulation of full scale SAFL RM1 turbine	94
Figure 5.13 Comparison of power coefficient predicted by the coupled FSI simulations with transient CFD analysis and experimental data.....	96
Figure 5.14 FSI simulation results for rotor power coefficient during two turbine rotations	97
Figure 5.15 FSI simulation results for rotor thrust coefficient during two turbine rotations	98
Figure 5.16 Rotor angular positions for presentation of results.....	99
Figure 5.17 Flap wise bending moment (normalized by cycle mean) for Blade 1 during two rotations.....	101
Figure 5.18 Torque coefficient C_θ for Blade 1 during two rotation cycles.....	101

Figure 5.19 Axial velocity (normalized by the free stream velocity) contour for (a) Uniform inlet velocity (b) Velocity profile	103
Figure 5.20 Velocity variation along depth of the channel at different downstream location for (a) Uniform velocity (b) Velocity profile (Red dash dot line represent location of turbine hub center and the black dashed lines represents the extent of blade tips).....	103
Figure 5.21 Velocity deficit along the length of channel at different channel depths for (a) Uniform velocity (b) Velocity profile.....	104
Figure 5.22 Contour plot of blade deformation for (a) Uniform velocity (b) Velocity profile	105
Figure 5.23 Contour plot of blade equivalent stress for (a) Uniform velocity (b) Velocity profile.....	105
Figure 5.24 Variation of Blade 1 (a) Deformation (b) Equivalent stress during two rotation cycles.....	106
Figure 5.25 Biaxiality indication for blade in uniform velocity and velocity profile.....	109
Figure 5.26 Fatigue factor of safety for blade (a) Uniform velocity (b) Velocity profile	109
Figure 6.1 Dimensional details of domain used for all the array simulations	114
Figure 6.2 Mesh in the computational domain (a) and turbine surfaces (b) for array simulations	115
Figure 6.3 Prism elements layers generated around the blade surfaces.....	116
Figure 6.4 Normalized velocity contour on a horizontal plane across the width of channel at mid depth for single turbine in standalone domain.....	119
Figure 6.5 Normalized velocity contour on a horizontal plane across the width of channel at mid depth for single turbine off-center located in experimental domain.....	119
Figure 6.6 Normalized velocity contour on a horizontal plane across the width of channel at mid depth for single turbine center located in experimental domain.....	120

Figure 6.7 Normalized velocity contour on a horizontal plane across the width of channel at mid depth for single turbine in array domain.....	120
Figure 6.8 Normalized velocity contour across the depth of channel on a vertical plane passing through turbine centerline for single turbine in standalone domain	122
Figure 6.9 Normalized velocity contour across the depth of channel on vertical plane passing through turbine centerline for single turbine off-center located in experimental domain.....	122
Figure 6.10 Normalized velocity contour across the depth of channel on a vertical plane passing through turbine centerline for single turbine center located in experimental domain	122
Figure 6.11 Normalized velocity contour across the depth of channel on a vertical plane passing through turbine centerline for single turbine in array domain	123
Figure 6.12 Velocity deficit along a line passing through the hub center throughout the length of domain	124
Figure 6.13 Schematic of three turbine co-axial array with 8D interdevice spacing.....	126
Figure 6.14 Schematic of three turbine staggered array with 2D transverse and 4D longitudinal spacing.....	126
Figure 6.15 Vertical profile of incident velocity for turbine operating in co-axial arrays recorded at 2D upstream of each turbine	128
Figure 6.16 Vertical profile of incident velocity for turbine operating in staggered arrays recorded at 2D upstream of each turbine	128
Figure 6.17 Mesh for three turbine arrays	130
Figure 6.18 Power extraction from co-axial configuration of turbine arrays	135
Figure 6.19 Power extraction from staggered configuration of turbine arrays.....	136
Figure 6.20 Velocity deficit for (a) Two turbine (b) Three turbine co-axial arrays	139
Figure 6.21 Velocity deficit for (a) Two turbine (b) Three turbine staggered arrays.....	141

Figure 6.22 Normalized velocity contours for CA-3T-L8D array on a vertical plane at mid width, horizontal plan at mid depth and cut outs of transverse plan immediately behind each turbine.....	143
Figure 6.23 Normalized velocity contours for CA-3T-L10D array on a vertical plane at mid width, horizontal plan at mid depth and cut outs of transverse plan immediately behind each turbine.....	145
Figure 6.24 Transverse profiles of normalized velocity 2D upstream of each turbine for the three turbine co-axial arrays (Red dash dotted lines represent the span of turbine blades)	146
Figure 6.25 Vertical profiles of normalized velocity 2D upstream of each turbine for the three turbine co-axial arrays (Red dash dotted lines represent the span of turbine blades)	147
Figure 6.26 Transverse and vertical profiles of normalized velocity 4D downstream of each turbine for the three turbine co-axial arrays (Red dash dotted lines represent the span of turbine blades).....	149
Figure 6.27 Normalized velocity contours for SA-3T-S1.5D-L4D array on vertical planes along the center line of each turbine and horizontal plan at mid depth	151
Figure 6.28 Normalized velocity contours for SA-3T-S1.5D-L6D array on vertical planes along the center line of each turbine and horizontal plan at mid depth	152
Figure 6.29 Normalized velocity contours for SA-3T-S2D-L4D array on vertical planes along the center line of each turbine and horizontal plan at mid depth	153
Figure 6.30 Normalized velocity contours for SA-3T-S2D-L6D array on vertical planes along the center line of each turbine and horizontal plan at mid depth	154
Figure 6.31 Normalized velocity contours for three turbine staggered arrays on cut outs of transverse plan immediately behind each turbine	155
Figure 6.32 Transverse profiles of normalized velocity for the three turbine S1.5D staggered arrays (black dashed lines represent the span of 1 st row turbines blades and the red dashed lines the span of downstream turbine C blades)	157

Figure 6.33 Vertical profiles of normalized velocity for the three turbine 1.5D staggered arrays (Red dash dotted lines represent the span of turbine blades)	160
Figure 6.34 Transverse profiles of normalized velocity for the three turbine S1.5D staggered arrays (dashed lines represent the span turbine blades).....	163
Figure 6.35 Vertical profiles of normalized velocity for the three turbine 2D staggered arrays (Red dash dotted lines represent the span of turbine blades)	166
Figure 6.36 Definition of blade loads for tidal current turbine.....	167
Figure 6.37 Pressure and viscous forces on wall boundaries in ASYS CFX	168
Figure 6.38 Moment loads on the blade of turbine A operating in co-axial array. Time history of moment loads (a) edge-wise (b) flap-wise and moment load normalized with respect to cycle mean during a single turbine rotation (c) edge-wise (d) flap-wise	169
Figure 6.39 Moment loads on the blade of turbine B operating in co-axial array. Time history of moment loads (a) edge-wise (b) flap-wise and moment load normalized with respect to cycle mean during a single turbine rotation (c) edge-wise (d) flap-wise	171
Figure 6.40 Moment loads on the blade of turbine C operating in co-axial array. Time history of moment loads (a) edge-wise (b) flap-wise and moment load normalized with respect to cycle mean during a single turbine rotation (c) edge-wise (d) flap-wise	173
Figure 6.41 Moment loads on the blade of turbine A operating in staggered array with transverse spacing of 1.5D. Time history of moment loads (a) edge-wise (b) flap-wise and moment load normalized with respect to cycle mean during a single turbine rotation (c) edge-wise (d) flap-wise.....	178
Figure 6.42 Moment loads on the blade of turbine B operating in staggered array with transverse spacing of 1.5D. Time history of moment loads (a) edge-wise (b) flap-wise and moment load normalized with respect to cycle mean during a single turbine rotation (c) edge-wise (d) flap-wise.....	179
Figure 6.43 Moment loads on the blade of turbine C operating in staggered array with transverse spacing of 1.5D. Time history of moment loads (a) edge-wise (b) flap-wise and	

moment load normalized with respect to cycle mean during a single turbine rotation (c)
edge-wise (d) flap-wise..... 181

Figure 6.44 Moment loads on the blade of turbine A operating in staggered array with
transverse spacing of 2D. Time history of moment loads (a) edge-wise (b) flap-wise and
moment load normalized with respect to cycle mean during a single turbine rotation (c)
edge-wise (d) flap-wise..... 185

Figure 6.45 Moment loads on the blade of turbine B operating in staggered array with
transverse spacing of 2D. Time history of moment loads (a) edge-wise (b) flap-wise and
moment load normalized with respect to cycle mean during a single turbine rotation (c)
edge-wise (d) flap-wise..... 186

Figure 6.46 Moment loads on the blade of turbine C operating in staggered array with
transverse spacing of 2D. Time history of moment loads (a) edge-wise (b) flap-wise and
moment load normalized with respect to cycle mean during a single turbine rotation (c)
edge-wise (d) flap-wise..... 188

List of Tables

Table 3.1	Blade element sections characteristics for the 1:40 RM1 SAFL model turbine blade of NACA 4415 profile.....	36
Table 4.1	Coefficients for the Willcox $k - \omega$ and SST turbulence models	47
Table 4.2	Grids Statistics	52
Table 4.3	Torque predictions from the mesh refinement study	53
Table 4.4	Difference between experimental and simulated performance coefficients .	55
Table 4.5	Details of fluid domain for blockage study.....	59
Table 4.6	Blade design parameters for full size SAFL RM1 Turbine	64
Table 4.7	Mesh details and predicted torque results for sensitivity analysis.....	73
Table 4.8	Quantitative comparison of turbine C_P between full scale simulations and model scale experiment.....	75
Table 5.1	Properties of the utilized structural steel material.....	83
Table 5.2	Quantitative comparison of Numerical and Experimental predictions.....	85
Table 5.3	Details of utilized computational resource and time.....	89
Table 5.4	Quantitative comparison of turbine C_P between coupled FSI simulations, transient CFD analysis and experimental data.....	96
Table 5.5	Turbine loads variation during a rotation cycle	100
Table 5.6	Turbine load fluctuations from the last rotation cycle	107
Table 6.1	Domains details for developing RANS CFD methodology for simulating flow over a turbine operating in array domain.....	113
Table 6.2	Quantitative comparison of RANS CFD prediction for turbine CP within different sizes computational domains.....	118
Table 6.3	Definition and nomenclature of simulated array configurations	125

Table 6.4	Depth averaged values of incident velocities and corresponding rotational speeds set for turbines in all simulated array configurations.....	130
Table 6.5	Grid statistics for array simulations	131
Table 6.6	Area averaged y^+ values on the turbine blades for array simulations	132
Table 6.7	Power coefficient CP values for turbines in all the array configuration.....	133
Table 6.8	Total power extracted by all simulated array configurations	135
Table 6.9	Load variation statistics for the blade of turbines operating in co-axial arrays	174
Table 6.10	Load variation statistics for the blade of turbines operating in the 1.5D staggered arrays	183
Table 6.11	Load variation statistics for the blade of turbines operating in the 2D staggered arrays	189

Chapter 1

Introduction

1.1 Motivation

The society is currently facing the issues of energy and climate change [1]. The global energy consumption is increasing with an associated increase in greenhouse gas emissions due to the burning of fossil fuels [2]. The contribution of energy production and use to the total greenhouse gas emissions is about 67%, which is quite substantial [3]. Therefore, the goals of climate change control can only be achieved by minimizing the energy related greenhouse gas emissions and that is only possible through the development of renewable energy technologies. The global energy system is going through a transformation phase and renewables are replacing conventional fossil fuels based energy resources. In 2017, renewable energy contributed about 25% to the total global power generation [3]. The wind and solar energy sectors are witnessing a substantial growth. Solar PV and wind added 94 GW and 47 GW respectively to the global power generation capacity in 2017 [4]. Many renewable energy technologies are maturing while some new concepts are also being explored. Tidal current energy is one such concept that is attracting a lot of interest from the developers and researchers all over the world.

Tidal current energy is a form of hydrokinetic energy extracted from the water flows in tidal channels. Such flows takes place due to the relative motion of the gravitational fields of the moon, sun and earth [5]. Normally the velocity of flow in tidal channels is very slow but in areas constrained with in the head lands and sea bed topography, narrow passages like creeks and estuaries, the currents are accelerated to higher velocities. Tidal current flow velocity of 1.5-2 m/s is generally considered suitable for economic power production [6-8]. The global tidal energy resource estimates are greatly varied and several such estimates are available in the current literature. Details about the estimates prepared by different global organizations is available in [9] and estimates reported in the research articles is available in [10-12]. Although, it is difficult to report a single or range of

estimates based on the available data. However, the global resource estimation work so far clearly suggest that the global tidal energy potential is quite significant and it can provide a new renewable energy source to the world.

Tidal energy technology has successfully gone through various development phases, with demonstration systems currently operating in relevant environments at pre-commercial scales [13, 14]. The Technology Readiness Level (TRL) of ocean energy technologies is shown in Figure 1.1.

	Full commercial application, technology available for consumer	
	First of kind commercial system. Manufacturing issues solved	
TRL 7	Demonstration system operating in operational environment at pre-commercial	Tidal Energy
TRL 6	Prototype system tested in intended environment	Wave Energy
TRL 5	Large scale prototype tested in intended environment	OTEC and Salinity Gradient
TRL 4	Small scale prototype built and tested in a laboratory environment	
TRL 3	Applied research. First laboratory test completed, proof of concept	
TRL 2	Technology formulation. Concept and application have been formulated	
	Basic research. Principles postulated and observed but no experimental proof available	

Figure 1.1 TRL of ocean energy technologies, according to the scale employed by European Commission Horizon 2020 [13]

Tidal energy resources are concentrated in narrow channels [15, 16]. Therefore, it is necessary to optimally utilize the available space for maximum energy extraction. This would require to install tidal turbines in the form of dense (i.e., closely packed) arrays, which at present is the last remaining hurdle on the way to commercialization [16, 17]. Additionally, the installation of turbines in arrays is also necessary because a stand-alone turbine could not justify the cost of grid connection and establishment of navigation and maintenance facilities [18].

The development of tidal turbine arrays and the design of turbines in these arrays require an understanding of the interaction between devices. A substantial part of the current research on tidal energy is focusing this understanding [19-21]. The downstream devices operating under the influence of operational effects of upstream devices would either receive an increased or decreased onset velocity depending upon the array design and turbine location within the array [17, 22]. Consequently, the performance and blade structural loads for the downstream devices would be influenced by the upstream devices. Because, the power output and blade structural loads are both functions of the onset velocity. Most of the current research is investigating the tidal turbine array micro and macro design/optimization with an objective to maximize the total array power output [23-25]. However, the other important array associated impact of blades structural loads have not been investigated so far.

The power output of a turbine deployed in array at a certain site would be different than its power output based on the same site conditions as a standalone device. Therefore, the criterion for the design of turbines needs to be changed and the devices may be designed for the intended operation in arrays rather than as standalone turbine. The blades structural loads follow the trend of power output of the turbine. Increased power output of a turbine means higher structural loads on the turbine and thus the turbine should be more robust having higher construction cost and vice versa. It is therefore very important to characterize the blade structural loads and quantify their variations for turbines operating in arrays to be able to develop comprehensive structural design specifications and ensure improved reliability of the turbine blades against early failures. The lack of understanding of the influence of devices interaction with in arrays on the blade structural loads would make the devices to be either over designed or under designed. Both these possibilities may impede further development of the technology by making it either costly or unreliable.

1.2 Research Problem

Arranging turbines in various configurations and inter device spacing in a tidal array results in the turbine experiencing different onset velocity. As a result, the turbines operating in array exhibit different performance and encounter different structural loads depending upon their respective location in the array and array design. Therefore, it is necessary to

investigate the effect of operation of upstream devices on the blades structural loads of downstream devices in different array layouts with different inter device spacing to enhance the understanding of turbine design from an array perspective.

1.3 Aim and Objectives

The aim of this study is to characterize the structural loads encountered by tidal turbine blades operating in different array layouts with different inter device spacing. The investigations in this research employ Reynolds-Averaged Navier-Stokes (RANS) Computational Fluid Dynamics (CFD) and Coupled Fluid Structure Interaction (FSI) simulations to achieve the following proposed objectives:

1. RANS CFD simulation of the scaled model SAFL RM1 tidal turbine performance in the experimental channel to investigate the influence of blockage and boundary proximity on turbine performance and their implications to tidal turbine arrays.
2. RANS CFD simulation of the transient performance of full scale SAFL RM1 tidal turbine with nacelle and support structure to model the turbine performance and flow field at full scale.
3. Development of coupled FSI methodology for modelling the performance and structural response of blades with realistic structural design for the SAFL RM1 tidal turbine to quantify the effect of blade deformation on the performance and blade loads predictions of the RANS CFD model in the evaluated flow conditions.
4. RANS CFD simulations of the three turbines co-axial and staggered arrays of full scale SAFL RM1 turbine with different inter device spacing to model the influence of operation of upstream devices on the performance and blade structural loads of downstream devices.

1.4 Research Methodology

The proposed research work utilized an open source tidal turbine design developed by the US Department of Energy named as Reference Model 1 (RM1). Experimental tests on the 1:40 scaled model of this turbine are conducted in the open channel facility at the University of Minnesota's St. Anthony Falls Laboratory [26]. Experimental performance data from these tests is used for the validation of numerical models throughout this thesis.

The ANSYS Workbench software is used with its fluid flow analysis system (CFX), structural analysis system (Transient Structural) and coupling component (System Coupling) for the simulations performed in this study. The study begins with steady state RANS CFD simulations using a Multiple Frame of Reference (MFR) approach and Shear Stress Transport (SST) turbulence model to simulate the performance curve of the scaled model RM1 turbine rotor. The RANS CFD method is spatially verified and experimentally validated with the open source experimental measurements of University of Minnesota's St. Anthony Falls Laboratory [26]. A blockage and boundary proximity study is performed with the validated CFD methodology to establish the effect of size of computational domain on the performance of turbine. The RANS CFD method for simulating turbine performance is further extended to model the transient performance and blade loads for a full scale complete tidal turbine including support tower and nacelle with a transient rotor stator frame change model employing a sliding mesh method. This approach more accurately models the relative motion between moving and stationary domains and the rotation of turbine is physically modelled at each time step.

The RANS CFD simulations are followed by the coupled FSI simulations for modelling the performance and structural response of blades for the scaled model rotor and full scale complete tidal turbine with blades consisting of realistic structural design. These simulations are necessary to quantify the deformation of blades of full scale SAFL RM1 turbine and its influence on the RANS CFD predictions of turbine performance and blade structural loads.

Finally, RANS CFD simulations of the three turbine co-axial and staggered arrays of full scale SAFL RM1 turbine with different inter device spacing are performed to model the influence of operation of upstream devices on the performance and blade structural loads of downstream devices. Details about all the simulation procedures and case studies are explained later in this thesis. The overall methodology flow chart is provided in Figure 1.2 to give a bird's eye view of the work carried out.

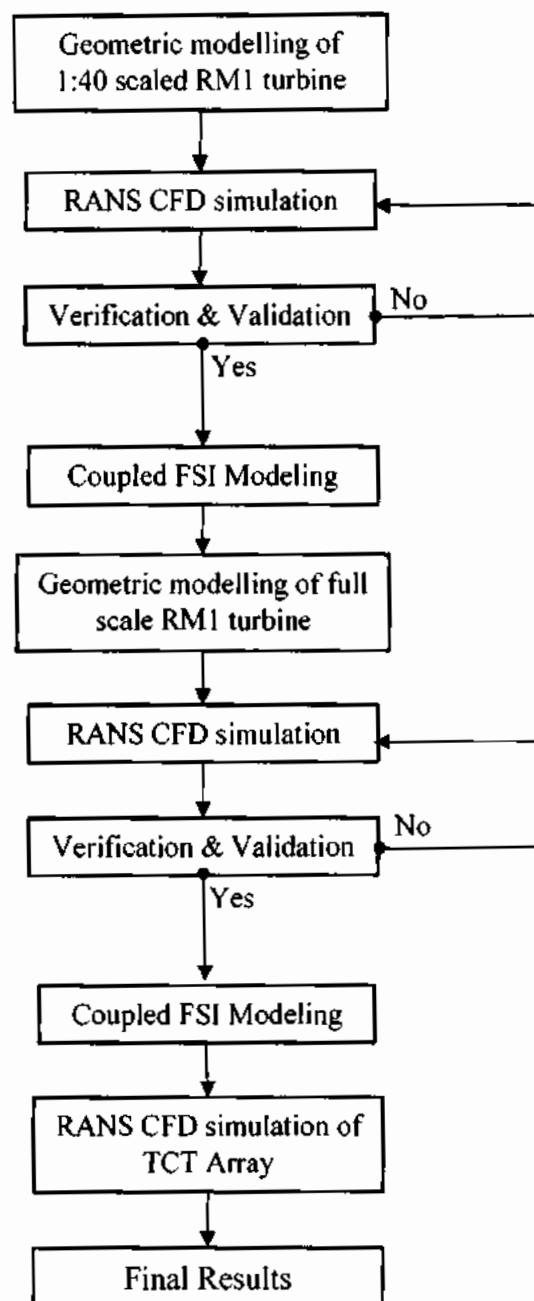


Figure 1.2 Flow chart of research methodology

1.5 Outline

This thesis is structured into 7 chapters to present details of the important aspects of study. Chapters in this thesis are ordered as follows:

Chapter 1: Introduction

This chapter contains the motivation behind this study with an update on the present status of tidal energy development and dynamics of turbines operating in tidal arrays. Aim and objectives of the proposed study are outlined to provide an overview of the project targets.

Chapter 2: Literature Review

This chapter presents a review of the main research work important in the context of current thesis with a discussion on the background theories and concepts. The performance prediction, structural loads, wake and arrays of tidal current turbines has been discussed and the relevant research conducted so far in these areas is reviewed.

Chapter 3: Turbine Design

This chapter presents an overview of the globally recognized potential design of future tidal energy devices. The design procedure for HAT is described with a discussion on how these design aspects would influence the turbine operation. The turbine design utilized in this research (SAFL RM1) is described along with a background of its evolution from the original RM1 design.

Chapter 4: Development of the RANS CFD Methodology for predicting Tidal Turbine Performance

In this chapter, the experimental setup used by the University of Minnesota's St. Anthony Falls Laboratory (UMN-SAFL) for the investigation of model scale turbine performance is presented. The development of steady state RANS CFD methodology for the performance prediction of 1:40 scale SAFL RM1 turbine rotor is described along with its verification and validation with experimental data. Necessary changes made to the developed RANS CFD methodology has been detailed for its extension to simulate the transient performance of full scale SAFL RM1 turbine including nacelle and support tower.

Chapter 5: Fluid Structure Interaction Modeling of Tidal Current Turbine Performance and Loads

This chapter describes the coupled FSI simulation methodology for modelling the performance and structural response of the scaled model SAFL RM1 tidal turbine rotor. A comparison of results from these FSI simulations with experimental data and RANS CFD simulations has been provided. Contour plots of rotor deformation, equivalent stress and

time histories of deformation and stress obtained from the structural analysis component of the coupled FSI simulations are provided to describe the structural response of the blade. Similarly, the hydrodynamic and structural response of full scale turbine blade has been described from the results of coupled FSI simulations of the full scale SAFL RM1 turbine with blade of realistic structural design and including nacelle and support tower.

Chapter 6: Effect of inter device spacing and array layout on the performance of tidal turbine and blade loads

This chapter presents the development of RANS CFD methodology to simulate tidal turbine arrays for the investigation of performance and blade structural loads variations of turbines operating in co-axial and staggered array configurations with different transverse and longitudinal interdevice spacing. Results from these array simulations for the performance of individual turbines and total array power output are described for 10 different array configurations. The wake of all tidal turbine arrays has been characterized and the results are presented in the form of normalized velocity contours, velocity profiles and velocity deficit along the channel length. Finally, the blade structural loads behavior and loads variations for turbines operating in arrays of different layouts with different inter device spacing has been quantified.

Chapter 7: Conclusions and Recommendation for Future Work

This chapter summarizes the conclusions drawn from the results achieved in this thesis and recommends directions for future research.

Chapter 2

Literature Review

This chapter provides a review of the main research work important in the context of current thesis with a discussion on the background theory and important concepts.

2.1 Historical Background

History reveals that the tide/water mills existed in the 7th century. Al-Muqadassi, a famous Arab geographer, described the tide mills operating in Iraq (Basra) in 10th century [27]. Ocean energy, particularly the tidal energy, for the production of electricity was first suggested by Romanoski in 1950 [28]. However, literature pertinent to the concept of energy from ocean currents existed well before him and these concepts are being investigated for the last forty years [29]. A functional tidal power station was available at the Boston Harbor in Massachusetts, USA in the latter part of the 19th century while another was operating in Husum, Germany that was dismantled in 1914 and another in China in 1958 [27]. However, the La Rance tidal power station established in France on November 26, 1966 is recognized as the first major tidal barrage for the extraction of tidal energy [30]. Research on the generation of renewable energy including tidal energy never continued along consistent lines. The 1973 oil crisis provided the basis for renewed interest, while the falling oil prices in 1980s caused a decline in the official support for developing renewable energy. In the mid-1990s, once again interest in large scale deployment of renewable energy increased due to the perceived threat of global warming highlighted by the Koyoto Process [31]. This renewed interest resulted in projects like the world's first, 10 kW scaled model, tidal current turbine that was tested on Loch Linnhe, a Scottish sea-loch, during 1994-95 by IT power UK [29]. In 1998, the company initiated the world's first tidal current energy system called Seaflow. This 300 kW tidal turbine was installed in North Devon in May 2003 [32]. Based on the concept of SeaFlow, Marine Current Turbine (MCT) installed a twin rotor steel mono pile mounted 1.2 MW commercial proto type turbine called SeaGen in July 2008 that is still successfully providing power to the grid

[29]. The installation and successful operation of Seaflow in open sea can be regarded as the turning point for the present day developments in tidal current technology.

2.2 Performance Prediction

The design and performance prediction of TCT is one of the research area that has attracted a lot of interest. The performance of TCT's can be estimated through lab scale experiments and numerical models.

Lab scale experimental tests have made enormous contribution to the existing knowledge on tidal turbine performance. The experimental trials by Bahaj et al. [33] quantified the power and thrust coefficient of a 0.8 m diameter TCT rotor in a cavitation tunnel and towing tank to prepare a robust experimental data set for the validation of numerical models. Similarly, Bal et al. [34] studied the cavitation inception with a 0.4 m diameter rotor and quantified the torque and thrust in a cavitation tunnel. Tedds et al. [35] investigated the near wake region behind a TCT in a recirculating water channel and provided three-dimensional velocity and Reynolds normal and shear stress data. The lab scale studies were later extended to investigate the effect of several hydrodynamic conditions for its implications to turbine design and performance. De Jesus Henriques et al. [36] reproduced wave current interaction effects in their recirculating water channel experiments to observe its influence on the turbine performance. In addition to these lab scale experiments, some real sea tests designed for quantifying the performance of TCTs have also been conducted, including those by Jing et al. [37] and Liu et al. [38]. Laboratory studies have over the years provided reliable information that have greatly helped in the development of tidal turbines to the present state. However, all the marine conditions cannot be replicated in the experimental channels and the results are also subjected to scaling issues and blockage corrections. Numerical models on the other hand are more capable to model the actual marine environment at full scale. Although these models have their own limitations and complexities but their intelligent use can greatly reduce the cost of experimental work.

Several numerical models have been proposed over the years for the design and performance evaluation of TCT to reduce the cost and address some of the limitations of experimental work. These numerical models have enabled the description of physical and

operational performance of TCT's to help in the design, optimization and performance evaluation. Blade Element Momentum (BEM) theory is one such model that has been successfully applied in wind turbine design and later extensively utilized in the tidal turbine performance evaluation and design. BEM theory is based upon the combination of general momentum and Blade Element theory [39]. The momentum theory is used for the calculation of axial and tangential induction factors while taking into account the tip losses. The Blade element theory divides the blade into a number of sections to calculate the torque and drag at each section. The integration of these sectional drags and torques gives the values of total blade torque and drag. In the BEM theory based methods, the blade is discretized into a number of stations along the blade length at radius " r " and the blade design parameters are evaluated as shown in Figure 2.1.

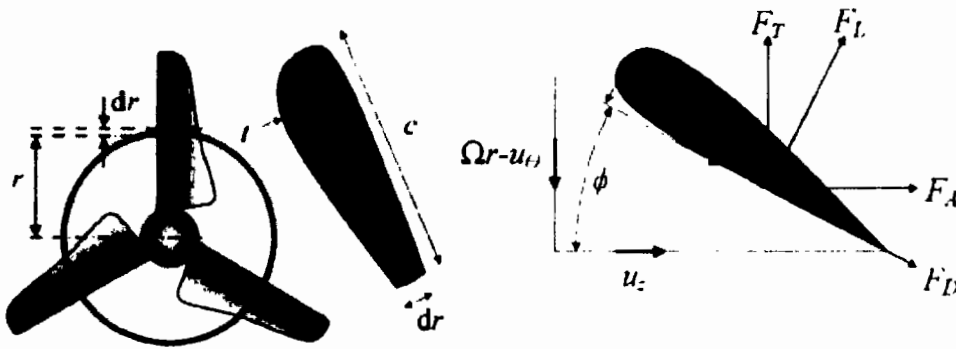


Figure 2.1 Schematic diagram of the discretization of rotor and resolution of the lift and drag forces [24]

The BEM theory model has been successfully used to develop numerical tools for the performance prediction of TCT and span wise distribution of blade loads [40, 41]. These numerical tools have been successfully validated through experimental tests in cavitation tunnels and towing tanks for several design exercises and parametric studies [33, 41]. Batten et al. [40] used their developed tool to study the cavitation inception and the effect of velocity profile, blade fouling and blade pitch angle on turbine performance. Whereas, O'Rourke et al. [42] used BEM model in the unsteady formulation to quantify the effect of velocity shear and yaw misalignment on the performance of TCT. To develop an understanding of the turbine design process based on the BEM theory model for this thesis, we also used the Harp_Opt tool developed by the National Renewable Energy Laboratory (NREL) to predict the performance of TCT and study the effect of number of blades on

turbine performance [41]. The BEM approach is computationally very efficient but it does not account for chord wise loading, variation in free stream flow and influence of rotor on the surrounding flow [24, 39].

Computational Fluid Dynamics (CFD) is another numerical approach that has been extensively used for the turbine design studies and performance evaluation. CFD accounts for the limitation of BEM because it can equally resolve the three-dimensional (3D) flow field in the near and far wake to provide more detailed flow field information. CFD derives its basis from the fact that the physics of any fluid flow can be described by three fundamental principles of conservation of mass, momentum and energy. These fundamental principles, in their most general form, are expressed either in the form of integral or partial differential equations. CFD is the art of converting these integral or partial differential equations, governing the fluid flow, into its discretized algebraic form that can be solved numerically [43]. These flow governing equations are called Navier-Stokes equation. CFD utilizes various numerical schemes for the solution of Navier-Stokes equations to provide detail information of the fluid flow. The information about the fluid flow is translated into performance parameters of TCT. The performance data includes thrust, torque and power estimates. CFD model can also map the pressure distribution on the blade surfaces to predict the inception of cavitation. Among, the various CFD approaches, the Reynolds Averaged Navier Stokes (RANS) models are more common due to comparatively less computational expense. In this approach the time averaged Navier-Stokes equation are solved through turbulence model to solve all the turbulent length scales. RANS models can be broadly classified into Reynolds-Stress Models based on transport equation for Reynolds stresses and Eddy Viscosity Models based on Boussinesq hypothesis. The Reynolds-Stress Models are complex, computationally expensive and difficult to converge. The Boussinesq hypothesis is based on the assumption of isotropic turbulence, which is only valid for small scale turbulence [44]. Contrarily, turbulence in the near wake region of a tidal turbine is strongly anisotropic in nature [45] and the size of turbulence structure is of the same order of magnitude as the diameter of turbine [46]. Alternately, the Large Eddy Simulations (LES) models solves the spatially averaged Navier-Stokes equations and directly resolve large turbulence structures (eddies) but eddies smaller than the mesh are modelled. LES models have recently been used more frequently

for modeling the fluctuations of structural loads in tidal turbines due to turbulence. The spectral distribution of blade bending moments can be reproduced by using LES models with realistic inflow turbulence [47, 48] and sea bed generated turbulence [49]. However, the LES models are computationally expensive and require greater mesh accuracy, therefore, they are only preferred for situations involving the accurate resolution of large scale turbulence structures.

Numerous TCT performance evaluation studies have been performed in recent years by utilizing the RANS CFD simulations. As a part of this thesis, a RANS CFD methodology is developed and validated with experimental data to replicate the performance of TCT in experimental channel [50]. Later this simulation methodology is used to study the effect of channel blockage and boundary layer on TCT performance. In a similar work, Nitin et al. [51] modelled the performance of TCT under boundary proximity and different blockage conditions. Tatum et al. [52] investigated the response of performance to shear flow and surface gravity waves. Tian et al. [53] explored the effect of yaw angle and turbulence intensity on the performance. Liu et al. [54] investigated the effect of blade twist and nacelle shape on the performance. Tatum et al. [52] investigated the effect of velocity profile on the performance of TCT subjected to in and out of phase waves. All these and numerous others similar studies based on RANS CFD simulations suggest that this model can efficiently simulate the hydrodynamic behavior of TCT with a reasonable accuracy compared to experimental data.

2.3 Structural Loads

The wind and tidal current turbines have much in common but there are also certain key differences. One of the differences is in the amount of structural loads and the sources as well as behavior of certain loads. Blades of TCT are subjected to higher pressures and complex load regimes compared to wind turbine. Therefore, it is important to comprehend the character of structural loads faced by the blades of TCT to ensure its reliable and safe design and operation. The most critical part of TCT subjected to structural loads is the turbine blade and some of the earlier prototype tests have witnessed an early blade failure [55].

Rotor of a TCT converts the kinetic energy of the flow into mechanical work governed by the law of conservation of momentum. While the exchange of momentum mainly takes place in the flow direction, the power is produced in the rotor plane perpendicular to the stream direction. The fluid flow passing the turbine blade creates lift and drag forces as shown in Figure 2.2.

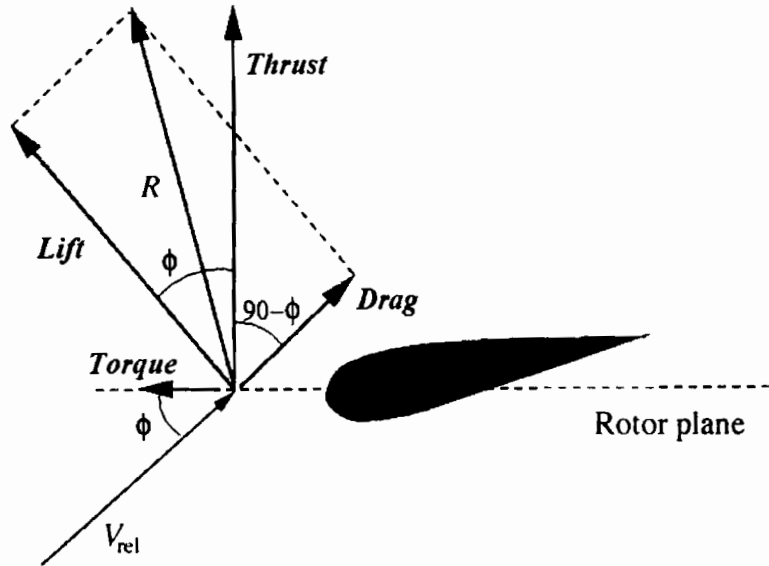


Figure 2.2 Local loads on a TCT blade [56]

The drag force is parallel, whereas the lift force is perpendicular to the resultant or relative flow velocity (V_{rel}). R is the vector sum of lift and drag, while torque and thrust are the normal and tangential components of R [56]. For Horizontal Axis TCT, the thrust force acts in the direction of flow and induce flap wise bending moment. The torque acts around the rotor shaft as edge wise bending moment and causes rotation. The possibility of failure due to these moments imposed by the flow can be minimized, if properly accounted for in the design. However, this would require detail knowledge of the tidal conditions and the way these would impact structural loads on the blade.

Hydrodynamic conditions in the actual marine environment are site specific and may vary considerably from site to site [46, 57]. A pictorial representation of some of these hydrodynamic conditions is shown in Figure 2.3.

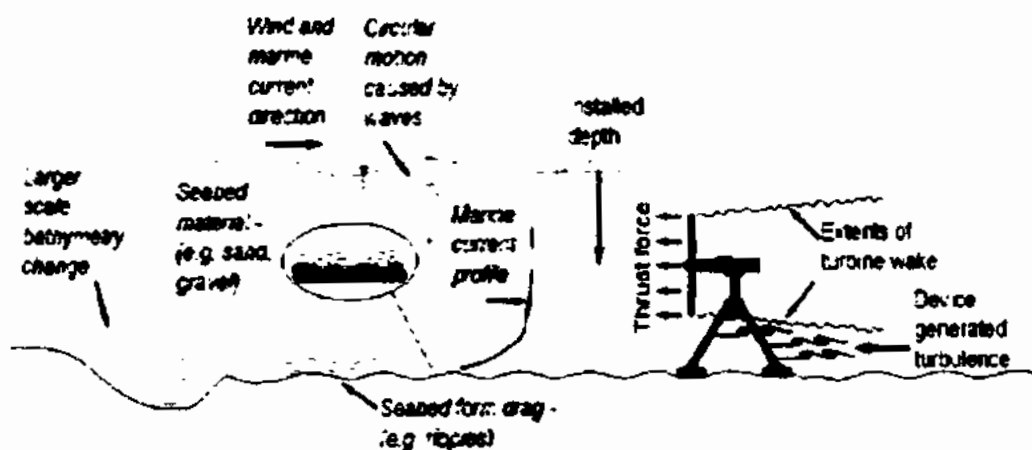


Figure 2.3 Variables affecting the flow field around tidal turbines [58]

Every hydrodynamic condition has different effects on the performance and structural loads of a tidal turbine [59]. Amongst the various hydrodynamic conditions, the inflow velocity [60], wave current interaction [61, 62], turbulence [20, 63] and velocity shear [64, 65] have been identified to have substantial effect on the turbine performance. Since the load forces follows the trend of power output, the effect of hydrodynamic conditions is also expected to influence the structural loads encountered by tidal turbine blades. The turbine blades may also be susceptible to fatigue failure caused by the rotation and periodic nature of hydrodynamic forces [66, 67]. A detail knowledge about the behavior and magnitude of loads variation and the effect of these loads variation on the fatigue life of blades due to various hydrodynamic conditions is therefore required to improve the reliability of turbines against structural failures.

A TCT should ideally be located near the free surface to utilize the higher flow velocities of tidal current. However, the optimum locating depth will be a compromise between the increased flow speed near the surface and distance from wave effects that could influence the turbine performance and structural loads [68]. The influence of a wave is expected to travel along the water column to a depth of about 50% of its wave length [69]. The wave effect may therefore be critically considered for selecting the limits of turbine locations and may be given due weightage in the design process [61, 67]. Although, the average performance of a turbine in terms of power and thrust is not affected by the wave influence [62, 68]. However, the wave current interaction imposes cyclic loading of increased amplitudes due to significant increase in the variation of thrust that increases the possibility

of fatigue failure [70, 71]. At lower current speeds the effect of wave only minimally affects the turbine thrust [61]. However, the change in wave height for longer waves greatly affects the fluctuation in edge-wise (in plane) and flap wise (out of plane) bending moments [72]. Similarly, For turbine operating at constant tip speeds, the shorter waves may force a stall that will cause a sudden increase in the thrust force [61].

Turbulence generated by various sources will impart stochastic loads to the turbine blades and is likely to cause most of the structural failures due to fatigue. The amplitude of flap-wise bending moment of the turbine blades increases due to unsteadiness in the hydrodynamic loads caused by the onset turbulence. This increase is much greater for turbine operating in dynamic stall and separation delays compared to the operating conditions of fully attached flow [73, 74]. The onset turbulence affects load fluctuations below the rotational frequency, while at higher frequencies the load fluctuations are governed by the operational phenomenon [75]. Additionally, the onset turbulence also influence the turbine power output with peak power coefficient variation of over 10% [63]. Since, a strong correlation exists between fluctuations in the blade root bending moments and rotor power coefficient. Therefore, the power fluctuation in turbine power output can be used as an indication of load variation and for the estimation of fatigue loads on turbine blades. Fatigue failure may also arise due to the sea bed generated turbulence that also needs careful consideration for evaluating turbine blades designs [76].

The velocity shear is caused by the sea bed friction, which reduces the current velocity such that its value at the bed is effectively zero. The height of the water column that is influenced by the sea bed friction is generally known as boundary layer thickness [40]. In relatively shallow waters with a depth range of 25-50 m, the boundary layer generally influences the entire water column. The first generation tidal devices will operate in shallow water and experience the effect of boundary layer [77, 78], which is typically termed as velocity profile. The effect of velocity profile will be more dominant if the turbine blades occupy a large percentage of the water column or located in the lower part of the water column. The velocity profile results in dropping the turbine power coefficient from its designed value compared to uniform velocity [64, 79]. Additionally, the velocity profiles cause cyclic oscillations in hydrodynamic loads due to the dependence of relative velocity on angular position, which can lead to fatigue damage. While these load

oscillations only minimally impact power and thrust fluctuation for rotors, they can significantly impact the load variations on individual rotor blades [52, 80]. The velocity profile increases the alternating stress on a turbine blade while the mean stress is decreased. The mean stress and stress range (alternating stress) are the two important parameters with prominent effects on the fatigue life of turbine blade. The fatigue strength of the blade under an axial load will decrease with increase in the mean stress and or stress range and vice versa.

2.4 Wake

Wake is the region of disturbed flow downstream of a solid body moving through a fluid or vice versa. A hydrokinetic turbine extracts momentum from the flow while the mass is conserved. The momentum loss downstream of the device creates a pressure jump and consequently an axial pressure gradient, an expansion of the wake and a decrease of the axial velocity. The wake is therefore characterized by a decrease in mean flow speed also called velocity/wake deficit and increased turbulence. Wake is a complicated and device specific phenomenon. The wake is generally divided into near and far wake region to simplify the physics governing the wake structure [81]. A simple representation of the wake characteristics and transition from near to far wake is shown in Figure 2.4.

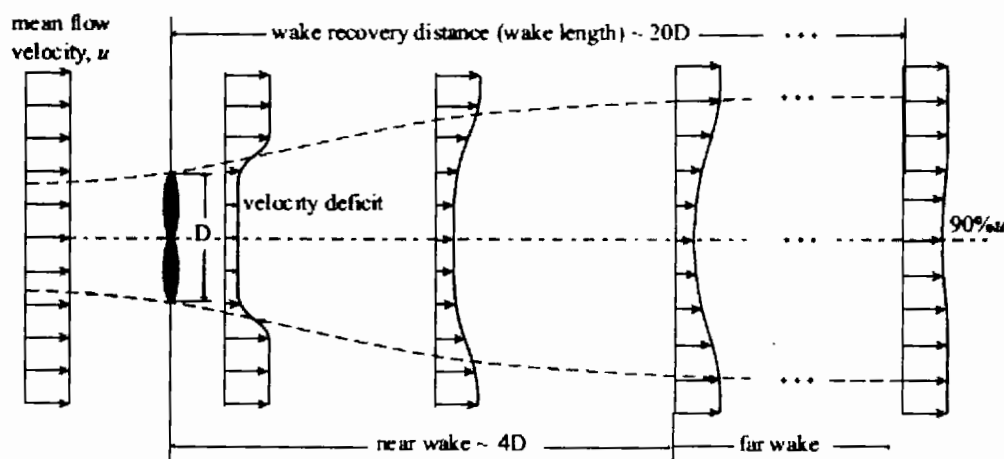


Figure 2.4 Illustration of wake characteristics [10]

A strict distinction of the near and far wake in terms of downstream distance may not be possible. In wind turbines, near wake is from 1-2 rotor diameters downstream [81], while for TCT it is considered to be from 0-3/4 rotor diameter downstream [82]. However, a clear understanding of near wake is that it is the region where the geometry of turbine has a

direct influence on the fluid flow. A hydrokinetic turbine converts energy extracted from the fluid flow into mechanical motion. The mechanical motion of blades produce vortex shedding from the blade tip. Vortices shedding along with support structure has a direct effect on the flow in the near wake region. Shedding of the vortices by the blade tip creates sharp velocity gradients and peaks in turbulence intensity. On the contrary, the turbine geometry affects the far wake indirectly. The indirect effect of geometry is in the form of decreased axial velocity and increased turbulence. The wake structure is governed by convection and turbulent mixing. For a completely inviscid flow the volume of slow moving fluid will just be convecting downstream at a slower rate than the free stream flow. But due to turbulent mixing the wake keeps on regaining energy and ultimately attains the free stream velocity farther downstream. In the near wake pressure field around the device is important, while in the far wake the turbulent mixing is important for the development of wake deficit. Mixing of the wake and recovery of velocity deficit in far wake takes place due to the turbulence and as a result the overall turbulence decreases [81, 83]. Wake is one of the most extensively researched area of tidal current energy. Wake studies are necessary to understand the effect of an upstream device on the performance and loading experienced by the downstream devices.

The research conducted on TCT wake so far suggest that wake deficit is maximum in the immediate wake region and tends to recover with increasing downstream distance. However, the wake persists for quite a long distance and up to twenty 20 rotor diameters about 90% of the free stream velocity is recovered [82]. A number of interdependent variable can affect the wake recovery rate. The main factors affecting the wake structure are the ambient turbulence, device thrust and the device induced turbulence [84]. The rate of wake recovery increases with increasing turbulence intensity [18, 60, 85, 86], while a higher device thrust reduces the wake recovery rate [85, 87]. The channel blockage and boundaries proximity also influences the wake behavior. TCT's operating in shallow waters will produce a different wake structure than those operating in deep waters. A satisfactory wake recovery will not be possible, if depth underneath the rotor is infinite [88]. The sea bed roughness contributes to the decrease in downstream wake velocity [85]. For turbines operating in shallow channels, the free surface and sea bed restricts the vertical expansion of the wake. However, at higher flow velocities, the wake expansion may reach

the free surface and create turbulence [83]. Additionally, at higher blockage ratios, the wake expansion raises the level of the free surface and will either increase the channel head further downstream or will mix with the wake of another adjacent TCT [83]. The support structure also has a substantial effect on the near wake along with synergetic effects from both the rotor and support structure in the downstream with diminishing effects in the increasing lateral distance [89].

2.5 Tidal Current Turbine Arrays

Majority of the identified tidal resources are in narrow channels [82, 86]. Full utilization of the available spaces and maximum energy extraction is imperative to fully exploit the global tidal energy potential. The concept of tidal turbines arrays or farms seems to be the ultimate solution to the problem. In addition, only tidal array can make the technology commercial and justify the cost of grid connection along with establishing, maintenance and navigation facilities [17]. Power generation from a standalone turbine will never be able to justify this huge cost [87].

Tidal arrays are classified into large and small arrays [17]. The term large array does not mean that channel will have a huge number of turbines. If the turbines extracts large portion of the channel potential, the array will be large irrespective of the number of turbines. A few turbines in a small channel can constitute a large array. Conversely, a number of turbines in a large channel can be a small array. A large array affects the “channel-scale dynamics” or improves the power co-efficient of turbines through “duct-effect”. Whereas a small array is one that cannot significantly affect the “channel-scale dynamics” and the performance of the individual turbine is not affected by other turbines or proximity to channel boundaries. It is essential to understand the dynamics of turbines with in large arrays for the development of tidal turbine arrays and the design of turbines in these arrays [22].

An array has two competing effects on the dynamics of flow in tidal channel. One is the “channel-scale dynamics” and other is the “duct-effect”. The channel-scale dynamics refers to the finite head loss due to power extraction from a channel [90]. A conceptual image of this head loss phenomenon is shown in Figure 2.5.



Figure 2.5 Tidal turbine array showing exaggerated changes in sea level [17]

This finite head loss causes additional drag and reduces free stream flow that limits the array power output. Due to this turbines in a channel interact with each other even if they are far enough from the wake effects of each other. In addition, any Bitz turbine operating in array, causes the array to lose 1/3 of its energy to turbulent mixing behind the turbine in near wake region [91]. About 5-10% of the energy is lost to support structure [92] and about 11% goes into electromechanical losses that imposes significant portion of the structural loads on turbine. The proportion of these loads highly depend upon the number of turbines, their arrangement and tuning in array. On the other hand, the duct-effect increases the free stream flow. Figure 2.6 describe the concept of duct effect in tidal arrays.

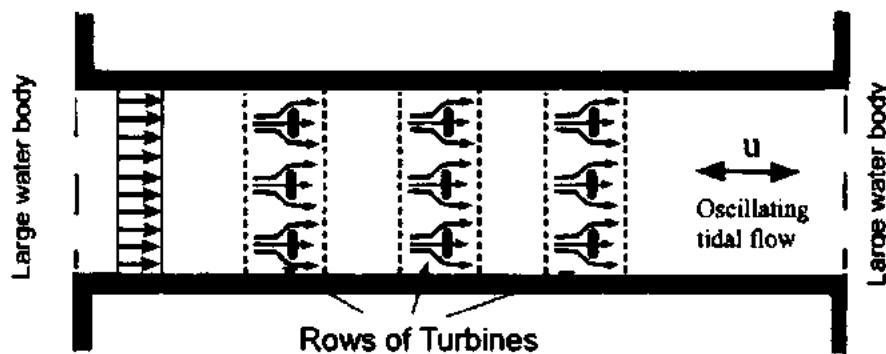


Figure 2.6 Duct effect in a tidal array [93]

Duct-effect improves the turbine thrust and power co-efficient in the array. It is possible for turbines operating in array to exhibit higher thrust and power co-efficient than that of a Bitz turbine [22].

In addition to these two effects, the design of array will dictate the amount of power output and loads on the individual turbine blades. Although, real turbine arrays would be based on complicated devices layouts and may not follow regular configurations. However, the

devices layout may somewhat resemble the axial and staggered configurations as shown in Figures 2.7-2.8.

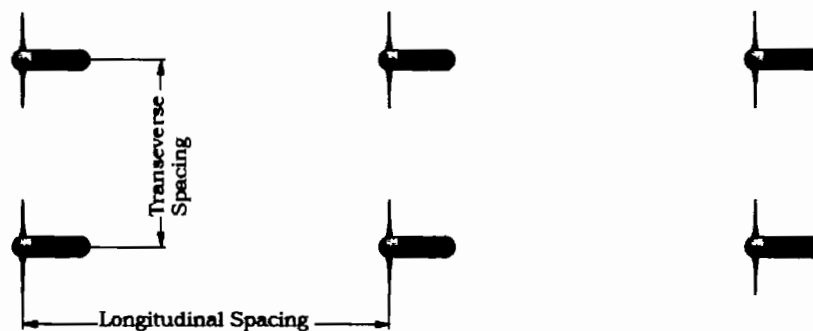


Figure 2.7 Axial array layout

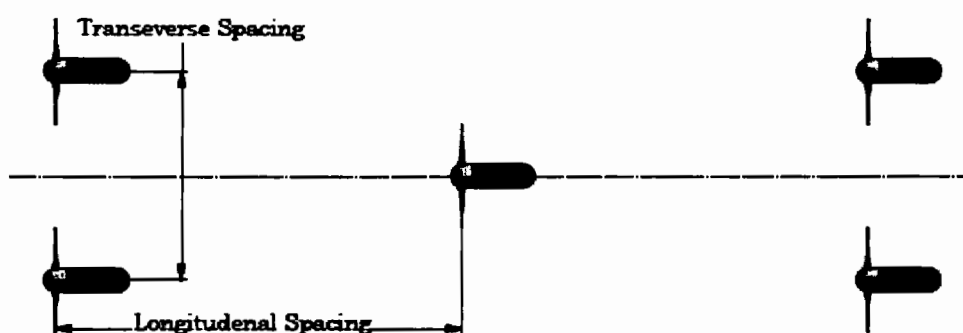


Figure 2.8 Staggered array layout

A simplified representation of staggered array is the offset configuration as explored in Stelzenmuller [94] and Javaherchi et al. [95]. The array layout and longitudinal as well as transverse/lateral spacing between turbines in array significantly influence the velocity and turbulence intensity of downstream flow [24]. The downstream devices in certain staggered configurations of arrays may receive a greater onset velocity than the free stream velocity of currents. This is because the flow can be accelerated between two laterally adjacent devices causing an increased thrust and power for the downstream devices in a staggered array configuration [24, 57, 96]. However, this definitely is not true for all lateral and longitudinal spacing and would also depend upon other several factors.

Several research studies have investigated the influence of array layout and interdevice spacing on the performance of turbines operating in arrays. Turnock et al. [23] observed higher power output compared to an unstaggered layout for the downstream turbine operating in the gap between turbines of the upstream row. However, the increase in power

output only took place for longitudinal and lateral spacing of less than six turbine diameters ($6D$). The optimal extent of lateral spacing for staggering turbines within arrays is array specific and therefore various researchers have suggested different values like $3D$ by Lee et al. [97], more than $2D$ by Malki et al. [24] and $2D$ by O'Doherty et al. [98]. The lateral spacing between 1st row upstream devices cannot be reduced beyond a certain limit because the wake recovery within the very closely packed staggered arrays is very slow with large areas of higher velocity deficits [99]. As observed by Nuernberg et al. [100], the shorter lateral spacing between the 1st row upstream devices would significantly decrease the power output of downstream device in staggered arrays. Malki et al. [24] observed that for lateral spacing of less than $2D$ between the adjacent turbines in the upstream row with downstream turbine located at more than $2D$, the performance of the downstream turbine is substantially reduced. Another important factor that would greatly influence decisions on the array design is the turbulence intensity in the approach flow known to enhance wake mixing [101]. Because, the relative advantage of increased longitudinal spacing in axial arrays diminishes with higher levels of turbulence intensity. Contrarily, in staggered arrays higher turbulence intensity reduces the relative disadvantage associated with increased lateral spacing between devices. Similarly, the wake recovery is minimally influenced by longitudinal spacing in a staggered array for flows with lower turbulence intensities, and therefore the associated advantages or disadvantages would no longer be applicable compared to arrays with flows of higher turbulence intensities [102]. Several other factors like the flow alignment is also crucial and can reverse the relative advantage of staggering compared to the axially aligned arrays. The staggered arrays produce more power for perfectly aligned flows along the turbine axis, while for misaligned flows the axial arrays are more efficient [103]. The direction of rotation of adjacent device can also influence the flow acceleration between staggered devices because the counter rotation of the adjacent devices reduce the shear rate that would further improve the performance of downstream devices [98, 104]. The array tuning adds another very important dimension to this discussion on the array layout, design and performance. The array tuning refers to employing or operating turbines with different thrust and power coefficients depending upon its respective location across the array. The differential tuning can be equally employed to both staggered and axial arrays. Although, the efficiency of an array can be

maximized by employing array tuning. However, the output of a staggered array cannot be maximized to an extent to exceed that achieved by an equivalent axial array [105]. Decision on turbine control strategies along with maximum number of turbines that could be installed to extract maximum power from an available resource would also have to be duly considered for the macro and micro design of arrays [106].

Although, it is an established fact now that staggering turbines within an array can increase the power output of downstream devices due to the local duct effect between adjacent upstream devices. However, this would depend on the inter row spacing and inter device spacing within a row specific to the array site and several other factors with some of them interdependent to each other. More importantly, this increase in the power output in terms of individual turbines would only be beneficial if it translates into an increase in the total array output. It is therefore still an unresolved challenge to optimize the array output by striking a balance between the blockage effects and wake interaction [107]. Because, single row arrays with higher local blockage are more efficient in terms of power output compared to multi row arrays with lower blockage [108]. Further investigations are required to establish the competitive advantages of single row arrays that exploit the duct effect or multiple rows staggered arrays that exploit accelerated flow between the gaps. While multiple row staggered arrays are more efficient than axial arrays, it is not clear that staggered layout is a better choice than single row array [104]. It is important to highlight that most of the array design efforts have focused regular grids of devices having identical performance coefficients. However, tidal flows in real channels have complex patterns and the optimal array layout therefore may not be a regular grid of devices with identical power coefficients [17]. An example of irregular grid arrays is as shown in Figure 2.9.

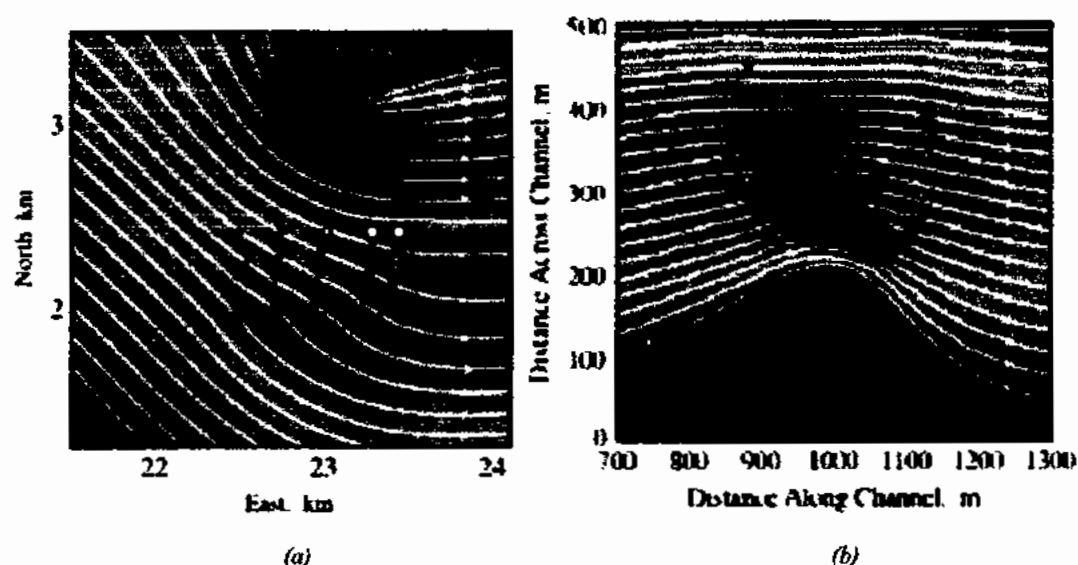


Figure 2.9 Irregular grid arrays (a) Example of optimized 50 turbine array in large channel in the south eastern Pentland Firth (b) Example of optimized 20 turbine array in the small channel with a headland constriction [17]

2.6 Summary

In this chapter, a review of the research related to the performance prediction, structural loads, wake and arrays of tidal current turbines is presented. These areas are selected because an understanding of the background knowledge and research in these areas is essential to conduct the proposed research in this thesis. Three different approaches consisting of experimental, BEM theory and RANS CFD models have been discussed along with a review of literature pertinent to the application of these techniques to the performance prediction of tidal current turbines. The structural loads on tidal turbine blade have been explained and a review of the literature has been provided to describe influence of various hydrodynamic conditions like the inflow velocity, wave current interaction, turbulence and velocity shear on the turbine performance and blade structural loads. Similarly, the wake structure behind a TCT has been described and literature discussing the effect of several variables like turbulence intensity, free stream velocity, turbine placement and channel blockage on the wake recovery rate has been reviewed. The effects of tidal turbine arrays on the dynamics of flow in a tidal channel have been described. A review of the current literature has been provided to highlight the implications of array layout and interdevice spacing on the turbine performance and blade structural loads.

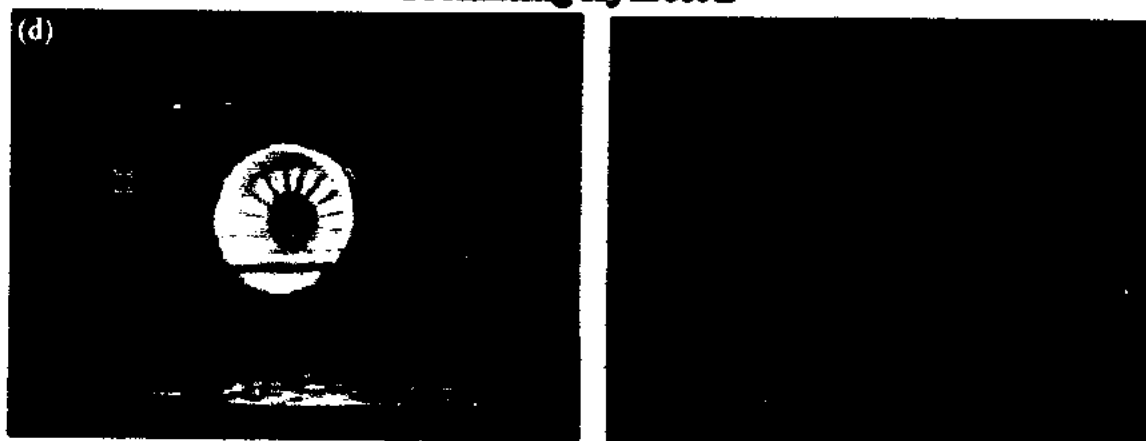
Chapter 3

Tidal Turbine Design

Significant developments in tidal turbine technology have taken place over the last few years. The Meygen project (1.5 MW) in Pentland Firth, Scotland and Shetland Array (200 Kw), Shetland Island, Scotland are operational since 2016 and these represent the most significant steps towards commercialization of tidal energy [109]. All tidal current turbines share the basic principal of converting kinetic energy of tidal flow into mechanical energy for rotating the generator. However, the way in which this design goal is achieved differs between various designs. Numerous designs of TCTs are reported in the literature and about forty new designs have been introduced in the period from 2006-13 [6]. However, this was the early phase of development and now the turbine technology has reached a higher level of technological maturity due to growing number of deployment projects. The turbine technology has not still fully converged. However, some turbine designs are now globally recognized as the potential designs of future tidal turbine. An overview of these turbine designs is as shown in Figure 3.1 and their Technology Readiness Level in Figure 3.2.



Horizontal Axis

**Vertical Axis****Oscillating Hydrofoil****Enclosed Tips**



Tidal Kite

Figure 3.1 Tidal Turbine Design (a) Horizontal Axis (b) Vertical Axis (c) Oscillating Hydrofoil (d) Enclosed Tips (e) Tidal Kite

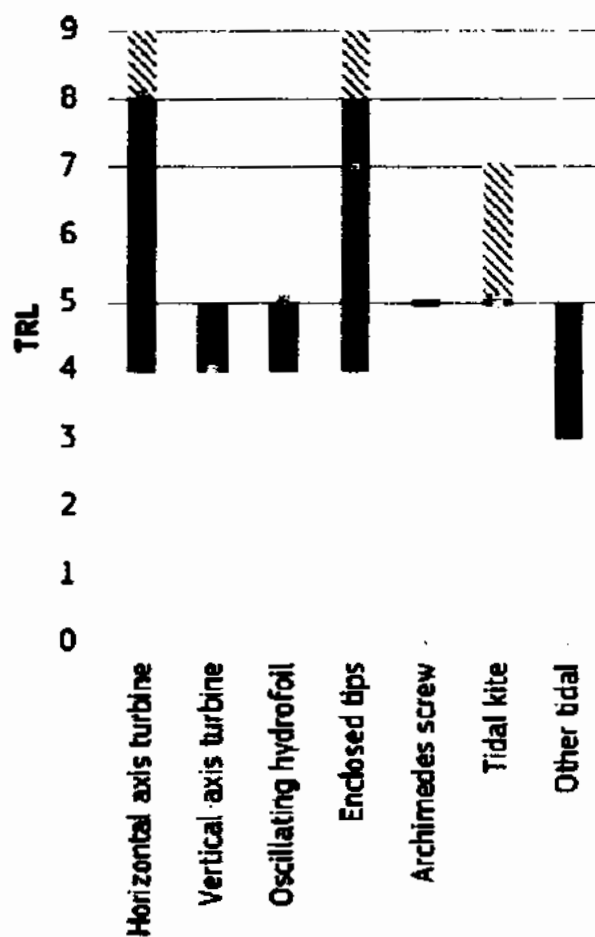


Figure 3.2 Technology Readiness Level (TRL) of tidal energy devices [109]

Figure Note: Blue bars refer to technology with significant progress in 2016. Red bars indicate technology with no considerable update/progress in 2016. Shaded bars indicated ongoing testing. The length of bar indicates the range of TRL attempted. The yellow dot indicates the maximum achieved TRL.

The Horizontal Axis Tidal Turbines (HAT) are currently at the highest level of development (TRL 8) (Figure 3.2). The tidal energy sector developers mostly believe that technology will converge on HAT [109]. HATs are attracting the major portion (76%) of the research and development (R&D) efforts [109, 110]. An overview of the R&D effort for tidal technologies in 2016 is as shown in Figure 3.3.

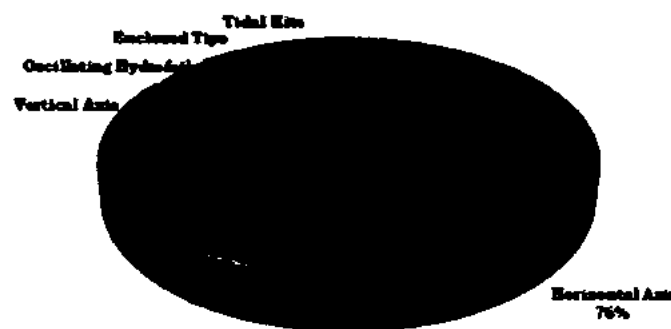


Figure 3.3 Share of tidal energy technologies among all the R&D effort for technologies tested at full-scale [109]

Although, designing a novel turbine is not the focus of this thesis. However, a brief overview of some of the design aspects and steps of the design process for HAT are provided to describe the underlying concepts.

3.1 Power Output

The power available in a flow stream is estimated as:

$$P_{Available} = \left(\frac{\rho \pi D^2 V^3}{8} \right) \quad (3.1)$$

According to Bitz limit only 16/27 of this available power can be extracted by a hydrokinetic turbine and this is the maximum power coefficient (C_p) that a standalone TCT can achieve [22]. In addition, the power train efficiency (η) sets another theoretical upper limit of 0.9 for the maximum power that can be extracted.

3.2 Blade Shape

The blade of TCT is composed of specific foil shapes located along the blade span having suitable twist angles and chord lengths. One of the most important consideration for selecting a hydrofoil for TCT blade is the glide ratio or turbine efficiency (ratio of lift to drag coefficient, C_L/C_D). But there are other aspects like the sensitivity to surface roughness which must also be duly considered. Additionally, tidal turbines operate in water and their blades face more loads as compared to wind turbine due to the higher density of water. Therefore, tidal applications require foils with relatively larger percentage thickness. Thicker foils also have the advantage to easily accommodate other necessary arrangements to make the blade stronger. Foils having low probability of stall are preferred for tidal turbine application. Because, sudden increase in current velocity creates sudden variation in the angle of attack (AOA). This sudden variation may force the turbine into a pre-stalled or stalled zone. Some special purpose airfoils have been developed for application in tidal turbines [111, 112]. However, some of the general purpose airfoils developed for other aerodynamic applications especially wind turbines can also be used for the tidal turbine blades. The turbine design utilized in this thesis is the University of Minnesota's St. Anthony Falls Laboratory (SAFL) Reference Model (RM1) and its blade profile is based on NACA 4415 airfoil. This is a cambered airfoil with a maximum camber of 4% at 40% chord length having a thickness of 15%.

3.3 Blade Chord

Mathematical expression for the determination of blade chord at a blade element is provided by the Schmitz formula [113]:

$$C = \frac{16\pi r}{C_L N} \sin^2 \left(\frac{1}{3} \tan^{-1} \left(\frac{R}{\lambda r} \right) \right) \quad (3.2)$$

Where C is the blade chord at a blade element at radius r, number of blades in the turbine is N, λ represents the tip speed ratio and R is the radius of turbine. " C_L " is the design coefficient of lift and its value is taken as 80% of the value corresponding to the design angle of attack (AOA) from the drag polar data of the airfoil.

3.4 Tip Losses

Rotating turbine blades form vertices at the blade tip. These vertices are a source of loss that decrease the lift force of the blade. The blade tip losses are determined using equation (3.3) presented by Ludwig Prandtl [113]:

$$f_{tip} = \frac{2}{\pi} \cos^{-1} \left[e^{((N/2)(1-\mu)/\mu) \sqrt{1+(\lambda\mu^2/(1-a^2))}} \right] \quad (3.3)$$

Where, “ μ ” is “ r/R ” with “ R ” representing the total radius of the turbine and “ r ” the radius of the respective blade element. The axial induction factor is represented as “ a ” and “ N ” represents the number of blades.

3.5 Blade Twist

The description of airfoil angles for a tidal turbine blade is shown in Figure 3.4. In this Figure α is the design AOA taken as the AOA for maximum glide ratio. The incidence angle is ‘ ϕ ’, $(U(1-a))$ is the component of velocity acting in the axial direction. $\omega_r(1+a')$ is the tangential velocity component and ‘ β ’ is blade twist angle. Twist at a blade element is determined from equation (3.4) [114].

$$\beta = \frac{2}{3} \tan^{-1} \left(\frac{R}{\lambda r} \right) - \alpha \quad (3.4)$$

The relation of twist angle β , inlet angle ϕ , and AOA α is as in equation (3.5) and (3.6) [115].

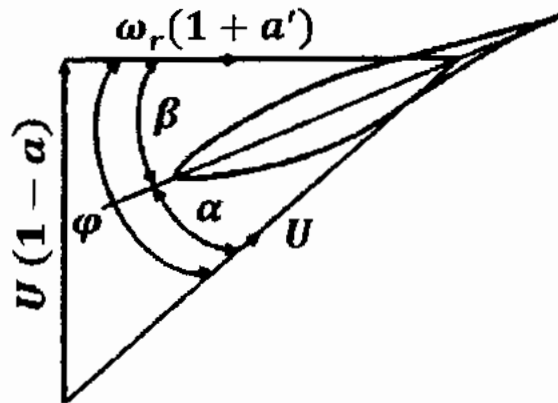


Figure 3.4 Angle definition of an airfoil

The relation of twist angle β , inlet angle ϕ , and AOA α is as in equation (3.5) and (3.6) [115].

$$\phi = \alpha + \beta \quad (3.5)$$

$$\phi = \tan^{-1} \left(\frac{1 - a}{\lambda \mu (1 + a')} \right) \quad (3.6)$$

Where, a is the axial flow induction factor, a' is the tangential flow induction factor and μ is the ratio of radial direction from hub to tip and is defined as r/R .

3.6 Tip Speed Ratio (TSR)

Tip speed ratio (TSR) is a non-dimensional parameter used for representing turbine performance in non-dimensional terms. It is defined as the ratio of blade tip velocity to relative flow velocity and mathematically expressed as [116]:

$$\lambda = \frac{\omega R}{U} \quad (3.7)$$

Where, “ ω ” is the angular velocity or speed of the turbine in rads/s, mathematically expressed as:

$$\omega = \frac{2\pi N}{60} \quad (3.8)$$

where N is the turbine rotational speed in rotations per minute (r.p.m). Turbines with higher optimum tip speeds are more efficient but they are subjected to higher hydrodynamic and centrifugal stresses [117]. Blades designed for higher TSR have comparatively smaller chords that will require less material and will have lower weight and cost.

3.7 Number of Turbine Blades

The number of blades in a turbine affects the stability, efficiency and cost considerations. A rotating disc is the most stable mechanical component [113]. Three blades in a turbine is the minimum requirement to enable stable operation of the turbine like a rotating disc. The effect of number of blades in a turbine is represented by its solidity. The Solidity of a turbine is a reflection of its size and weight and depends upon the number of blades, mean

chord length and turbine radius. Solidity is the ratio of the area covered by the turbine blade to the total swept area of the turbine and is mathematically expressed as:

$$\sigma = \frac{BC}{2\pi R} \quad (3.9)$$

Where, B is the turbine number of blades, C is the mean chord and R is the radius of the turbine.

The solidity in tidal turbine has not been much investigated for its effects on tidal turbine performance and most of the knowledge is transferred from the wind turbine research. Nevertheless, Morris [118] and Mujahid et al. [41] performed studies on the effect of solidity on the performance of TCT. These studies suggest that devices with less number of blades have a higher optimal TSR and therefore require smaller size gear box. Smaller gear box size and less number of blades reduces the weight, size and cost of turbine. Additionally, devices operating at higher TSR creates a more significant wake that could have some implications for operation of turbine in arrays. The chances of cavitation are also higher for devices operating at higher TSR. The value of turbine power coefficient (C_P) increases marginally with increasing the number of blades from 2 to 3 and this increase is negligible for increasing the number of blades from 3 to 4. The value of torque coefficient increases significantly with increasing the number of blades. The value of total turbine thrust is minimally influenced by the increase in number of blade, while the value of thrust per blade reduces with increasing number of blades. The increase in thrust per blade and corresponding flap moment with reduction in number of blades could have serious consequences for the reliability of turbine blades. Moreover, the increased deflection due to increased flap moment may also affect the power output of turbine.

3.8 Performance and load Parameters

The performance of TCT's in non-dimensional terms is generally expressed by the relations provided in Equations (3.10)-(3.14).

The power coefficient (C_P) of turbine is the ratio of the power actually generated by the turbine computed as torque time rotational speed to the total power available in the flow stream. The power coefficient of turbine is mathematically represented as:

$$C_P = \frac{Q\omega}{0.5\rho AU_\infty^3} \quad (3.10)$$

The thrust coefficient (C_T) of turbine is mathematically expressed as:

$$C_T = \frac{T}{0.5\rho AU_\infty^2} \quad (3.11)$$

Structural loads on the turbine blades are determined from the blade root bending moments. The two most prominent and structurally significant bending moments are the flap and edge-wise root bending moments. These are schematically represented as in Figure 3.5.

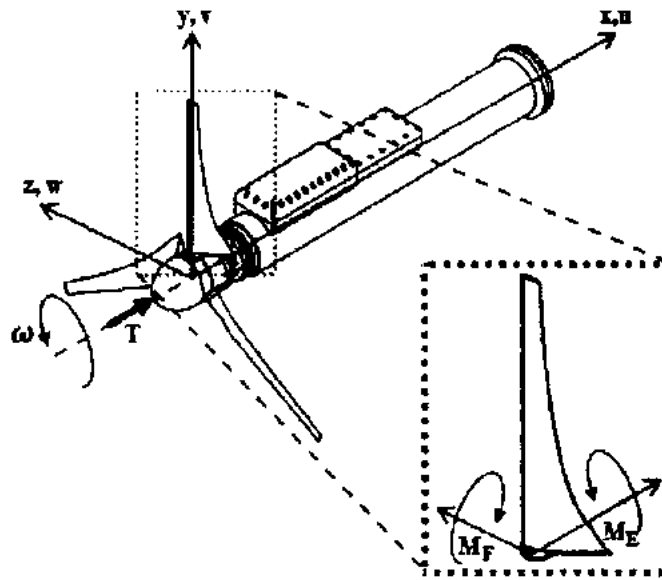


Figure 3.5 Graphical representation of blade root bending moments [63]

The thrust force (T) acts along the stream wise direction and is responsible for the flap wise bending moment (M_F). The flap wise bending moment is the dominant parameter for structural stresses at the blade hub junction. It is a critical design parameter because its value is much higher compared to the torsional or edge-wise bending moment [49]. The edge-wise bending moment (M_E) is caused by the tangential force generated by the blades. Mathematically, these structural moments in terms of their coefficients are expressed as:

$$C_{M_F} = \frac{M_F}{0.5\rho AU_\infty^2 R} \quad (3.12)$$

$$C_{M_E} = \frac{M_E}{0.5\rho AU_\infty^2 R} \quad (3.13)$$

in these equations U_∞ (m/s) represent the free stream velocity, ω (rad/s) the angular speed of the blade tip, R (m) the radius of the rotor, A (m²) the swept area of the rotor and Q (Nm) the torque generated by the rotor. Flap wise bending moments M_F (Nm) is the moment of thrust force and acts along the chord line and M_E (Nm) is the edge wise bending moment.

3.9 Turbine design utilized for research

The U.S Department of Energy initiated a program to develop open source designs of marine hydrokinetic devices as study objects for research and development [119]. The objective of this program was to provide researchers a common turbine design for different research objectives that would allow a direct comparison of results and facilitate the development of related turbine technologies. As a part of this program, a two-bladed counter rotating twin rotor horizontal axis TCT design was developed named as Reference Model (RM1). This turbine has a diameter of 20m and its blade profile is based on the NACA 63(4)-424 airfoil. A full scale turbine based on the RM1 design was initially utilized in some numerical studies [120, 121]. However, later experimental tests carried out on 1:45 scaled model RM1 turbine with a diameter of 0.45 m in the recirculating flume at Bamfield Marine Science Centre (BMSC) in British Columbia, Canada revealed that experimental performance of the turbine is significantly lower than the Blade Element Momentum Theory (BEMT) predictions [94].

Reduced performance of the turbine in experimental trials was suspected to be due to the lower chord-based Reynolds numbers ($Re \leq 80,000$) for operation in a flow speed of 0.65 m/s. The performance of a turbine is expected to sharply decrease below a critical Re value due to laminar flow separation. However, it was not possible to remove this un-certainty due to the unavailability of low Re ($\approx 70,000$) lift (C_L) and drag (C_D) coefficient wind tunnel tests data for the NACA 63(4)-24 airfoil. Additionally, the acquisition of required data from the potential flow solvers like Xfoil was deemed inadequate due to its lack of accuracy near transitional Re numbers for predicting airfoil performance because of its inability to capture laminar separation bubble dynamics [122]. To resolve the issue of performance mismatch between experiment and BEMT computations at low Re , the blade

profile of RM1 turbine was changed to NACA 4415. The NACA 4415 airfoil was selected due to its superior performance at low Re , lower dependency on Re , availability of experimental data and higher percentage thickness to resist higher fluid loads. A comparison of the original and modified RM1 turbine designs performance from experiments with the lab scale model (1:45) and full scale from BEMT computations is shown in Figure 3.6.

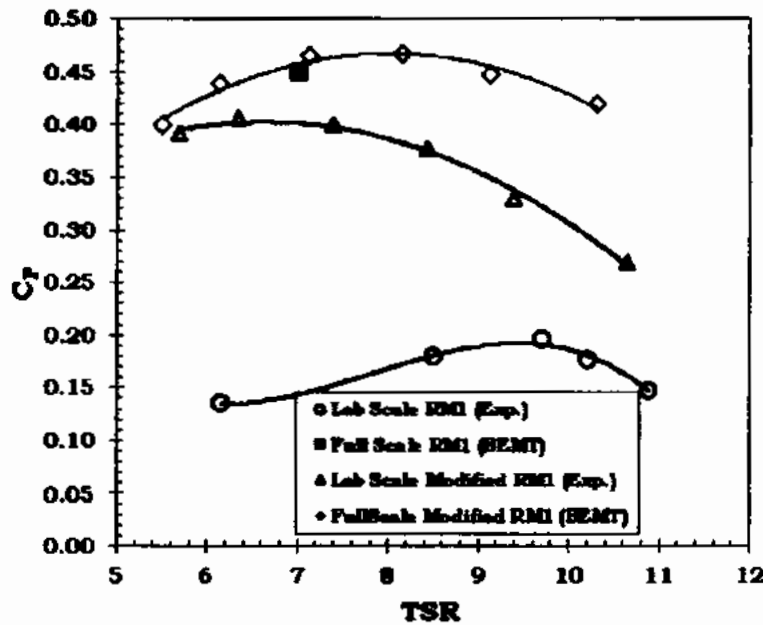


Figure 3.6 Performance comparison of the original and modified RM1 TCT [94]

Further, experiments on the SAFL modified version of RM1 turbine lab scale model showed that the performance of turbine is not much sensitive to Reynold number variations as shown in Figure 3.7.

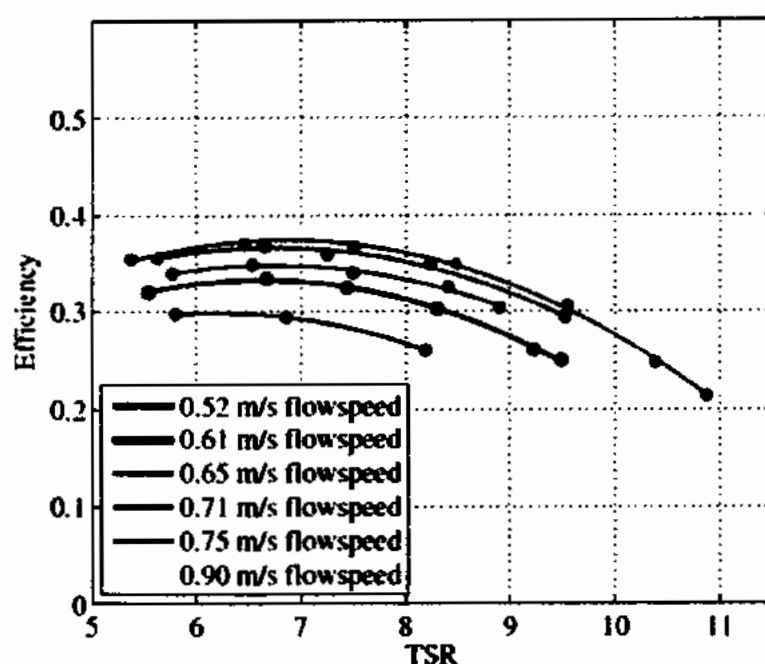


Figure 3.7 Performance of 1:45 lab scaled modified RM1 turbine at different flow speeds [94]

Later, the University of Minnesota's St. Anthony Falls Laboratory (UMN-SAFL) also tested a 1:40 scale model of the modified RM1 turbine design with dual counter rotating rotors of 0.5m diameter in their large open channel facility [26]. The blade element sections characteristics of the 1:40 scaled model SAFL RM1 turbine is as in Table 3.1.

Table 3.1 Blade element sections characteristics for the 1:40 RM1 SAFL model turbine blade of NACA 4415 profile

r/R (-)	Radius (mm)	Pre-Twist (Degree)	Chord (c) (mm)	t/c (%)	Thickness (t) (mm)
0.21	53.3	13.16	30.0	100.0	30.0
0.24	60.0	13.16	30.0	100.0	30.0
0.27	66.7	13.16	34.2	84.9	29.0
0.29	73.3	13.16	46.8	51.8	24.2
0.32	80.0	13.16	57.2	31.1	17.8
0.35	86.7	13.16	62.6	19.4	12.1
0.37	93.3	13.16	64.5	15.0	9.7
0.40	100.0	11.28	64.4	15.0	9.7
0.43	106.7	10.24	63.2	15.0	9.5
0.45	113.3	9.43	61.5	15.0	9.2
0.48	120.0	8.76	59.5	15.0	8.9

0.51	126.7	8.17	57.4	15.0	8.6
0.53	133.3	7.64	55.3	15.0	8.3
0.56	140.0	7.16	53.2	15.0	8.0
0.59	146.7	6.70	51.1	15.0	7.7
0.61	153.3	6.27	49.2	15.0	7.4
0.64	160.0	5.86	47.3	15.0	7.1
0.67	166.7	5.46	45.6	15.0	6.8
0.69	173.3	5.07	44.0	15.0	6.6
0.72	180.0	4.69	42.4	15.0	6.4
0.75	186.7	4.31	40.9	15.0	6.1
0.77	193.3	3.93	39.5	15.0	5.9
0.80	200.0	3.55	38.2	15.0	5.7
0.83	206.7	3.17	37.0	15.0	5.6
0.85	213.3	2.78	35.8	15.0	5.4
0.88	220.0	2.38	34.6	15.0	5.2
0.91	226.7	1.98	33.5	15.0	5.0
0.93	233.3	1.57	32.3	15.0	4.8
0.96	240.0	1.14	31.2	15.0	4.7
1.00	250.0	0.70	30.0	15.0	4.5

The objectives of these experimental tests were to obtain an open source robust data set that can be utilized to assess the ability of various turbulence models for predicting turbine performance and wake. This thesis also utilized the SAFL version of the RM1 turbine design with single rotor configuration to utilize their open source experimental data for the validation of results from numerical simulations.

3.10 Summary

In this chapter, an overview of the globally recognized potential design of future tidal energy devices is presented. The design aspects for HAT is described with a discussion on how these would influence the turbine operation. The turbine performance and load parameters that will repeatedly appear in this thesis are also described. The turbine design utilized in this research (SAFL RM1) is described along with a background of the evolution of this design from the original RM1 design.

Chapter 4

Development of RANS CFD Methodology

The development of Reynolds Navier-Stokes (RANS) Computational Fluid Dynamic (CFD) methodology for simulating the performance of horizontal axis TCT is discussed in this chapter. The ANSYS Workbench software is utilized to replicate the experimental model tests conducted at the University of Minnesota's St. Anthony Falls Laboratory for the performance prediction of SAFL modified version of RM1 turbine rotor in the RANS CFD model. A steady state RANS CFD methodology is first developed and validated with experimental data for the performance of turbine represented by its rotor over the entire range of turbine operating conditions from TSR 1-9. The RANS CFD methodology is then extended to model the performance of full scale turbine including nacelle and support tower in steady state and transient simulations. The development of the validated RANS CFD model for the performance and wake modeling of standalone RM1 TCT is necessary before extending the simulations to tidal turbine arrays that will be discussed in the later chapters. The results presented in this chapter are mostly based on our published research articles.

4.1 Experimental setup

Experimental investigations were conducted on the RM1 turbine in the large open channel facility at the University of Minnesota, St. Anthony Falls Laboratory (SAFL) to develop an open source robust data set of experimental measurements that can be utilized for the validation of numerical models for turbine performance and wake [26]. These experimental results have been used for the validation purpose throughout this thesis. While experimental work is not a part of this research, it is briefly described for the completeness of discussion in this thesis. The SAFL main channel has depth of 1.8m, width of 2.75m and length of 85m with continuous water supply system. The channel is equipped with discharge control system, flow rate monitor and depth control mechanism. Two rows of vertically oriented baffles are installed in the channel to avoid the entry of large size turbulent structures into the testing section. The 1:40 scale SAFL modified version of RM1

dual rotor turbine including major components and measuring instruments for the rotor RPM and torque is utilized in all the model tests. Each rotor has a diameter of 0.5m, with a spacing of 0.7m between the rotors. The experiments were conducted with a channel depth of 1m and the model was located in the depth wise centre at a distance of 40m downstream from the inlet. A schematic representation of the experimental setup is shown in Figure 4.1.

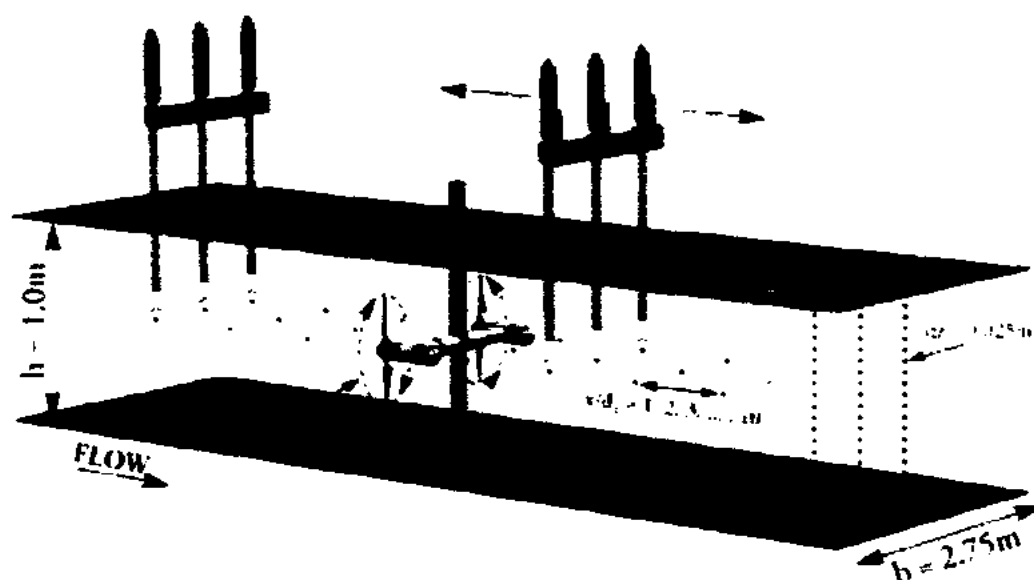


Figure 4.1 Schematic of the SAFL RM1 experimental setup [26]

The channel carriage is equipped with Data Acquisition system and capable of three axis automated motion to position various sensors for monitoring fluid environment around the turbine. Discharge measurements are continuously recorded at a sample rate of 1Hz with an ultrasonic range sensor to monitor the water surface elevation. The Acoustic Doppler Velocimeters (ADV) are used to record flow velocity in the test section at a sample rate of 200Hz. For each rotor an ADV was located aligned to the axis of rotation at the hub height, whereas a third ADV was positioned at the same depth aligned to the tower. The angular velocity of rotor is precisely controlled through a stepper motor and indexer drive. Single automation direct rotary encoder on the motor shaft referenced to turbine blade position records the blade angular position. The turbine hubs are equipped with miniature reaction torque sensor to measure the rotor torque. The angular velocity is precisely controlled through a stepper motor and indexer drive connected to the rotor shaft with a

chain drive. The rotor angular positions are measured with a rotary encoder connected to the motor shaft. The measurements are transmitted to a computer in the form of voltage signals via a system of torque transducer, slip ring, signal conditioner and analog to digital acquisition board.

4.2 Review of research on CFD Simulations of RM1 Turbine

The experimental performance of SAFL RM1 1:40 scale turbine is replicated through RANS CFD simulations as a part of this thesis. However, a few other researchers have also modelled the performance of RM1 full scale or scaled model turbine utilizing an almost similar methodology. Lawson et al. [120] were the 1st to develop a RANS CFD model using the full scale DOE RM1 turbine design for three different operation conditions all representing a fully attached flow and compared the results with BEM computations. They presented a well-documented spatial and temporal discretization study utilizing steady state and transient CFD simulations respectively. The predicted torque results were found to be sensitive to grid resolution, while they were minimally influenced by the time step of simulation. Javaherchi et al. [121] also performed RANS CFD simulation of the full scale DOE RM1 turbine. The computed torque from these simulations closely matched the torque values of previous RANS CFD based computations of Lawson et al. [120]. Results for the turbine torque, lift and drag coefficients and wake was also described. The effect of shear stress transport ($SST\ K - \omega$) and Spalart-Allmaras (SA) turbulence model on the performance prediction was also evaluated. It was suggested that the two equation ($SST\ K - \omega$) model is comparatively a better choice for performance studies as compared to the one equation (SA) model. Later, Javaherchi et al. [123] also performed flume experiments and RANS CFD simulations of the modified design 45:1 model scale DOE RM1 turbine. The experimental and numerical results were compared at the similar conditions and scale. The objective of the study was to develop a methodology for the performance and wake studies and to establish a data base of experimental data. The CFD simulations were performed at a TSR range of 5.5-10.3 to match the experimental conditions. Javaherchi et al. [95] extended their numerical and experimental work to the investigation of energy extraction efficiency and wake flow studies on a three turbine array utilizing a modified scaled model of DOE RM1 turbine. The numerical results for turbine

performance and wake deviated from the experimental measurements at low TSR's due to flow separation at the blades.

The proceeding sections in this chapter describes the RANS CFD simulation methodology developed in this thesis.

4.3 Software and Governing Equations

The RANS CFD simulations performed in this research utilized the ANSYS CFX solver, which is a node centered finite volume solver, employing an element based finite volume method to the solution of Navier-Stokes equations [124]. CFX is a fully implicit code that utilizes co-located (non-staggered) grid layouts and a modified form of Rhie and chow discretization for the mass flow that avoids decoupling. The software uses an incomplete lower upper (ILU) factorization technique with a particular implementation of algebraic multigrid acceleration known as additive correction for the solution of discrete system of linearized equations. The exact solution of discrete equations is obtained through an iterative procedure over the course of several iterations.

CFX numerically models the advection term (i.e. the often dominant term accounting for bulk fluid motion) in several different ways known as advection schemes. In general, the CFX advection schemes are interpreted as the integration point value is equal to the upstream value plus a correction due to the gradient.

$$\varphi_{ip} = \varphi_{up} + \beta \nabla \varphi \cdot \Delta \vec{r} \quad (4.1)$$

Where $\nabla \varphi$ is the variable gradient and \vec{r} the vector between the upstream node and the integration point. Whereas, β can assume any value between 0 and 1 that results in different advection schemes. Several options for the selection of an advection schemes are available in CFX. Amongst these, the upwind difference advection scheme uses a pre-specified β value of 0 to employ no correction. While this scheme is robust, it is only first order accurate. Contrarily, the specified blend scheme allows the specification of β values between 0 and 1 to employ between no corrections up to full correction. However, this scheme is unbounded and may therefore cause the solution to overshoot or undershoot and cause non-physical oscillations in regions of rapid solution variation. The CFX “high resolution” scheme maximizes the value of β to a value to be as close to 1 as possible while

keeping the solution bounded. While a β value of 1 effectively renders the advection scheme to be second order accurate in space, a β value of zero employs a first order accurate scheme. The “high resolution” advection scheme in ANSYS CFX is a blend of the second order accurate central difference scheme and the first order accurate upwind scheme. The blend factor tries to implement the central difference scheme unless there is a situation that could compromise the stability of the solution. For all simulations contributing to this thesis a “high resolution” advection scheme was employed in view of its additional accuracy especially on boundary layers with unstructured meshes.

The ANSYS CFX software is a general-purpose fluid dynamics code equipped with a variety of simulation approaches. However, during the course of this thesis, the Reynolds-averaged Navier Stokes (RANS) equations are used for all simulations. For an incompressible Newtonian flow, the RANS equations in Einstein notation in Cartesian coordinates are written as:

$$\text{Continuity Equation:} \quad \frac{\partial \bar{u}_i}{\partial x_i} = 0 \quad (4.2)$$

$$\text{Momentum Equation:} \quad \rho \frac{\partial \bar{u}_i}{\partial t} + \rho \bar{u}_j \frac{\partial \bar{u}_i}{\partial x_j} = \rho \bar{f}_i + \frac{\partial}{\partial x_j} [-\bar{p} \delta_{ij} + 2\mu \bar{S}_{ij} - \rho \overline{u'_i u'_j}] \quad (4.3)$$

where, S_{ij} is the mean rate of strain tensor and mathematically expressed as:

$$\bar{S}_{ij} = \frac{1}{2} \left(\frac{\partial \bar{u}_i}{\partial x_j} + \frac{\partial \bar{u}_j}{\partial x_i} \right) \quad (4.4)$$

The time derivative is eliminated because the integration in time removes the time dependence of the resultant term and the momentum equation reduces to:

$$\rho \bar{u}_j \frac{\partial \bar{u}_i}{\partial x_j} = \rho \bar{f}_i + \frac{\partial}{\partial x_j} [-\bar{p} \delta_{ij} + 2\mu \bar{S}_{ij} - \rho \overline{u'_i u'_j}] \quad (4.5)$$

where, vector f_i represents the external forces and δ_{ij} is the Kronecker delta function. $\delta_{ij} = 1$ for $i = j$ and zero otherwise. For TCT, the incompressibility assumption holds and the energy equation is also omitted because the thermal effects are negligible. Therefore, the simulations will neither account for the contribution of heat due to the dissipation of turbulence kinetic energy nor viscous shear.

4.4 Turbulence Model

Turbulence in a flow field refers to the unsteady and irregular motion due to fluctuation of the transport variables in time and space. The fluid properties and velocity exhibit random variations in turbulent flow that enhances the mixing of matter, momentum and energy. Turbulent flows are generally characterized by high Reynolds numbers. However, other factors like free stream turbulence, surface condition and disturbances in the flow may cause transition to turbulence even at low Reynolds number. Turbulence is a complex physical phenomenon due its unsteady three dimensional nature consisting of many scales. The turbulent flow structures contains a wide range of turbulent eddy sizes (scales spectrum). The large eddies derive energy from the mean flow and therefore, travels with a velocity of the same order. Whereas, the smaller eddies receive energy from the larger eddies, which is converted to internal energy by viscous dissipation.

The Navier-Stokes equations can equally resolve laminar and turbulent flows directly through Direct Numerical Simulation (DNS). However, this would require the resolution of whole scales spectrum that would require much higher computational power than what could be possible in the near future. The resolution of whole scales spectrum would generally require resolving length scales much smaller than the finest volume mesh of any practical use in the numerical analysis. The Large Eddy Simulation (LES) type models are developed to address this issue by solving the spatially averaged Navier-Stokes equations. In this approach the large size eddies (i.e. turbulence structures) are directly resolved and eddies smaller than the mesh are modelled. Although the LES models are less expensive than DES, the requirement of computational resources and efforts are still infeasible for most applications. The LES models have been recently used for modeling the spectral distribution of blade bending moments for TCT's [48, 49, 125].

Additionally, several turbulence models have been developed to resolve turbulent flows without requiring a prohibitively finer mesh. These models employ a statistical averaging procedure to account for the turbulence related transport mechanism and are therefore also termed as statistical turbulence models. The averaging procedure introduces averaged and fluctuating quantities into the original unsteady Navier-Stokes equations to produce Reynolds Averaged Navier-Stokes (RANS) equations.

The RANS CFD approach solves time averaged Navier-Stokes equations and models all the length scales. The time averaging is used to extract mean flow properties from the instantaneous properties by splitting the instantaneous velocity, u_i , into average, \bar{u}_i , and fluctuating, \hat{u}_i , component as:

$$u_i(X, t) = \bar{u}_i(X, t) + \hat{u}_i(X, t) \quad (4.6)$$

The Reynolds-averaged momentum equation can also be written as:

$$\rho \left(\frac{\partial \bar{u}_i}{\partial t} + \bar{u}_k \frac{\partial \bar{u}_i}{\partial x_k} \right) = -\frac{\partial \bar{p}}{\partial x_i} + \frac{\partial}{\partial x_j} \left(\mu \frac{\partial \bar{u}_i}{\partial x_j} \right) + \frac{\partial R_{ij}}{\partial x_j} \quad (4.7)$$

Here, $R_{ij} = -\rho \overline{\hat{u}_i \hat{u}_j}$ is the Reynold stress tensor. The time averaging introduces additional unknowns (Reynolds stresses) in order to close the system of governing equations. In the RANS CFD approach, the unknown Reynolds stresses are related to the known mean flow variables through additional equations representing turbulence models. Several turbulence models are available with some of these only applicable to very specific applications while others are applicable to a wider class of flows. There is not yet a single turbulence model that can reliably predict all turbulent flows with sufficient accuracy.

The turbulence models are generally classified into Reynolds-Stress Models (RSM) and Eddy Viscosity Models. Reynolds-Stress Models are based on the transport equations for Reynolds stresses. They are more suitable for anisotropic flows as they model all the components of the Reynolds stress tensor. However, they are computationally expensive due to solving six additional partial differential equation and difficult to converge due to the absence of stabilizing eddy viscosity term [126]. Alternately, the Eddy Viscosity Models are based on the Boussinesq hypothesis and the Reynold stresses are modelled using an eddy (or turbulent) viscosity as:

$$R_{ij} = -\rho \overline{\hat{u}_i \hat{u}_j} = \mu_T \left(\frac{\partial \bar{u}_i}{\partial x_j} + \frac{\partial \bar{u}_j}{\partial x_i} \right) - \frac{2}{3} \mu_T \frac{\partial \bar{u}_k}{\partial x_k} \delta_{ij} - \frac{2}{3} \rho k \delta_{ij} \quad (4.8)$$

A review of the previous RANS CFD modelling works on tidal turbine over the last decade reveal that the $k - \omega$ based Shear Stress Transport (SST) model has generally performed better for tidal turbine applications [127-130]. The $k - \omega$ SST model is known to predict the onset and amount of flow separation under adverse pressure gradient with better

convergence [124]. Therefore, the $k - \omega$ based Shear Stress Transport (SST) model is also used for all the simulations in this thesis. The SST model belongs to the group of eddy viscosity models, and considers the Reynolds stress term to be proportional to the mean rate of deformation:

$$\overline{u'_i u'_j} = -\nu \left(\frac{\partial \bar{u}_i}{\partial x_j} + \frac{\partial \bar{u}_j}{\partial x_i} \right) + \frac{2}{3} \rho k \delta_{ij} \quad (4.9)$$

where, k represent the turbulent kinetic energy per unit mass expressed as:

$$k = \frac{1}{2} (\overline{u_i'^2}) \quad (4.10)$$

The SST model combines the Willcox $k - \omega$ model and standard $k - \varepsilon$ model to utilize the advantages of both models. This is accomplished using a blending function to apply $k - \omega$ model in the viscous sub layer region of the no slip boundary and $k - \varepsilon$ model in outer part of the boundary layer. The SST model uses transport equation for the turbulent kinetic energy " k " as:

$$\frac{\partial k}{\partial t} + \bar{u}_i \frac{\partial k}{\partial x_i} = \frac{\partial}{\partial x_i} \left[\left(\nu + \frac{\nu_t}{\sigma_k} \right) \frac{\partial k}{\partial x_i} \right] + P_k + P_{k,b} - \beta k \omega \quad (4.11)$$

The term $P_{k,b}$ represent the buoyancy production term. The buoyancy has not been modelled in all the simulations through out this thesis. Because, we have assumed that the free surface would not influence the turbine performance for the evaluated case studies. The shear production term P_k is mathematically expressed as:

$$P_k = \nu_t \frac{\partial \bar{u}_i}{\partial x_j} \left(\frac{\partial \bar{u}_i}{\partial x_j} + \frac{\partial \bar{u}_j}{\partial x_i} \right) \quad (4.12)$$

The specific dissipation " ω " is evaluated through a second transport equation as:

$$\begin{aligned} \frac{\partial \omega}{\partial t} + \bar{u}_i \frac{\partial \omega}{\partial x_i} = & \frac{\partial}{\partial x_i} \left[\left(\nu + \frac{\nu_t}{\sigma_\omega} \right) \frac{\partial \omega}{\partial x_i} \right] + \alpha \frac{\omega}{k} P_k + P_{\omega,b} + \beta \omega^2 \\ & + (1 - F_1) \frac{2}{\sigma_{\omega 2}} \frac{\partial k}{\partial x_i} \frac{\partial \omega}{\partial x_i} \end{aligned} \quad (4.13)$$

Despite combining the advantages of Willcox $k - \omega$ and standard $k - \varepsilon$ model, the baseline model still fails to predict the onset and amount of flow separation from smooth

surfaces. This is primarily because of the over prediction of eddy-viscosity arising due to not accounting for the transport of turbulent shear stress. This deficiency in the proper modeling of transport behavior is addressed by applying a limiter to the formulation of the eddy-viscosity as:

$$v_t = \frac{a_1 k}{\max(a_1 \omega, S F_2)} \quad (4.14)$$

where

$$v_t = \mu_t / \rho \quad (4.15)$$

and S is an invariant measure of the strain rate expressed as:

$$S = \sqrt{2 S_{ij} S_{ij}} \quad (4.16)$$

The formulation of blending functions is based on the distance to the nearest surface and on the flow variables. The blending function F_1 is expressed as:

$$F_1 = \tanh(\arg_1^4) \quad (4.17)$$

$$\arg_1 = \min \left[\max \left[\frac{\sqrt{k}}{\beta \omega y}, \frac{500\nu}{y^2 \omega} \right], \frac{4\rho k}{CD_{k\omega} \sigma_{\omega 2} y^2} \right] \quad (4.18)$$

where “y” is the distance to the nearest wall and

$$CD_{k\omega} = \max \left[2\rho \frac{1}{\sigma_{\omega 2} \omega} \frac{\partial k}{\partial x_i} \frac{\partial \omega}{\partial x_j}, 1.0 \times 10^{-10} \right] \quad (4.19)$$

The blending function F_2 is expressed as:

$$F_2 = \tanh[\arg_2^2] \quad (4.20)$$

$$\arg_2 = \max \left[\frac{2\sqrt{k}}{\beta \omega y}, \frac{500\nu}{y^2 \omega} \right] \quad (4.21)$$

The coefficients for SST model are a linear combination of the corresponding coefficients formed by blending the coefficients of $k - \omega$ and $k - \varepsilon$ models as:

$$\phi = F_1 \phi_1 + (1 - F_1) \phi_2 \quad (4.22)$$

where ϕ representing the coefficient for the SST model is a linear function of ϕ_1 and ϕ_2 representing the coefficients for $k - \omega$ model and transformed $k - \varepsilon$ model respectively. The turbulent Schmidt number σk_1 assumes a value of 1.176 for SST model in the $k - \omega$ regime against a value of 2 in the original Willcox $k - \omega$ model. All other coefficients between the two models have identical values as in Table 4.1.

Table 4.1 Coefficients for the Willcox $k - \omega$ and SST turbulence models

Coefficient	Value
$\hat{\beta}$	0.09
α_1	5/9
β_1	0.075
$\sigma_{\omega 1}$	2
α_2	0.44
β_2	0.0828
σ_{k2}	1
$\sigma_{\omega 2}$	1/0.856

4.5 RANS CFD modeling of scale model SAFL RM1 Turbine

Steady state CFD simulations are performed to model the performance of SAFL RM1 1:40 scale model TCT. The flow domain is subdivided into a stationary rectangular domain and rotating cylindrical domain. The stationary domain of rectangular shape represents the flow channel and the cylindrical domain encloses the turbine blades and hub. A Multiple Frame of Reference (MFR) technique with a frozen rotor frame change model is used to simulate the rotation of rotor about an axis with a specified angular velocity. In this approach, the governing equations are solved in a rotating reference frame and the computational grid is not physically rotated. In a Frozen Rotor model the two frames connect such that their relative position is fixed throughout the calculation. This provides a steady state solution to the multiple frame of reference problem and require less computational effort [131].

The turbine blades are assumed to be neutrally buoyant. It is also assumed that the density of sea water is constant and that the chances for cavitation are negligible. This assumption

is made because SAFL RM1 turbine design is used. During the initial design made using BEMT code Harp_Opt, it is ensured that the turbine should be free from cavitation. This is accomplished by comparing the minimum pressure over the blade to the fluid vapor pressure and avoiding blade designs for which cavitation is likely over the entire range of turbine operating conditions.

The main objective of the CFD simulations is to model the experimental performance curve of the 1:40 scale model SAFL RM1 turbine rotor. The experiments utilized the counter rotating twin rotor turbine, while the CFD simulations took advantage of the design symmetry and modelled only one rotor. The earlier research work, [94, 95, 121, 123, 132] have successfully adopted this strategy for modelling the performance of RM1 turbine to reduce the computational cost of the simulations without any influence on the outcome of results.

The Shear Stress Transport (SST) turbulence model is used in its low Reynolds number formulation. The convergence criteria is based on the stabilization of residuals of numerical solution and deemed to be achieved when the residuals are reduced to the order of $1E-4$. Further, the torque values on turbine blades are also monitored during the solution process to ensure the convergence. All the simulations are performed on the HP Z840 Workstation with Intel(R) Xeon(R) CPU E5-2699 v3 @ 2.30 GHz, 36 Core(s), 72 Logical Processor(s) having an Installed Physical Memory (RAM) of 128 GB.

4.5.1 Computational domain and boundary conditions

The flow domain is subdivided into a rectangular stationary domain to represent the flow channel and rotating cylindrical domain enclosing the rotor to model the rotation of turbine as shown in Figure 4.2.

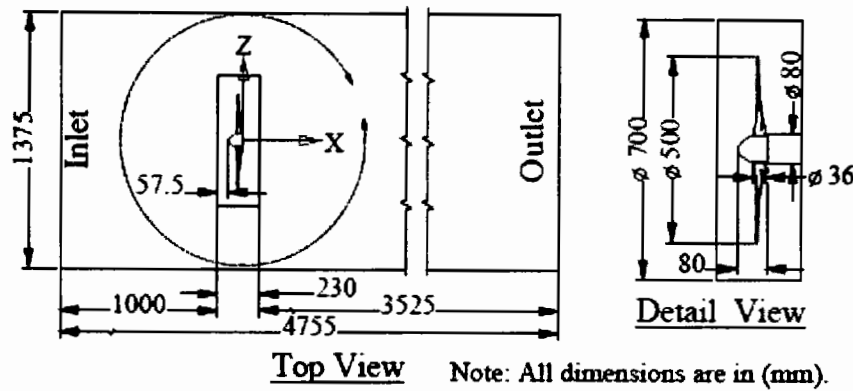


Figure 4.2 Geometric details of turbine and computational domain

The dimensions for the rectangular channel domain are selected to replicate the water channel actually used in the experiments. The depth [1m] of the domain is set equal to the flow depth of channel used in the actual experiment. However, the width [1.375m] for the domain is half the width of the experimental channel, because only one rotor of the twin rotor turbine is modelled. Similarly, the length [4.755m] of the domain is set to 10 rotor diameters (10D), a length suggested to be sufficiently large to mitigate the end effects and minimize the computational cost [51, 133]. The turbine rotor is enclosed in cylindrical domain to model the rotation of turbine with a Multiple Frame of Reference (MFR) approach. This domain has a diameter of 0.70m (1.4D) to ensure a clearance of about 50% of the blade length between the circular interface and blade tip to avoid poor numerical diffusion [79]. The length of cylindrical domain is 0.23m, with its front face located at 1m (2D) from the inlet face.

The boundary conditions are specified to conform to the actual experiment. A uniform velocity of 1.05 m/s and medium turbulence intensity (TI) of 5% with a viscosity ratio of 10 is specified at the inlet. The density of water is set to 1000 kg/m³ to match the density of water used in the actual experiment and dynamic viscosity of 8.9x10⁻⁴ Pa s. The Turbine diameter based Reynolds number Re_D is $\approx 5.2 \times 10^5$ and chord based Re_c is $\approx 3.0 \times 10^5$. The Re_c and turbulence intensity in CFD model is similar to the University of Minnesota's St. Anthony Falls Laboratory (UMN-SAFL) water channel experiment intended to be replicated. The outlet is specified as an outlet with 0 Pa relative pressure. Specifying velocity at the inlet and static pressure at the outlet represents the most robust boundary conditions in CFX [131]. This boundary condition forces the flow solver to erect an

artificial wall to stop the flow from entering into the domain from outlet. The floor and side wall that represent the wall of the test channel are specified as no slip walls. For no slip walls the fluid immediately next to the wall assumes the velocity of wall, which is zero by default. This boundary condition is the most appropriate to represent the physical model of experimental water channel as the experiments are conducted in a flow channel and not a towing tank. The side wall that represents the middle of channel is defined as symmetry and the top as free slip wall. All the hub and blade surfaces are specified as no slip walls. The three connecting surfaces of the inner and outer domain are defined as mesh interfaces to allow for the transport of flow properties across both the domains. The interface condition of General Grid Interface (GGI) is used for all the three interfaces connecting the stationary and rotating domains.

4.5.2 Mesh definition and refinement

High fidelity solutions of CFD simulations are subjected to the quality of CFD mesh. For most industrial application, it is very difficult to generate a structured mesh. Contrarily, tetrahedral mesh can be efficiently generated for problems involving complex geometrical shapes. The tetrahedral meshes can efficiently resolve the complex three dimensional (3D) computational domains of TCT and can provide spatially accurate results. Therefore, tetrahedral mesh has been extensively used for 3D CFD simulations of TCT [52, 54, 133-135]. For the steady state CFD performance modeling of scaled model RM1 turbine in this thesis, a selective body meshing technique is used with a patch confirming method to setup a tetrahedral mesh. The geometric model is converted into a single part consisting of multiple bodies to obtain a matching conformal mesh on the shared faces between bodies. The mesh generation is started with the turbine blades in the mesh component system of ANSYS Workbench. The mesh used in these simulations is shown in Figure 4.3.

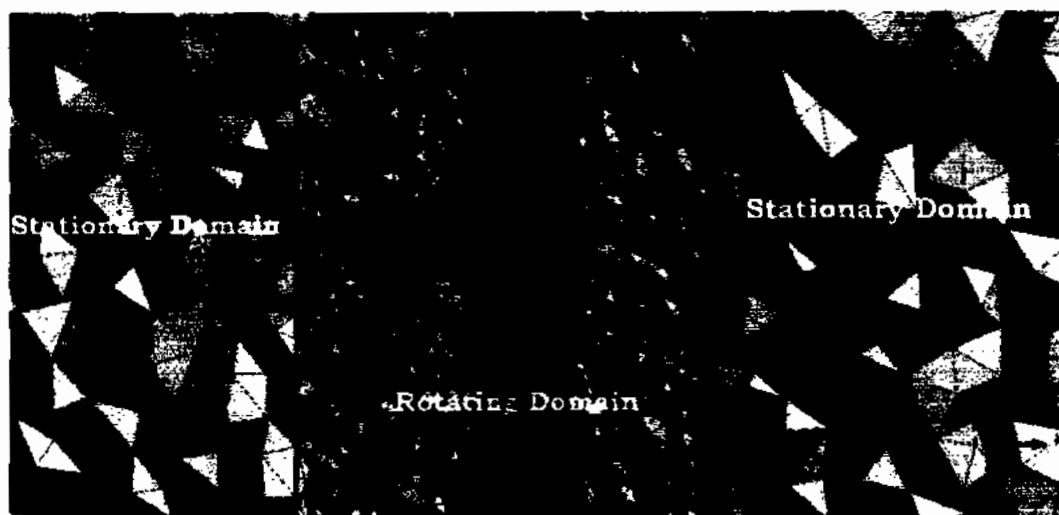


Figure 4.3 Mesh on the rotor, rotating and stationary domains utilized in the CFD simulations

Although three different meshes are generated for the grid refinement study, but the proceeding discussion only describes the selected mesh that also gives an idea of the overall meshing strategy. Tetrahedral mesh elements are used to generate mesh on blades with an element size of 0.75 mm, hub 2 mm and rest of the cylindrical domain with 6 mm. The stationary rectangular domain is meshed with an element size of 30 mm. Prism layer elements are generated around the blade surfaces to capture the boundary layer flow separation as shown in Figure 4.4.



Figure 4.4 Prism layer elements around the blade surfaces for the selected mesh

Distance of the first node away from the wall (blade surface) is set to 2.1×10^{-3} mm, with a growth rate of 1.2 and the total number of layers is 27. This mesh setup ensured that the

value of dimensionless wall distance (y^+) is less than 1 along the lower and upper blade surfaces for all the simulated TSR's. This (y^+) value is required for fully resolved boundary layer mesh when using SST turbulence model with its low Reynolds Number formulation [124]. Additionally, it is ensured that the total thickness of boundary layer is resolved with the 27 prism layers. The number of elements in rotor domain is 10.3×10^6 elements and in channel domain the number of elements is 3.1×10^6 for the selected grid. The total mesh count for problem is 13.4×10^6 elements with $\approx 77\%$ of the elements in rotating domain and $\approx 23\%$ in the stationary domain.

Three grids with progressively greater densities are generated for the grid refinement study. The number of elements for these grids and their distribution between the rotating and stationary domains is as in Table 4.2.

Table 4.2 Grids Statistics

Grid #	No. of Elements		
	Inner Domain	Outer Domain	Total
1	5.89×10^6	1.5×10^6	7.43×10^6
2	8.09×10^6	3.10×10^6	11.20×10^6
3	10.3×10^6	3.10×10^6	13.40×10^6

The meshing strategy is to use 70-80% of elements in the rotating domain with similar number of 27 inflation layers and keep the y^+ value to less than 1 to ensure the proper resolution of boundary layer with SST turbulence model in its low R_e formulation.

The CFD model is aimed to simulate performance of turbine over the entire range of TSR. Therefore, all meshes are required to be tested for different operating conditions corresponding to different flow regimes. These flow regimes can be identified from the experimental performance curve of the turbine. Three turbine operating conditions each represented by a TSR from the lower, optimum and higher TSR regions are selected from the experimental performance curve for the grid refinement study. This is done because all these three operating conditions offer a different CFD modelling challenge and it is important that each is accurately represented. These operating conditions are represented here by their respective TSRs. The 2.23 TSR represents an operating condition where the AOA at the turbine blade is high and the flow is separated. The 5.11 TSR represents an

operating condition where the turbine is producing maximum power. Finally, the 9.02 TSR represents the operating condition with the maximum blade tip velocity. Each of these TSRs are simulated utilizing the three generated grids to evaluate the turbine torque. For the mesh refinement study, the turbine torque is selected as the target variable because it is a direct output of the CFD solution. The quantitative evaluation of turbine torque for each operating condition is plotted against the total number of grid elements in the three generated grids in Figure 4.5.

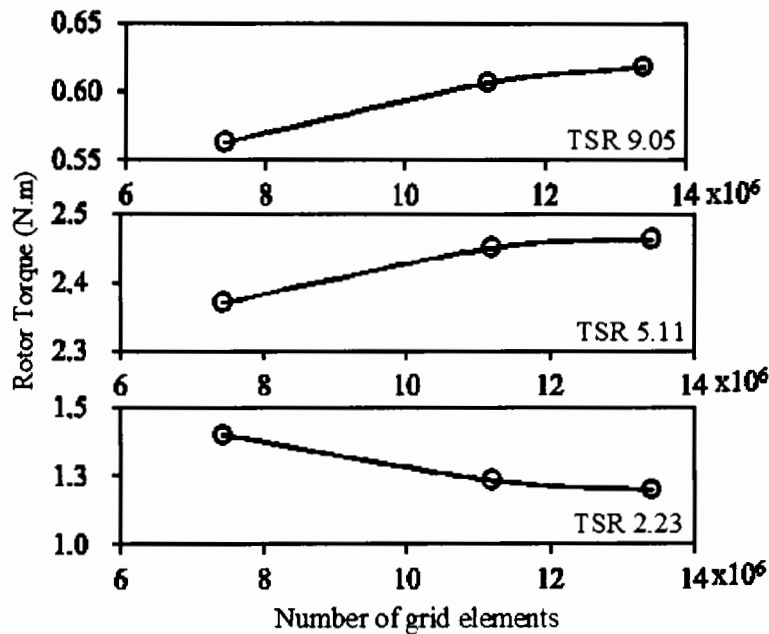


Figure 4.5 Variation of blade torque with grid density at (a) TSR 9.05 (b) TSR 5.11 (c) TSR 2.23

An increase in grid density resulted in monotonic convergence of the predicted torque values. The difference between the torque value predictions for grids 1-2, with respect to grid 3, is presented in Table 4.3.

Table 4.3 Torque predictions from the mesh refinement study

Grid #	Predicted Torque (N-m)			Difference to grid #3 (%)		
	TSR 2.2	TSR 5.11	TSR 9.05	TSR 2.2	TSR 5.11	TSR 9.05
1	1.398	2.371	0.563	16.7	-3.8	-8.9
2	1.233	2.450	0.606	2.9	-0.5	-1.9
3	1.198	2.463	0.618	-	-	-

The torque prediction for grid 2 and grid 3 are nearly similar, with a maximum difference of less than 3% for all operating conditions. Therefore, it is concluded that further

refinement of grid is not required in view of the associated increase in computational time and grid 3 is selected for further simulations.

4.5.3 Validation of RANS CFD methodology

Eight simulations at TSRs ranging from 1.42-9.05 are conducted to simulate the full performance curve of scale model SAFL RM1 turbine. These TSRs corresponds to the rotor rotational rates from 56.9-363.1 RPM. Simulation of the complete performance curve require RANS CFD models that can accurately simulate the attached as well as separated flow regimes. This requires higher fidelity CFD models that accurately capture flow separation and reattachment. The boundary conditions described in Section 4.5.1 are used with selected Grid# 3.

To validate the utilized CFD methodology simulated results are compared with the University of Minnesota's St. Anthony Falls Laboratory (UMN-SAFL) water channel experimental data [26]. The coefficient of power obtained from the CFD simulations is compared with experimental data over TSRs from 1.42-9.05 as shown in Figure 4.6.

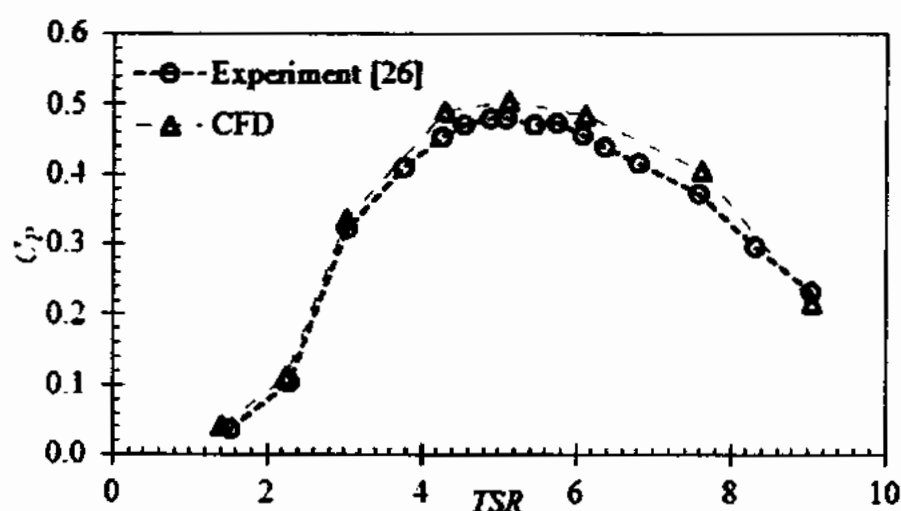


Figure 4.6 Comparison of experimental and RANS CFD simulated performance curve

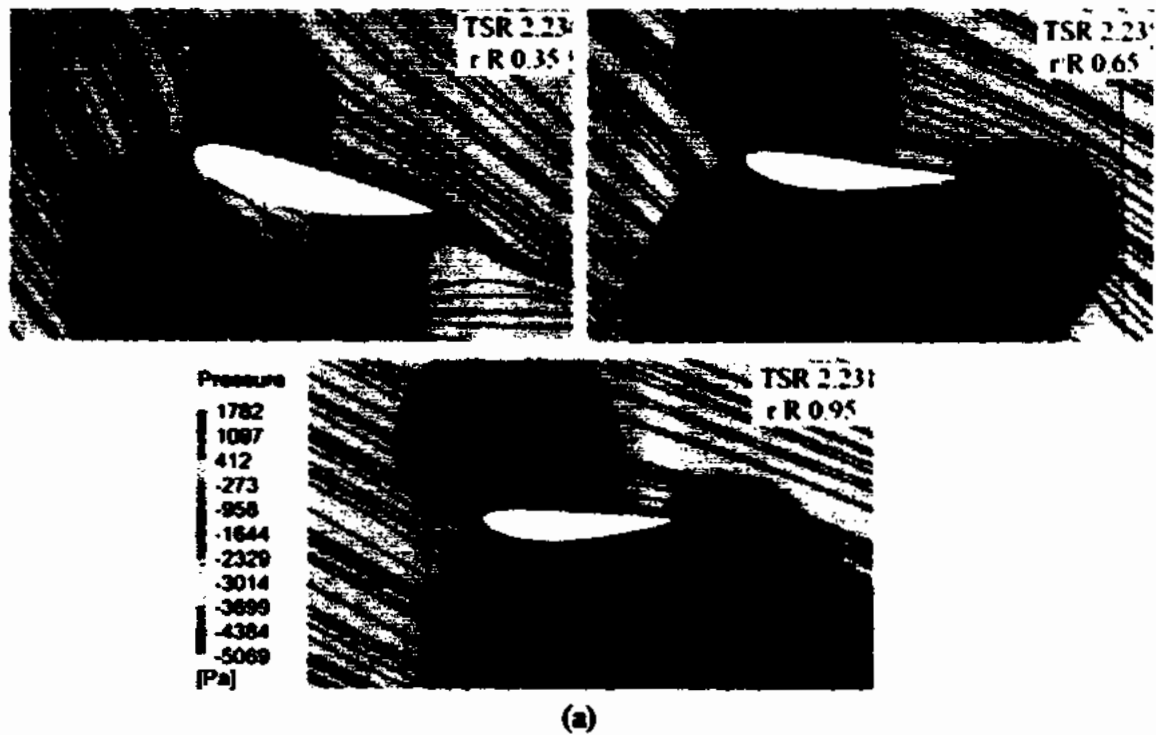
The average error is 6.4% and the maximum error is 9.2%, with an error of 4.9% occurring near the TSR associated with maximum power production. Therefore, the CFD predictions for C_p are a reasonable approximation of experimental data, indicating the adequacy of developed CFD methodology for simulating turbine performance. The computed C_p increases with TSR up to a peak value of 0.503 near TSR 5. Experimental data showed a

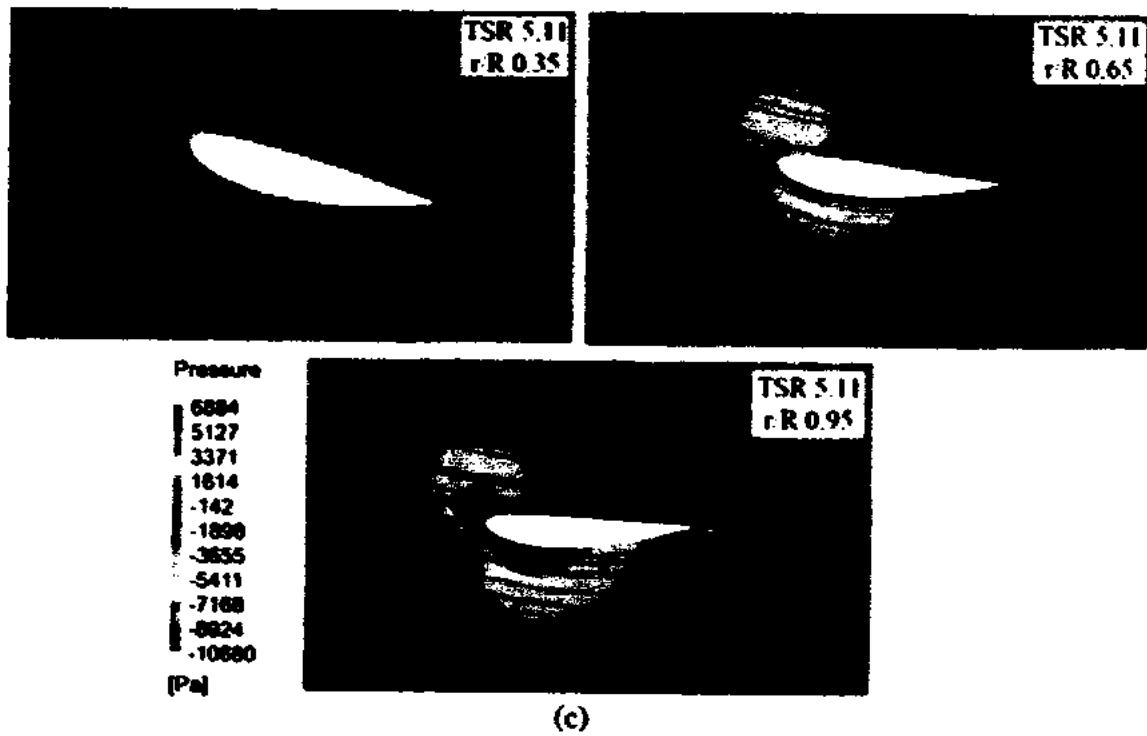
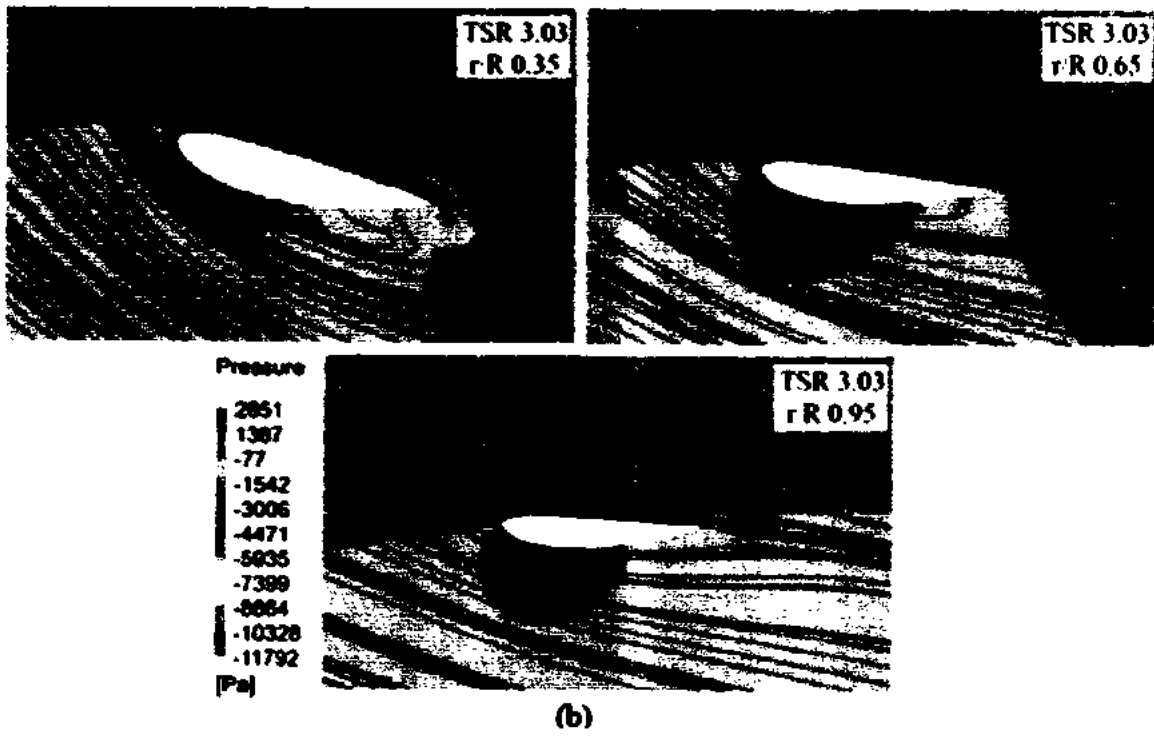
similar peak value of 0.479, occurring at TSR 5.07. The quantitative difference between experiment and RANS CFD simulation for C_p are as in Table 4.4.

Table 4.4 Difference between experimental and simulated performance coefficients

TSR	Power Coefficient (CP)		% Difference
	Experimental [26]	RANS CFD Simulations	
1.52	0.038	0.040	5.2
2.27	0.105	0.112	6.6
3.03	0.321	0.335	4.3
4.26	0.453	0.489	7.9
5.07	0.479	0.503	4.9
6.06	0.455	0.483	6.1
7.58	0.370	0.404	9.2
9.04	0.232	0.216	6.9

To understand the flow field near the blade, contour plots for pressure and velocity streamlines at selected TSRs for three blade stations are presented in Figure 4.7.





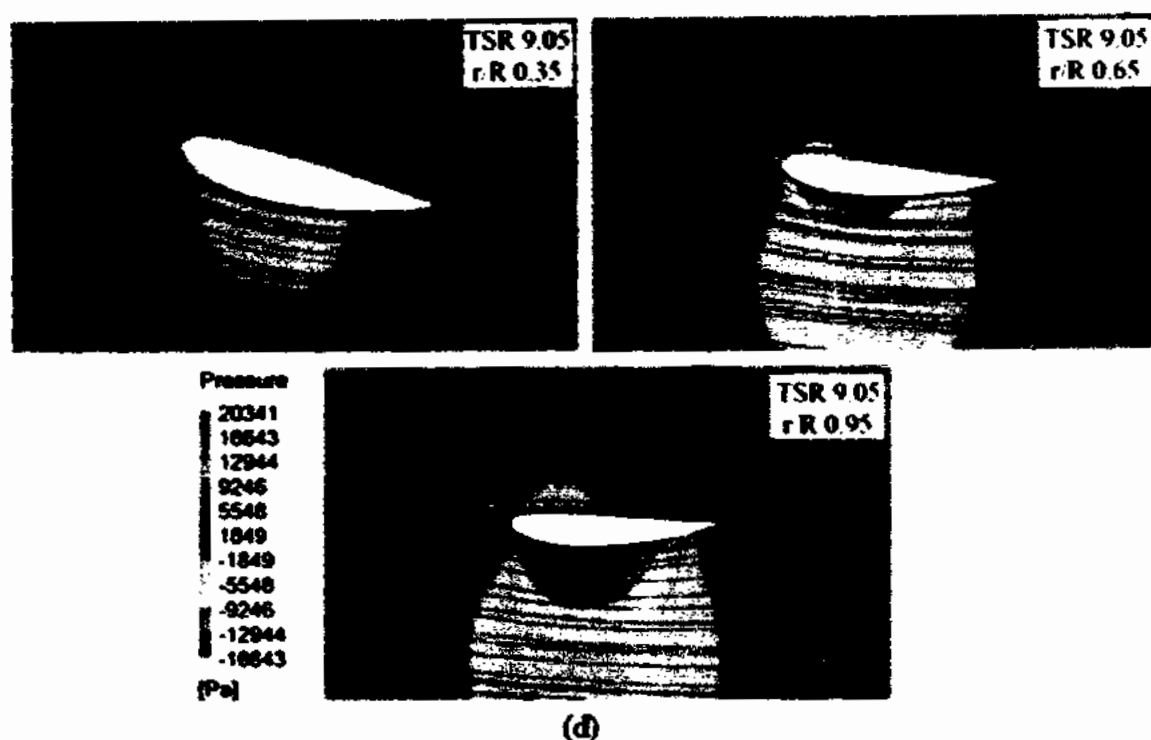


Figure 4.7 Velocity stream lines with pressure contour at selected blade sections for (a) TSR 2.23 (b) TSR 3.03 (c) TSR 5.11 (d) TSR 9.05

Flow separation is clearly visible along the low pressure face of the entire blade at TSR of 2.23. A similar flow pattern was observed at TSR of 1.42, but has not been shown here for brevity. At these TSRs the turbine blade is stalled throughout its full span. The structure of flow separation at TSR 1.42 and TSR 2.23 changes along the blade span because the AOA decreases as we move from blade root to tip. Weak flow separation is observed at trailing edge of the airfoil near the blade root, $r/R=0.35$, for a TSR of 3.03. This separation gets weaker as distance from the hub increases (see $r/R=0.65$). It also gets weaker as TSR increases (see TSR= 5.11, $r/R=0.35$). The separation at the root portion (i.e., transition region) is not important because the contribution of root portion to the overall power output is minimal. The flow is fully attached at 65% and 95% of the blade length at TSR 4.29 (not shown in Figure 4.7) and the entire blade length for TSRs from 6.11-9.05. Within this range only a TSR of 9.05 is shown in Figure 4.7 for brevity.

4.5.4 Effect of blockage on turbine performance

The performance of turbine operating in a tidal array or as a standalone device in a channel will be impacted by the spacing, size and placement of turbines within the channel. These

deployment specific effects can be evaluated in more general terms by investigating the blockage ratio (i.e., the ratio of turbine swept area to the channel cross sectional area) and boundary layer effects on the turbine performance. In a tidal array, blocked flow conditions are associated with adding turbines to a channel, which alters the hydrodynamic performance of each turbine [136]. For a standalone turbine, the relative size of a turbine with respect to the channel size determines the blockage conditions. When blockage ratios are small an infinite flow field can be assumed, where water freely accelerates around a turbine. However, boundaries near turbine restrict this expansion, typically resulting in increased power production. For a standalone device, the performance of turbine increases with increasing blockage ratio [137, 138]. However, the information available thus far are insufficient to properly explain all the dimensions of the effect of blockage ratio on turbine performance and the way it would impact array design. Therefore, it is necessary to study the effect of blockage and boundary proximity on the performance of TCT before extending the investigations to tidal turbine arrays.

Most TCT deployments will likely be in relatively shallow waters. These TCTs will be subjected to a collective blockage effect due to solid and wake blockages. The solid blockage refers to flow restriction caused by the turbine swept area and is commonly represented by the blockage ratio. The wake blockage is created by the rotation of blades which creates a low pressure and low velocity region behind turbine. These blockage effects accelerate the flow near rotor, resulting in improved turbine performance compared to an unblocked condition.

Steady state CFD simulations are conducted using the developed CFD methodology for scaled model SAFL RM1 turbine to investigate the effect of blockage on turbine performance. The investigation is accomplished using eight computational fluid domains with varying blockage ratios and constant depth of 2D as in Table 4.5.

Table 4.5 Details of fluid domain for blockage study

Domain	Width	Blockage Ratio
1	19.6D	0.02
2	9.8D	0.04
3	6.5D	0.06
4	4.9D	0.08
5	3.6D	0.11
6	2.8D	0.14
7	2.4D	0.165
8	2.1D	0.19

Three different TSRs (2.23, 5.11 and 9.05) are simulated for an inflow velocity of 1.05m/s and turbulence intensity of 5% with a viscosity ratio of 10. Symmetry boundary conditions are applied to the bottom and lateral walls of fluid domain. This is done to eliminate the effect of channel boundaries to solely study the effect of blockage on performance.

For TSR 2.23, blockage ratio has negligible effects on TCT performance over the entire range of evaluated blockage ratios. The C_p and C_T of turbine for this TSR is minimally changed by 0.04% and 0.6% respectively over the entire range of evaluated blockage ratios. A similar observation of minimal performance change at lower blockage ratios is also reported by Nitin et al. [51]. One reason for this is that the thrust coefficient is lower at this TSR, allowing a greater volume of water to pass through the area swept by the blade. Another reason is associated with the angle of attack (AOA) being higher at low rotation speeds. This higher AOA causes separation at the low pressure surface of blade, as seen in Figure 4.7. An increased blockage ratio increases the effective flow velocity and corresponding AOA. This increased flow velocity and AOA further increases flow separation and decreases device performance. These competing effects, an increase in effective velocity that increases the turbine torque and aggravated flow separation that decreases the turbine torque, counteract each other and reduce TCT sensitivity to blockage ratio.

The variation in turbine performance with increasing blockage ratio for TSRs of 5.11 and 9.05 is shown in Figure 4.8.

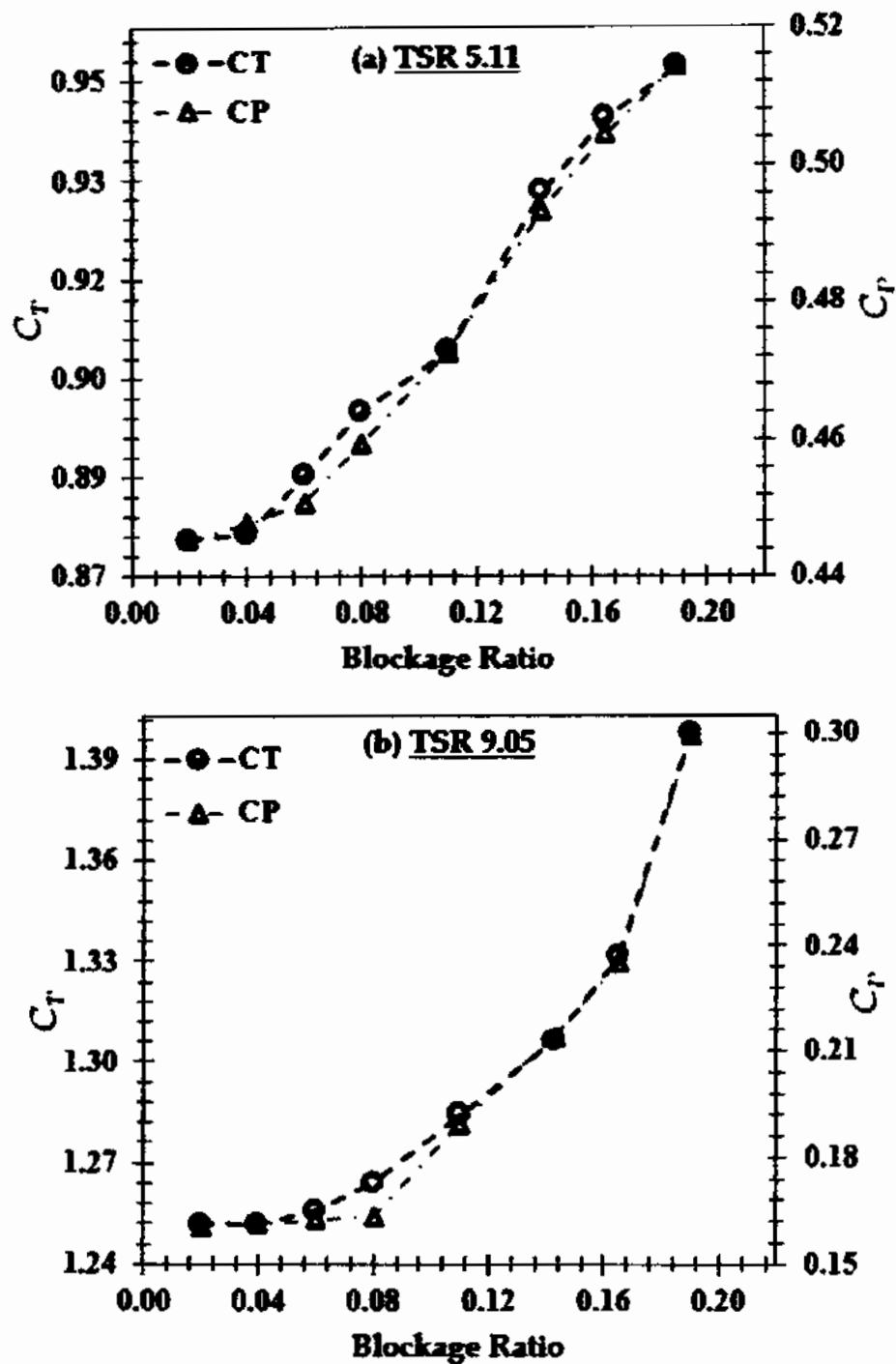


Figure 4.8 Effect of Blockage Ratio on Turbine Performance at (a) TSR 5.11 (b) TSR 9.05

The power coefficient of turbine (C_p) increases by 13% for TSR 5.11 and 47% for TSR 9.05 when the blockage ratio is increased from 0.02 to 0.19. Similarly, C_T also increases over this blockage ratio range with increase of 8% and 10% for TSRs of 5.11 and 9.05

respectively. These findings are consistent with results of other blockage studies on marine hydrokinetic turbine [51, 138, 139]. It is clearly evident from Figure 4.8 that a positive correlation exist between performance and blockage ratio for the turbine operating at and beyond optimum TSR for the evaluated range of blockage ratios.

To better compare our results with other studies we focus our analysis on blockage ratios from 2-11%. For a small wind turbine in a wind tunnel, it has been shown that variation in blockage ratio below 10% does not affect performance [140]. A scaled tidal turbine rotor in RANS CFD simulation also exhibited a similar variation in performance for variation of blockage ratios in this range [51]. A similar blockage study utilizing an actuator disc model observed a linear relationship between performance and blockage ratio for the evaluated blockage ratios of 1.9, 3.3 and 8.7% [138]. The blockage study presented in this thesis extended these studies by utilizing a real turbine rotor and added data points representing additional blockage ratios in this range. Furthermore, boundary conditions are also changed to study the sole effect of blockage to further clarify the relation between performance and blockage ratios below 10%. Over this range, the increase in C_p and C_T is 6% and 3% respectively for a TSR of 5.11 and 16% and 3% respectively for a TSR of 9.05. These results does not compliment the findings presented in [51, 138, 140]. The conflict might be attributed to the difference in level of details between the two turbine models and the difference in boundary conditions, as well as the fact that most relations seems linear if we only have a few sets of results. The discrepancy in effect for blockage ratios below 10% will be increasingly important as the size of turbine farms increase. Thus, it is suggested that further studies may be carried out at an increased range of blockage ratios containing more data points and equal distribution below and above the value of 10% to resolve this conflict.

4.5.5 Effect of boundary layer on turbine performance

TCTs operating in shallow water are expected to be impacted by boundary proximity [138]. For a standalone device, this effect will predominantly be from the sea bed. However, in the case of a tidal farm it could be due to proximity to the side of the channel where a strong shear layer exist between the slow and relatively faster moving sea water. It is considered

necessary to develop a clear understanding of the effect of boundary proximity on TCT performance before extending our investigations to tidal turbine arrays.

Two sets of CFD simulations are conducted using eight fluid domains described in Table 4.5, to investigate the effects of boundary layer on TCT performance. These two sets of simulations have different boundary conditions at the bottom and side walls of the channel. Symmetry boundary conditions are used for the 1st set, whereas no slip boundary conditions are used for the 2nd set for the bottom and side walls of the channel. The simulation condition of optimum TSR of 5.11, inlet velocity of 1.05 m/s and TI as 5% are used for both sets of simulations. All the channels used in the simulations have a Froude number of 0.34.

The effect of boundary layer on the flow is presented through a contour plot of the stationary frame velocity along longitudinal vertical center plane for the two sets of simulations representing a case for each of flow with and without boundary layer for the domain with blockage ratio of 14.3% in Figure 4.9.

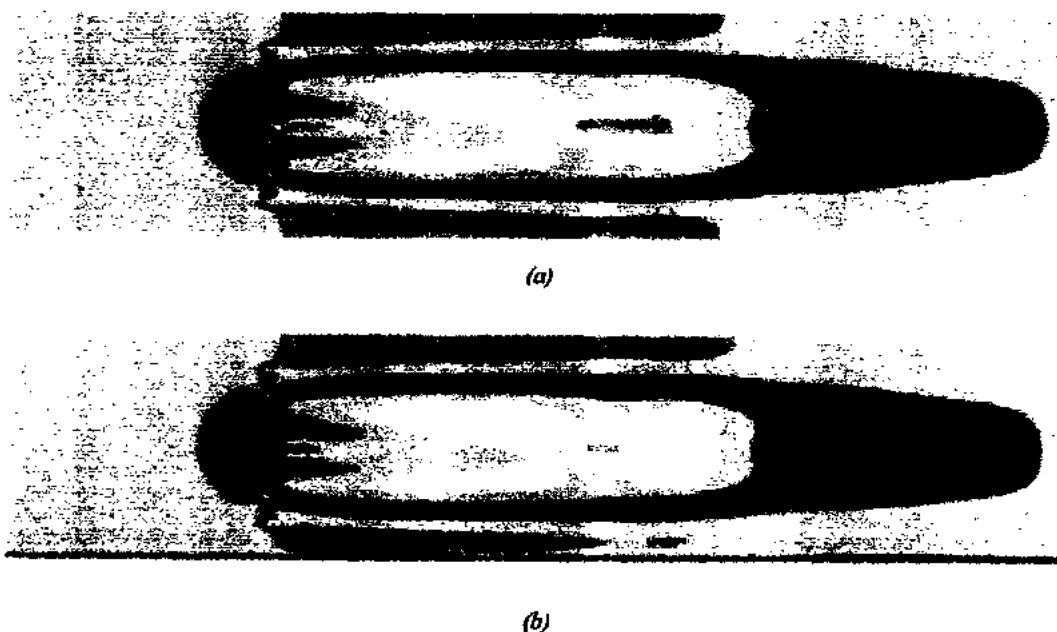


Figure 4.9 Velocity contour through the centerline plane of turbine (a) Without Boundary Layer (b) With Boundary Layer

The bypass flow between the turbine and channel bottom has been constrained in Figure 4.9(b) compared to Figure 4.9(a) by the effect of boundary layer. Moreover, the decrease

in volumetric flow rate in the lower bypass region has caused an increase in flow rate in the upper bypass region as evident from a stretched upper bypass region in Figure 4.9(b).

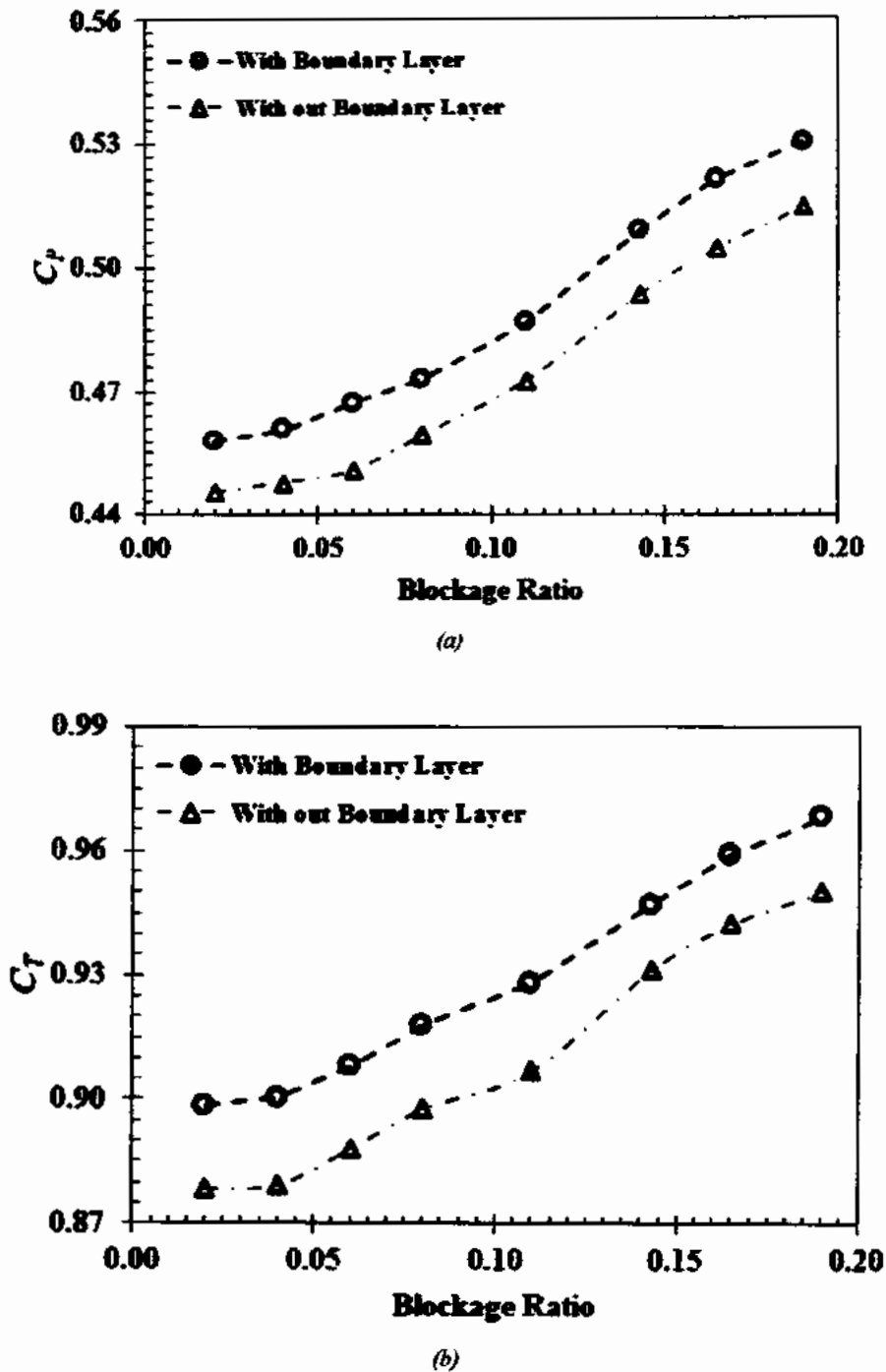


Figure 4.10 Effect of Boundary Layer on turbine (a) power coefficient (b) thrust coefficient

The presence of boundary layer increased the predicted performance for all blockage ratios as shown in Figure 4.10.

Power coefficient of the turbine C_p increased between 2.7 and 3.5%, whereas the thrust coefficient C_T increased between 1.6 and 3.5% for the evaluated blockage ratios.

4.6 RANS CFD modeling of full scale SAFL RM1 turbine

Section 4.5 presented the development of CFD methodology for the performance prediction of 1:40 scale model SAFL RM1 turbine. In this section, the developed CFD methodology is further extended to simulate the performance of full scale SAFL RM1 turbine of 20 m diameter including nacelle and monopile support tower. This is necessary because our ultimate goal is to extend these simulations to tidal turbine arrays. Where the role of support structure may be crucial for the performance of downstream devices. The blade design for full size SAFL RM1 turbine adopted in this thesis is as in Table 4.6.

Table 4.6 Blade design parameters for full size SAFL RM1 Turbine

r/R	Radius	Pre-Twist	Chord (c)	% Thickness (t/c)	Thickness (t)
(-)	(mm)	(deg)	(mm)	(%)	(mm)
0.21	2100	13.16	1200	100.0	1200.0
0.24	2400	13.16	1200	100.0	1200.0
0.27	2700	13.16	1368	84.9	1161.4
0.29	2900	13.16	1872	51.8	969.7
0.32	3200	13.16	2288	31.1	711.6
0.35	3500	13.16	2504	19.4	485.8
0.37	3700	13.16	2580	15.0	387.0
0.40	4000	11.28	2576	15.0	386.4
0.43	4300	10.24	2528	15.0	379.2
0.45	4500	9.43	2460	15.0	369.0
0.48	4800	8.76	2380	15.0	357.0
0.51	5100	8.17	2296	15.0	344.4
0.53	5300	7.64	2212	15.0	331.8
0.56	5600	7.16	2128	15.0	319.2
0.59	5900	6.70	2044	15.0	306.6
0.61	6100	6.27	1968	15.0	295.2
0.64	6400	5.86	1892	15.0	283.8

0.67	6700	5.46	1824	15.0	273.6
0.69	6900	5.07	1760	15.0	264.0
0.72	7200	4.69	1696	15.0	254.4
0.75	7500	4.31	1636	15.0	245.4
0.77	7700	3.93	1580	15.0	237.0
0.80	8000	3.55	1528	15.0	229.2
0.83	8300	3.17	1480	15.0	222.0
0.85	8500	2.78	1432	15.0	214.8
0.88	8800	2.38	1384	15.0	207.6
0.91	9100	1.98	1340	15.0	201.0
0.93	9300	1.57	1292	15.0	193.8
0.96	9600	1.14	1248	15.0	187.2
1.00	10000	0.70	1200	15.0	180.0

Several critical parameters need to be related for translating the performance of 1:40 scale model to a full size turbine. For TCT, the scaling of physical properties can be adopted from the proven and established practices used in marine propellers outlined in tidal measurement best practice manual [141]. The identity of kinematic condition can be ensured through identical tip speed ratios for comparing the performance of different size of devices of similar design. The performance of fully immersed turbines would mainly depend on the device scale Reynolds number. The Strouhal Number similarity would be important when dealing with unsteady, oscillating flow problems as it will influence the wake shedding by structural members. The Froud number scaling would be necessary for device operating in shallow waters under some influence from the free surface. However, it would generally be impossible to achieve similarity for all the scaling parameters.

The non-dimensional scaling parameters for TCT has been derived by Mason-Jones et al. [64] and described here for the completeness of discussion. The power output (P) of TCT is a function of the turbine size represented by its diameter(D), angular velocity(ω), fluid density (ρ), dynamic viscosity (μ) and flow velocity (V) as:

$$P = f(D, \omega, \rho, \mu, V) \quad (4.23)$$

This relationship contains ($n = 6$) independent variable with ($k = 3$) repeating variable as D, ρ, V and can therefore be represented through ($n - k = 3$) non-dimensional groups using Buckingham Pi theorem as:

$$\frac{P}{\rho D^2 V^3} = f\left(\frac{\rho V D}{\mu}, \frac{\omega D}{V}\right) \quad (4.24)$$

The non-dimensional groups in equation (4.24) is expressed in more conventional terms as:

Reynolds number:
$$R_e = \frac{\rho V D}{\mu} \quad (4.25)$$

Tip Speed Ratio (TSR):
$$\text{TSR} = \frac{\omega D}{2V} \quad (4.26)$$

Power coefficient:
$$C_p = \frac{P}{\frac{\pi}{8} \rho D^2 V^3} \quad (4.27)$$

The constant $\pi/8$ and $1/2$ does not change the dimensionless form of the groups, therefore we can express the relationship in equation (4.24) as:

$$C_p = f(R_e, \text{TSR}) \quad (4.28)$$

Similar non-dimensional analyses for the turbine torque (T) and thrust (F) would yield:

$$C_\theta = f_1(R_e, \text{TSR}) \quad (4.29)$$

$$C_T = f_2(R_e, \text{TSR}) \quad (4.30)$$

Equations (4.28-4.30) shows that the performance in terms of coefficients of power (C_p), torque (C_θ) and thrust (C_T) for turbines of similar design having different sizes would be same at similar R_e and TSR.

Mason-Jones et al. [64] developed a CFD model for the performance of a scaled model TCT and validated it through flume experiments. Later, the performance of several sizes of turbines of similar design was simulated through RANS CFD model as shown in Figure 4.11.

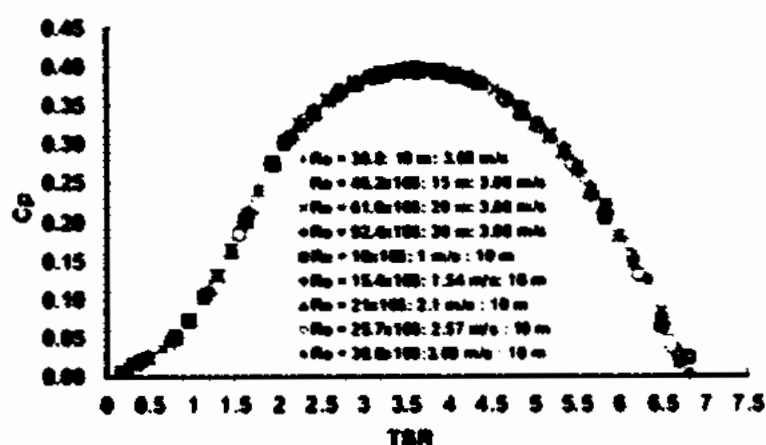


Figure 4.11 Power coefficient (C_p) vs TSR with increasing turbine diameter and velocity [64]

Figure 4.11 shows that the performance of turbine has neither been varied by the variation of turbine diameter nor upstream velocity. This indicates that the performance of this turbine is insensitive to Reynolds number variation within the Re range ($1 \times 10^7 - 9.24 \times 10^7$). However, this independence of performance in terms of non-dimensional performance parameters was achieved for $Re > 5 \times 10^5$. In a similar experimental study, Tedds et al. [142] also showed that the critical Reynolds number for their turbine design is 5×10^5 . Below this critical Reynolds number the performance of turbine significantly varies, while above this value the performance is insensitive to Reynolds number variations. For the SAFL RM1 turbine design, the subject of investigation in this thesis, Stelzenmuller [94] in their experimental study utilizing the 1:45 scaled model demonstrated that the performance of turbine is insensitive to Reynolds number variation above the Re value of 3.2×10^5 .

For the study presented in this thesis, the turbine diameter based Reynolds number of model scale turbine is 5.2×10^5 , whereas the Reynolds number for full scale device is 3×10^7 . Therefore, enough justification to conclude that the performance of full scale device for this thesis in terms of non-dimensional parameters will be comparable to the 1:40 scale model without the need for Reynolds number scaling. Further, the blockage ratio for the model scale device is 14.27%, whereas for the full scale device the blockage ratio is 6.54%. The effect of this difference in blockage ratio on turbine performance has been discussed later in this chapter in section 4.6.4. Finally the Froud number for the channel in model scale is 0.34, whereas for the full scale channel it is 0.06. However, since we are not

modeling the free surface effects, therefore no scaling would be applied for the Froude number.

A similar approach to the one described in section 4.5 is adopted for the development of CFD methodology for the performance prediction of full scale RM1 turbine. However, some necessary changes are made to the domain specification, mesh definition and boundary conditions that are discussed in the proceeding sections. Additionally, for the full scale device both steady state and transient simulations are conducted.

4.6.1 Numerical method

The simulation methodology adopted is such that for each TSR a steady state simulation utilizing a Multiple Frame of Reference (MFR) technique with frozen rotor frame change model is first conducted. The steady state method has been discussed in detail in section 4.5. This converged steady state solution is then used as the starting point for transient simulation. The time dependent (Transient) models simulate the rotating turbine in a manner comparatively more closely to real turbine. For the transient simulations, Transient Rotor Stator (TRS) frame change model is used with a sliding mesh method and the transient terms is solved through Second Order Backward Euler implicit time stepping scheme. A frame change model decides the way in which the interfaces between the domains communicate with each other. This approach simulate the transient relative motion between the components on each side of the interface and accurately models the relative motion. Although, this approach more accurately models the relative motion but expends more CPU time, computational power and disk storage. In the transient rotor stator approach, the inner cylindrical domain containing the rotor is physically rotated at every time step using a sliding mesh technique. Mesh deformation is enabled for the rotating domain with region of motion specified and displacement relative to previous mesh.

For the model scale device a wall resolved turbulence model is adopted and the distance of the first node away from the wall is set such that to ensure that the value of y^+ is less than 1. The value of $y^+ < 1$ with a growth rate of not greater than 1.2 is the necessary condition for wall resolved turbulence model. However, for the full scale models achieving a target value of $y^+ \leq 1$ would require a higher level of grid stretching from the wall resulting in higher aspect ratio cells [143]. These cells can possibly cause solution instabilities and

convergence problems. An alternate approach to the wall resolved turbulence model could be the effective use of wall function model that works with relatively coarser grids in the near wall regions. The wall functions determine the near wall profiles, which are often predictable, rather than actually resolving the profile with a very fine mesh. The ANSYS CFX implements the wall function models through an automatic wall function switch, and its activation is subjected to the value of y^+ . If y^+ is too low the first node will lie in the laminar (viscous) part of the boundary layer where wall functions are not valid. On the other hand, if y^+ is too high the first node is outside the boundary layer and wall functions will be imposed too far into the domain. The necessary condition for the wall function model is that the first node be located in the logarithmic layer with $30 < y^+ < 100$ [143]. The ANSYS CFX documentation prescribes this range to be $2 \leq y^+ \leq 300$ and the minimum number of nodes to be greater than 10 to take full advantage of the automatic wall function switch for the SST turbulence model [131]. This shift from a wall resolved turbulence model to a wall function model is necessary to ensure the quality of mesh necessary for the stability and convergence of solution.

The total time of simulation for the transient runs are set to correspond to a time length which the turbine takes to complete three rotations at the respective angular velocity against each TSR. The time step for simulation corresponds to six degrees rotation of the turbine. A time step study is conducted to establish the adequacy of this time step value in view of the computational expense, accuracy and system memory requirements provided in section 4.6.4. The convergence criterion is set to the residual target value of $1E-3$ with maximum coefficient loops set to 5 to limit the number of iterations within each time step. Further, the torque values on turbine blades are also monitored during the solution process to ensure the convergence. All the simulations are performed on the HP Z840 Workstation with Intel(R) Xeon(R) CPU E5-2699 v3 @ 2.30 GHz, 36 Core(s), 72 Logical Processor(s) having an Installed Physical Memory (RAM) of 128 GB.

4.6.2 Computational domain and boundary conditions

The domain configuration for the full scale model is conceptually similar to the scaled model simulations. However, the nacelle and support structure is included and the dimensions are changed as detailed in Figure 4.12.

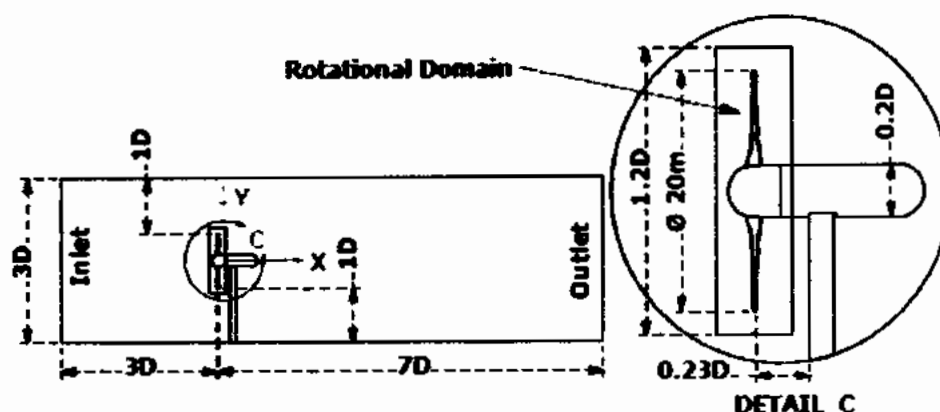


Figure 4.12 Dimensions of the full scale simulation domain

The full scale simulations utilized a more realistic turbine design with hub, nacelle and support tower. The full scale turbine has 20 m rotor diameter and the support structure is a 28 m long steel tubular monopile with a diameter of 2 m. The stationary domain of rectangular shape is $3D$ deep, $4D$ wide and has length of $10D$ to represent the flow channel in the CFD model. The cylindrical rotational domain uses a diameter of $1.2D$ and width $0.3D$ to enclose the turbine blades and hub for modeling the rotation at turbine angular velocity. The domain reference $(x,y,z)=(0,0,0)$ is set at the center of the back face of turbine hub. In the transient CFD simulations, the rotational domain containing the rotor is physically rotated through a sliding mesh approach at every time step. Mesh deformation is enabled for the rotating domain, with the region of motion specified using the displacement relative to previous mesh. For the rectangular channel domain, the inlet is specified with a turbulence intensity of 5% and viscosity ratio of 10 for all simulations. Velocity specified inlets intended for incompressible flows are predominantly used for regions where inflow is expected. To make the boundary condition robust, the outlet of the flow channel is specified as a pressure outlet, with a relative static pressure of 0 Pa [131]. No slip wall boundary condition is assigned to the bottom and two sides of rectangular channel domain, as well as to the turbine blades, hub, nacelle and tower surfaces. In a no slip wall boundary condition the velocity of the fluid immediately next to the wall is zero. The top of the rectangular channel is assigned a free slip wall boundary condition, specifying that the velocity of fluid immediately next to the wall is not retarded by wall friction effect. The free surface deformation is neglected, although this omission could have an effect on the predicted turbine performance. However, this effect depends upon

the clearance between the blade tip and top surface. Several previous studies [33, 51, 144] have established that a clearance of 1D is large enough to make the free surface effects negligible, and the simulation results presented in this thesis shows that this assumption is reasonable for the utilized simulation conditions. Three mesh interfaces are specified at the three connecting surfaces between the cylindrical and rectangular domains. These interfaces are essential for connecting the two domains, as well as to model the changes in reference frame between domains. For these interfaces, a general connection interface model is used with transient rotor stator frame change model and the meshes are connected through a General Grid Interface (GGI) method. The interface models and mesh connection method controls the way data are transferred across the interfaces. Additionally, for the rotational domain side of interfaces, an interface boundary condition is specified and the mesh motion is activated. Similarly, for all the no slip wall boundaries in the rotating domain specified for the blades and hub, the mesh motion is activated and the wall velocity is set relative to boundary frame.

4.6.3 Mesh definition

The meshing scheme utilized for the model scale simulations is adopted with a few necessary adjustments. A selective body meshing technique is used with a patch confirming method to setup a tetrahedral mesh starting from the turbine blades in the mesh component system of ANSYS Workbench. The geometric model is converted into a single part consisting of multiple bodies to obtain a matching conformal mesh on the shared faces between bodies. The mesh used in these simulations is shown in Figure 4.13.

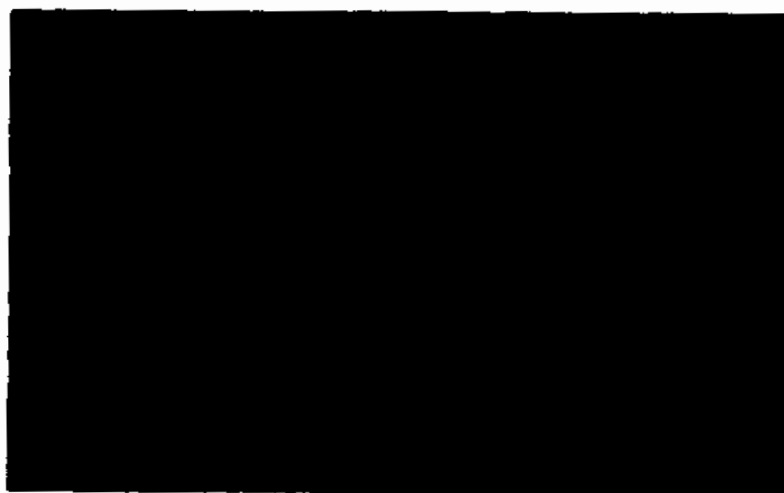


Figure 4.13 Mesh used for the full scale turbine simulations

Tetrahedral mesh elements are used to generate mesh on blades with an element size of 60 mm, hub and nacelle with 150 mm and rest of the cylindrical domain with 260 mm. The distance of first node away from the wall (y^+) and number of nodes in the boundary layer depends upon the choice of turbulence model and the selection of either a fully resolved wall or wall function model. A wall function model is intended to be utilized for the full scale simulations to avoid higher aspect ratio cells in the near wall mesh. The necessary condition for the wall function model is that the first node be located in the logarithmic layer with $30 < y^+ < 100$ [143]. The ANSYS CFX documentation prescribes this range to be $2 \leq y^+ \leq 300$ and the minimum number of nodes to be greater than 10 to take full advantage of the automatic wall function switch for the SST turbulence model [131]. With these guidelines in mind, prism layer elements are generated around the blade surfaces to capture the boundary layer flow. Distance of the first node away from the wall (blade surface) is set to 0.18 mm, with a growth rate of 1.2 and the total number of layers is 11. This mesh setup ensured that the value of y^+ and minimum number of nodes is within the prescribed range to properly utilize the automatic wall function switch for the SST turbulence model. The value of y^+ on the lower and higher pressure surfaces of the blade is monitored throughout the solution by creating user functions through expressions. The value of y^+ is $31 \leq y^+ \leq 43$ for all the steady state and transient CFD simulations of full scale turbine, which is within the prescribed range of y^+ values required for the proper functioning of SST turbulence model with wall function approach. For the cylindrical domain the total mesh count is 3.1×10^6 elements (7.6×10^5 nodes). The stationary rectangular domain is meshed with an element size of 2900 mm except the surface of the monopile support tower that is meshed with an element size of 100 mm. The total mesh count for the rectangular domain is 1.4×10^6 elements (2.7×10^5 nodes).

4.6.4 Verification and validation of RANS CFD methodology

A mesh sensitivity study is performed to verify that the fluid dynamic model is providing a mesh independent solution. For this purpose the steady state RANS CFD (MFR) model is utilized on four different grids generated with almost a similar mesh scheme but having different grid densities in the rotating and stationary domains detailed in Table 4.7.

Table 4.7 Mesh details and predicted torque results for sensitivity analysis

Grid	No. of Elements ($\times 10^6$)			Torque Difference ¹ (%)
	Inner Domain	Outer Domain	Total	
1	1.34	0.72	2.07	-3.2
2	2.23	1.07	3.30	-1.1
3	3.10	1.40	4.50	-0.5
4	5.02	2.39	7.42	-

¹ % Torque difference denotes the difference of predicted torque value from each grid with respect to Grid 4.

The meshing strategy is to use 70% or more elements in the rotating domain and keep the number of inflation layers and y^+ value nearly constant for all the grids utilized in the mesh sensitivity study. The MFR model is selected to eliminate the uncertainties associated with temporal discretization at this stage. The simulations are conducted at uniform velocity of 1.5 m/s and turbulence intensity of 5% with a viscosity ratio of 10 for the turbine operating at optimum TSR of 4.87. The value of torque on a single blade is a direct output of the CFD solution, and is used to evaluate the effect of grid density on the simulation results as shown in Figure 4.14.

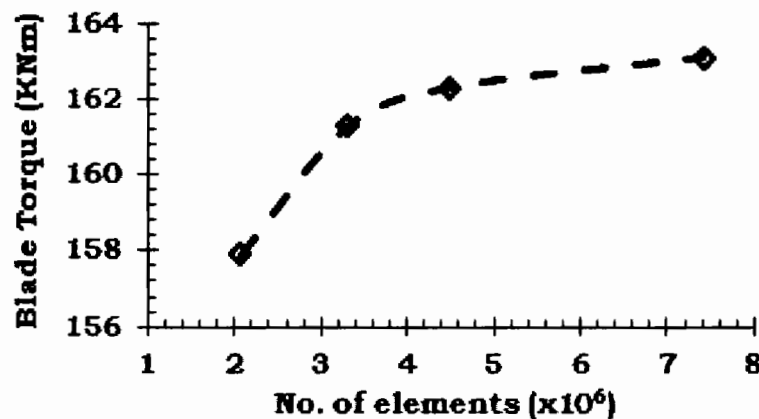


Figure 4.14 Variation of blade torque with grid density

It is evident from Figure 4.14 that increasing the grid density monotonically increases the predicted torque value between the last two grids. Difference in the predicted values of torque for a single blade is only about 0.5% between the last two grids (Table 4.7). Therefore, grid with 4.5×10^6 elements (Grid 3) is selected for further simulations. To establish the temporal accuracy of the fluid dynamic model a time step sensitivity study is

performed by utilizing the transient CFD model described in section 4.6 with selected Grid 3. Three simulations at time steps corresponding to 2° , 4° and 6° of turbine rotations and total time corresponding to three turbine rotations are conducted at the optimum TSR 4.87 and each simulation is initialized by the steady state solution. The difference between the torque values with respect to the 2° case is 0.08% and 0.32% for the 4° and 6° case respectively. The value of predicted torque is found to be less sensitive to the size of time step. This observation is similar to the findings in other similar studies [51, 120] and supported by the fact that ANSYS CFX is an implicit solver and does not require very small Courant numbers for stability [124]. Thus, a time step corresponding to 6° of turbine rotation is selected to ensure computational efficiency is achieved without compromising the accuracy and stability of numerical solution.

To validate the utilized CFD methodology, power coefficients predicted by the steady state and transient performance analysis of the full scale model is compared with model scale experimental data [26] in Figure 4.15 and Table 4.8.

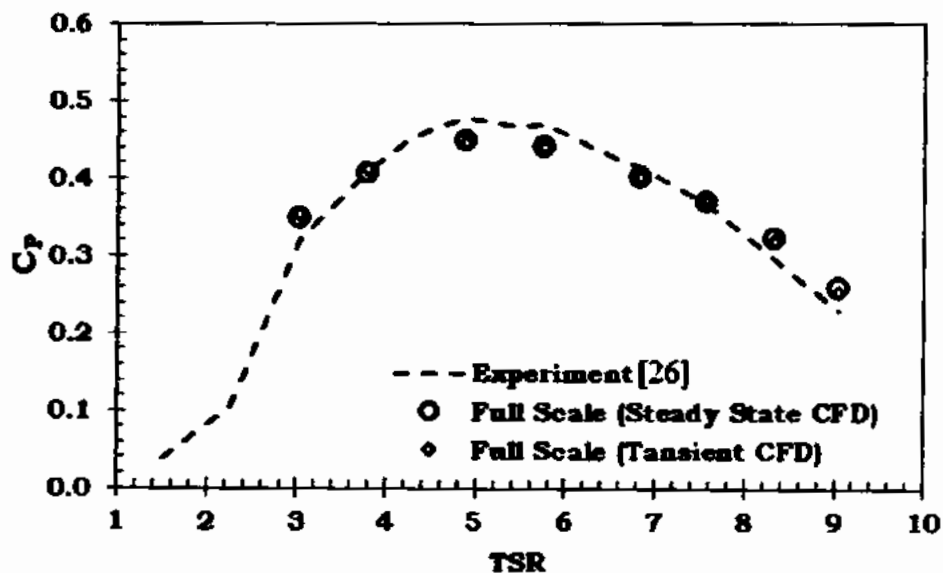


Figure 4.15 Comparison of model scale experimental and full scale simulated performance curve

Table 4.8 Quantitative comparison of turbine C_p between full scale simulations and model scale experiment

TSR	Experiment	Steady State CFD		Transient CFD	
	C_p [26]	C_p	% Difference*	C_p	% Difference*
3.02	0.320	0.347	8.5	0.354	10.7
3.79	0.408	0.406	0.4	0.411	0.8
4.87	0.477	0.449	5.8	0.447	6.3
5.76	0.471	0.440	6.6	0.442	6.2
6.82	0.414	0.401	3.2	0.402	2.8
7.57	0.368	0.369	0.4	0.368	0.1
8.32	0.295	0.322	9.2	0.319	8.2
9.05	0.230	0.260	13.0	0.254	10.4

* % Difference indicates the absolute percentage difference to the experimental values in [26].

The value of turbine (C_p) is different than the experimental value by 6.3% at the optimum TSR. The maximum difference between the steady state and transient CFD simulation in term of (C_p) prediction is observed at the extreme operating conditions at the lowest and highest TSR. Similarly, both the models provided an average difference of 1.9% with the model scale experimental data. The maximum difference for the transient model is 10.7% against a value of 13% for the steady state CFD model. For the sole purposes of performance prediction of turbine, it can be concluded that both the steady state and transient CFD models are similar. However, the development of transient CFD model is necessary for the achievement of the other outlined objectives in this thesis that will be discussed in chapter 6. It is further mentioned here that the blockage ratio for model scale and full scale device is 14.3% and 6.5% respectively. Additionally, in the experiment each rotor of the twin rotor turbine is located at off center position. Therefore, the results outlined in Table 4.8 are subjected to corrections. Later in chapter 6 section 6.1.2, the effect of this blockage ratio and location change between the experimental channel and simulation domain on the turbine (C_p) at the optimum TSR is quantified in Table 6.2. The value of turbine (C_p) in a simulation domain with a blockage ratio (14.3%) and the turbine located at a position similar to the experimental channel is predicted to be different than the experimental value by 0.2%. However, when the turbine is shifted to the center of the

same simulation domain, the value of (C_p) is predicted to be different than the experimental data by 2.8%.

4.7 Summary

In this chapter the experimental setup used for the investigation of model scale turbine performance is presented. The experimental data obtained from these tests is used for the validations of our computational models throughout this thesis. The development of steady state RANS CFD methodology for the performance prediction of 1:40 scale SAFL RM1 turbine rotor is described. The numerical method is verified through a mesh independence study and successfully validated with experimental data over the entire range of turbine operating conditions from TSR 1-9. This validated RANS CFD method is then used to investigate the effect of blockage and boundary layer on the performance of SAFL RM1 model scale TCT rotor. This study is necessary for extending the RANS CFD methodology to the simulation of tidal turbine arrays. The RANS CFD methodology for the model scale rotor is further extended with necessary modifications to the steady state and transient RANS CFD simulations of the full scale SAFL RM1 turbine including nacelle and support tower. The CFD methodology for the performance prediction of full scale turbine is once again verified through mesh and time step sensitive study and validated with experimental data.

Chapter 5

Development of Fluid Structure Interaction

Methodology

This chapter describes methodology for the development of coupled Fluid Structure Interaction (FSI) simulations for modeling the performance and structural response of SAFL RM1 turbine. Transient coupled FSI simulations are conducted for the simple 1:40 scaled model RM1 turbine rotor. Results from these simulations are successfully validated with the experimental data. This model is modified to simulate the performance and structural response of the full scale RM1 turbine with realistic blade structure and including nacelle and support tower in transient FSI simulations. The FSI investigations are necessary to establish the effect of blade deformation on the performance of full scale turbine based on realistic blade design. The fatigue and structural response of real turbine blades would also be described. These simulations would help to understand the pros and cons of both the CFD and FSI models and their utility for simulating tidal arrays. The Results presented in this chapter are mostly based on our published research articles.

5.1 Fluid Structure Interaction (FSI) modeling

CFD based numerical models treat the turbine blade as a rigid structure and does not take into account the hydroelastic interaction between the blades and flowing water. Whereas, in reality the tidal turbine blades are flexible and deform due to the onset flow [145]. A deflected turbine blade would present different angle of attack and pressure difference across the blade surfaces when compared to a rigid un-deflected blade. The hydrodynamic and structural response of a deformed turbine blade is expected to be different than an undeformed rigid blade, if the blade deformation is significant. Therefore, the CFD models may be less accurate for modeling the turbine performance, wake and structural response for cases involving larger blade deformations. Additionally, the CFD based numerical

models only solve the fluid field and are unable to describe the structural mechanics of turbine in terms of structural stresses and deformations. Most of the turbine CFD performance studies including those presented in chapter 4 have provided an acceptable accuracy because the experimental data is based on model scale turbines with solid blade designs that undergo minimal deflections. However, for real size turbines, the blades are large and hollow that can face larger deformations due to the onset flow. Therefore, it is expected that the FSI based numerical methods that can model interaction between the fluid and structure as well as take into account the hydroelastic behavior of the blades can more closely assess the turbine performance.

Fluid Structure Interaction (FSI) occurs when a fluid interacts with a solid structure in such a way that the fluid pressure causes deformation to the structure, and the deformed structure in return alters the flow field. An FSI problem can be solved either through a monolithic (single domain) or a partitioned (independent domain) approach. In the monolithic approach a single system of equation represents the structural mechanics and fluid dynamics systems that are solved simultaneously. In the partitioned approach the structure and fluid computational domains are treated separately and solved in their respective domains. Both the systems are represented explicitly by their respective systems of equations and are solved separately in their respective domains. The partitioned approach can further be classified into uncoupled, coupled or integrated approach. Similarly, the coupled approach could either be a strongly or loosely coupled approach and the data transfer could be either 1-way or 2-way. In the 1-way data transfer arrangement, data from the CFD solver is transferred to the FEA solver. However, data from the FEA solver is not transferred to the CFD solver. Whereas, in the 2-way data transfer arrangement, both the solver transfer data to each other at every coupling step. In this thesis, a loosely coupled partitioned (independent domain) approach has been adopted. In this approach, two separated codes for the solution of fluid field and structural field are coupled through a coupling scheme to establish a communication mechanism between the two participating codes. This approach does not require any modification to the constituent CFD or Finite Element Analysis (FEA) code. The coupling scheme acts as a “black box” to manipulate the output of CFD and FEA and to exchange data between the solvers at each coupling step.

The use of coupled FSI models in tidal turbine research has thus far been very limited due to the associated computational cost. However, their use is growing due to advancement in the numerical models, computational capabilities and greater access to the necessary computers. Kim et al. [146] and Jo et al. [147] used the uncoupled FSI approach where the data transfer is executed after obtaining solution from a steady state CFD model with 1-way data transfer to investigate the structural integrity of turbine and tower respectively. Habib et al. [148] and Hafeez et al. [149] also used a similar post CFD mapping 1-way data transfer FSI approach to model the vibration and fatigue response of TCT. But this approach is only useful for modelling minimal non-linearity and the shared data represent a single point solution. Nicholls-Lee et al. [150] adopted a loosely coupled modular FSI approach but utilized a 2D panel code flow model to assess the performance of new concept (i.e. bend twist coupled) blades made from adaptive composite. Suzuki et al. [151] used an integrated approach by combining the beam element theory based structural solver and Blade Element Momentum Model for the hydrodynamics solver to investigate the performance of turbine through simulating a single blade. Tatum et al. [134] performed the loosely coupled modular FSI simulations with 2-way data transfer. However, the focus of the study was solely on the hydrodynamic performance of turbine under the effect of wave current interaction. Nevertheless, these studies have provided a good foundation for executing more robust and higher fidelity coupled FSI models capable of simulating the hydrodynamics and structural mechanics of a full scale tidal turbine design.

5.2 FSI simulation methodology for scale model rotor

Transient Coupled FSI simulations are setup in the ANSYS Workbench software by using the fluid flow analysis system (ANSYS CFX) and transient structural analysis system (ANSYS Transient structural) that are coupled through the component system (ANSYS System coupling). This is an independent domain (partitioned) FSI approach with 2-way data transfer. This approach does not require any modification to the constituent CFD or Finite Element Analysis (FEA) code. The flow chart for the loosely coupled 2-way FSI solution procedure implemented in ANSYS Workbench is shown in Figure 5.1.

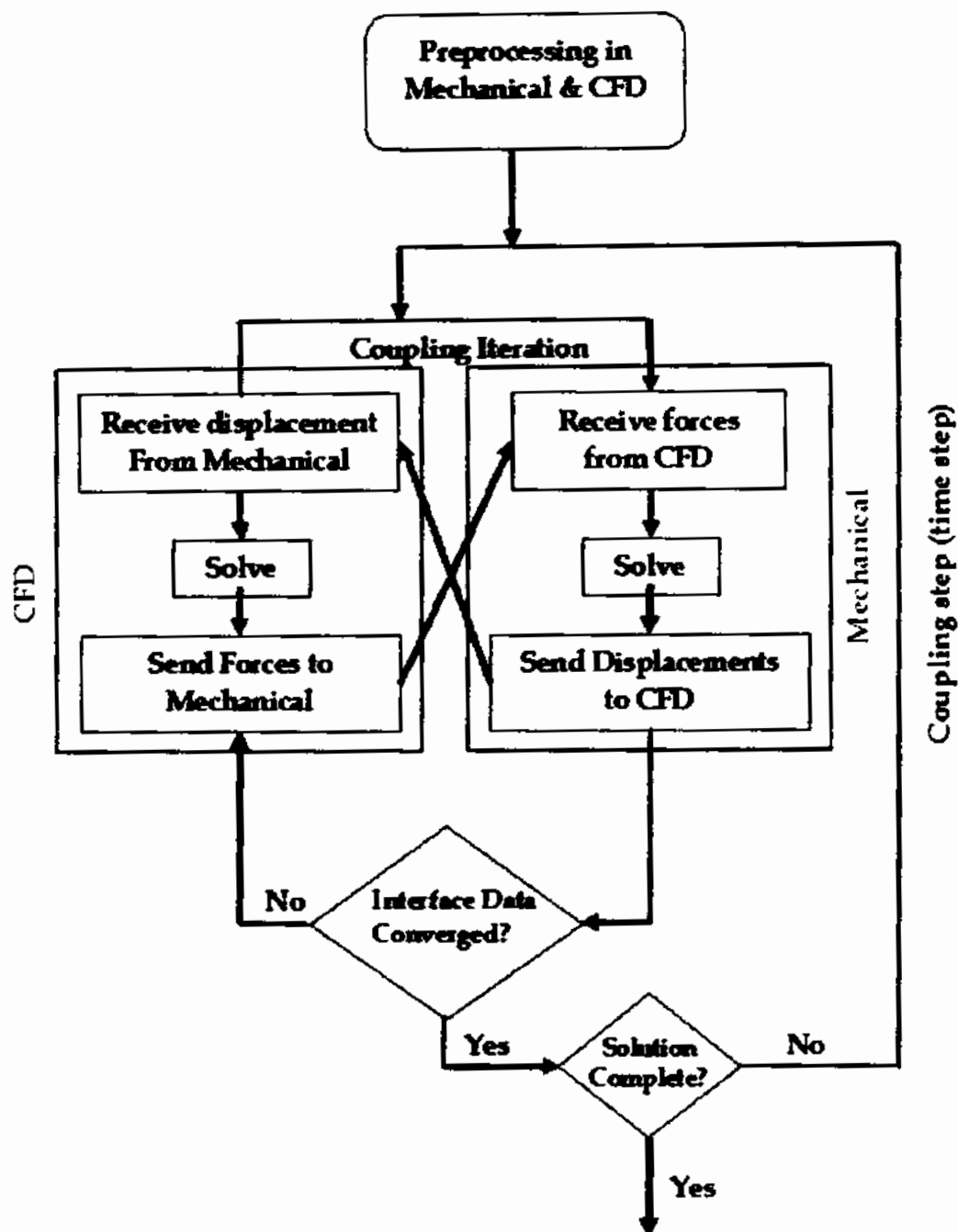


Figure 5.1 Flow chart of loosely coupled modular 2-way FSI solution procedure

The 1:40 scaled model rotor of the SAFL RM1 turbine design with solid blades discussed in detail in section 3.3 is utilized in these simulations. The optimum Tip Speed Ratio (TSR) of 5.11, corresponding to an angular velocity of 21.48 rads/sec, is selected as the calculation condition.

5.2.1 CFD setup

The fluid field is modelled through transient CFD simulations in ANSYS CFX. The simulation setup discussed in section 4.5 for the steady state CFD simulation of the scaled model SAFL RM1 rotor is modified into transient simulations. The transient CFD simulations utilized a Transient rotor stator approach to physically rotate the rotor through a sliding mesh method that has already been discussed in detail in section 4.6.1. The meshing scheme for the CFD domain, adopted a similar settings as those already described in section 4.5.2. However, in view of the increased computational cost of FSI simulations, the boundary layer mesh is changed to utilize the automatic wall function switch with $k - \omega$ SST turbulence model. The number of prism layers are reduced to 16 and the distance of the first node away from the wall is increased to 0.17 mm. This mesh setup ensured a value of $y^+ = 4$ for the dimensionless wall distance for the simulated TSR of 5.11. Additionally, the ANSYS prescribed criteria of $2 \leq y^+ \leq 300$ and minimum number of nodes greater than 10 has been satisfied [131]. It has been already verified in section 4.6.4, that once this criteria is satisfied the wall function switch would work properly and the results will almost be similar to those of the wall resolved turbulence model. The total mesh count for the fluid domain is $\approx 4 \times 10^6$ elements with $\approx 2 \times 10^6$ elements in the rotational domain. A similar fluid domain definition is used as that described in section 4.5.1. The boundary conditions are specified such that the inlet is setup with a uniform velocity condition of 1.05m/s and uniform turbulence intensity of 5%. The outlet is set as a pressure outlet with floor and side wall of the tank set to a no slip walls. The top is specified as a free slip wall. The side wall representing the longitudinal centerline of the test tank is specified as a symmetry boundary. Three conformal mesh interfaces are defined at the three surfaces connecting the stationary and rotating domains with a general connection interface model and the meshes are connected through General Grid Interface (GGI) method. These boundary and interface conditions are similar to those setup for the uncoupled CFD model of the full scale device described in section 4.6.2. However, for the coupled FSI simulations, the Rotor is assigned a no slip wall boundary condition and set to receive mesh motion from the system coupling to account for the deformation of the rotor at each coupling step that will be received from the FEA solver. The total simulation time for the turbine was 0.6 sec to model two full rotations of the turbine. A time step equivalent to 2^0

of the turbine rotations was set as 0.0016 sec in view of the numerical stability, accuracy and computational expense. The solver settings and convergence criteria is setup with similar settings as those employed for the uncoupled CFD model. The CFX solver is run in a shared memory parallel distribution mode utilizing 18 CPU cores (36 logical processors). One of the major issues with coupled FSI simulations is the requirement of higher computational time, partly due to the simultaneous solution of two independent physics fields of fluid dynamics and structural mechanics at every time step and the data transfer between the two fields. Secondly, these solutions are required to be run for enough rotor rotations to achieve a stable solution. In order to run the simulations for lesser number of rotor rotations while still obtaining a stable solution, an uncoupled steady state CFD solution of the fluid field is first obtained. This solution is used to provide initial values to another uncoupled transient CFD simulation of the fluid field, and this solution is then used to provide initial values to the fluid solver participating in the coupled FSI simulations. This approach provides fast and improved convergence of the coupled FSI simulations.

5.2.2 FEA and system coupling setup

The transient structural analysis system within the Ansys workbench is used for the FE analysis. The RM1 turbine design geometry used for the CFD analysis is shared between the FE and CFD modules. The FEA system only requires the solid parts and therefore the fluid domain is suppressed. The turbine rotor is assumed to be made from structural steel. The use of steel material for the FE analysis reduces the model complexities as compared to composite material. In addition, the carbon steel is amongst the prospective materials for turbine blades and intended to be used for one of the two types of turbines planned for the world first commercial array project [152]. Material properties of the utilized steel material are as in Table 5.1.

Table 5.1 Properties of the utilized structural steel material

Density	7850	Kg/m ³
Young Modulus	2E+11	Pa
Poisson's Ratio	0.3	(-)
Tensile Yield Strength	2.5E+08	Pa
Compressive Yield Strength	2.5E+08	Pa
Tensile Ultimate Strength	4.60E+08	Pa

The mesh is different than the CFD mesh and is more suited for the FE analysis. The loosely coupled modular approach has this advantage to use different meshes for the CFD and FE analysis. The CAD geometry of turbine rotor and fluid domain is a single part consisting of multiple bodies and therefore a conformal mesh with almost 100% node to node correspondence is generated on the shared faces of the rotor and fluid domain. A patch confirming method is used to generate tetrahedral mesh elements with body sizing of 2 mm applied to the blades and hub. The FE model for the rotor is meshed with 8.9×10^5 elements containing 1.3×10^6 nodes. The mesh used for the FE analysis of the structural field is shown in Figure 5.2.

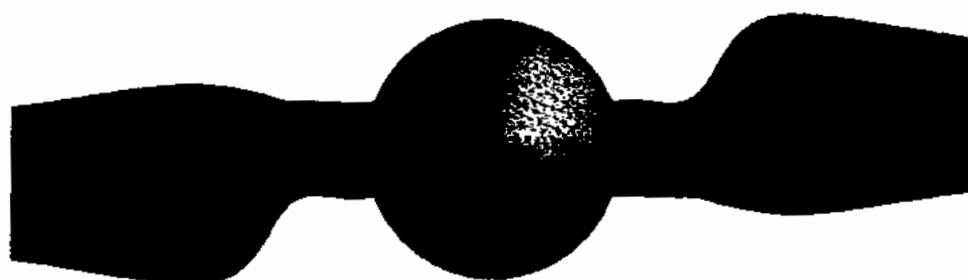


Figure 5.2 Mesh on the turbine rotor for FE Analysis

Time settings for the FE analysis are kept similar to the CFD settings with a time step of 0.0016s and total time of 0.6s. To include the effect of centrifugal forces the rotor is assigned an angular velocity of 21.48 rad/s for rotation along the x-axis to match the rotational velocity assigned in the CFD domain. A remote displacement boundary conditions is applied at back face of the hub and large displacement is assumed. Remote displacement is a type of constraint that enables to apply rotation at an arbitrary location in space. A fluid solid interface is specified at the rotor surfaces to receive force data and transfer displacement data to the CFX solver.

In the coupled FSI simulations, both the constituent solvers can be run in parallel mode to enable the solution of large problems. The FEA solution of the transient structural analysis system is performed with a shared memory parallel solver distribution utilizing 4 CPU cores and GPU acceleration.

For the system coupling setting the analysis type parameters is set to transient to setup a transient FSI simulation. The coupling duration definition is set to end time and similar time settings as those employed in the transient structural and CFX systems are employed. To communicate information between the two solvers, two data transfers are created for the turbine rotor to act as a 2-way data transfer interface. One of the data transfer is set to transfer incremental displacement from the FEA system as mesh displacement to the CFD system. Whereas the other data transfer is set to transfer force from the CFD system as force to the FEA system. The RMS convergence target for all data transfers are set to 0.1, and no ramping is employed for the data transfer. The simulation is executed such that the FEA system is to be solved first.

5.2.3 Results and discussion

To compare the accuracy of the FSI simulations, the results are plotted against the experimental data [26] and results from the steady state RANS CFD simulations described in section 4.5. Figure 5.3 shows the comparison of power coefficient C_p obtained from the experimental data, Steady state RANS CFD and FSI simulations. The quantitative comparison of experimental data and predictions of the numerical models are as in Table 5.2.

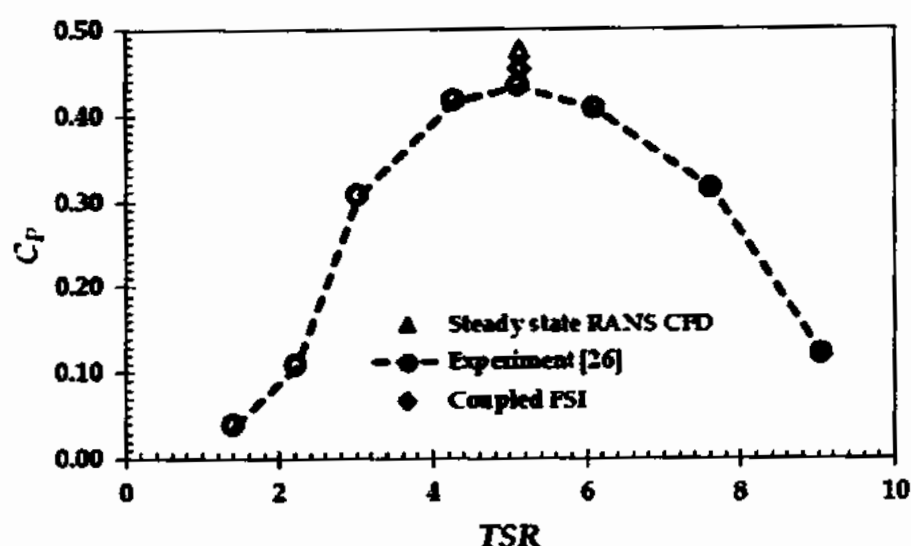


Figure 5.3 Comparison of experimental and simulated performance coefficient

Table 5.2 Quantitative comparison of Numerical and Experimental predictions

	Torque (N.m)	C_p (-)	Thrust (N)	C_p Error (%)
Experiment	2.08	0.4337	-	-
Steady state RANS CFD Model	2.28	0.4761	100.22	9.78
Coupled FSI Model	2.18	0.4545	99.29	4.80

The difference between experimental value of C_p and predicted value from the steady state RANS CFD and FSI models is less than 10%. The coupled FSI model predicted a lower value of turbine C_p (0.45) compared to a C_p value of 0.48 predicted by the uncoupled rigid blade CFD model. This result is in contrast to Tatum et al. [134] where the FSI model predicted a greater value of C_p than the RANS CFD model. Tatum et al. [134] attributed this discrepancy to the fact that initially blades of their turbine were not in its optimum position. A thrust force of 100.22 N and 99.29 N is predicted by the steady state RANS CFD and FSI models respectively. Experimental data for the thrust force is not available to validate the thrust results and evaluate the prediction difference. However, the prediction pattern is totally in accordance to the physical observation that the deformed blade will experience a lesser thrust as compared to an undeformed blade. To further investigate the reason for the difference in C_p prediction between the two numerical models, pressure

contour with velocity stream lines at blade sections at 37% and 96% of the blade length are plotted in Figure 5.4.

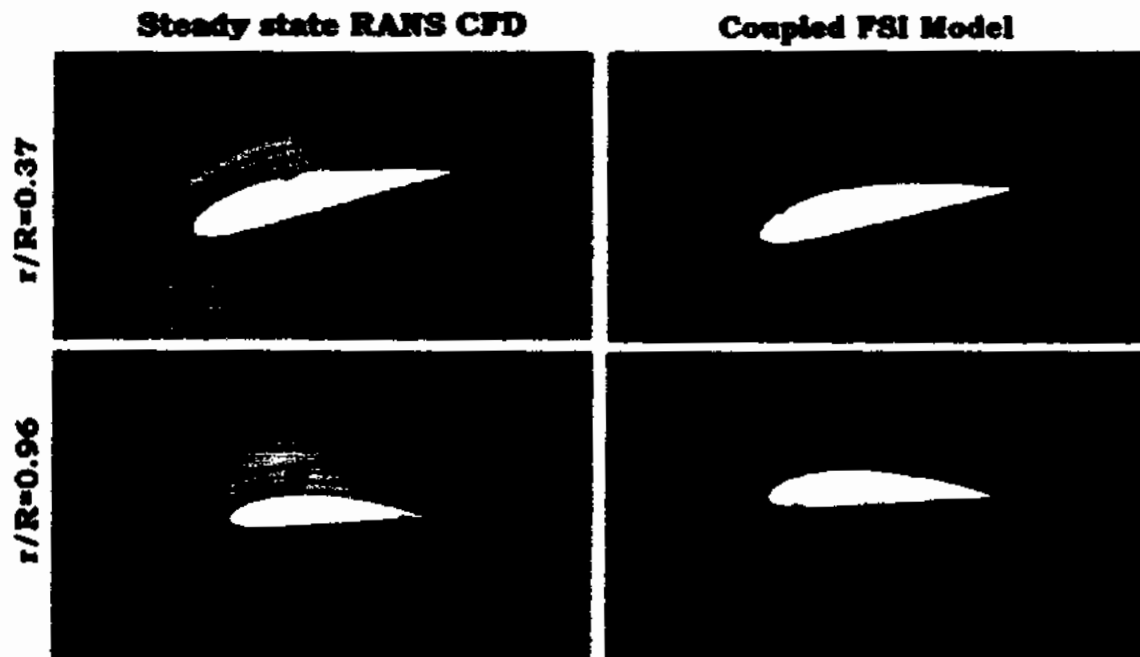


Figure 5.4 Pressure contour with velocity streamlines at TSR 5.11

Both the numerical models clearly show fully attached flow at both the blade sections. The blade deformation has not resulted in a significant change in the angle of attack that could have resulted in any variation in the separation and reattachment behavior. However, the pressure contour shows a difference in pressure at low pressure side of the blade between both the models. To more clearly elaborate this difference, pressure contour along the blade length with velocity streams is plotted in Figure 5.5.

The maximum pressure for the Steady state RANS CFD model is more as compared to the coupled FSI model. To further visualize changes in the flow behavior due to blade deformation, velocity contour at 96% of the blade length for both models is plotted in Figure 5.6.

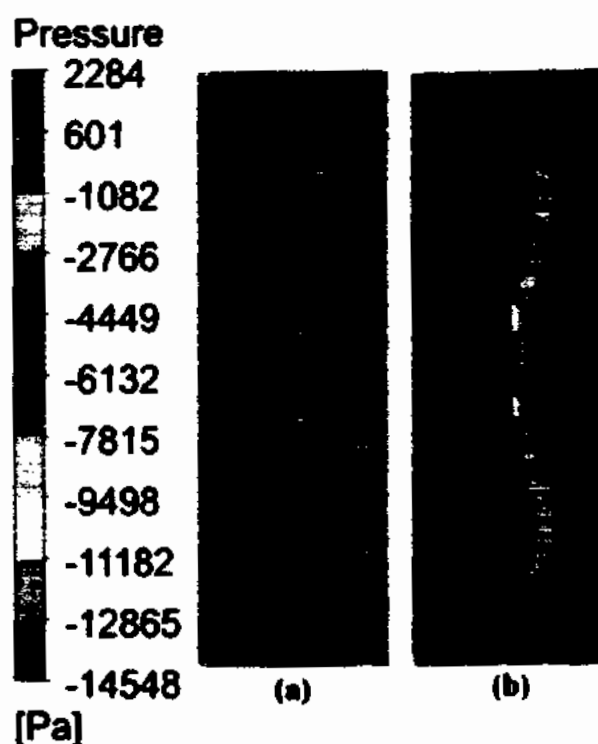


Figure 5.5 Pressure contour with velocity streamlines along the blade length (a) Steady state RANS CFD (b) Coupled FSI

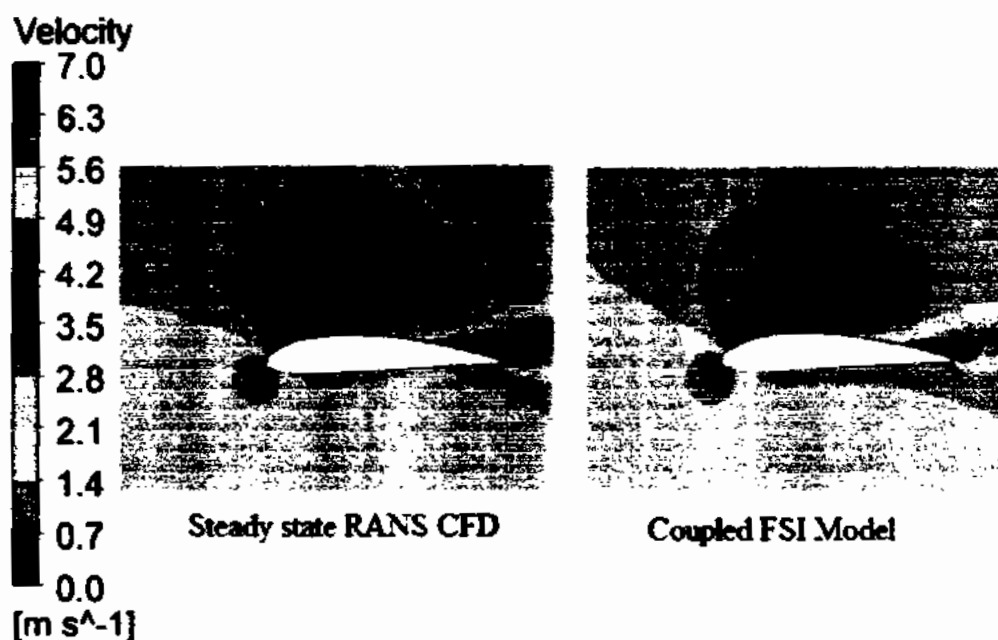


Figure 5.6 Velocity contour around the blade foil at 96% of the blade length

A small increase in local flow velocity along the high pressure side of the foil can be clearly observed for the coupled FSI model. Reading Figure 5.4 along with Figure 5.5 and 5.6, the reason for the difference in C_p prediction between the two models is attributed to the

difference in pressure difference and flow velocity across the low pressure and high pressure side of the blade. In the coupled FSI model the blade has deflected but the extent of deflection is not enough (0.12 mm) to create a significant variation in the angle of attack but it certainly has changed the pressure difference and flow velocity across the blade surfaces. The pressure difference across the blade surfaces is responsible for generating the lift force. For the Steady state RANS CFD model the pressure difference is more therefore, the predicted C_p is on higher side.

One of the advantages of coupled modular FSI simulations is that results of individual component systems can be post processed in their respective post processors. All the results that are possible in standalone FEA and CFD system solutions can be obtained from the coupled FSI simulations. Taking advantage of this utility, the contour plot of deformation and equivalent stress on rotor obtained from the couple FSI simulations is provided in Figure 5.7. Similarly, the time histories of deformation and stress predicted by the FSI model at every time step during the solution are provided in Figure 5.8.

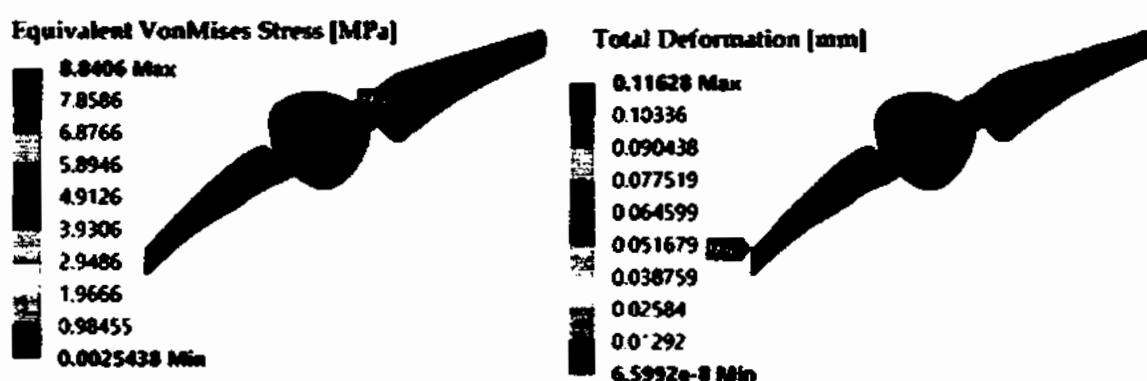


Figure 5.7 Contour plot of equivalent stress and deformation at the rotor

A maximum deformation of 0.116 mm occurred at the blade tip. This deformation is very small due to the reason that the blade is completely solid. It is highly unlikely for a real turbine blade to be made in this manner but this was necessary to replicate the actual model utilized in the experiments.

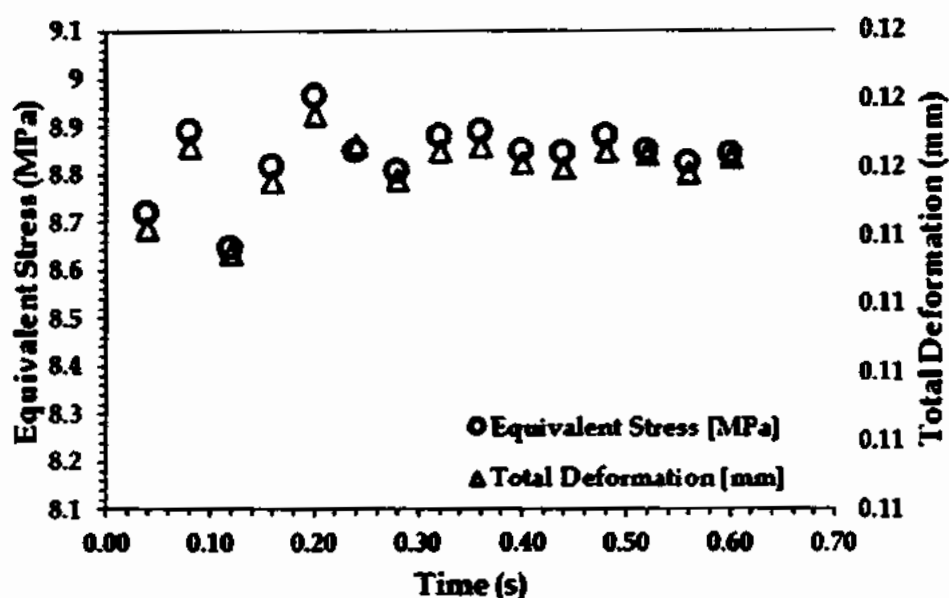


Figure 5.8 Stress and deformation at the rotor at every time step during the FSI solution process

There is not much too choose between the two models in terms of the accuracy for turbine performance prediction for the evaluated turbine design and flow conditions. However, the requirement of computational resource and solution time are very different. Both the uncoupled CFD and coupled FSI simulations presented in this thesis are performed on the HP Z840 Workstation with Intel(R) Xeon(R) CPU E5-2699 v3 @ 2.30 GHz, 36 Core(s), 72 Logical Processor(s) having an Installed Physical Memory (RAM) of 128 GB. The details of utilized computational resource and time are as in Table 5.3.

Table 5.3 Details of utilized computational resource and time

Numerical Model		No. of Utilized Cores	Solution Time		
			Days	Hours	Minute
RANS CFD	Steady State	30 Cores/ 60 Partitions	-	2	30
	Transient	36 Cores/ 72 Partitions	-	3	9
Coupled-FSI	CFD Solver	18 Cores/ 36 Partitions	11	19	16
	FEA Solver	04 Cores and 1 GPU			

Although, the computational resources dedicated to different simulations are not similar. However, Table 5.3 still provides a clear picture of the computational solution time requirement for both the methods. The uncoupled CFD model clearly has far lower solution time compared to the coupled FSI model.

5.3 FSI simulation methodology for full scale turbine

The coupled FSI simulation methodology described in section 5.2 is extended to utilize the full scale SAFL RM1 turbine with nacelle, support structure and realistic blade design shown in Figure 5.9.

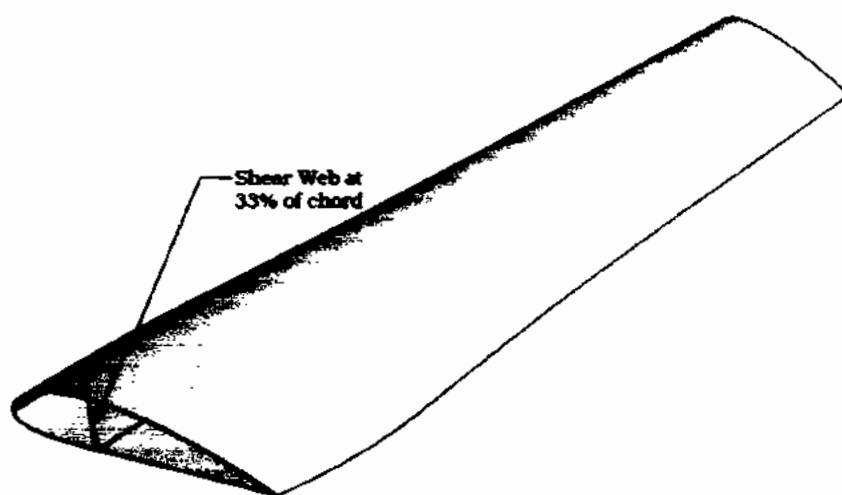


Figure 5.9 Internal structure of the blade utilized in the FSI simulations of full scale turbine

The blade cross section is hollow with 10 mm skin thickness and re-enforced with a shear web of 10 mm thickness. The transition region (not shown in Figure 5.9) is completely solid. The large scale turbine has a 20 m rotor diameter and the support structure is a 28 m long steel tubular monopile with a diameter of 2 m.

5.3.1 Simulation conditions

Two sets of operational conditions are simulated. These operating conditions are 1) uniform velocity and 2) a velocity profile following the $1/7^{\text{th}}$ power law, which are used as the inlet velocity conditions to model the fluid dynamics and structural mechanics of tidal turbine. Tidal turbine rotor blades are typically nearly neutrally buoyant. In this case, the buoyant forces and gravitational forces approximately balance and therefore the gravitational/buoyant effects are ignored in the simulation. The turbine is considered to be

fixed pitched with neutrally buoyant blades. The density of sea water is assumed to be constant (1000 Kg/m^3), and that the flow was free of cavitation. Therefore, the effects of cavitation are also not considered in the simulations. The turbine is simulated at the peak power condition of Tip Speed Ratio (TSR) 4.87 corresponding to the turbine rotational rate of 0.7 rad/s . This operational condition is selected because the largest bending moments occur when the turbine operates near peak power [48]. For the uniform velocity case, mean free stream velocity is set at 1.5 m/s , with a turbulence intensity of 5% and viscosity ratio of 10. For the velocity profile case, it is assumed that the velocity profile follows the $1/7^{\text{th}}$ power law. While velocity profiles vary considerably from site to site depending on the local bathymetric conditions, these velocity profiles can typically be approximated using power laws. The $1/7^{\text{th}}$ and $1/10^{\text{th}}$ power laws have been used to estimate the velocity profiles for EPRI North American tidal in stream power feasibility demonstration project [153] and other previous research works [79, 154]. The flow is assumed to only vary along the depth, and stays uniform across the width of domain. The velocity profile is estimated using a simple $1/7^{\text{th}}$ power law equation ($V_y = V_0 \times (y_i/y_D)^{1/7}$). Here, V_0 is the velocity at the surface of fluid domain, y_i is the depth at position i and y_D is the total domain depth. To enable direct comparison with the uniform velocity case, the velocity is distributed such that velocity at the hub height is 1.5 m/s . The mean velocity above the hub height is therefore greater than this value, while the velocity below the hub is smaller. The average velocity across the turbine swept area is 1.496 m/s , and the turbine rotational velocity is calculated using this velocity for an estimate of the optimum TSR. A plot of the velocity profile used at the inlet condition is provided in Figure 5.10.

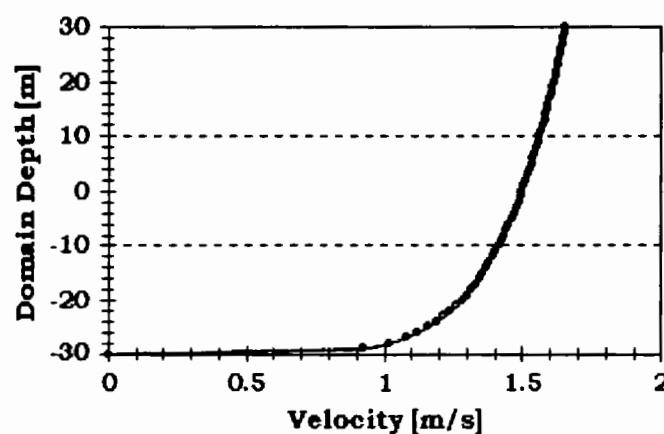


Figure 5.10 Velocity profile based on $1/7^{\text{th}}$ power law (dashed lines represent turbine location)

5.3.2 Numerical method

The simulation methodology adopted is similar in essence to that described in section 5.2. The coupled FSI simulations full scale device only considered the elastic behavior of turbine blades, while the support tower is considered rigid. The transient structural analysis system is coupled through system coupling with CFX in ANSYS Workbench to perform coupled simulations with two way data transfer. The individual physics of the fluid and structural field are solved separately and set to exchange data with each other at every coupling step through the coupling system by passing information across the fluid solid interfaces. The turbine blades, hub, nacelle and tower are all assumed to be made from structural steel with material properties defined in Table 5.1. The computational domain for the simulation is shown in Figure 5.11.

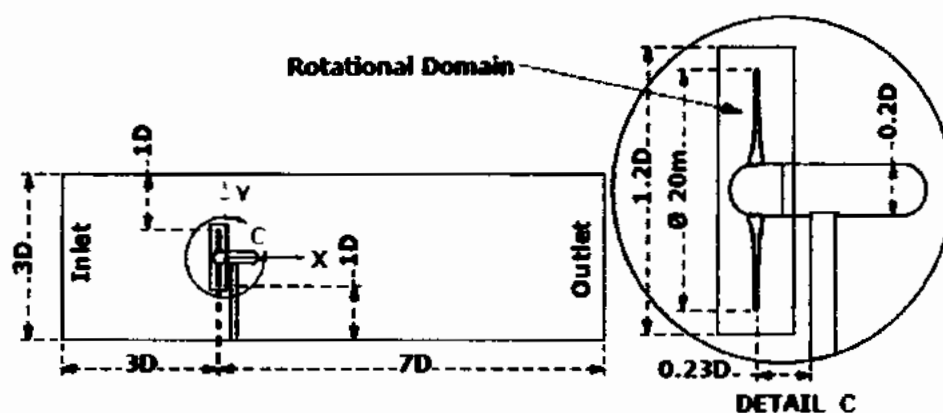


Figure 5.11 Dimensions of the (a) Fluid domain; (b) Turbine

The stationary domain of rectangular shape used a domain that is $3D$ deep, $4D$ wide and has length of $10D$ to represent the flow channel in the CFD model. The cylindrical rotational domain uses a diameter of $1.2D$ and width $0.3D$ to enclose the turbine blades and hub for modeling the rotation at turbine angular velocity. The domain reference $(x,y,z)=(0,0,0)$ is set at the center of the back face of turbine hub. The Transient Rotor Stator frame change model is used and the inner cylindrical domain containing the rotor is physically rotated using a sliding mesh approach at every time step. Mesh deformation is enabled for the rotating zone, with the region of motion specified using the displacement relative to previous mesh. The shear stress transport (SST) turbulence model is used with an automatic wall function model. Details about the values of y^+ used for the simulations

are available in section 4.6.3. A turbulence intensity of 5% with a viscosity ratio 10 is specified at the inlet for all simulations. The outlet of the flow channel is specified as a pressure outlet, with a relative static pressure of 0 Pa. No slip wall boundary condition is assigned to the bottom and two sides of rectangular channel domain, as well as to the turbine blades, hub, nacelle and tower surfaces. The wall boundaries specified at the two blades and hub are set to receive mesh motion from the system coupling. The top of the rectangular channel is assigned a free slip wall boundary condition, specifying that the velocity of fluid immediately next to the wall is not retarded by wall friction effect. The free surface deformation is neglected, although this omission could have an effect on the predicted turbine performance. However, this effect depends upon the clearance between the blade tip and top surface. Several previous studies [33, 51, 144] have established that a clearance of 1D is large enough to make the free surface effects negligible, and our simulation results show that this assumption is reasonable for the simulation conditions utilized in this study. Three mesh interfaces are specified at the three connecting surfaces between the cylindrical and rectangular domains. Mesh motion is activated for these interfaces connecting the meshes between the domains with a General Grid Interface (GGI) method. The total time of simulation for the fluid solver, structural solver and system coupling is set to 25.86 seconds, corresponding to three complete rotations at angular speed of 0.7 rad/s (TSR 4.87). Throughout this study the data has been presented for only two rotations, because the data from the first few time steps during the first rotation is not stable. This is an acceptable behavior normally associated with CFD and FSI simulations. The time step for simulation is taken as 0.144 seconds, and this corresponds to six degrees rotation of the turbine in a single time step. A time step study is conducted to establish the adequacy of this time step value in view of the computational expense, accuracy and system memory requirements. For the structural analysis system participating in the coupled FSI simulations, the turbine rotor is assigned an angular velocity of 0.7 rad/s, corresponding to the turbine TSR of 4.87 to account for the centrifugal forces. A remote displacement support is assigned at the turbine hub center and the turbine is fixed with two fix supports at the nacelle tower connection and tower base. Two fluid solid interfaces are defined at the two blades to receive force data and transfer displacement data to the CFX solver. ANSYS system coupling has the capability to solve each physics in serial or parallel mode.

In this paper, the FEA solution is performed with a shared memory parallel solver distribution utilizing 18 CPU cores and one GPU for solver acceleration. The CFX solver is also set to run in a shared memory local parallel mode utilizing 72 CPU cores and the solution is initialized with an already completed uncoupled transient CFD simulation. For the system coupling setting the analysis type parameters is set to Transient. The coupling duration definition is set to end time and similar time settings as those employed in the transient structural and CFX systems are employed. To communicate information between the two solvers, two data transfers are created for each blade. One of the data transfer will transfer incremental displacement from the FEA system as mesh displacement to the CFD system. Whereas the other data transfer will transfer force from the CFD system as force to the FEA system. The RMS convergence target for all data transfers are set to 0.1, and no ramping is employed for the data transfer. The simulation is executed such that the FEA system will be solved first.

The meshing scheme for CFD solver is the same as that already described in section 4.6.3 and shown in Figure 4.13. For the structural analysis system participating in the coupled FSI simulations, the turbine model is meshed with a patch conforming tetrahedral method. The turbine blades are meshed with a body sizing of 60 mm, hub and nacelle 300 mm and tower 200 mm. The mesh for the structural solver of the coupled FSI simulations is shown in Figure 5.12.

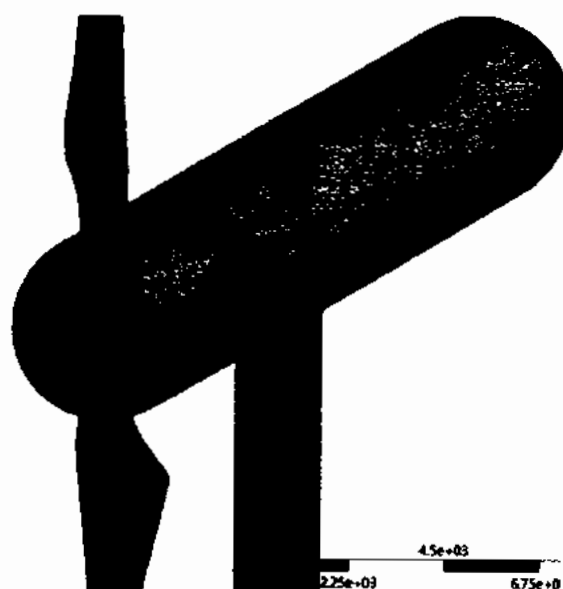


Figure 5.12 FEA mesh used in the coupled FSI simulation of full scale SAFL RM1 turbine

For blades the mesh size function is set to curvature to properly resolve the leading edge. The hub, nacelle and tower had a uniform size function. The FEA model has a total mesh count of 4.4×10^5 elements (7.1×10^5 nodes), of which 67% of the elements are at the turbine blades.

5.3.3 Verification and validation of numerical method

The accuracy of coupled FSI simulations depends largely on the constituent fluid and structural dynamic models. If the spatial and temporal discretization of the constituent fluid and structural dynamic models is verified then the other parameter that can possibly affect the accuracy of coupled simulation is the mapping error in data transfer. The mesh and time step sensitivity study described in section 4.6.4 also applies to the CFD solver participating in the coupled FSI simulations and is not discussed here to avoid repetition. Additionally, conformal mesh at the shared faces between the blade surfaces and fluid domain guarantee a node to node correspondence and 100% mapping of the nodes for data transfers between the meshes of CFD and structural solver. However, to reassure the proper execution of data transfer between the fluid and structural dynamic models, the expert parameter “DumpInterfaceMeshes” in the FSI model setup is set to the CFD post. A summary of the data transfer report displayed on the solver run window of the coupled simulation and contour plot of “DumpInterfaceMeshes” showed that 100% of node data is successfully exchanged between the solvers.

To further validate the results, power coefficient predicted by the coupled FSI simulations of full scale device is compared with transient CFD analysis of the full scale device and model scale experimental data [26] in Figure 5.13 and Table 5.4.

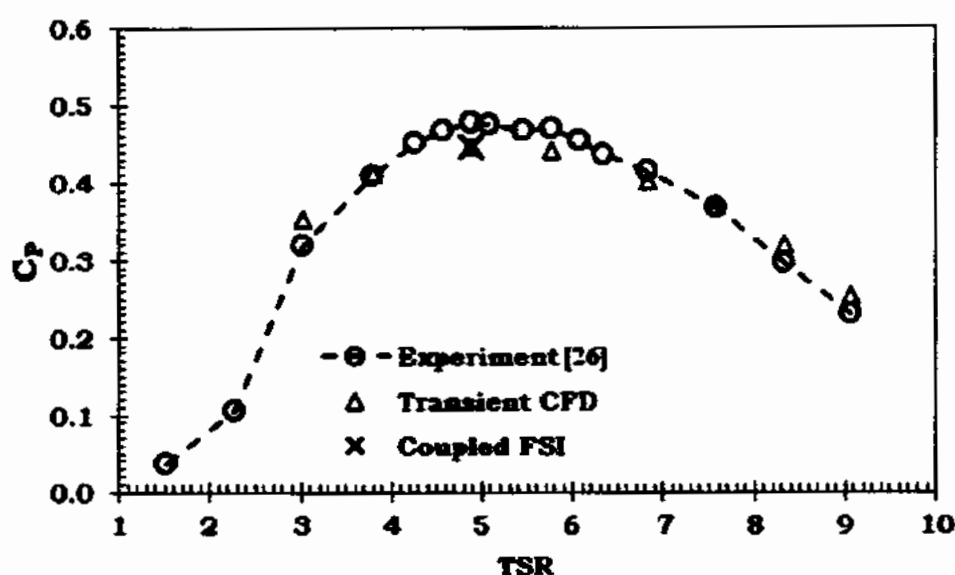


Figure 5.13 Comparison of power coefficient predicted by the coupled FSI simulations with transient CFD analysis and experimental data

Table 5.4 Quantitative comparison of turbine C_p between coupled FSI simulations, transient CFD analysis and experimental data

TSR	Experiment	Transient CFD		Coupled FSI	
	C_p [26]	C_p	% Difference*	C_p	% Difference ¹
3.02	0.320	0.354	10.7	-	-
3.79	0.408	0.411	0.8	-	-
4.87	0.477	0.447	6.3	0.447	6.2
5.76	0.471	0.442	6.2	-	-
6.82	0.414	0.402	2.8	-	-
7.57	0.368	0.368	0.1	-	-
8.32	0.295	0.319	8.2	-	-
9.05	0.230	0.254	10.4	-	-

¹ % Difference indicates the absolute percentage difference to the experimental values in [26].

The coupled FSI simulation predicted similar values to those measured in the experiment for the turbine power coefficient (C_p) at the optimum TSR. Experimental values for turbine thrust coefficient (C_T) are not available. However, both the numerical models predicted similar values of thrust coefficient (C_T) that confirm the consistency of the simulated results. The turbine diameter based Reynold number ($Re_D = U_\infty \times D/\nu$) for the utilized

turbine design in this study is 3×10^7 , whereas the turbine in experiment has a Reynold number of 5.2×10^5 . But still the performance coefficients of full scale model matched well with the scaled model experimental data. This observation is consistent with the findings in [64] and supports the fact that performance in terms of non-dimensional parameters is independent of Reynold number beyond a critical value. Detailed discussion about all the scaling parameters and justification is described in section 4.6 and is not provided here to avoid repetition.

5.3.4 Results and discussion

This section presents important results from the coupled FSI simulations of full scale SAFL RM1 turbine with realistic blade design and including nacelle and support structure. These results would help to present the effectiveness of the utilized coupled FSI simulation methodology and describe the performance and structural response of a full scale device.

5.3.4.1 Turbine performance

Power and thrust coefficients of the whole rotor during two rotations, predicted by the coupled FSI simulations, for a uniform inlet velocity and velocity profile are presented in Figures 5.14-5.15.

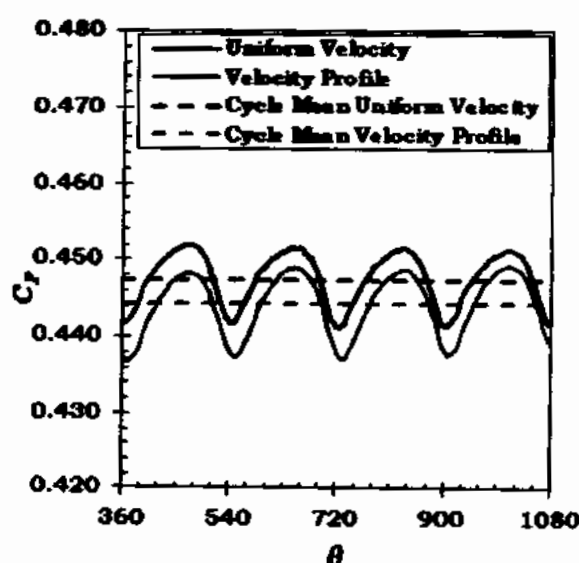


Figure 5.14 FSI simulation results for rotor power coefficient during two turbine rotations

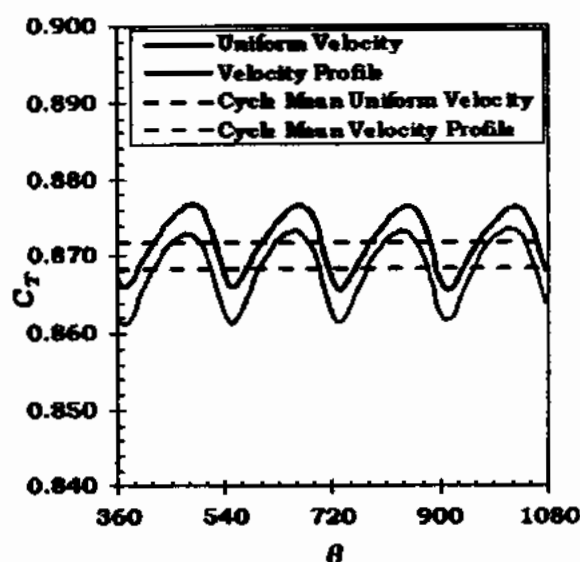


Figure 5.15 FSI simulation results for rotor thrust coefficient during two turbine rotations

The mean cycle values of power and thrust coefficient has decreased by about 0.69% and 0.38% respectively due to the effect of velocity profile. The percentage drop in power and thrust coefficient is considerably small compared to Mason-Jones et al. [79]. This is mainly because of the velocity profile employed in this study. Two maxima and minima per cycle are evident in Figure 47 and Figure 48, which are due to the effect of two blades passing the tower. When any of the turbine blade passes the tower the whole rotor power and thrust drops below its mean value due to the tower effect. The whole rotor power and thrust coefficients vary from its mean value by 2.31% and 1.25% respectively due to the sole effect of tower. For a combined effect of velocity profile and tower the variation in power and thrust coefficients is 2.73% and 1.42% respectively. Although, it seems that velocity profile will complement the tower shadow effect in reducing the rotor power and thrust. Because when a blade passes the tower it is also operating in the lower part of the water column. However, Figures 47-48 show that the combined effect of velocity profile and tower on the whole rotor power and thrust is not much different than the sole effect of tower. This finding is in accordance to similar studies for wind turbines [155, 156]. This is because the rotor achieves its peak value near the horizontal position ($\theta = 90^\circ - 270^\circ$) (Figure 5.16).

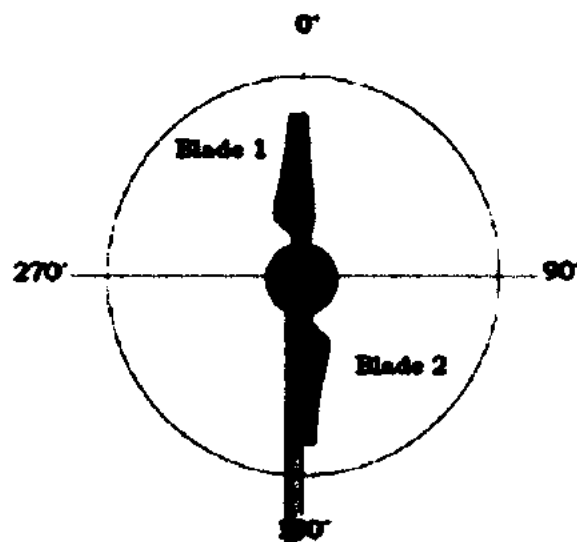


Figure 5.16 Rotor angular positions for presentation of results

At this position the effect of velocity profile is not prominent and the onset velocity is almost equal to the hub height velocity of the uniform velocity case. Therefore, the effect of velocity profile is almost negligible. Similarly, the rotor achieves minimum power when it is aligned vertically with the tower ($\theta = 0^\circ - 180^\circ$). At this position the lower blade experiences the maximum effect from tower and velocity profile. However, at the same time the upper blade is almost free from the effect of tower and operates in the maximum velocity region in the water column. Therefore, the cumulative effect balances out and the resultant combined effect of tower and velocity profile on the whole rotor power coefficient is not much extravagant.

Another important finding is that the variation in mean cycle values of the thrust coefficient for the whole rotor is smaller than the power coefficient as clear from Table 5.5.

Table 5.5 Turbine loads variation during a rotation cycle

Parameter	Value	Uniform Velocity		Velocity Shear	
		Single Blade	Rotor	Single Blade	Rotor
Thrust Coefficient	Peak	0.437	0.877	0.445	0.869
	Mean	0.433	0.872	0.429	0.864
	Range	0.012	0.011	0.039	0.012
	% Variation ¹	2.8	1.3	9.0	1.4
Torque Coefficient	Peak	0.046	0.093	0.048	0.092
	Mean	0.045	0.092	0.045	0.091
	Range	0.002	0.002	0.009	0.002
	% Variation ¹	5.2	2.3	19.3	2.7
Flap Wise Bending	Peak	1.013	-	1.078	-
Moment Coefficient	Mean	1.0	-	1.0	-
	Range	0.049	-	0.185	-
	% Variation ¹	4.9	-	18.5	-

¹ % Variation indicates the variation from mean cycle value during a rotation.

This observation is significant for the useful life of turbine shaft, bearings, seals and other associated components. It was anticipated that a two bladed rotor would exhibit larger power and thrust coefficient variation compared to a tri-bladed rotor due to the effect of velocity profile and support tower. However, for a tri bladed device [47] the mean cycle values of power coefficient varied by about 10% with three maxima and minima per cycle. The two bladed device in this study and another similar study [157] showed a much lower variation in power coefficient of 2.73% and 5.72% respectively with two maxima and minima per cycle. However, since these studies utilized different turbine design and tidal conditions therefore, this conflict may be resolved by utilizing similar turbine design with different number of blades operating in similar flow conditions.

In terms of structural loads, Flap wise bending moment at the blade root is considered a critical design load for causing blade failures [48]. Flap wise bending moment is caused by the moment of thrust force and acts along the chord line. The peak rotor loads predominantly comes from the thrust characteristics of turbine. The thrust behavior of a

single blade is similar to the flap wise blade bending moment but has not been shown here for brevity. Contrary to the total rotor loads represented in terms of thrust force, the velocity profile has a significant effect on the variation of individual blade loads as presented in Figure 5.17 by the flap wise bending moment coefficient. Similarly, the variation of blade torque or edge wise bending moment is also significantly influenced by the effect of velocity profile (Figure 5.18).

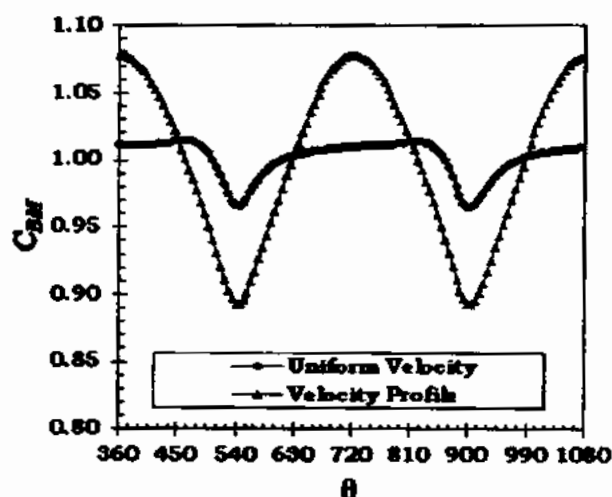


Figure 5.17 Flap wise bending moment (normalized by cycle mean) for Blade 1 during two rotations

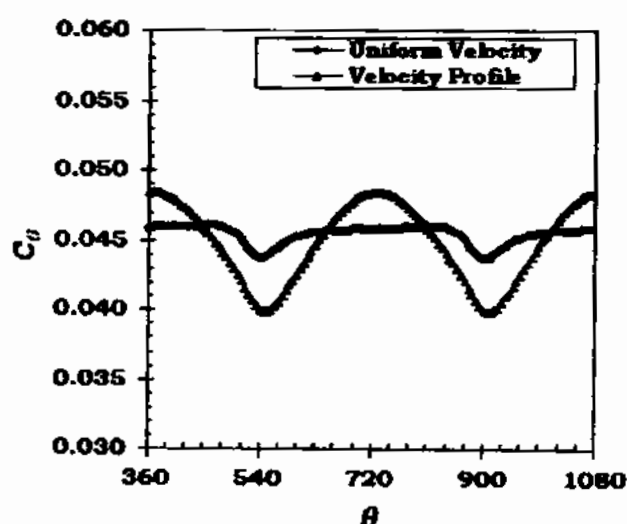


Figure 5.18 Torque coefficient C_t for Blade 1 during two rotation cycles

Table 5.5 quantitatively shows that the sole effect of tower on load variation on an individual blade is about twice the load variation on whole rotor. Due to the combined effect of velocity profile and tower, the variation in thrust coefficient from mean cycle value of an individual blade increases from 2.8% to 9%. Whereas, for flap wise bending

moment the addition of velocity profile increases the load variation on a single blade from 4.9% to 19%. The change in both these loads variation is quite significant and indicative of the importance of considering the velocity profile as a possible source of fatigue failure. For the uniform velocity case, the rotor thrust reduced by about 1.3% due to the tower shadow effect. A similar reduction in thrust of 1-2% due to tower shadow has been reported for wind turbines [155, 156]. The mean value of the blade wise thrust decreases due to combined effect of tower and velocity profile compared to the tower only effect (Table 5.5). But the peak and range of blade wise thrust increases resulting in increasing the variation. The thrust behavior between the two cases is significantly different from each other and can have serious consequences for the fatigue life of turbine components. For the sole effect of tower, both the blade will almost contribute a similar value of thrust that will be transferred to the shaft and associated components. The thrust force can be expected to act almost along the center line of the shaft. For the combined effect of tower and velocity profile the upper blade will contribute significantly more to the rotor thrust compared to the lower blade. The thrust force in this case will not act in axisymmetric manner and will affect the life of shaft, bearings, seals and other associated components. Moreover, the significant variation in flap wise bending moment reasserts its position as the most dominant and critical design load consideration for tidal turbine blade. Torque as a moment (edge wise bending moment) and torsional bending moment are less critical and their contribution towards causing blade failure is not significant. Therefore, they are not discussed here in details. The torque variation are more relevant for the representation of power fluctuations and has been represented in terms of power coefficient variations in the earlier part of this discussion. The results presented so far in this section are purely based on simulations and are not compared with full scale experimental data due to the unavailability of required details. Nevertheless, this study is important as a preliminary step upon which future studies can be based.

A part from load variations, the constituent fluid dynamic component of the coupled FSI analysis is capable to provide a very good visualization of the turbine flow field as shown in Figure 5.19.

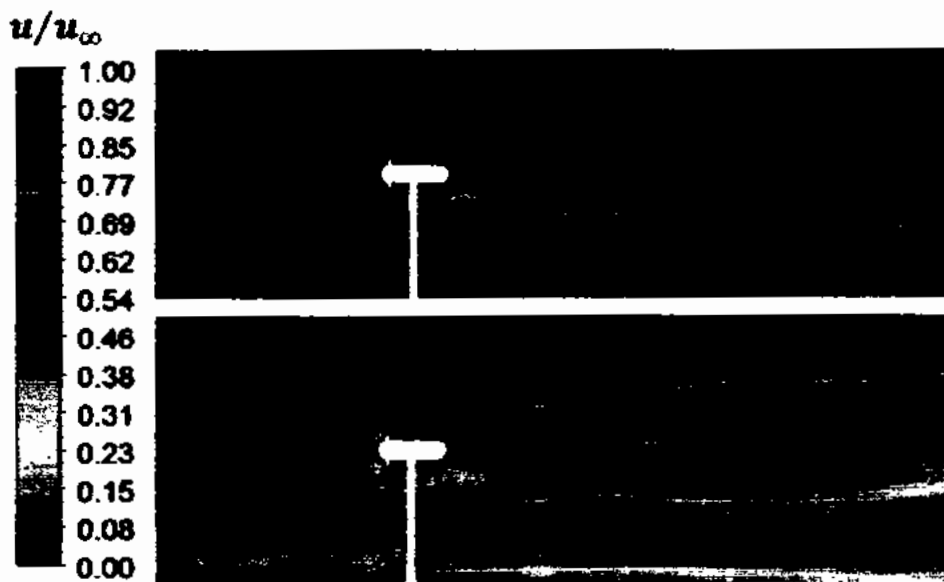


Figure 5.19 Axial velocity (normalized by the free stream velocity) contour for (a) Uniform inlet velocity (b) Velocity profile

It is quite evident from Figure 5.19 that for uniform velocity case the wake is axisymmetric. However, the addition of velocity profile has shifted the wake upwards and velocity in the lower part of the wake has decreased. To further quantify this effect, velocity variation along depth of the channel at different downstream locations is provided in Figure 5.20.

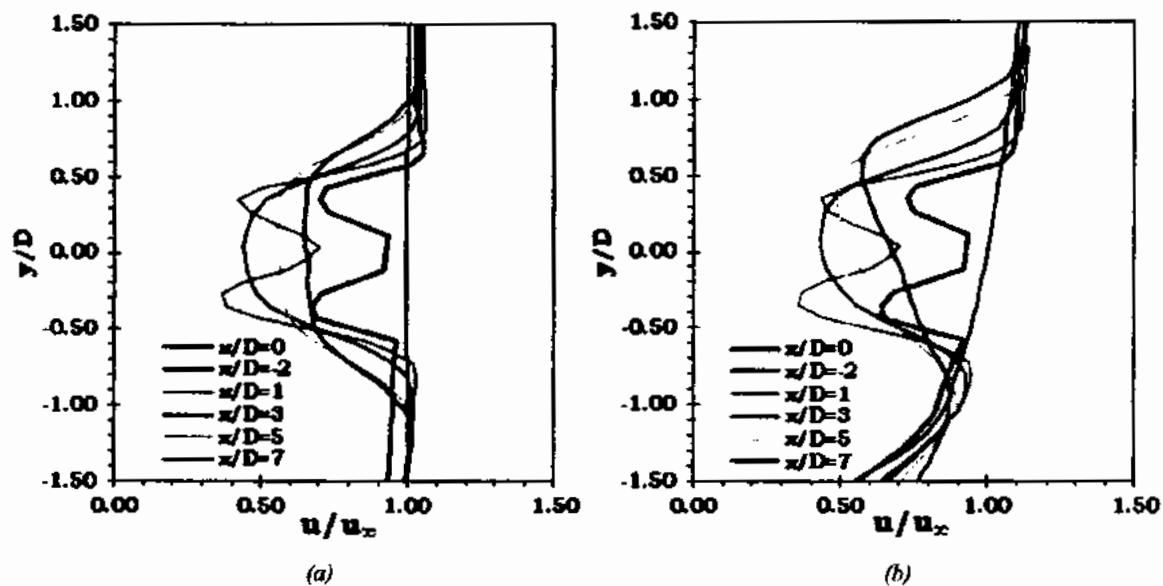


Figure 5.20 Velocity variation along depth of the channel at different downstream location for (a) Uniform velocity (b) Velocity profile (Red dash dot line represent location of turbine hub center and the black dashed lines represents the extent of blade tips)

The inflow velocity is unaffected upto a distance of $2D$ upstream ($x/D = -2$) in both cases. At the turbine location ($x/D=0$) and $1D$ downstream ($x/D=1$), the velocity variation is almost similar between the two cases. However, further downstream at ($x/D=3$) and beyond that the wake has clearly shifted upwards. For the velocity profile case, the velocity in the upper by pass region of the wake has increased.

To further clarify this phenomenon, a plot of velocity deficit along the length of channel at different channel depths for the uniform velocity and velocity profile case is shown in Figure 5.21.

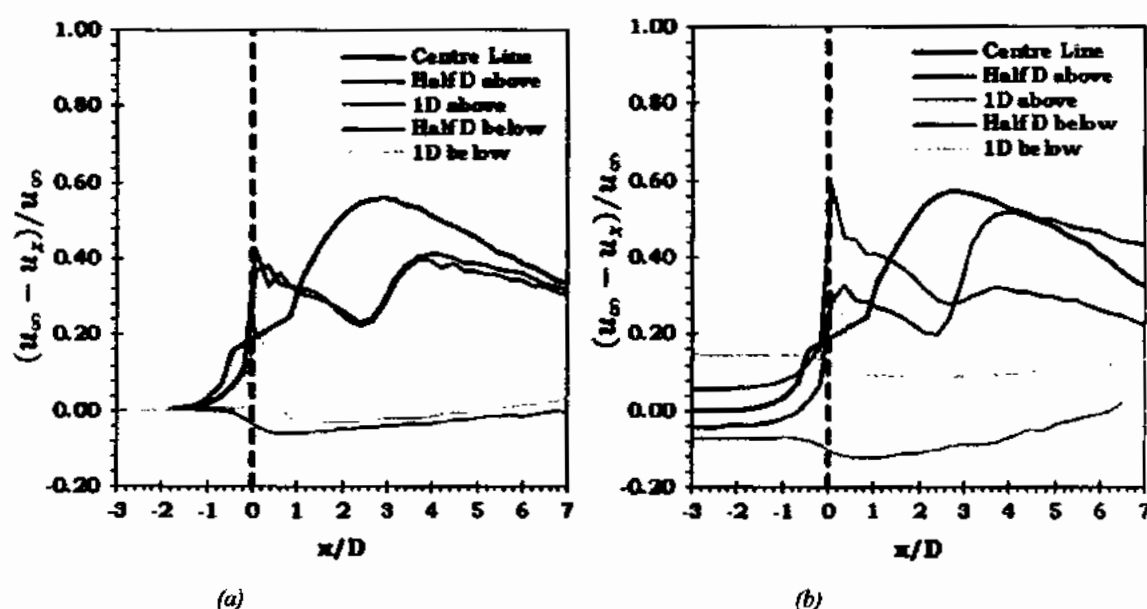


Figure 5.21 Velocity deficit along the length of channel at different channel depths for (a) Uniform velocity (b) Velocity profile

Figure 5.21 shows that for the uniform velocity case at $1D$ above and below the turbine, the velocity deficit gradually reduces along the channel length with almost a similar velocity recovery. However, for the velocity profile, at $1D$ above turbine the velocity deficit is negative throughout the length of the channel. This indicates that higher velocity than the mean free stream velocity is available at this height. This finding can be utilized for the future array designs as the power out of turbine is a function of the cube of velocity. In an axial array layout, if the downstream devices are positioned successively higher than the upstream devices, this higher velocity can be utilized to obtain higher power outputs.

However, there are several other complications and site constraints that needs to be further analyzed.

5.3.4.2 Blade structural response

The coupled FSI model provides a detailed insight into the structural response of turbine components against the imposed fluid loads by providing all the results that are possible from a standalone FEA analysis. The maximum blade deformation in the evaluated cases is relatively small about 40.9 mm for the uniform velocity case and 41.9 mm for the velocity profile as shown in Figure 5.22.

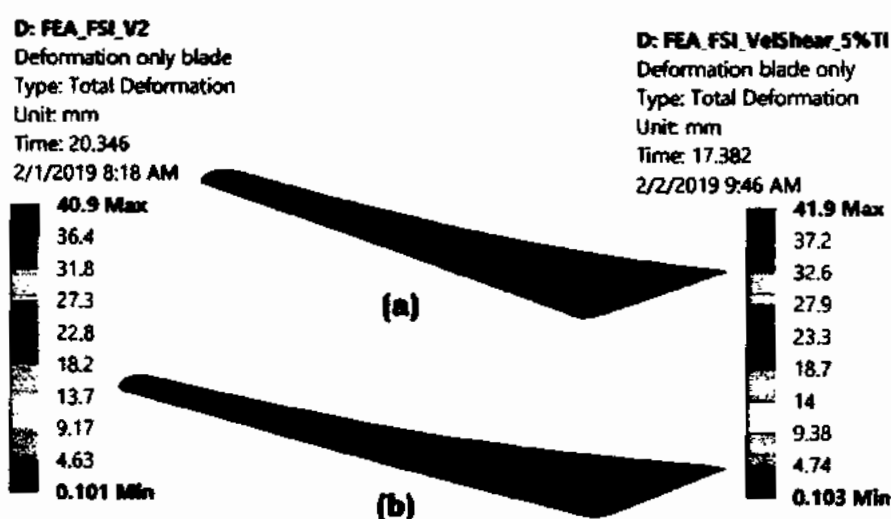


Figure 5.22 Contour plot of blade deformation for (a) Uniform velocity (b) Velocity profile

Similarly, the maximum equivalent stress for the uniform velocity and velocity profile is 118 MPa and 121 MPa respectively as shown in Figure 5.23.

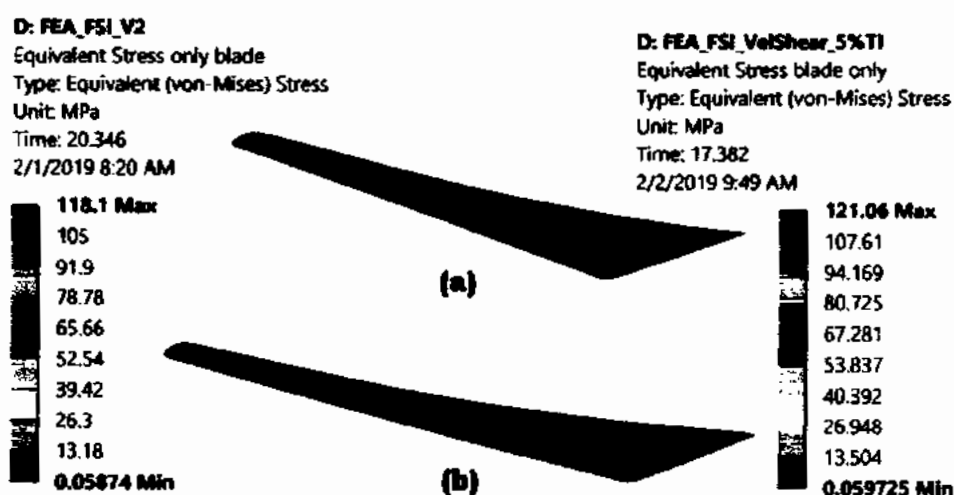


Figure 5.23 Contour plot of blade equivalent stress for (a) Uniform velocity (b) Velocity profile

Just like the load forces, the blade deformation and stress vary with the blade angular position during a rotation cycle as shown in Figure 5.24.

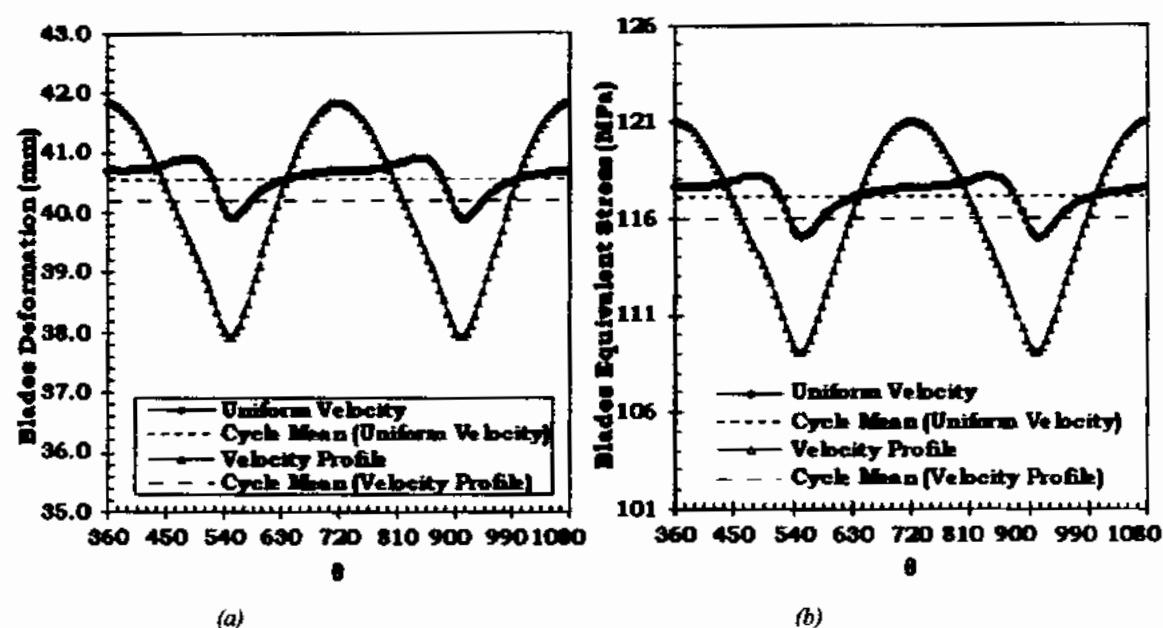


Figure 5.24 Variation of Blade 1 (a) Deformation (b) Equivalent stress during two rotation cycles

The blade deformation and stress varies by about 2.5% and 2.8% respectively from its mean cycle value during a rotation cycle due to the sole effect of tower. The variation in blade deformation and equivalent stress are significantly increased to a value of 9.8% and 10.3% respectively due to the added effect of velocity profile. The velocity profile augments the tower effect resulting in increased variation in blade deformation and stress. It is however interesting to note that the mean cycle value of deformation and stress decreases with the added effect of velocity profile as given in Table 5.6.

Table 5.6 Turbine load fluctuations from the last rotation cycle

Parameter	Value	Uniform Velocity	Velocity Profile
Deformation [mm]	Peak	40.9	41.9
	Mean	40.6	40.2
	Range	1.0	3.9
	% Variation ¹	2.5	9.8
Stress [MPa]	Peak	118.1	121.1
	Mean	117.1	116.0
	Range	3.2	12.0
	% Variation ¹	2.8	10.3

¹ % Variation denotes variation from cycle mean value during a rotation cycle.

This is because, when a blade comes in front of the tower along its rotation cycle, at this moment it is in the lower velocity region of the water column. Therefore, the minimum value of thrust force is further reduced due to the combined effect of tower and velocity profile. Contrarily, when a blade is at the top, it is free from the tower effects and operates in the higher velocity region of the water column. Therefore, the maximum value of thrust force further increases due to the combined effect of tower and velocity profile. This reduction in the minimum value of thrust and increase in the maximum value of thrust causes a reduction in the mean value of stress due to the added effect of velocity profile. On the contrary, the values of stress range and variation is considerably increased. The mean stress and stress range (alternating stress) are the two important parameters with prominent effects on the fatigue life of turbine blade. The fatigue strength of the blade will decrease with increase in the mean stress and or stress range and vice versa. The fatigue strength under an axial load is decreased due to increase in the tensile mean stress. However, in case of torsion the fatigue strength is unaffected by the increase or decrease in mean stress. For the case study presented here, the mean stress decreases by a very little margin however, the stress range (alternating stress) increases considerably by more than three times due to the added effect of velocity profile. The stress response of blade (Figure 5.24b) shows a repeating cyclic behavior indicating the possibility of fatigue failure.

To further investigate the fatigue behavior of rotating turbine blade, fatigue analysis was performed using a stress life fatigue model. The stress life fatigue model determines the total fatigue life and does not differentiate between crack initiation and propagation. The stress life fatigue model is based on S-N curve and deals with high cycle fatigue. A constant amplitude proportional loading was assumed because the principal stress axis does not change over time. A stress ratio, ($R = \sigma_{Min}/\sigma_{Max}$) of 0.97 and 0.90 is used for the uniform velocity and velocity profile case respectively. Fatigue S-N curves for materials are mostly generated from fully reversed constant amplitude experimental tests. For in service application such loading condition is very rare and mostly a mean stress will exist that must be accounted for in the fatigue analysis. In the stress life fatigue model of the ANSYS fatigue module the mean stress effect can be taken into account through direct interpolation between experimental S-N data. But such experimental data is usually not available due to the cost of experimental tests. Empirical relations like Goodman, Soderberg and Gerber theories can be used as an alternate to the experimental data. These empirical relations use the static material properties together with the S-N data to account for the mean stress effects. The experimental data generally lies between the Goodman and Gerber relation. For brittle materials the Goodman relation is considered as a better choice whereas for the ductile materials the Gerber relation is often preferred. The turbine blades for the current study are made from structural steel and therefore a Gerber equation is selected. Equivalent (VonMises) stress was used as the stress component for the fatigue analysis to convert from a multiaxial stress state obtained from FE analysis to the uniaxial stress state of the experimental fatigue data.

The stress state of the blade for the evaluated cases of uniform velocity and velocity profile is shown in Figure 5.25.

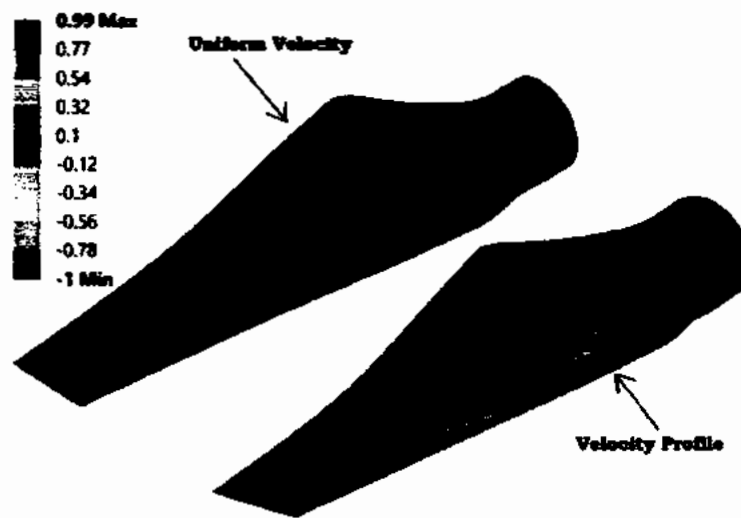


Figure 5.25 Biaxiality indication for blade in uniform velocity and velocity profile

The green color corresponds to a biaxiality indication of (0) indicating a uniaxial stress state at majority of the blade. The blue color with a biaxiality indication of (-1) indicate a pure shear and red with a biaxiality indication of (1) represent a pure biaxial state. The contour plot clearly shows that major portion of the blade is in a uniaxial stress state (green color) and S-N data for torsional loading is not required for the fatigue analysis of turbine blades for the evaluated case. The contour plot of fatigue factor of safety for both the cases is shown in Figure 5.26.

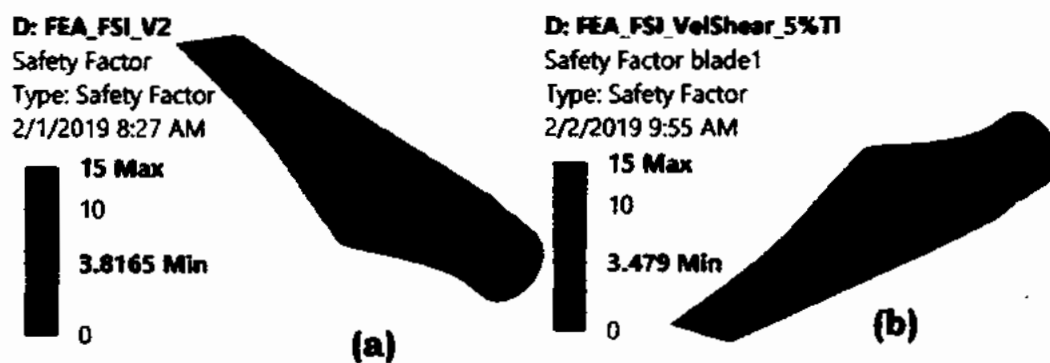


Figure 5.26 Fatigue factor of safety for blade (a) Uniform velocity (b) Velocity profile

Figure 5.26 shows that for the uniform velocity the fatigue factor of safety is 3.8. The additional effect of velocity profile has reduced the fatigue factor of safety by about 8% to a value of 3.5. It is important to note that although this study utilized a near to real turbine design but only the hydrodynamic conditions of velocity profile is modelled with

contribution to the fatigue failure of blades. But other important contributors like turbulence and waves etc., will also contribute to decide the final fatigue life of the blade.

5.4 Summary

Coupled FSI simulation methodology for modelling the performance and structural response of 1:40 scale model SAFL RM1 tidal turbine rotor comprised of blades with simplistic design has been developed. Results of the FSI simulations are compared with experimental data and steady state RANS CFD simulations. A good agreement between the result of numerical simulations and experimental results has been observed with a maximum difference of less than 10%. The coupled FSI model predicted a lower value of turbine C_p (0.45) compared to a C_p value of 0.48 predicted by the steady state RANS CFD model. The blade deformation (0.12 mm) in the evaluated case was not enough to result in a significant change in the angle of attack that could have resulted in any variation in the separation and reattachment behaviour. However, the pressure contour shows a difference in pressure at low pressure side of the blade between both the models. The reason for the difference in C_p prediction between the two models is attributed to the difference in pressure difference and flow velocity across the low pressure and high pressure side of the blade elaborated through contour plots. Contour plot of rotor deformation equivalent stress and time histories of deformation and stress obtained from the structural analysis component of the coupled FSI simulations has been used to describe the structural response of the blade. The maximum blade deformation (0.12 mm) observed in the evaluated case is very small due to the reason that blade is completely solid. It is highly unlikely for a real turbine blade to be made in this manner but this was necessary to replicate the actual model utilized in the experiments.

To gain in insight into the hydrodynamic and structural response of full scale SAFL RM1 turbine, the developed coupled FSI simulation methodology is utilized to simulate the turbine operation for a uniform velocity and velocity profile case. Results from the simulations are spatially and temporally verified and validated with experimental data. It was observed that the influence of velocity profile on the whole rotor power and thrust is not much different than the sole effect of tower. The variation in mean cycle values of the thrust coefficient for the whole rotor was observed to be smaller than the power coefficient.

The variation in thrust coefficient from mean cycle value of an individual blade increases from 2.8% to 9% due to the influence of velocity profile. Whereas, for flap wise bending moment the addition of velocity profile increases the load variation on a single blade from 4.9% to 19%. The change in both these loads variation is quite significant and indicative of the importance of considering the velocity profile as a possible source of fatigue failure. While the influence of velocity profile decreases the mean cycle value of blade wise thrust, the peak and range is increased resulting in increasing the variations. Contrarily, it was observed that for the profiled inlet velocity the mean value of stress and deformation decreases as compared to a uniform inlet velocity.

It was observed that the blade deformation and stress also vary with the blade angular position during a rotation cycle like the blade loads. For the evaluated case of uniform velocity this variation was 2.5% and 2.8% for the deformation and stress respectively during a rotation cycle. However, for a profiled inlet velocity the variation in deformation and stress during a rotation cycle significantly increased to 9.8% and 10.3% respectively. The velocity profile augments the tower effect resulting in increased variation in blade deformation and stress. It is however interesting to note that the mean cycle value of deformation and stress decreases with the added effect of velocity profile. For the evaluated case of profiled inlet velocity, the mean stress decreases by a very little margin however, the stress range (alternating stress) increases considerably by more than three times compared to a uniform inlet velocity. To investigate the effect of load variation on the fatigue life of rotating turbine blade, a stress life fatigue model based analysis was performed. The stress state of the blade for the evaluated cases of uniform velocity and velocity profile showed that major portion of the blade was in a uniaxial stress state. The fatigue factor of safety was reduced by about 8% due to the influence of velocity profile. However, it was also pointed out that this reduction can further increase due to the contribution of turbulence and wave effects that were not considered in these simulations.

Chapter 6

Effect of array layout and inter device spacing on the performance and structural loads on the blade

The RANS CFD simulation methodology adopted for investigating the influence of array layouts and inter device spacing on the performance and structural loads variations on the blade of TCT is discussed in this chapter. RANS CFD methodology for a standalone turbine has been developed in chapter 4. However, that methodology cannot be readily extended to simulate tidal turbine arrays. Because, the size of computational domain is not sufficient to accommodate three turbines array. Therefore, this chapter starts with the development of RANS CFD simulations for a standalone turbine operating in a domain that can accommodate all the array layouts planned for this research.

6.1 Single turbine in array domain

A verified and validated RANS CFD methodology for modelling flow over a single turbine has been developed for full scale device as discussed in section 4.6. However, the computational domain utilized in those simulation described in section 4.6.2 could not accommodate three turbines array. To ensure a similar domain for all the array simulations and verify new domain definition and new hybrid mesh scheme, a series of simulation is again conducted for the single device. This is necessary because due to change in meshing scheme the already performed verification and validation of RANS CFD method for single turbine is no more valid. The changes in domain sizes result in the change of blockage ratios and wall effects that would in turn affect the turbine performance and flow field. Therefore, the changes to domain definition are executed sequentially and successively to monitor the effect of every change individually on the turbine performance and flow field. The simulation are executed in a sequence such that:

1. In the 1st simulation the hybrid meshing scheme is implemented and the domain length is changed from 200 to 600 m (10D to 30D). The blockage ratio (6.5%) is kept unchanged.
2. In the 2nd simulation, the domain width and depth is changed to make the blockage ratio (14.5%) and the turbine is located off center to exactly replicate the experimental channel.
3. In the 3rd simulation, domain dimensions are unchanged while the turbine is shifted to the center of domain.
4. In the 4th simulation, the domain is sized such that it would be able to simulate all the array layouts planned in this thesis with in a channel of blockage ratio 4.4% and length of 600 m (30D).

Domains definition for all the simulations conducted as part of the development of RANS CFD methodology for single device in array domain is as in Table 6.1.

Table 6.1 Domains details for developing RANS CFD methodology for simulating flow over a turbine operating in array domain

S#	Simulation	Domain Size (m)			Blockage Ratio
		Width	Depth	Length	(%)
	Experiment	1.38	1	12.0	14.3
1	Single turbine with hex mesh (standalone domain)	80	60	600	6.5
2	Single turbine off-center located (experimental domain)	55	40	600	14.3
3	Single turbine center located (experimental domain)	55	40	600	14.3
4	Single turbine (array domain)	120	60	600	4.4

6.1.1 RANS CFD methodology

All simulations listed in Table 6.1 are conducted using a steady state approach through Multiple Frame of Reference (MFR) model. However, the single turbine located in array domain is also simulated through a transient model using a transient rotor stator approach.

Because the single turbine simulations in array domain would be extended to the simulation of tidal turbine arrays for investigating the performance and blade loads variation. The adopted RANS CFD methodology is similar in essence to that described in section 4.6. However, certain changes have been sequentially and successively implemented to evolve a RANS CFD methodology for simulating turbine arrays. The domain size required for array simulations is much larger to accommodate three turbines, therefore the blockage ratio for simulating a single turbine in the array domain would drop from 6.5% of the already developed RANS CFD methodology to 4.4%. The dimensional details of computational domain for single turbine in array domain are shown in Figure 6.1.

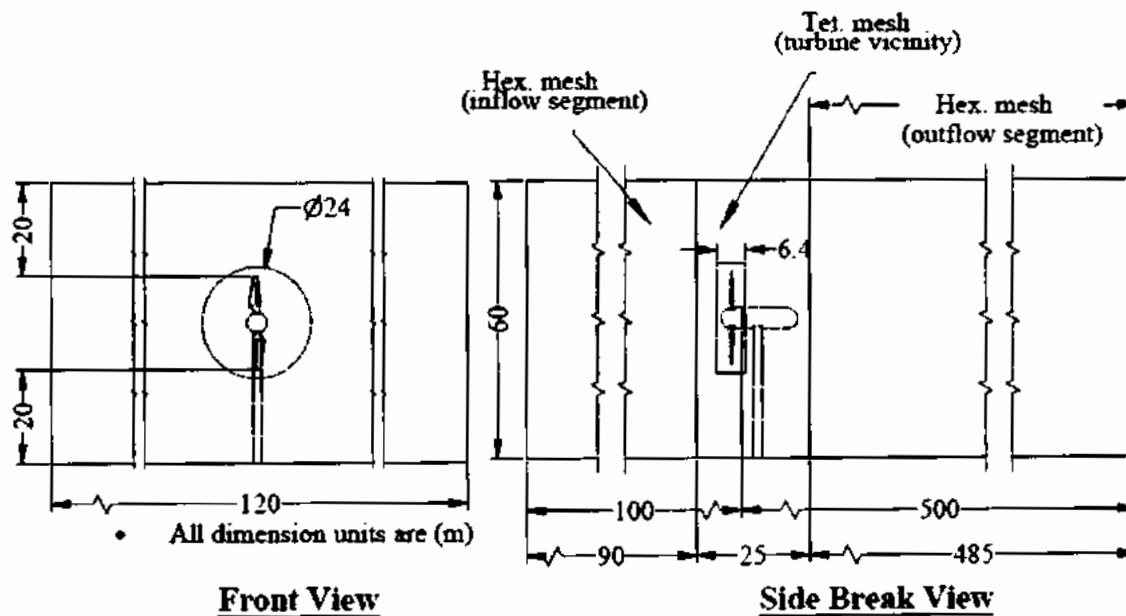


Figure 6.1 Dimensional details of domain used for all the array simulations

Additionally, for the larger size domain containing 1-3 turbines, the number of mesh elements would also significantly increase. Therefore, the meshing scheme is changed from tetrahedral to a hybrid mesh scheme to keep the number of mesh elements within the range of available computational resource. The mesh used for simulation domain and turbine surfaces is shown in Figure 6.2.



(a) Mesh in the computational domain



(b) Mesh on the turbine surfaces

Figure 6.2 Mesh in the computational domain (a) and turbine surfaces (b) for array simulations

A similar hybrid mesh scheme for modelling flow over tidal turbines is not rare and has been successfully implemented in other research studies like Nitin et al. [51]. In the new hybrid mesh scheme, the blade surfaces and major portion of stationary rectangular domain, except a small portion of 25 m domain length in the vicinity of turbine, is meshed with a structured hexahedral mesh. The exact dimensions of these domain segments with

hexahedral and tetrahedral mesh are provided in Figure 6.1. A selective body meshing technique is used and conformal meshes are generated on the shared faces between bodies. The mesh generation is started from the blade surfaces and a sweep method is applied for generating a hexahedral mesh. The blade is divided into 126 divisions along the airfoil edges at the blade tip and 217 divisions in the span wise direction. A patch conforming tetrahedral mesh method is used for generating mesh on the hub, nacelle, tower, rotating domain and part of the stationary domain in the vicinity of turbine. The turbine hub and nacelle is meshed with tetrahedral element of 150 mm and rotating domain with an element size of 260 mm. The growth rate throughout meshing is kept at the default rate of 1.2. Prism element layers are generated around blade surfaces to capture the boundary layer flow as shown in Figure 6.3.



Figure 6.3 Prism elements layers generated around the blade surfaces

The thickness of first layer normal to blade surface is set at 0.7 mm and 11 layers of prism elements are generated with a growth rate of 1.2. This mesh setting ensured an area averaged y^+ value of 151 and 231 along higher and lower pressure surfaces of the blade respectively. The combined area averaged y^+ value along both blade surfaces is 191 recorded for the final converged state of solution. These y^+ values are well within the range $2 \leq y^+ \leq 300$ as prescribed by ANSYS CFX along with 11 number of nodes in the boundary layers for the proper functioning of $k - \omega SST$ turbulence model with an automatic wall function switch [131]. Mesh generation in the rotating domain is followed by generating a swept hexahedral mesh for the inflow segment of rectangular domain. The

inflow segment of rectangular domain is divided into 60, 30 and 45 divisions along the width, depth and flow direction respectively. Similarly, the outflow segment of the rectangular domain is divided into 60, 30 and 243 divisions along the width, depth and flow direction respectively. Finally, mesh for the tetrahedrally meshed segment of stationary domain in the vicinity of turbine is generated. The tower is first meshed with an element size of 100 mm followed by the rest of domain with an element size of 1000 mm. Total mesh count of the model is 6.7×10^6 elements with 4.3×10^6 elements in the rotating domain.

The boundary conditions is adopted similar to those as described in section 4.6.2, except that boundary conditions at the side walls and bottom is changed to symmetry from a no slip wall and the top to symmetry from a free slip wall. These changes are necessary to ensure that simulation results are minimally affected due to the wall effects between various configurations of arrays. All the simulations represent the optimum operating TSR of 4.87 and the inflow velocity is 1.5 m/s with a turbulence intensity of 5%.

6.1.2 Results and discussion

The performance of turbine in terms of power coefficient (C_p) computed through RANS CFD simulations for various domain sizes is as in Table 6.2.

Table 6.2 Quantitative comparison of RANS CFD prediction for turbine C_p within different sizes computational domains

S#	Simulation Name	Torque [KN.m]		Rotor (C_p)	C_p diff. to experiment [%]
		Blade 1	Blade 2		
1	Single turbine (standalone domain)	156	154	0.428	-10.2
2	Single turbine off-center located (experimental domain)	176	171	0.478	0.2
3	Single turbine center located (experimental domain)	169	167	0.464	-2.8
4	Single turbine steady state (array domain)	141	137	0.384	-19.5
5	Single turbine transient (array domain)	139	138	0.382	-20.0

Table 6.2 shows that steady state RANS CFD simulations with new hybrid mesh scheme has very closely predicted the turbine C_p with a difference of 0.2% to the experiment. However, when the turbine is shifted to the center of domain, this difference increases to 2.8%. For simulation listed at serial No. (1), the change in domain blockage ratio (from 14.3%-6.5%) and increasing distance from the side wall has jointly resulted in dropping the turbine C_p value to 10.2% compared to the experimental value. Similarly, the turbine C_p further drops to 19.5% due to reduction in the blockage ratio of computational domain from 6.5% to 4.4%. From the understanding developed in section 4.5.4 and 4.5.5, it can be concluded that the change in difference between experiment and simulation for turbine C_p from 10.2% to 19.5% could not be the sole effect of blockage ratio due to the range of blockage ratios (6.5%-4.5%) involved. Therefore, this drop in turbine C_p is attributed to the combined effect of blockage ratio and wall/boundary effect.

The flow passing through turbines operating in channels with different cross sections under the influence of changing wall/boundary effects is further described through the contour plots of stationary frame velocity normalized with respect to free stream velocity (U/U_∞) for all simulations. Figures 6.4-6.7 show the contours of normalized velocity along a

horizontal plane across the width of domain at mid depth of the channel. An enlarged view for the portion from $-1D$ to $8D$ has been provided along with complete normalized velocity contour. Because, in this portion of wake further devices will be installed to extend our investigations to tidal turbine arrays.

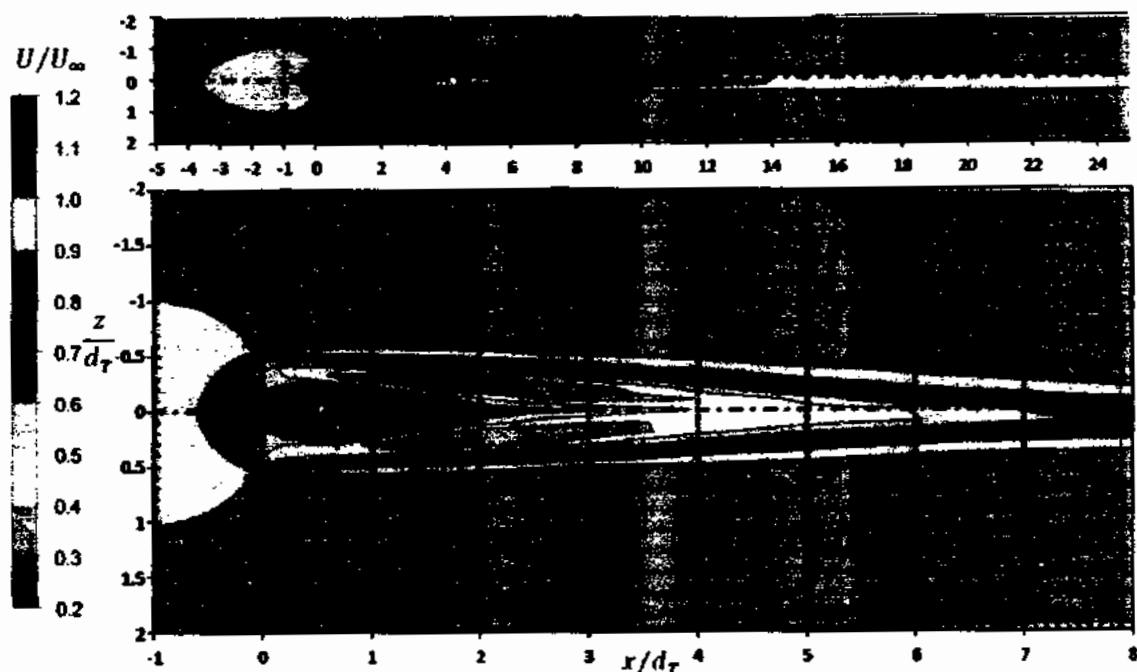


Figure 6.4 Normalized velocity contour on a horizontal plane across the width of channel at mid depth for single turbine in standalone domain

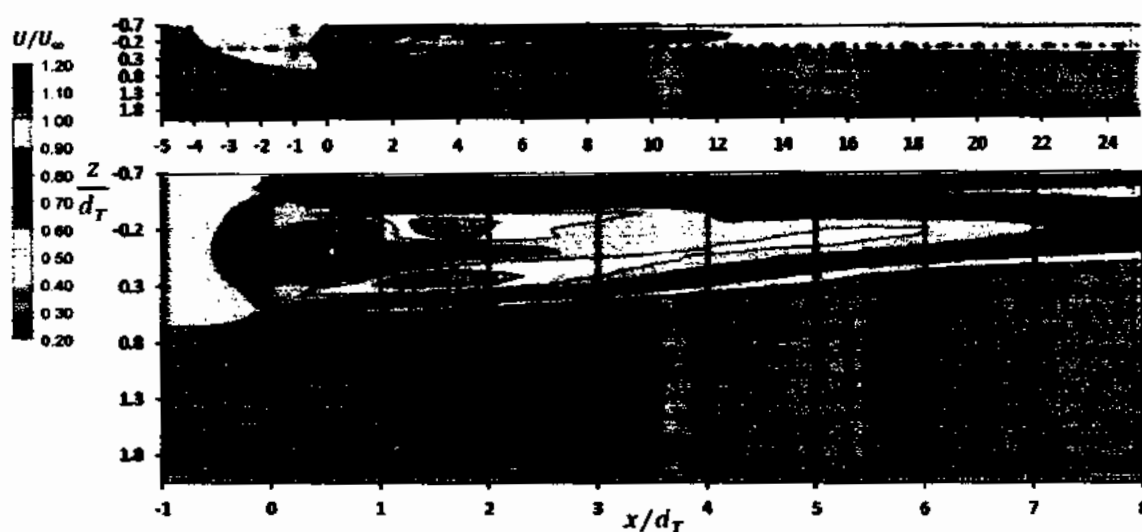


Figure 6.5 Normalized velocity contour on a horizontal plane across the width of channel at mid depth for single turbine off-center located in experimental domain

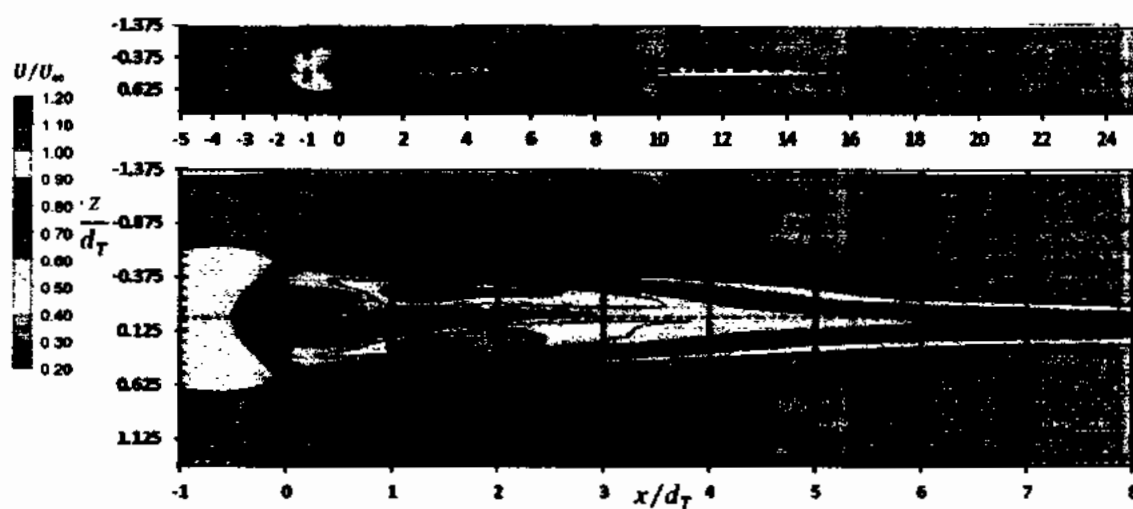


Figure 6.6 Normalized velocity contour on a horizontal plane across the width of channel at mid depth for single turbine center located in experimental domain

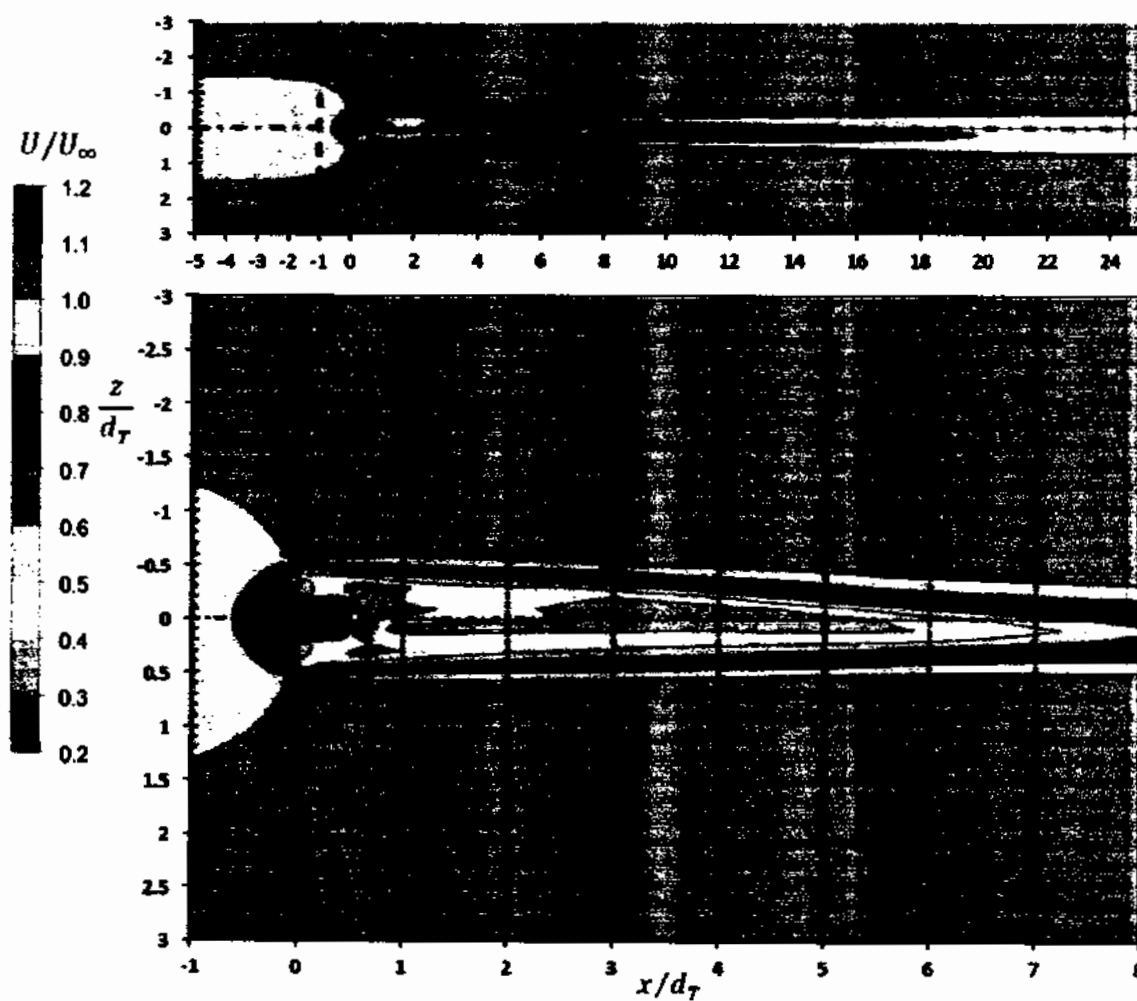


Figure 6.7 Normalized velocity contour on a horizontal plane across the width of channel at mid depth for single turbine in array domain

Figure 6.4 shows a symmetric wake that has travelled along the entire length of the channel and up to a distance of about $25D$ the velocity has not fully recovered its free stream value along the turbine center line. However, the wake is restricted in a narrow portion around the turbine centerline and is mixing with the surrounding fluid as it travels along the length of channel. The narrow yellow strips along the channel side boundaries are indication of wall/boundary effect. For a turbine operating off-center in a channel having the same configuration as the experimental setup, the flow is accelerated between the side boundaries and turbine as shown in Figure 6.5. Since, the area between channel boundaries and turbine is not similar therefore, the flow acceleration is also different in these areas. The friction effect caused by the shear layer between faster and slower moving fluids is also not similar and therefore wake is shifted towards side wall located close to the turbine. When the turbine is shifted to the center of channel as shown in Figure 6.6, the wake become symmetric along the turbine centerline with similar flow acceleration in the upper and lower bypass regions. These highly accelerated flow regions extend upto about $5D$ downstream of turbine. Whereas, the core of wake region travels about $16D$ downstream before it mixes with the bulk channel flow. The blockage ratio of channel in this case is 14.3% compared to 6.5% for the channel in Figure 6.4, therefore an enhanced wake mixing takes place and the velocity deficit does not extend along the entire length of channel. In Figure 6.7, the turbine is operating in the enlarged size domain of 4.4% blockage ratio and the wall effects have also been eliminated by applying symmetry boundary conditions. This domain is intended to be used for simulating all array cases in this thesis. The wake is symmetric and travels along the entire length of channel due to a lesser blockage ratio.

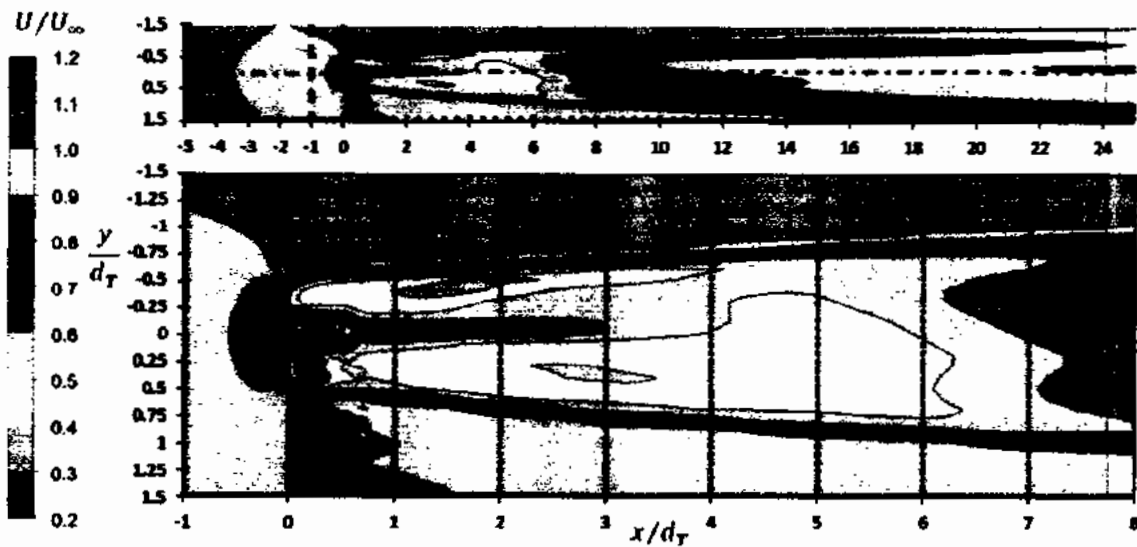


Figure 6.8 Normalized velocity contour across the depth of channel on a vertical plane passing through turbine centerline for single turbine in standalone domain

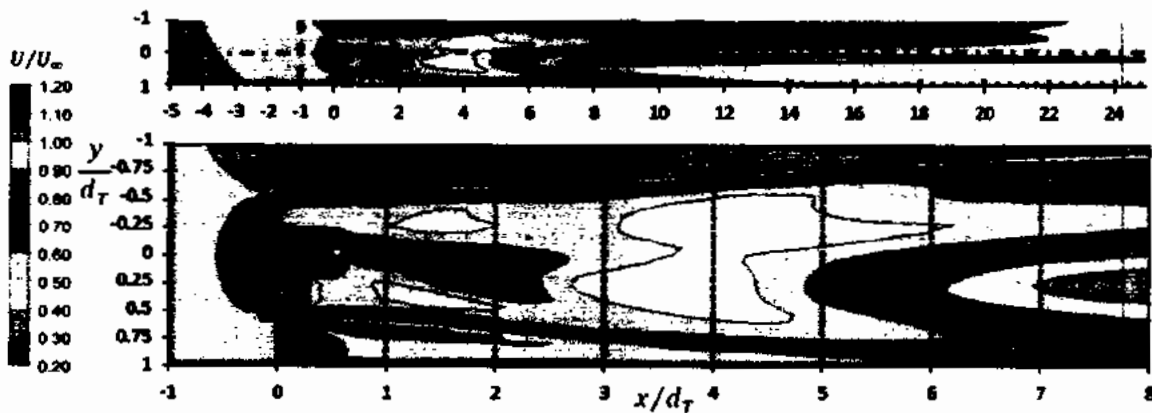


Figure 6.9 Normalized velocity contour across the depth of channel on vertical plane passing through turbine centerline for single turbine off-center located in experimental domain

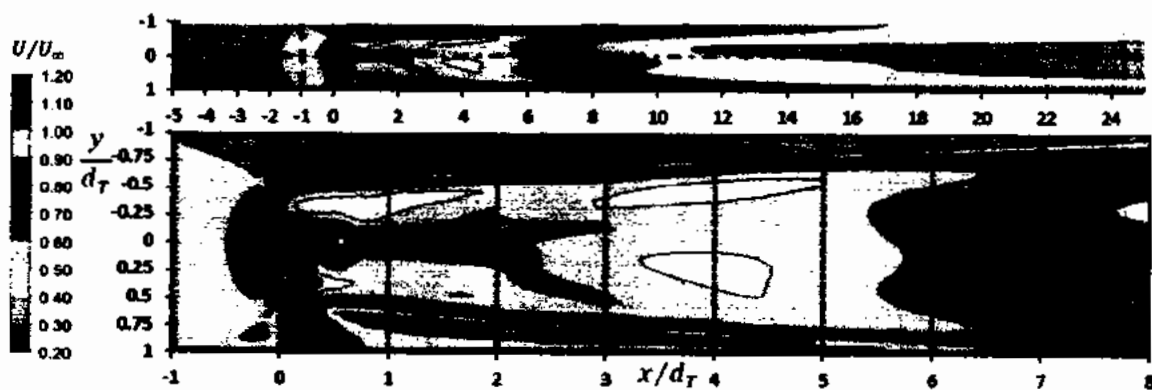


Figure 6.10 Normalized velocity contour across the depth of channel on a vertical plane passing through turbine centerline for single turbine center located in experimental domain

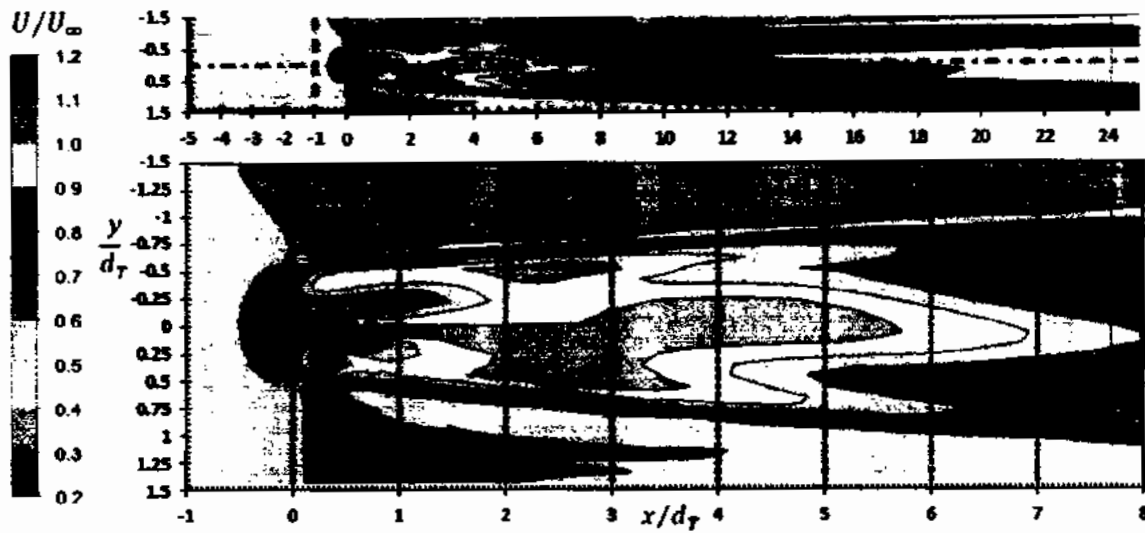


Figure 6.11 Normalized velocity contour across the depth of channel on a vertical plane passing through turbine centerline for single turbine in array domain

The vertical placement of turbine is at the mid depth of channel for all simulations. The normalized velocity contour in vertical plane for the case of standalone domain in Figure 6.8 shows that the wake extends throughout the length of channel beyond $25D$. The velocity of fluid in upper bypass region is more compared to the lower bypass region due to the bottom effect and tower. The dominant effect of tower on slowing down the fluid velocity diminishes upto a distance of about $1.5D$. However, the effect of tower and bottom on the velocity continues upto a distance of about $15D$ till the core wake mixes with the tower wake. The accelerated fluid in upper bypass region also keeps mixing with core wake along the length of channel. However, a narrow strip of brown color in upper bypass region shows that all of the accelerated fluid does not mix with core wake upto a distance of about $25D$. For the off-center located turbine in the experimental domain in Figure 6.9, the accelerated flow regions in the upper and lower bypass regions completely mixes with the core wake upto a distance of about $8D$ due to enhance wake mixing because of increased blockage ratio. The contour also shows that horizontal off-center placement has also caused vertical asymmetry in the wake. The overall enhancement in the mixing process has further reduced the dominant effect of tower on the flow velocity to a distance of about less than $1D$. A similar velocity contour for the center located turbine in experimental domain is shown in Figure 6.10. This contour is almost similar to Figure 6.9 except that the wake has become vertically symmetric. For turbine operating in the larger size domain intended for

array simulations shown in Figure 6.11, the wake is symmetric along the turbine centerline. However, the lower bypass region of wake is influenced by the tower effect and shows comparatively less velocity than the upper bypass region. The wake mixing is slower due to reduced blockage ratio of 4.4% and the core wake does not mix with upper bypass region even upto a distance of 25D.

The velocity deficit for all the simulations aimed at developing RAN CFD methodology for simulating turbine arrays is shown in Figure 6.12.

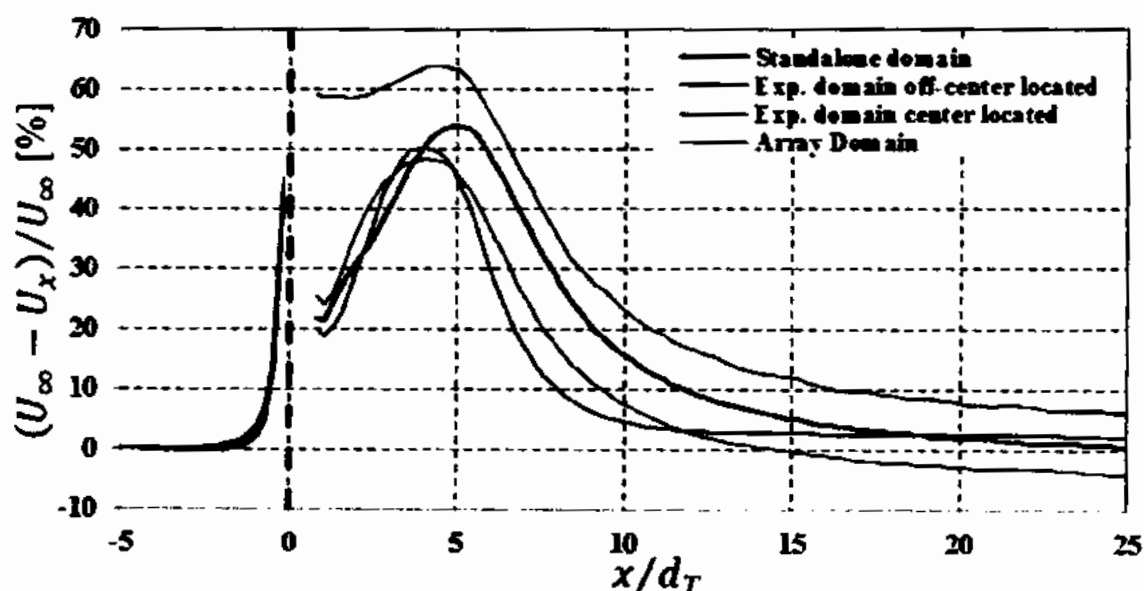


Figure 6.12 Velocity deficit along a line passing through the hub center throughout the length of domain

For turbine operating in standalone domain and array size domain, the centerline velocity deficit exhibits almost a similar behavior. However, for the standalone domain the velocity recovery is more due to enhance wake mixing because of increased blockage ratio. For the turbine operating in domains with blockage ratio of 14.3% equal to the experimental channel, the velocity deficit behavior is almost similar upto about a distance of 10D downstream for the case of off-center located and center located turbines. However, after this distance the velocity deficit behavior changes between the two cases due to asymmetry of wake along the turbine centerline. Additionally, for both these cases the velocity recovery is more compared to the other two cases of lower blockage ratios.

6.2 Tidal turbine arrays

The RANS CFD methodology adopted for simulating a single turbine in array domain is further extended to simulate two and three turbine co-axial and staggered arrays. These array configurations are simulated to investigate the effect of array layouts and inter device spacing on the performance and structural loads on the blade of TCT operating in arrays. The description of all simulated array configurations is provided in Table 6.3. A nomenclature has also been provided to avoid lengthy array descriptions while presenting and discussing results throughout this chapter.

Table 6.3 Definition and nomenclature of simulated array configurations

Array Description	Nomenclature
(A) Co-axial array	
1 Two turbine (8D interdevice spacing)	CA-2T-L8D
2 Two turbine (10D interdevice spacing)	CA-2T-L10D
3 Three turbine (8D interdevice spacing)	CA-3T-L8D
4 Three turbine (10D interdevice spacing)	CA-3T-L10D
(B) Staggered array	
1 Two turbine (1.5D transverse spacing)	SA-2T-S1.5D
2 Two turbine (2D transverse spacing)	SA-2T-S2D
3 Three turbine (1.5D transverse and 4D longitudinal spacing)	SA-3T-S1.5D-L4D
4 Three turbine (1.5D transverse and 6D longitudinal spacing)	SA-3T-S1.5D-L6D
5 Three turbine (2D transverse and 4D longitudinal spacing)	SA-3T-S2D-L4D
6 Three turbine (2D transverse and 6D longitudinal spacing)	SA-3T-S2D-L6D

The schematic of co-axial and staggered arrays along with turbine identifiers A, B and C is shown by a representative case from each group shown in Figures 6.13-6.14.

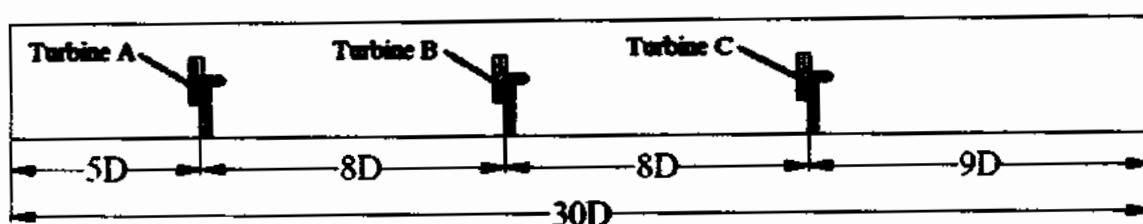


Figure 6.13 Schematic of three turbine co-axial array with 8D interdevice spacing

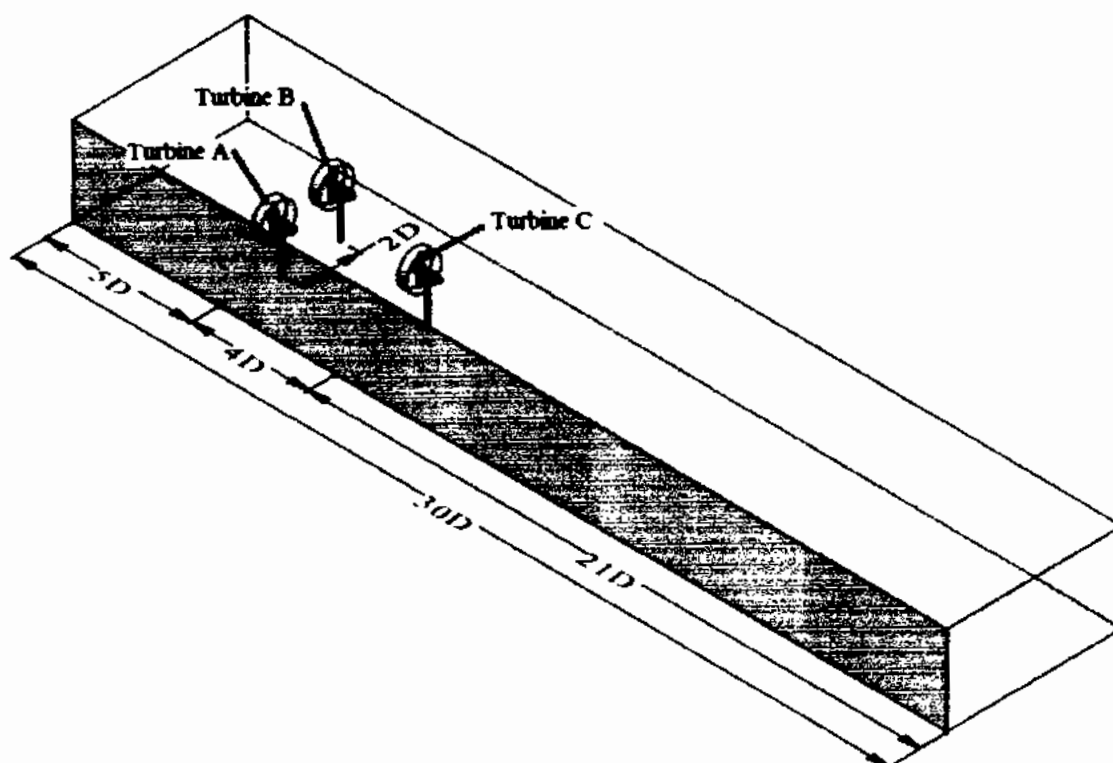


Figure 6.14 Schematic of three turbine staggered array with 2D transverse and 4D longitudinal spacing

6.2.1 RANS CFD methodology

The numerical methodology adopted for simulating turbine arrays is similar in essence to that of a single turbine in array domain described in section 6.1. The domain definition for all array simulations is similar and has already been provided in Figure 6.1. A steady state RANS CFD converged solution is first obtained for each three turbine array configuration using Multiple Frame of Reference (MRF) model. This solution is used as the starting point for transient simulation based on transient rotor stator approach for each configuration of three turbine array. The steady state RANS CFD simulation would have been sufficient, if the focus of these investigations was only the performance. But we are also interested to study the structural loads behavior of turbines blade, therefore transient simulations are

necessary. Additionally, initiating transient simulations with a converged steady state solution would ensure a stable solution for transient simulations and the final converged transient results would require less number of turbine rotations and corresponding total simulation time. The boundary conditions for all array simulations are similar to that of standalone turbine in array domain described in section 6.1.1. All array devices have the same TSR of 4.87.

The first row device/devices receive an inflow velocity of 1.5 m/s and rotates at 0.73 rad/s corresponding to the optimum TSR of 4.87 for full scale SAFL RM1 turbine. The rotational speed for downstream devices corresponding to the optimum TSR of 4.87 is selected in a similar way to the experimental procedures. In this procedure, vertical velocity profile at 2D upstream of the 2nd turbine placement location is obtained from the simulation results of standalone device operating in array domain. The depth averaged velocity is calculated from vertical velocity profile and rotational speed for the 2nd downstream device is computed from this velocity corresponding to the optimum TSR. Similarly, steady state simulation for the two turbine array with intended interdevice spacing is performed for the determination of rotational speed for the third turbine. The velocity profile at 2D upstream of the 3rd turbine placement location is obtained from the simulation results of two turbine array. The depth averaged velocity corresponding to this velocity profile is used to compute rotational speed of the 3rd device corresponding to the optimum TSR. The velocity profiles used for calculation of rotational speeds for downstream devices in all the array configurations is shown in Figures 6.15-6.16.

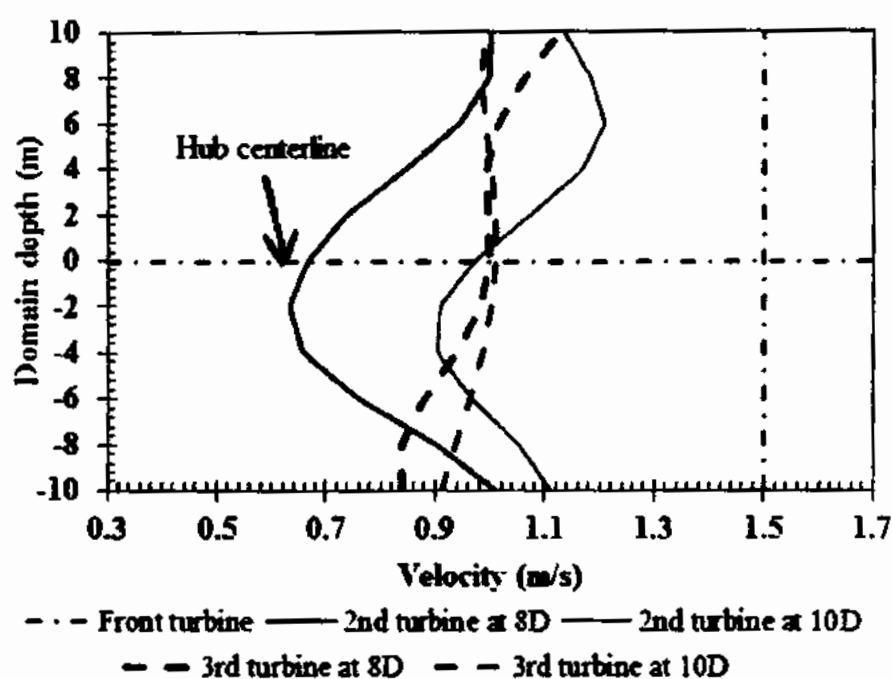


Figure 6.15 Vertical profile of incident velocity for turbine operating in co-axial arrays recorded at 2D upstream of each turbine

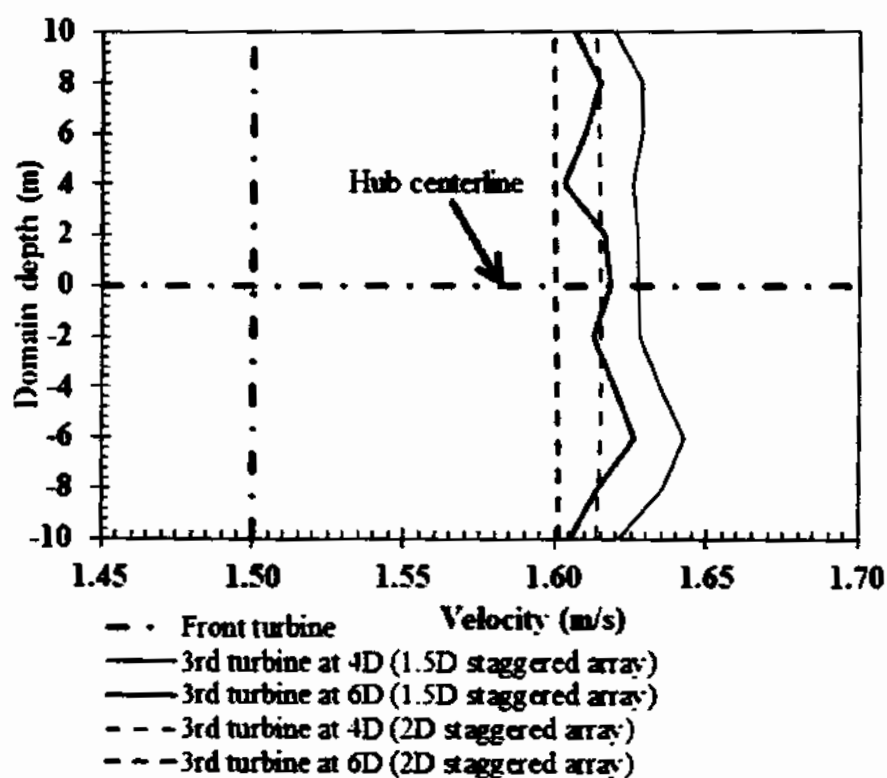


Figure 6.16 Vertical profile of incident velocity for turbine operating in staggered arrays recorded at 2D upstream of each turbine

Although, this procedure is quite lengthy because each three turbine array simulation would first require the simulation of a two turbine array with similar configuration. However, this is essential to ensure the comparison of performance and structural loads behavior of blades for turbines operating in arrays at the similar operating conditions. Otherwise, the effect on performance and structural loads would not be solely due to the array configuration and interdevice spacing. Turbine operating condition is one of the most dominant parameter and comparing performance and structural loads on the blades between devices at different operating conditions would be misleading. The rotational speeds set for all turbines in the simulation of all array configurations are as in Table 6.4. The total simulation time for all array configurations is set such that to ensure that turbine operating at the lowest angular velocity completes six turbine rotations. Similarly, the time step for all array simulations is set such that turbine operating at the highest angular velocity completes 6 degree rotation in one time step. The adequacy of this time step has already been discussed in section 4.6.4. Where it has been established through a time step study that a time step equivalent to 2° , 4° and 6° of turbine rotations would yield similar results.

Table 6.4 Depth averaged values of incident velocities and corresponding rotational speeds set for turbines in all simulated array configurations

Array Configuration	Depth averaged value of the incident Velocity (m/s)			Rotational speed at $TSR_{opt}=4.87$ (rad/s)		
	<u>Turbine location</u>			<u>Turbine location</u>		
	A	B	C	A	B	C
CA-2T-L8D	1.500	0.818	-	0.731	0.398	-
CA-2T-L10D	1.500	1.057	-	0.731	0.515	-
CA-3T-L8D	1.500	0.818	0.969	0.731	0.398	0.472
CA-3T-L10D	1.500	1.057	0.984	0.731	0.515	0.479
SA-2T-S1.5D	1.500		-	0.731		-
SA-2T-S2D	1.500		-	0.731		-
SA-3T-S1.5D-L4D	1.500		1.629	0.731		0.794
SA-3T-S1.5D-L6D	1.500		1.614	0.731		0.786
SA-3T-S2D-L4D	1.500		1.614	0.731		0.786
SA-3T-2D-L6D	1.500		1.600	0.731		0.779

6.2.1.1 Mesh setup

A similar technique of selective body conformal meshing and sizing is utilized for all array simulations as described in section 6.1.1. This meshing strategy ensured a similar mesh like the one utilized for standalone turbine simulations shown in Figure 6.2 for the simulations of all array configurations. An instance of mesh utilized for three turbine arrays is shown in Figure 6.17 to give an overall idea of the utilized mesh for array simulations.



Figure 6.17 Mesh for three turbine arrays

The enlarged views showing details of mesh near turbine and on turbine surfaces has already been provided in Figure 6.2 and is not provided here to avoid repetition. The total

number of mesh elements and its breakup in the rotating and stationary domains for all array simulations is as in Table 6.5.

Table 6.5 Grid statistics for array simulations

Array Configuration	Total number of mesh elements (x 10 ⁶)				
	Rotating Domain			Stationary Domain	Total
	A	B	C		
CA-2T-L8D	4.3	4.3	-	4.4	13.0
CA-2T-L10D	4.2	4.2	-	4.4	12.8
CA-3T-L8D	4.3	4.3	4.3	6.2	19.1
CA-3T-L10D	4.2	4.3	4.3	6.2	19.0
SA-2T-S1.5D	4.2	4.1	-	2.9	11.2
SA-2T-S2D	4.3	4.2	-	2.9	11.4
SA-3T-S1.5D-L4D	4.3	4.2	4.3	4.7	17.5
SA-3T-S1.5D-L6D	4.2	4.2	4.2	4.7	17.3
SA-3T-S2D-L4D	4.3	4.2	4.3	4.7	17.5
SA-3T-2D-L6D	4.2	4.2	4.2	4.7	17.3

The specification of prism elements layers generated around blade surfaces for capturing the boundary flow is also similar to that described in section 6.1.1 shown in Figure 6.3. For all the turbine blades in all array configurations, it is ensured that the values of y^+ stay within the range of $2 \leq y^+ \leq 300$ with 11 number of nodes in the boundary layer to meet the criteria specified by ANSYS CFX for the proper utilization of $k - \omega$ SST model with an automatic wall function switch [131]. The value of area averaged y^+ for the blades of all turbines in all simulated array configurations is as in Table 6.6.

Table 6.6 Area averaged y^+ values on the turbine blades for array simulations

Array Configuration	Area averaged y^+					
	<u>Turbine A</u>		<u>Turbine B</u>		<u>Turbine C</u>	
	Blade 1	Blade 2	Blade 1	Blade 2	Blade 1	Blade 2
CA-2T-L8D	189	188	125	116	-	-
CA-2T-L10D	189	188	146	142	-	-
CA-3T-L8D	189	188	125	123	142	141
CA-3T-L10D	190	188	144	148	141	136
SA-2T-S1.5D	194	192	188	190	-	-
SA-2T-S2D	190	189	184	182	-	-
SA-3T-S1.5D-L4D	192	188	183	182	206	207
SA-3T-S1.5D-L6D	195	191	191	191	209	208
SA-3T-S2D-L4D	192	189	183	182	202	201
SA-3T-2D-L6D	193	192	191	190	203	202

6.2.2 Results and discussion

6.2.2.1 Power output

The performance in terms of non-dimensional parameters for a single turbine is generally quantified through its power coefficient (C_p) computed at certain tip speed ratios (TSR). This method has attained wider acceptability for describing the performance of a standalone turbine. In the case of multi device tidal arrays, this method can be applied to describe the performance of front row turbines. However, for the downstream array devices, the turbine power coefficient (C_p) can be computed through ratio of the power extracted by turbine to either the undisturbed free stream velocity or the actual onset velocity for a specific device. Although, the later approach is more accurate but could not provide a physically meaningful sense of the overall power extraction from the array. The former approach may be based on an abusive notation but provides a clear picture of the overall power extraction from various array configurations and performance of individual turbines deputed in the array. The power coefficient values computed in this way may be treated as nominal values and the actual values based on true incident velocity for downstream devices will be higher than these nominal values. A similar procedure for

describing the downstream turbines performance in tidal turbine arrays has previously been used by Mycek et al. [158] and Stelzenmuller [94]. To clearly convey in a true physical sense, the effect of interdevice spacing in different array configuration on the performance of array as well as individual array devices, the power coefficient (C_p) for all array devices in this thesis is calculated on the basis of undisturbed free stream velocity of 1.5 m/s. The (C_p) values for all turbines in all array configuration simulated in this thesis is as in Table 6.7.

Table 6.7 Power coefficient (C_p) values for turbines in all the array configuration

Array Configuration	C_p based on undisturbed free stream velocity		
	Turbine A	Turbine B	Turbine C
CA-2T-L8D	0.39	0.18	-
CA-2T-L10D	0.42	0.24	-
CA-3T-L8D	0.42	0.18	0.18
CA-3T-L10D	0.41	0.21	0.16
SA-2T-S1.5D	0.40	0.44	-
SA-2T-S2D	0.40	0.45	-
SA-3T-S1.5D-L4D	0.43	0.43	0.39
SA-3T-S1.5D-L6D	0.43	0.44	0.40
SA-3T-S2D-L4D	0.42	0.43	0.50
SA-3T-2D-L6D	0.43	0.44	0.49

The power coefficient of downstream devices significantly drops compared to the upstream devices for both the two turbine co-axial array configurations. However, for 8D interdevice spacing the drop in power coefficient is comparatively greater than 10D spacing. For three turbine co-axial array with 8D interdevice spacing the power coefficient of the 2nd and 3rd turbine is similar. Similarly, the power coefficients of all array devices minimally changes for a change in inter device spacing from 8D to 10D in three turbine co-axial arrays. However, the power coefficient of 2nd downstream device is more influenced compared to 3rd downstream device by a change in interdevice spacing from 8D to 10D. The downstream device exhibits higher power coefficient compared to the upstream devices in a three turbine staggered array configuration with transverse spacing of 1.5D between the

1st row devices. Nuernberg et al. [100] in their experimental work also observed that for shorter transverse spacing between upstream devices the power coefficient of downstream device would significantly decrease in staggered arrays. This decrease in power coefficient for the downstream device in very closely spaced staggered arrays is due to the slower wake recovery with large areas of higher velocity deficits [99]. However, still the power coefficient of downstream devices in 1.5D staggered array is considerably greater than any of the co-axial configuration. Turnock et al. [23] presented a similar finding in analyzing the power capture of tidal turbine arrays. Contrarily, the power coefficient of downstream device is significantly higher compared to the upstream devices in staggered array with transverse spacing of 2D between the upstream devices. Several other researchers have observed similar increase in power coefficient of downstream device in optimally spaced staggered arrays [24, 58]. The downstream device located at 4D in the staggered array configuration with 2D lateral spacing exhibit the maximum power coefficient compared to all other devices in all simulated array configurations. However, this is closely followed by the 6D downstream located device in staggered array with 2D lateral spacing.

To further compare the performance of arrays, the overall power extracted from all array configurations is quantified in Table 6.8 and pictorially represented in Figures 6.18-6.19.

Table 6.8 Total power extracted by all simulated array configurations

Array configuration	Power extracted [kW]			Array total power [kW]
	Turbine A	Turbine B	Turbine C	
Standalone	203.3	-	-	203
CA-2T-L8D	204.3	92.8	-	297
CA-2T-L10D	222.4	128.7	-	351
CA-3T-L8D	224.8	98.0	97.1	420
CA-3T-L10D	218.1	113.8	84.0	416
SA-2T-S1.5D	213.8	233.1	-	447
SA-2T-S2D	213.2	238.8	-	452
SA-3T-S1.5D-L4D	226.9	228.3	207.3	663
SA-3T-S1.5D-L6D	227.2	235.5	212.7	675
SA-3T-S2D-L4D	222.9	230.3	263.5	717
SA-3T-2D-L6D	230.3	234.0	258.0	722

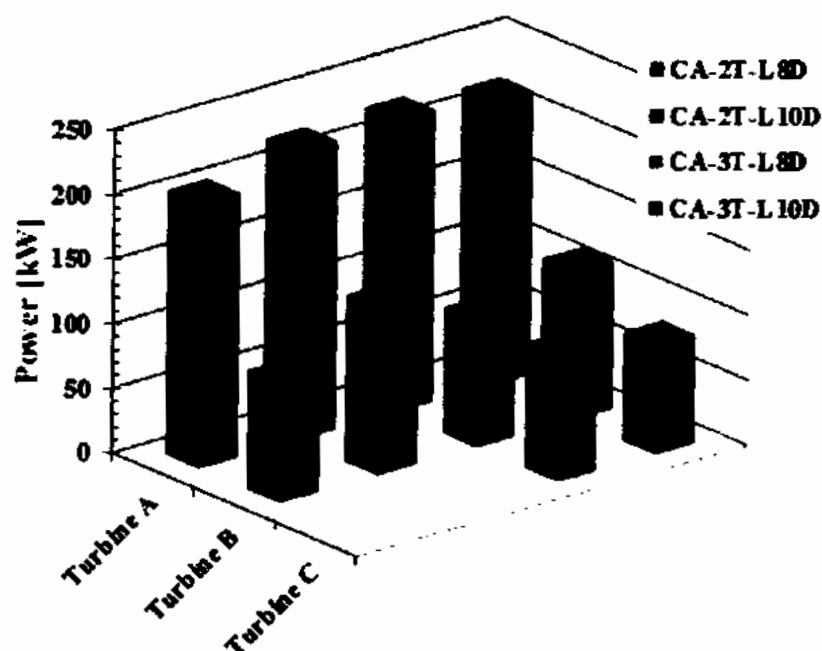


Figure 6.18 Power extraction from co-axial configuration of turbine arrays

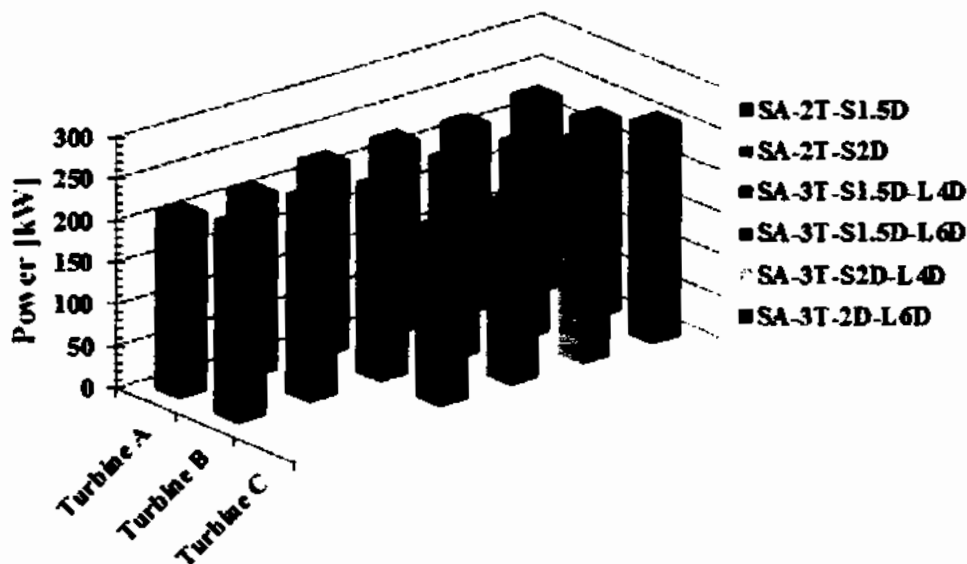


Figure 6.19 Power extraction from staggered configuration of turbine arrays

The staggered configuration arrays clearly outperform their counterpart of co-axial arrays in terms of total array power output. However, the results show that transverse spacing between the upstream devices should be optimal for the downstream device located at certain longitudinal spacing to maximize the total array power extraction. The optimal extent of transverse spacing between the upstream devices is array specific and also depends upon the longitudinal spacing of downstream device. Turnock et al. [23] suggested a broad range of less than $6D$ for both the longitudinal and transverse spacing in staggered arrays for optimal power extraction, while Malki et al. [24] suggested that the minimum staggering distance should be more than $2D$. Other researchers like Lee et al. [97] and O'Doherty et al. [98] suggested that the optimal staggering distance between upstream devices should be $3D$ and $2D$ respectively. The study presented in this thesis observed that optimal staggering distance between the upstream devices would depend upon spacing between the front row and downstream device. Because, accelerated flow region along the gap of 1st row adjacent devices would mix with surrounding flow as it travels along the length of channel. Therefore, the area of this higher velocity region would increase with increasing downstream distance along the channel length. The closely located downstream devices would therefore require a wider staggering distance between the upstream devices compared to the farther located downstream devices. For the 2D staggered configuration in this study, the tip to tip clearance between the front row turbines is $1D$ and this should be the lowest possible distance to ensure that blades of the downstream turbines receive a

higher velocity throughout the most part of its length. Whereas, for the case of 1.5D staggered configurations, the tip to tip distance between the front row adjacent devices is only 0.5D. Which means that major portion of the downstream turbine blades (about 50% of the blade length) operates in a flow regime that has been largely influenced by blades of the upstream devices. This fact can be clearly observed from the incident depth wise velocity profiles for the staggered arrays as already shown in Figure 6.16. For 2D staggered configurations, the relatively closely spaced (4D) downstream device produces more power compared to when the device is located at 6D. Contrarily, in the case of non-optimally close staggered configuration of 1.5D, the widely spaced (6D) downstream device produces more power compared to when the device is located at 4D. Again this increase in power with increasing downstream distance in a staggered array is attributed to the momentum gain in regions where it was influenced by the blades of upstream devices. Although, the 1.5D staggered configuration may be non-optimal but still it produces more power compared to any of the co-axial configuration. The total array power output for the two turbines arranged in a staggered configuration is significantly greater than even the three turbine co-axial arrays. This clearly highlights the relative advantage of staggered arrays compared to co-axial arrays both in terms of array output and capital cost. However, this is a very simplistic view based upon a very simplistic representation of limited number of array configurations.

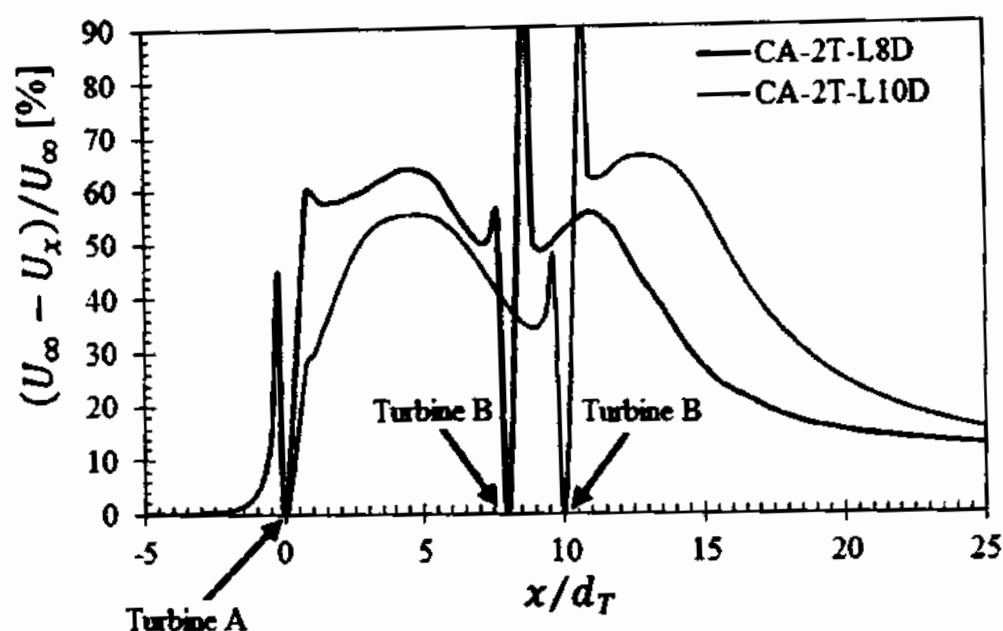
The real scenario is much more complicated and would involve several other factors like for example, the flow alignment that can reverse the relative advantage of staggering compared to the axially aligned arrays. The staggered arrays produces more power for perfectly aligned flows, while for misaligned flows the axial arrays are more efficient [103]. The counter rotation of adjacent devices can also influence the flow acceleration between staggered devices by reducing the shear rate that would further improve the performance of downstream devices [98, 104]. The differential tuning can be equally employed to both staggered and axial arrays to maximize their efficiencies. However, the output of a staggered array cannot be maximized to an extent to exceed that achieved by an equivalent axial array [105]. Decision on turbine control strategies along with maximum number of turbines that could be installed to extract maximum power from an available resource would also have to be duly considered for the macro and micro design of arrays

[106]. Although, it is an established fact now that staggering turbines within an array can increase the power output of downstream devices due to the local duct effect between adjacent upstream devices. However, this would depend on the inter row spacing and inter device spacing within a row specific to the array site and several other factors with some of them interdependent to each other. More importantly, this increase in the power output in terms of individual turbines would only be beneficial if it translates into an increase in the total array output. It is therefore still an unresolved challenge to optimize the array output by striking a balance between the blockage effects and wake interaction [107]. Because, single row arrays with higher local blockage are more efficient in terms of power output compared to multi row arrays with lower blockage [108]. Further investigations are required to establish the competitive advantages of single row arrays that exploit the duct effect or multiple rows staggered arrays that exploit accelerated flow between the gaps. Multiple row staggered arrays are more efficient than axial arrays, while it is not clear that staggered layout is a better choice than single row array [104].

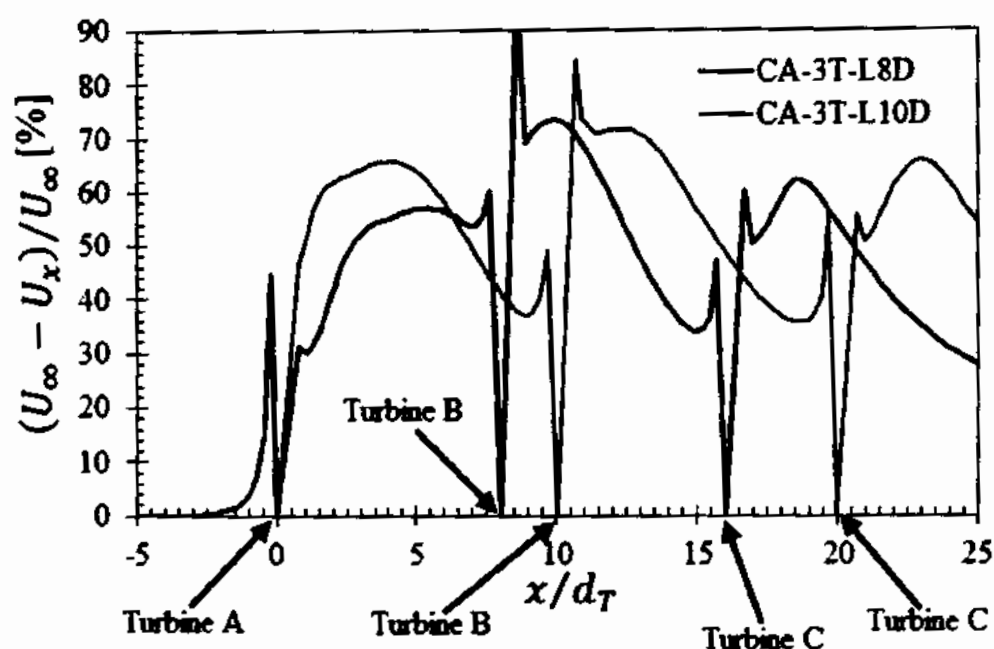
For the co-axial arrays these results suggest that the 2nd downstream device would produce more power when located at larger downstream distance. Contrarily, for the 3rd downstream device the increased spacing would reduce the power output. This finding is in accordance to the fact that wake mixing would enhance due to device generated turbulence added by the devices as it flow through more and more devices. Although, this data set is not enough to provide a certain conclusion. However, these results suggest that the downstream distance between adjacent devices would need to be incrementally reduced to obtain maximum power output from co-axial arrays.

6.2.2.2 Wake characteristics

The wake field within the computational domain is studied to examine the influence of turbines operation on the flow. The velocity deficit $(U_\infty - U_x)/U_\infty$ is the measure of velocity reduction as the flow travels along the channel. The velocity deficit along the centerline of the computational domain for the co-axial array configurations is shown in Figure 6.20.



(a) Two turbine co-axial arrays



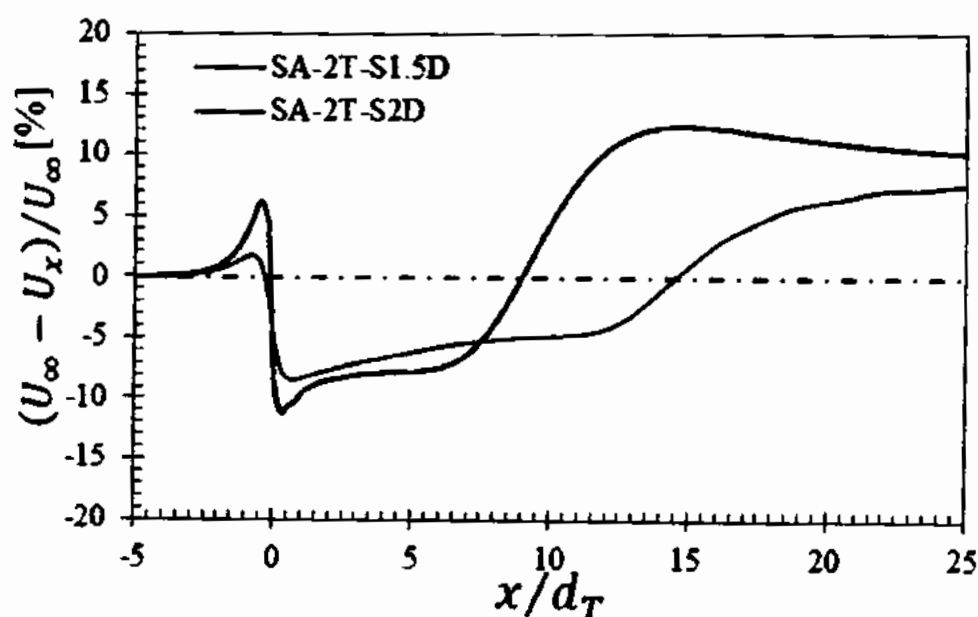
(b) Three turbine co-axial arrays

Figure 6.20 Velocity deficit for (a) Two turbine (b) Three turbine co-axial arrays

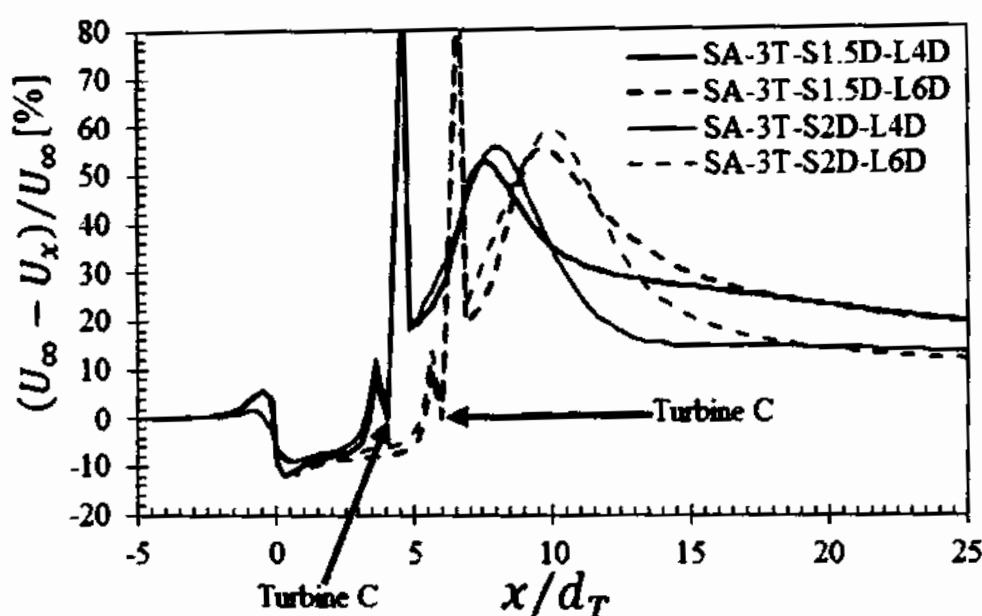
The overall behavior of the velocity deficit is similar between all the co-axial configurations. Turbine B in the case of two turbines separated by 8D receive about 60% less velocity compared to the undisturbed free stream velocity at the hub height. Whereas, in the case of 10D spaced two turbine configuration the approach velocity for turbine B at

the hub height is about 40% less than the undisturbed free stream velocity. The velocity deficit at the exit of the channel is about 13% and 16% for the 8D and 10D spaced two turbine co-axial arrays respectively. For the three turbines co-axial arrays, the approach velocity for turbine C in the 10D spaced three turbine array is about 2% less than the 8D case. The velocity deficit at the channel exit is about 28% and 54% for 8D and 10D spaced three turbine co-axial arrays respectively.

The velocity deficit along the centerline of computational domain for the staggered configuration arrays is shown in Figure 6.21.



(a) Two turbine staggered arrays



(b) Three turbine staggered arrays

Figure 6.21 Velocity deficit for (a) Two turbine (b) Three turbine staggered arrays

For both the two turbine staggered arrays the velocity accelerates between the front row adjacent devices as evident from Figure 6.21 (a). For the 1.5D staggered arrays the maximum flow velocity is about 11.2% greater than the undisturbed free stream velocity at the widthwise centerline of the channel at about 0.3D downstream of the 1st row devices. Whereas for the 2D staggered arrays the maximum velocity is about 8.4% greater than the undisturbed free stream velocity at the channel widthwise centerline at about 0.8D downstream of 1st row devices. For the 1.5D transversely spaced devices the flow accelerations starts immediately downstream of the 1st row devices and extends upto about 9D downstream along the channel length, while for the 2D spaced configuration the accelerated flow extends upto about 14D. The hub height undisturbed free stream centerline velocity accelerates by about 7-8% within the range 4D-6D along the channel length for the two turbines 1.5D staggered configurations. For the 2D spaced devices the flow acceleration within this region is about 1% less than the 1.5D staggered arrays. The velocity deficit for the 1.5D case at the channel exit is about 10% compared to 8% for the 2D spaced devices. Although, this velocity deficit plot shows that the closely spaced configuration of 1.5D may be marginally better suited for placing a downstream device to extract more power from the channel. However, this is not actually true because the

velocity deficit plot is along the centerline of the channel and represent the approach flow velocity along a line at the hub center for the third downstream device. The blades of the third downstream device may be operating in a highly disturbed flow regime in this case of non-optimally closely spaced devices. This aspect will be further explained in the proceeding discussion in this section. The approach velocity 2D upstream of turbine C for the case of 1.5D transversely spaced 1st row and turbine C longitudinally spaced at 4D downstream is about 8% greater than the undisturbed free stream velocity. Increasing the longitudinal spacing from 4-6D in this case results in negligible reduction in the approach velocity for the downstream stream device. In the case of 2D transversely spaced staggered configuration the approach velocity at the hub centerline for the downstream device located at either 4D or 6D is about a percent less than the 1.5D configuration. However, as already described this may be misleading as the turbine power extraction would not depend on the velocity received at the hub center but the overall velocity in the flow area swept by the turbine rotor.

The normalized velocity contour for the three turbine co-axial array with 8D interdevice spacing in Figure 6.22 further elucidate the flow behavior with in the channel.

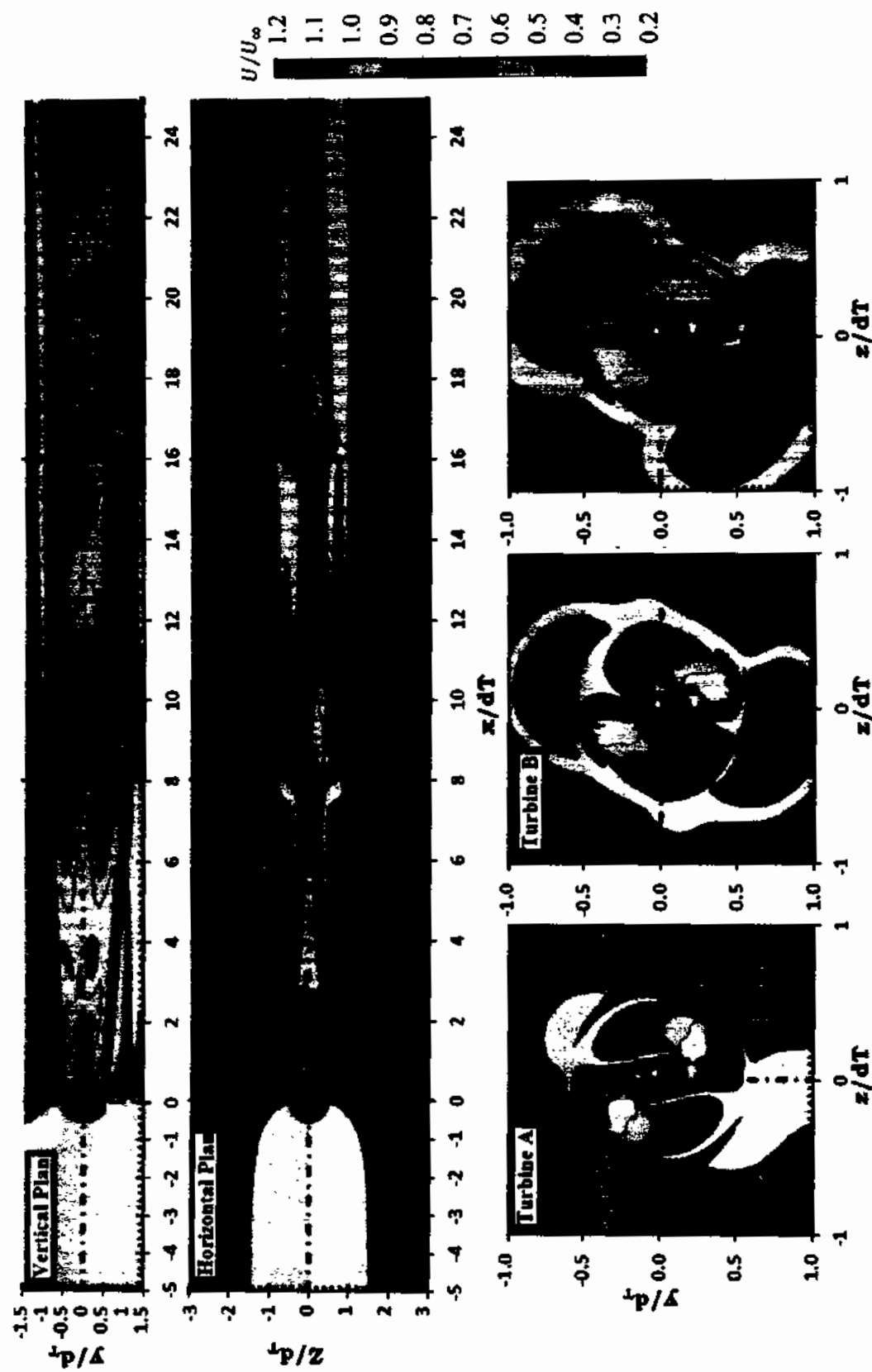


Figure 6.22 Normalized velocity contours for CA-3T-L8D array on a vertical plane at mid depth, horizontal plan at mid width, horizontal plan at mid depth and cut outs of transverse plan immediately behind each turbine

The velocity contour shows that turbine B is operating with in the wake of turbine A and would therefore be subjected to lower velocity than the undisturbed free stream velocity. The vertical contour shows that downstream of turbine A, the wake of rotor and tower are clearly separated upto turbine B and the dominant effect of tower is upto $2D$ downstream. However, the less pronounced effect of tower extends upto turbine B located at $8D$. Immediately downstream of turbine B the rotor wake along the depth expands and the tower and rotor wake merges to form a single wake. The wake extends throughout the length of the entire channel. The wake expansion along the depth increases after passing through successive devices and almost covers the entire depth of the channel after passing the third turbine. On the horizontal plan the wake downstream of turbine A is narrow and contains comparatively less velocity for the most part of horizontal span of the wake. The wake in this portion is strong and the mixing rate seems be uniform and slow throughout the entire interdevice space of $8D$. The wake expands horizontally after passing through turbine B as in the case of vertical contour. Downstream of turbine B, the strong portion of the wake central core remains intact only upto about $4D$. The mixing of the wake central core with the surrounding flow is easily noticeable upto about $4D$ downstream of turbine C and after this distance the wake mixing seems to slow down and convect downstream almost unaffected till the exit of the channel. The normalized velocity contours on the ($2D \times 2D$) cutouts from the transverse plan immediately behind each turbine shows that turbine C significantly contributes to the vertical and horizontal expansion of the wake. All these cutouts show that the wake is not symmetric.

A similar behavior is also exhibited by the three turbine co-axial array with $10D$ interdevice spacing as shown in Figure 6.23. In this case the approach flow and wake behavior of turbine A is essentially similar to the earlier case. However, the behavior of turbine B and C is markedly different than the $8D$ case. This is quite obvious because these downstream devices are located at comparatively larger distance of $10D$ compared to $8D$ in the 1st case. Therefore, the flow has comparatively more distance to regain its undisturbed momentum and shape before reaching the downstream device. In the horizontal plan, the wake successively expands after passing through each additional downstream device. Unlike the earlier case, the wake mixing may be different between the devices of array but it is uniform

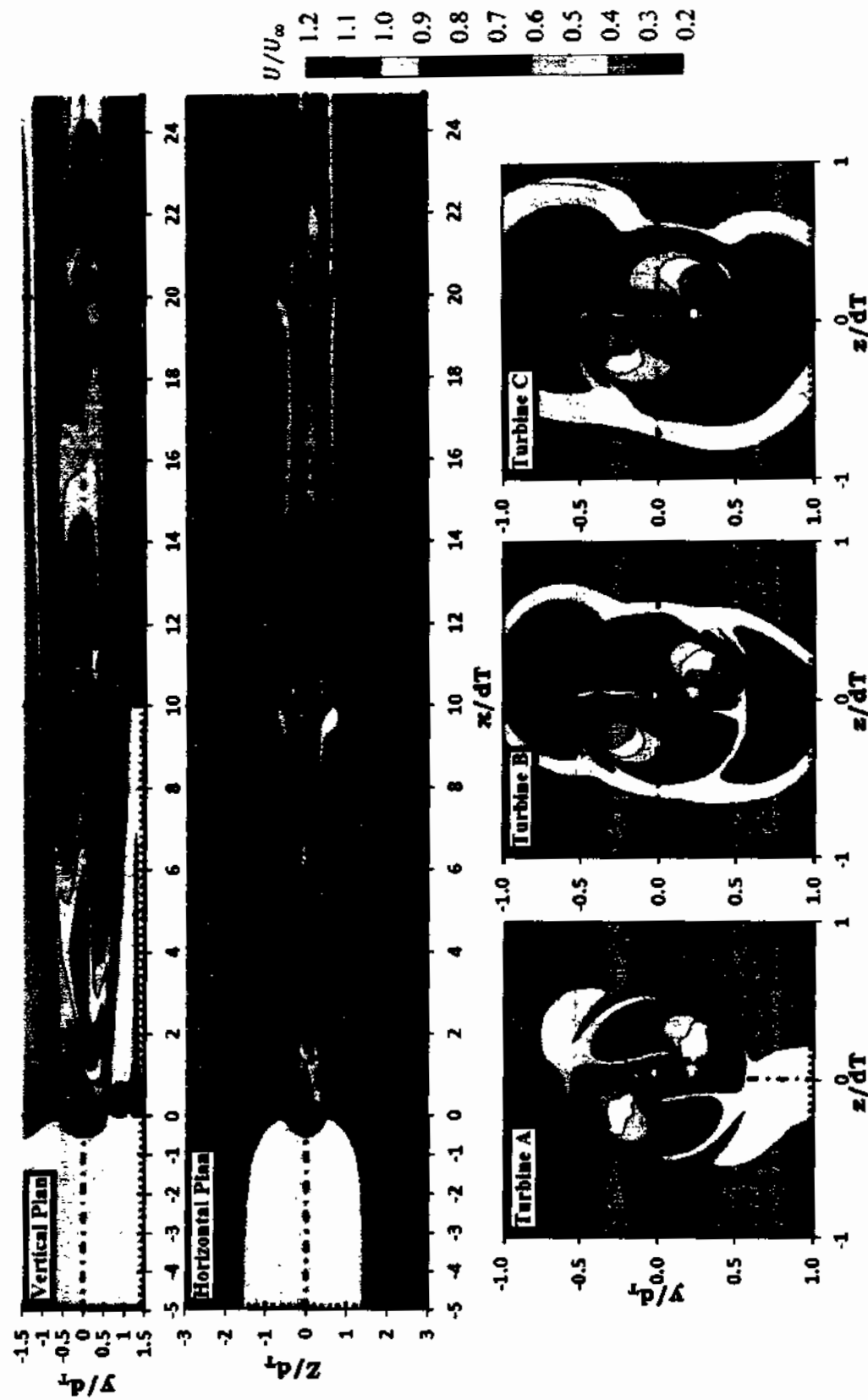


Figure 6.23 Normalized velocity contours for CA-3T-L10D array on a vertical plane at mid depth, horizontal plane at mid width and cut outs of transverse plan immediately behind each turbine

downstream of each device. The cutout of transverse plan for turbine B also shows that the wake immediately behind this turbine is comparatively more uniform. Similarly, the turbine C is now also exhibiting a more uniform wake compared to the earlier case of 8D spaced co-axial array.

The transverse (width wise) profiles of normalized velocity (U/U_∞) 2D upstream of each turbine for both the 8D and 10D spaced co-axial three turbine arrays is provided in Figure 6.24 to further elucidate the flow approaching each device.

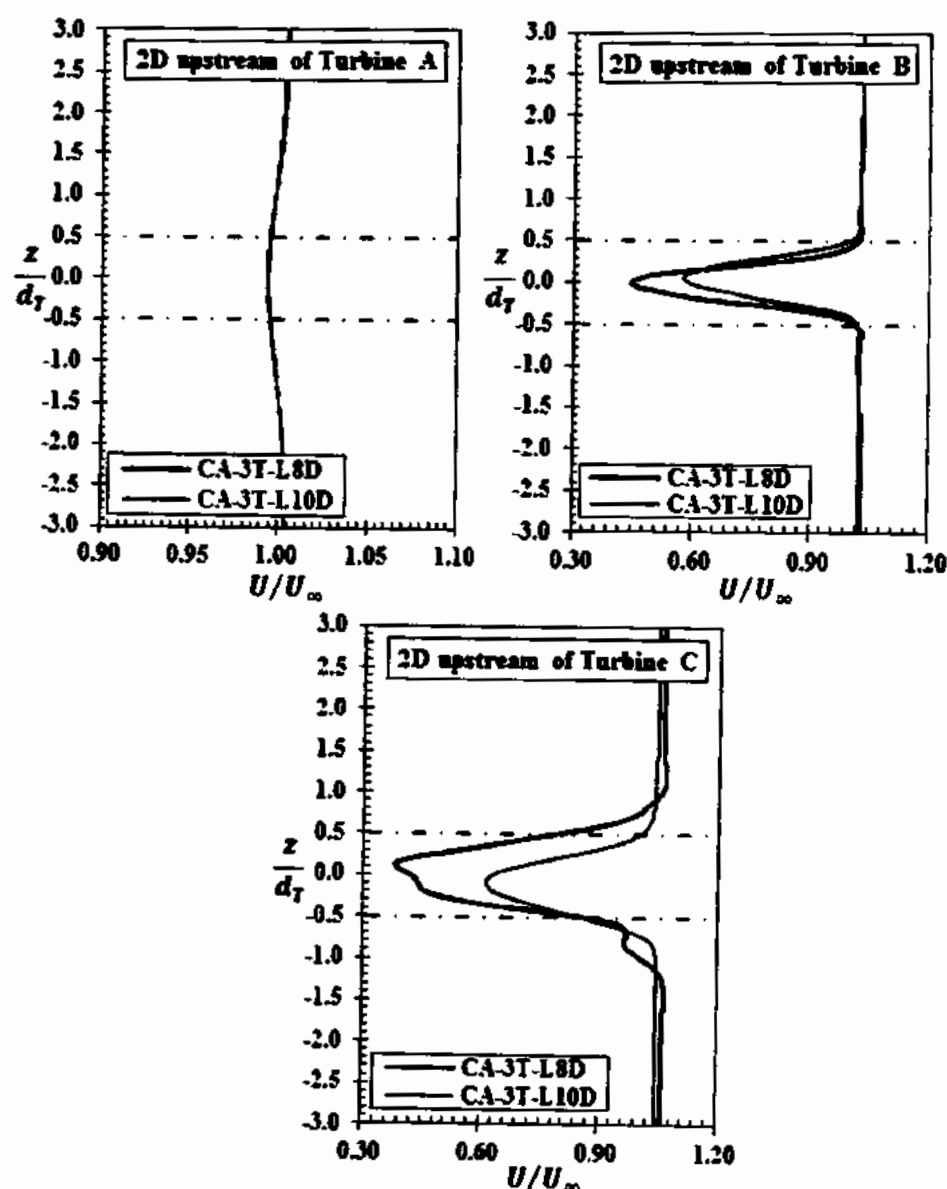


Figure 6.24 Transverse profiles of normalized velocity 2D upstream of each turbine for the three turbine co-axial arrays (Red dash dotted lines represent the span of turbine blades)

The transverse profile of velocity at mid depth (hub height) at 2D upstream approaching turbine A is similar for both the 8D and 10D longitudinally spaced co-axial arrays. For turbine B and C the approach velocity in the 8D spaced co-axial array is less than the 10D spaced array. However, this reduced velocity does not cover the entire span of the rotor but is limited to a narrow region covering the hub and only a smaller portion of the rotor near the hub. However, the vertical profiles (Figure 6.25) over the same distance 2D upstream of turbine B shows that the whole span of this turbine rotor is operating in a comparatively reduced velocity in the case of 8D spaced compared to the 10D spaced array.

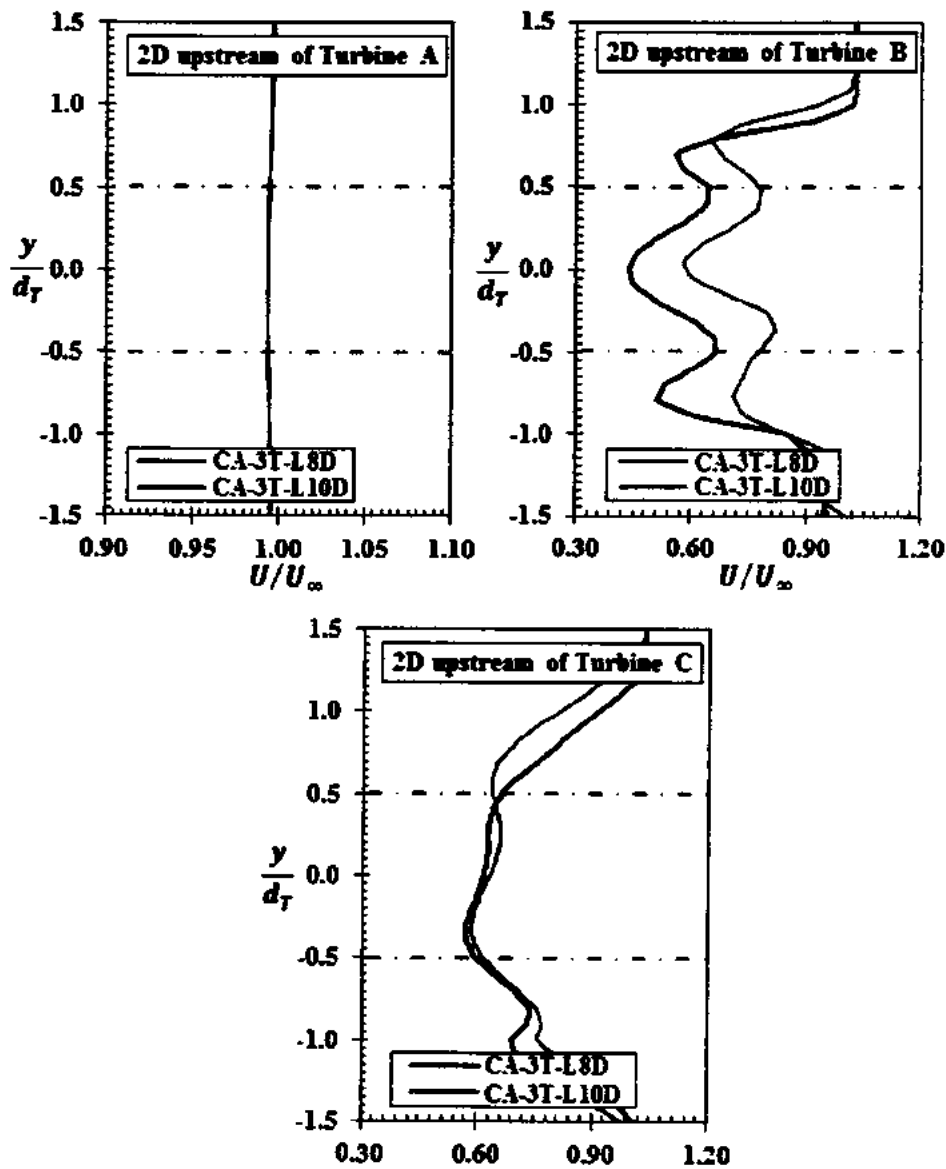


Figure 6.25 Vertical profiles of normalized velocity 2D upstream of each turbine for the three turbine co-axial arrays (Red dash dotted lines represent the span of turbine blades)

The transverse profiles clearly shows that turbines B and C are better positioned in the case of 10D spaced array to produce comparatively more power. However, the vertical profile shows that only turbine B has this competitive edge in the case of 8D placement. Whereas, the output of turbine C will nearly stay the same for both the cases of 8 and 10D spaced arrays.

To understand the effect of devices on the channel flow the transverse and vertical profiles 4D downstream of each turbine is provided in Figure 6.26. The velocity behavior is similar in essence for both the cases in the transverse and vertical directions. The transverse profile shows that the velocity reduction at 4D downstream for the 10D spaced array is about 8-10% greater than the 8D array at the center of the channel for all the turbines. Similarly, for the vertical profile the velocity reduction for the 10D spaced co-axial array is about 7% greater compared to the 8D spaced array. All these profiles suggest that the 10D spaced arrays have marginally greater effect on the channel flow compared to the 8D spaced arrays.

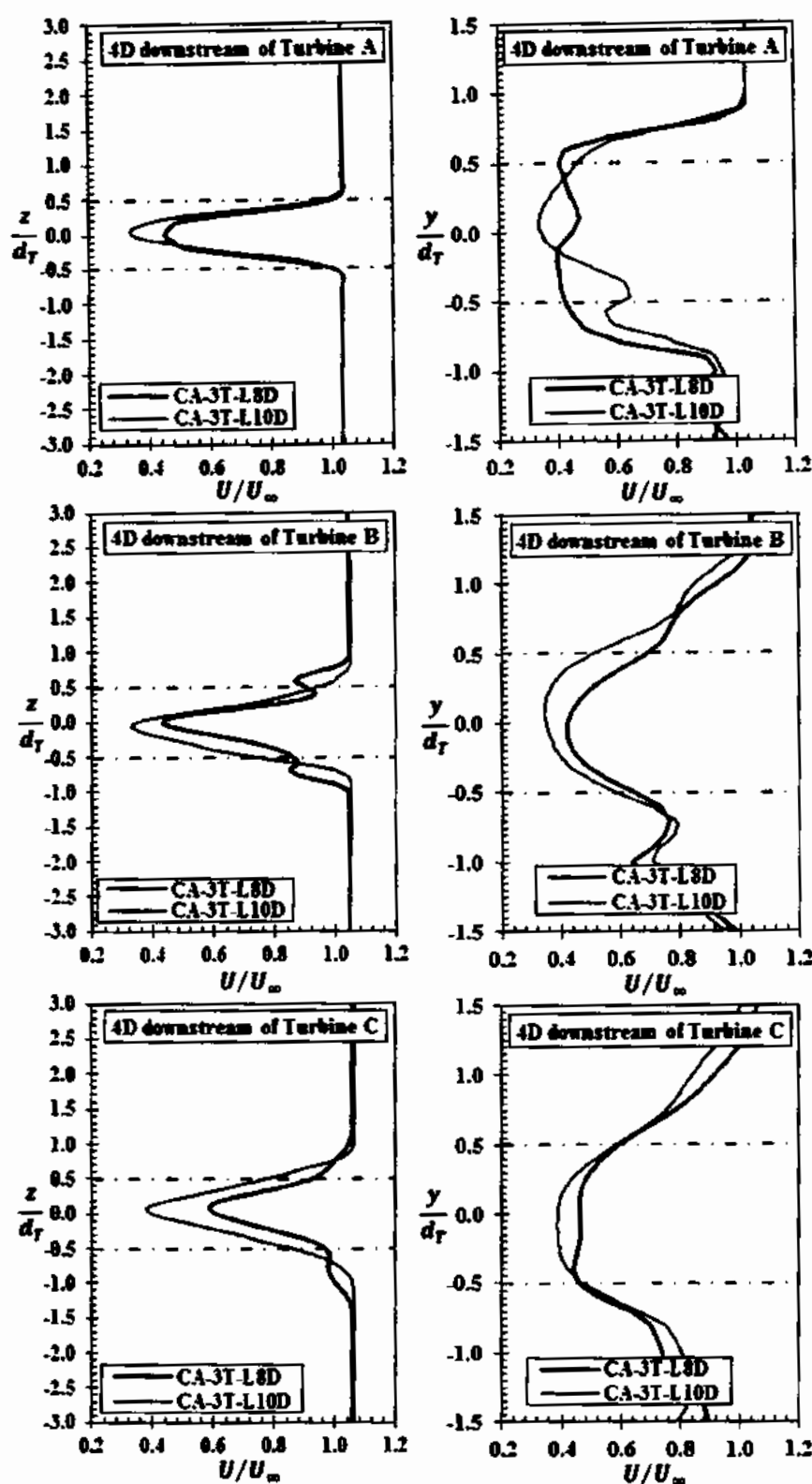


Figure 6.26 Transverse and vertical profiles of normalized velocity 4D downstream of each turbine for the three turbine co-axial arrays (Red dash dotted lines represent the span of turbine blades)

The normalized velocity contours in the vertical and horizontal plans for the 1.5D staggered arrays is given in Figures 6.27-6.28. These contour plots show that the wake of the front row turbines separated by a transverse spacing of 1.5D from hub center to center is clearly separated up to the downstream turbine C. The vertical and horizontal contour plots show that the flow is accelerated between the gap of 1st row devices and the approach velocity for turbine C is greater than the undisturbed free stream velocity. However, the clearance between the blade tips of the 1st row turbines is 0.5D and therefore a significant portion of the blades of turbine C has to pass through the disturbed flow in the near wake. The vertical contours of turbine A and B are similar and seem to be the upside down images of each other. The wake of turbine A is shifted upwards and that of turbine B is shifted downwards. This is due to the fact that all the array devices form a single wake after turbine C and these vertical contours should be viewed as the cut outs along the vertical central plan along the center of each turbine. The combined wake of all the array devices is almost symmetric in both the vertical and horizontal planes and travel along the entire length of the channel. The wake mixing is slow and uniform and till the exit of the channel the velocity recovery within the wake is about 80%. For the 2D laterally separated staggered arrays, the blades tip to tip clearance between the 1st row devices is 1D. The normalized velocity contour for the 2D staggered arrays (Figures 6.29-6.30) also shows that the flow is accelerated within the gap of 1st row turbines and the approach velocity to turbine C is greater than the undisturbed free velocity. Unlike the previous case, the wake of 1st row turbines does not immediately mix with the wake of turbine C to form a single wake. The horizontal contour for the 2D staggered array with turbine C placed at 4D downstream (Figure 6.29) shows that the wake merging is not symmetric and the wake of turbine B and C merges at about 5D. Whereas, the wake of turbine A and C is separated till about 11D. After this distance the wake of all array devices merges together to form a single wake. However, still the velocity in the lower part of the wake (i.e. the combined wake of turbine A and C) is comparatively greater than the upper part. This non-uniformity in the wake velocity diminishes completely at about 19D. On the contrary, the velocity contours of the 2D staggered array with downstream turbine located at 6D longitudinal spacing (Figure 6.30) shows an almost uniform wake merging. In this case the wake of all array devices merges together before 8D to form a single wake.

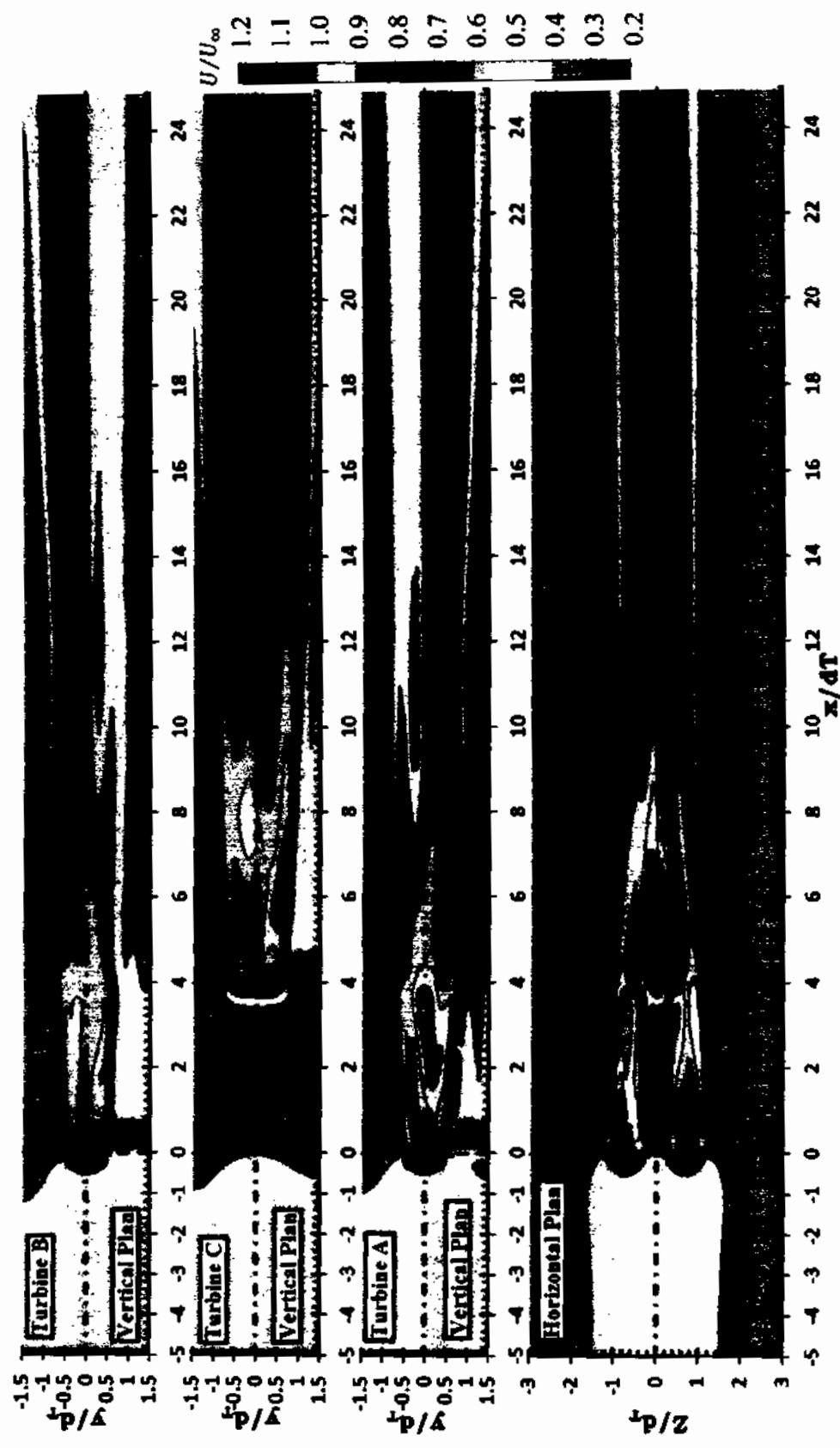


Figure 6.27 Normalized velocity contours for SA-3T-SI 5D-LAD array on vertical planes along the center line of each turbine and horizontal plan at mid depth

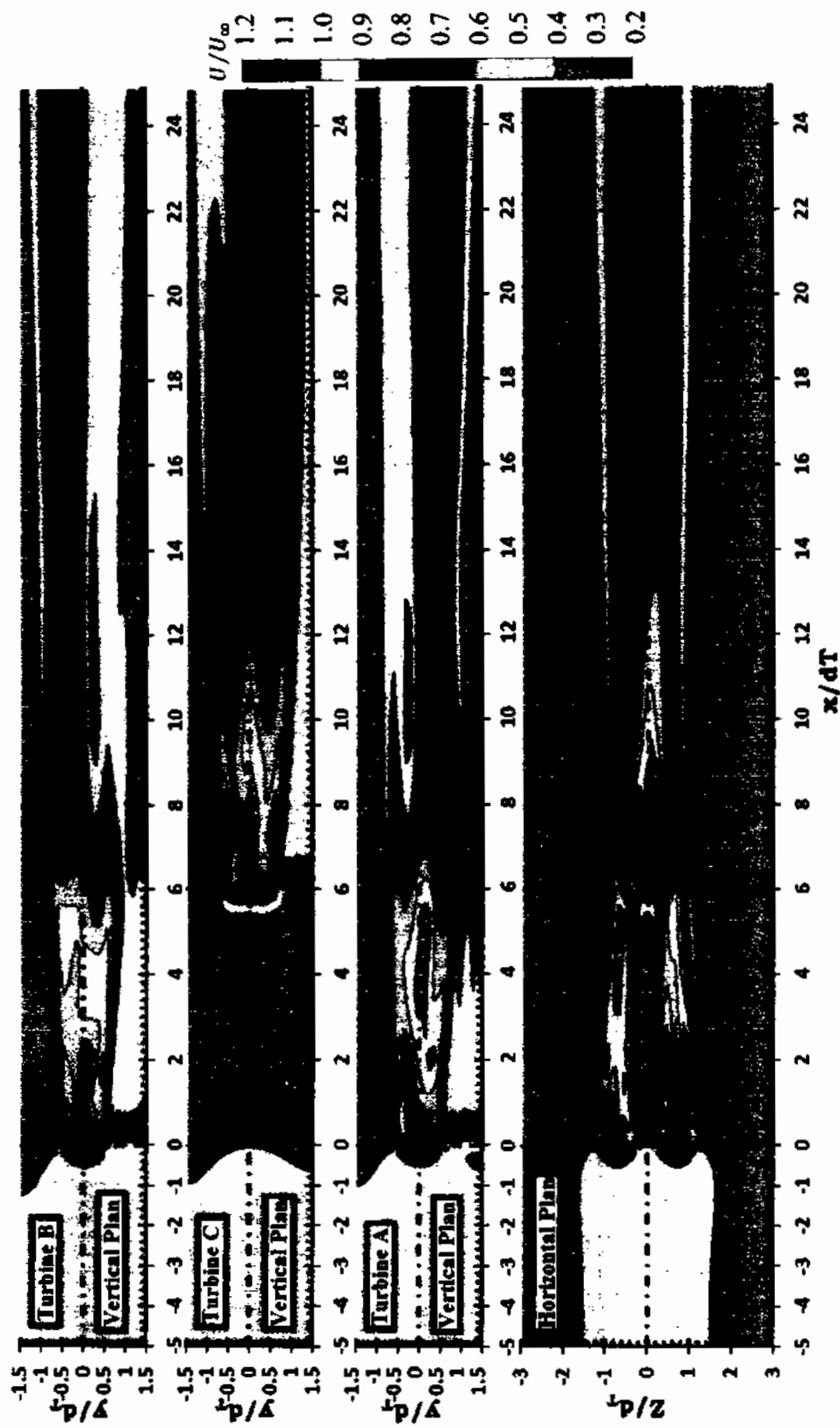


Figure 6.28 Normalized velocity contours for SA-3T-S1.5D-L6D array on vertical planes along the center line of each turbine and horizontal plan at mid depth

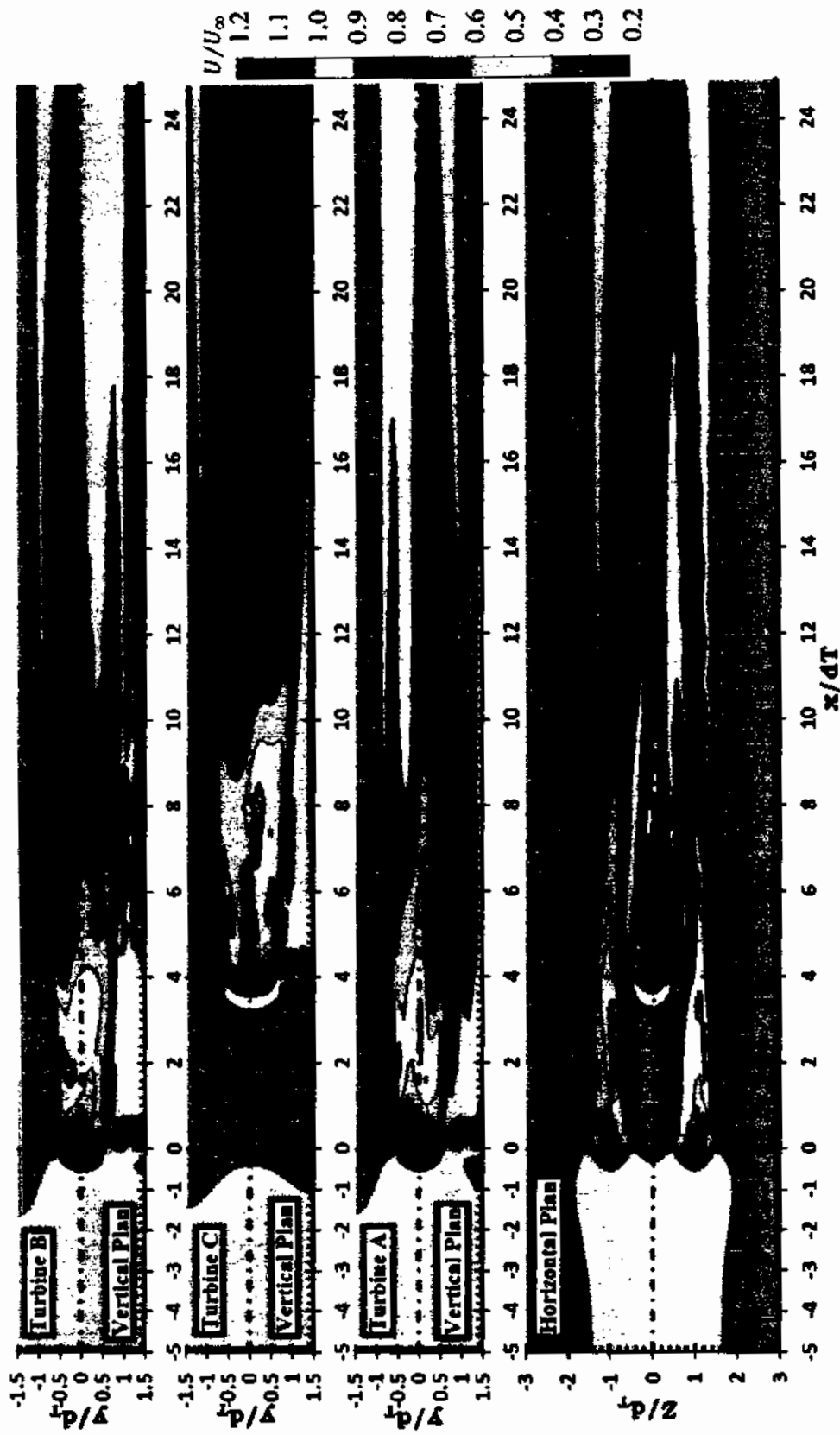


Figure 6.29 Normalized velocity contours for SA-3T-S2D-L4D array on vertical planes along the center line of each turbine and horizontal plan at mid depth

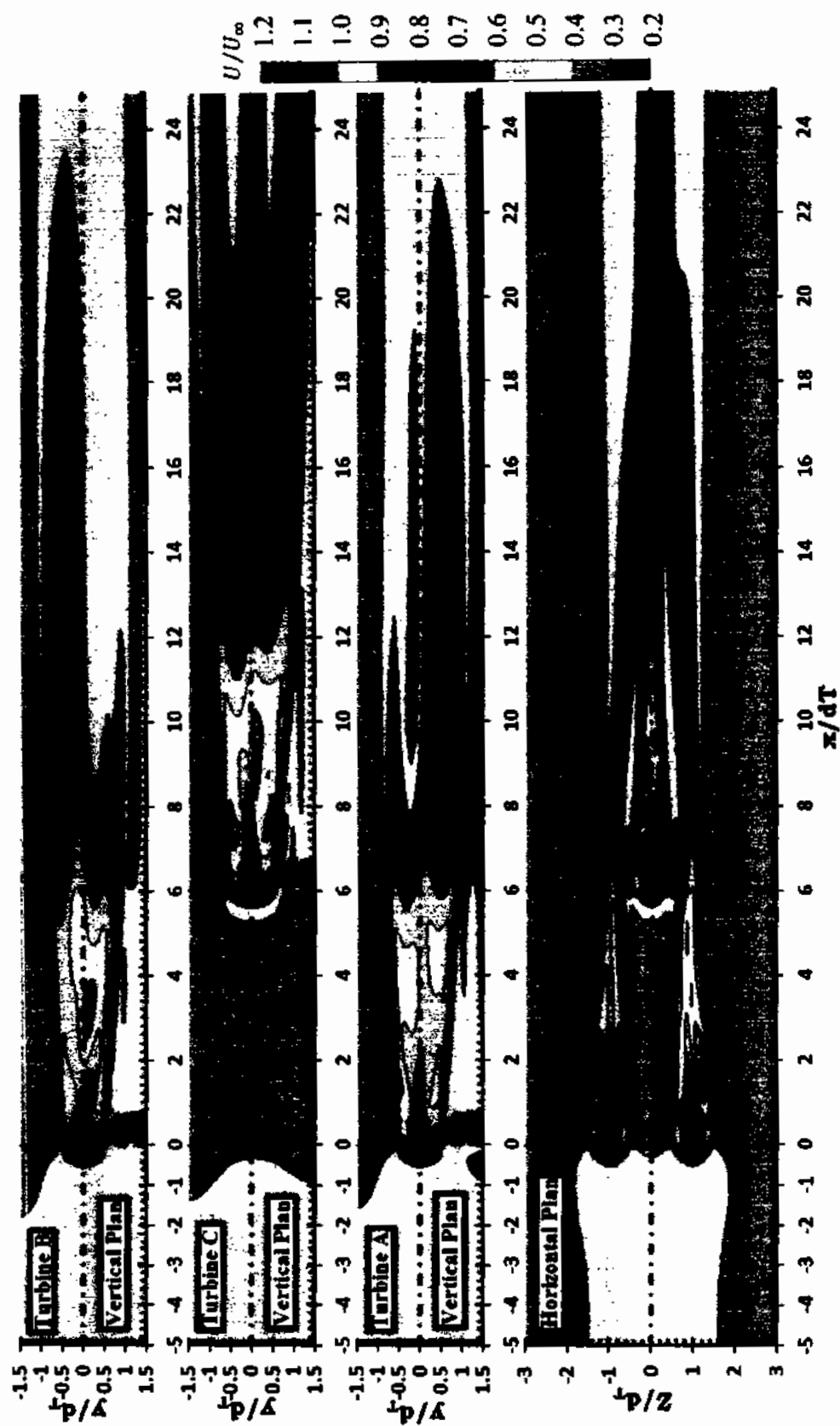


Figure 6.30 Normalized velocity contours for S4-3T-S2D-L6D array on vertical planes along the center line of each turbine and horizontal plan at mid depth

The cutouts of velocity contours from the transverse plan (Figure 6.31) shows that the direction of rotational flow is counter clock wise as seen from the front for all the turbines. The interaction of turbine C with the wake of 1st row turbines is stronger for the two staggered array configurations having the third device longitudinally spaced at 4D. Looking into the transverse contours it can be anticipated that for counter rotating turbines in the 1st row, the flow through the gap between devices would be more uniform and probably more energetic and the wake merging would be smoother.

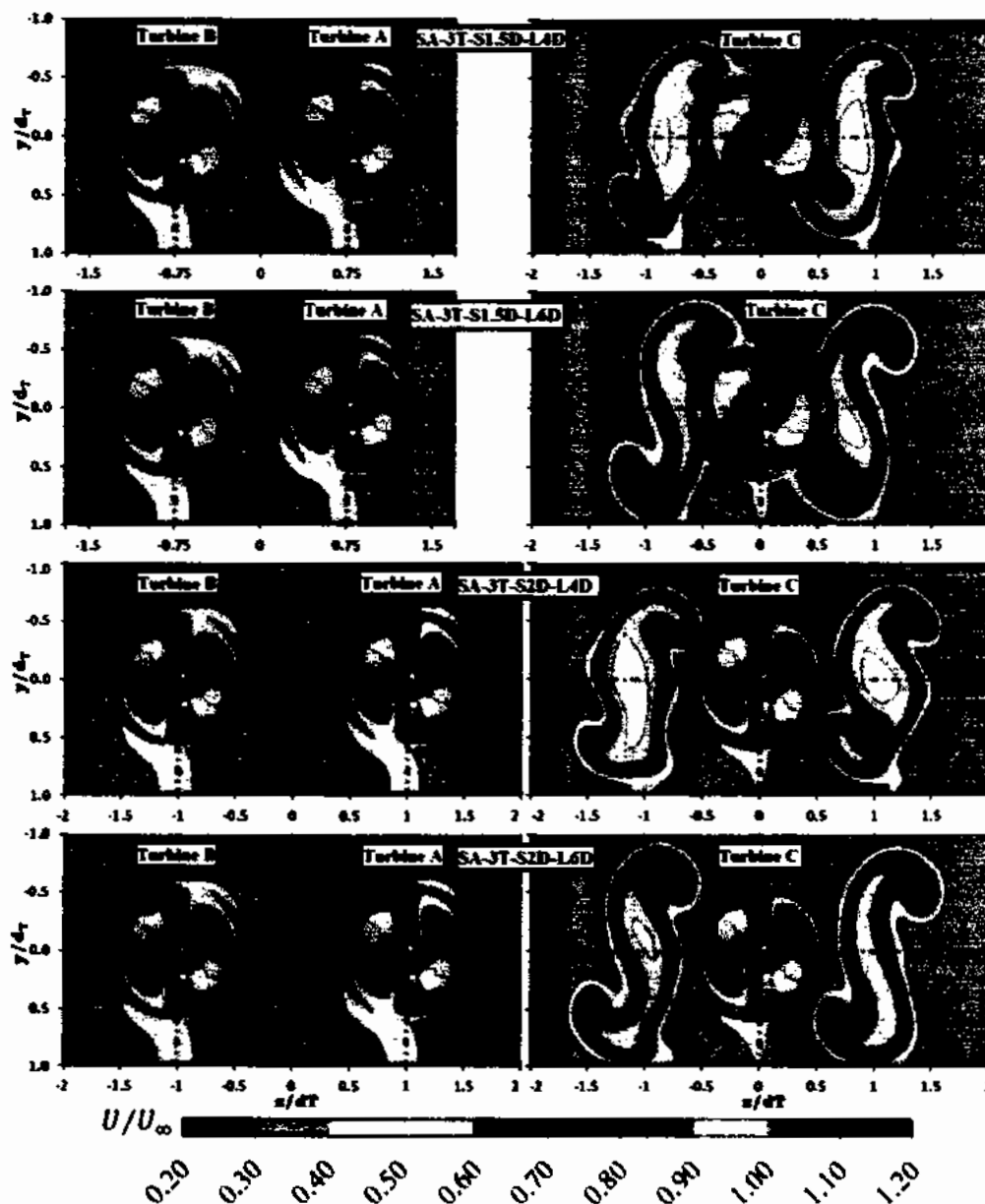
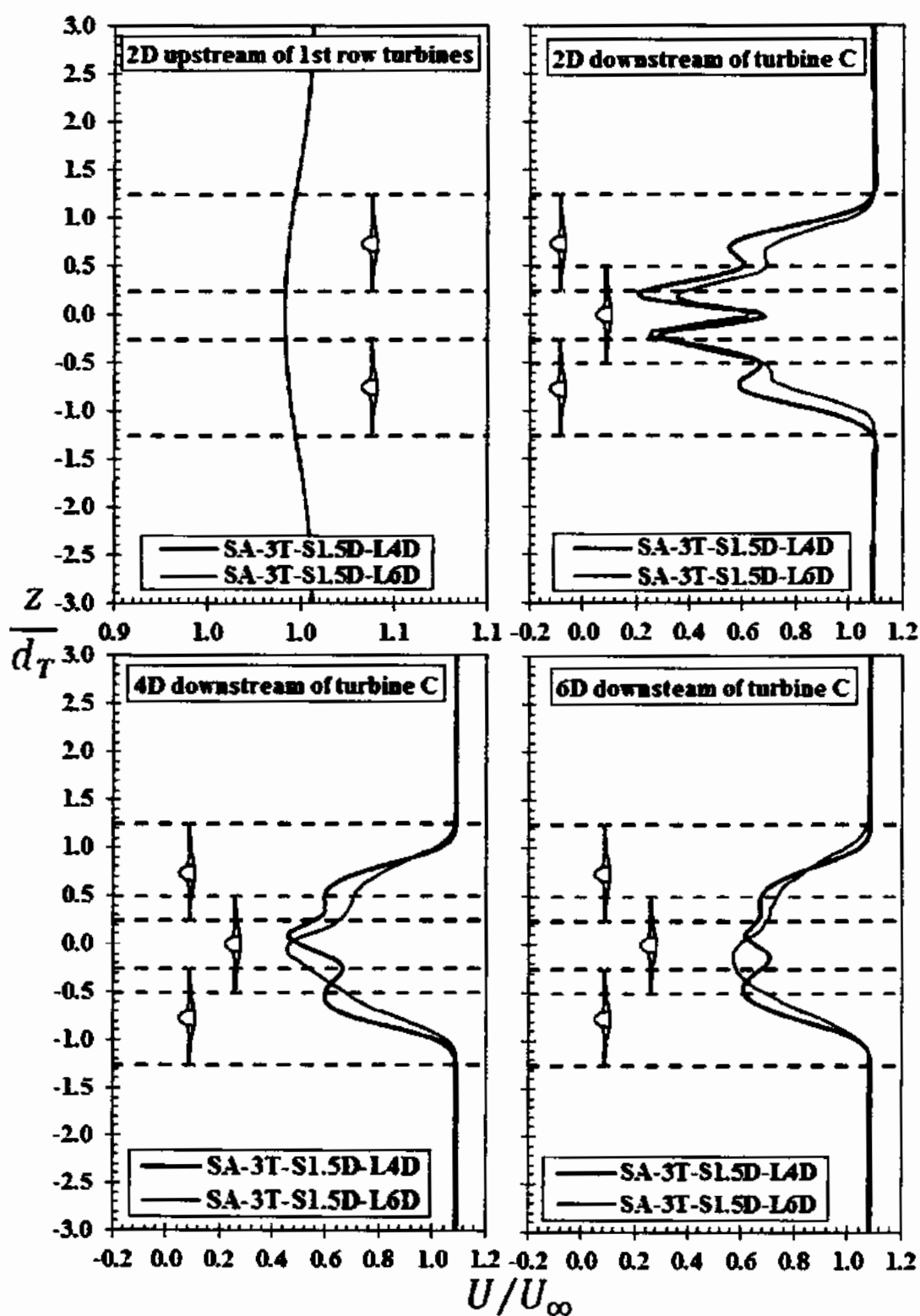


Figure 6.31 Normalized velocity contours for three turbine staggered arrays on cut outs of transverse plan immediately behind each turbine

The normalized velocity profiles in the transverse direction up and downstream of the devices in the two staggered arrays with 1st row devices laterally spaced at 1.5D is given in Figure 6.32 to further illustrate the behavior of flow.



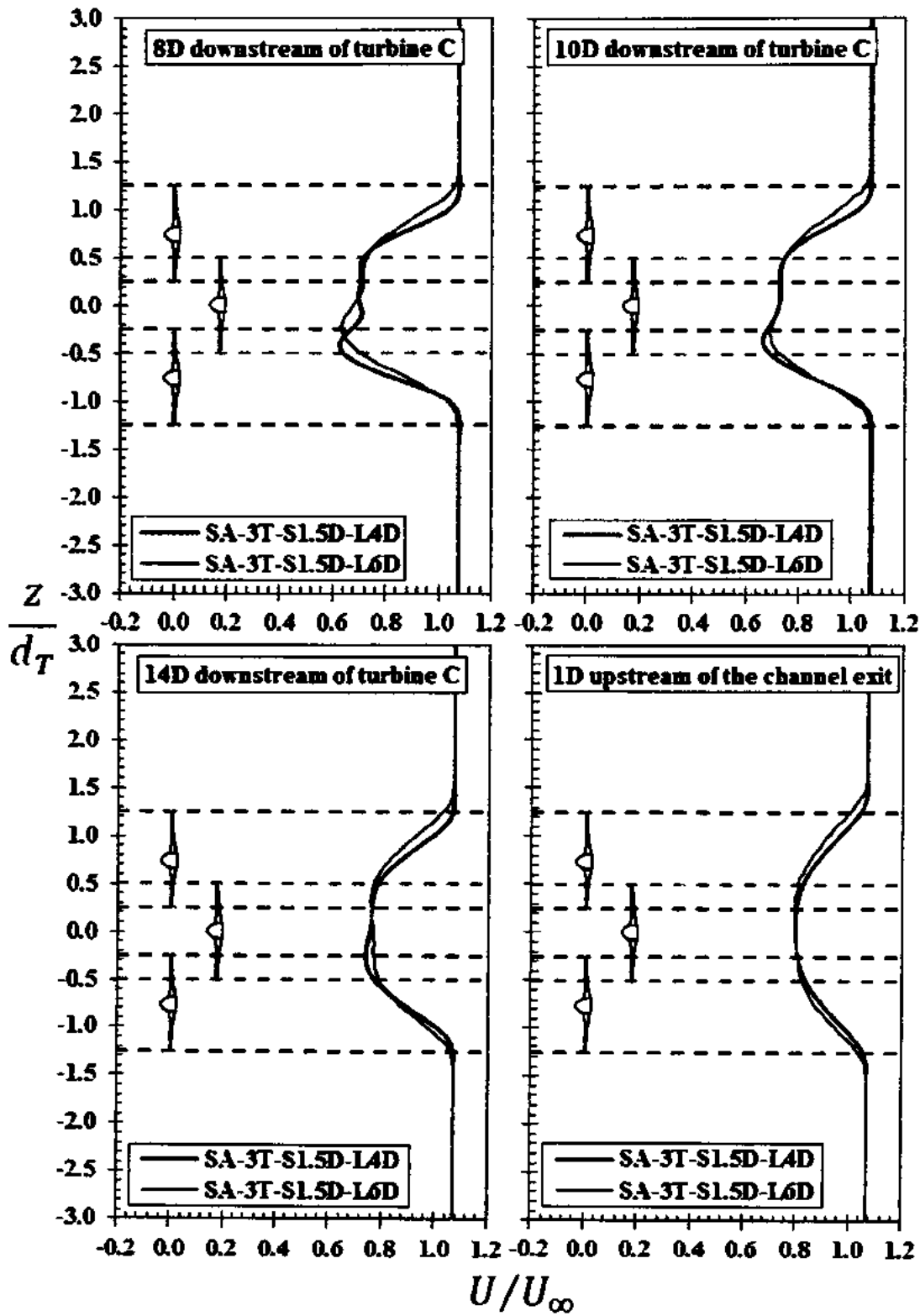
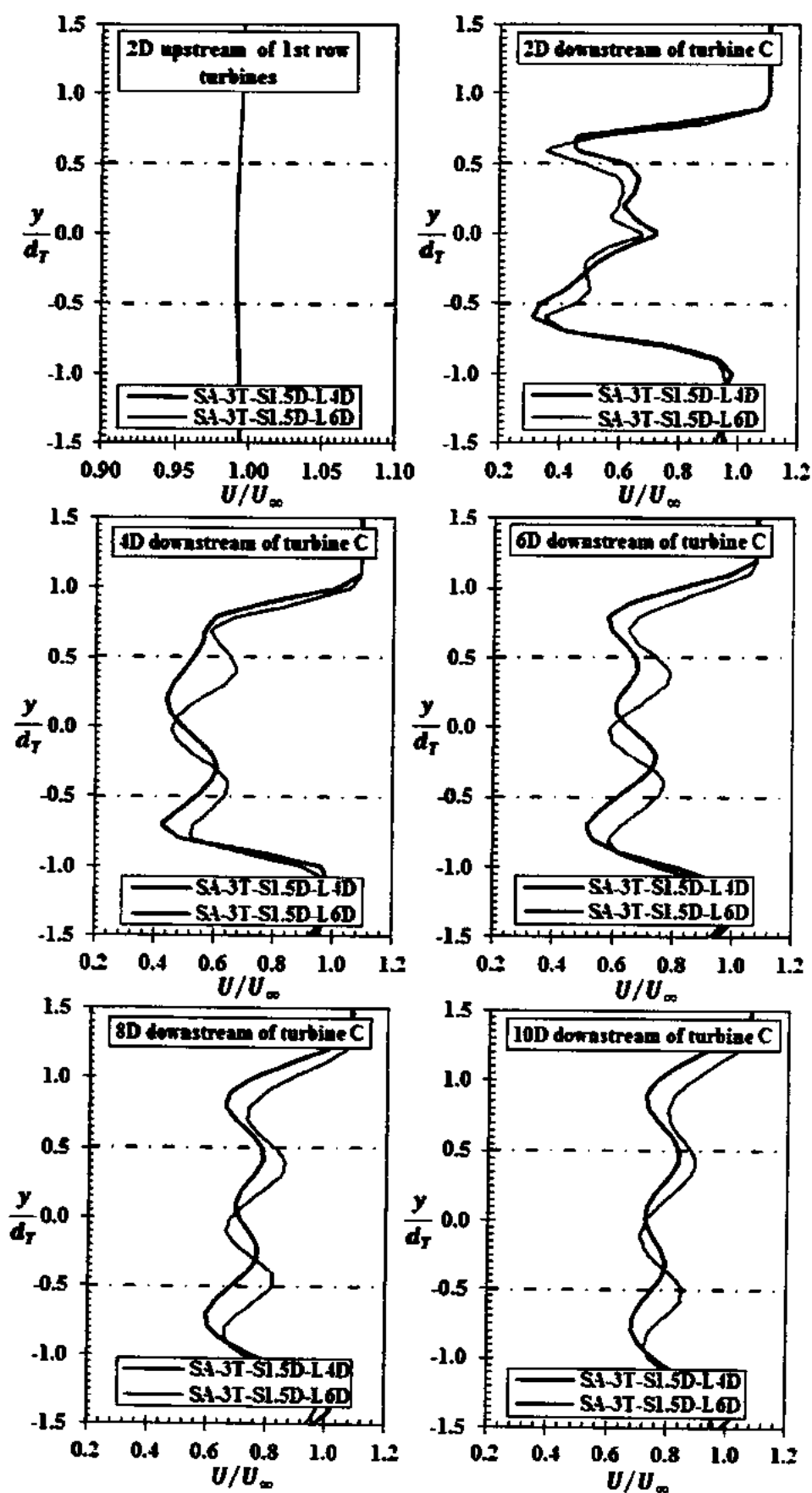


Figure 6.32 Transverse profiles of normalized velocity for the three turbine S1.5D staggered arrays (black dashed lines represent the span of 1st row turbines blades and the red dashed lines the span of downstream turbine C blades)

The upstream velocity for both the cases of turbine C placed at 4D and 6D is similar. At 2D downstream of turbine C the velocity outside the wake zone in the bypass regions is about 9-10% greater than the undisturbed free stream velocity for both the cases. However, the velocity in the bypass region for the case of turbine C placed at 4D is about 1% greater than when turbine C is placed at 6D. The velocity gradually decreases as we move from the sides of the channel to the center of the channel. A sharp gradient of velocity increase is observed in the velocity profile where the wake of the 1st row turbine merges with the wake of downstream device. However, shortly the velocity again starts to decrease at the extent of the downstream turbine blades and continue to decrease till the limits of the gap between the upstream turbines. Here the velocity once again starts increasing till the center of the gap. The velocity at the center of the channel is about 65% and 63% of the undisturbed free stream velocity for the cases of turbine C longitudinally spaced at 4D and 6D respectively. Further downstream of turbine C at 4D, the sharp gradient due to the wake merging of the 1st row and downstream devices diminishes for the case of turbine C placed at 6D longitudinal spacing. However, for the case of turbine C placed at 4D the effect of wake merging between the upstream and downstream devices is still visible. Additionally the wake centerline velocity which was greater than the rest of the wake at 2D downstream is now less than the rest of the wake region at 4D downstream. The velocity at the wake centerline at 4D downstream for both the cases of turbine C placed at 4 and 6D longitudinal spacing is about 47-48% of the undisturbed free stream velocity. At 6D downstream the wake has started to attain a uniform shape with no clear distinction for the wake of upstream and downstream devices. Further down at 8D and then 10D the wake attains almost a uniform shape that extend throughout the entire length of the channel till 25D. At 1D upstream of the channel exit the wake flow recovers almost about 80% of the undisturbed free stream velocity for both the array configurations.

The vertical (depth wise) profile of normalized velocity at the mid width of the channel for the staggered arrays with transverse spacing of 1.5D is given in Figure 6.33.



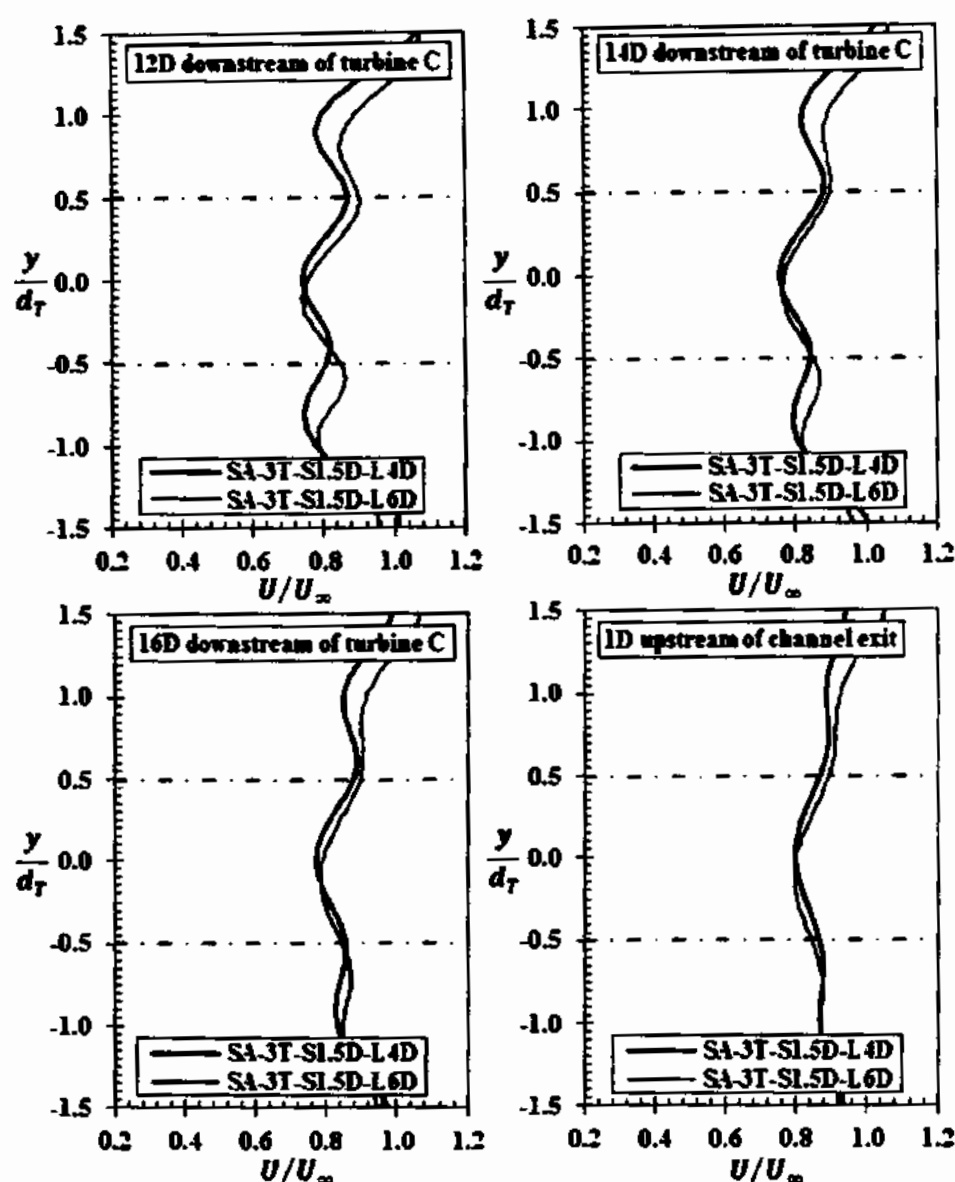
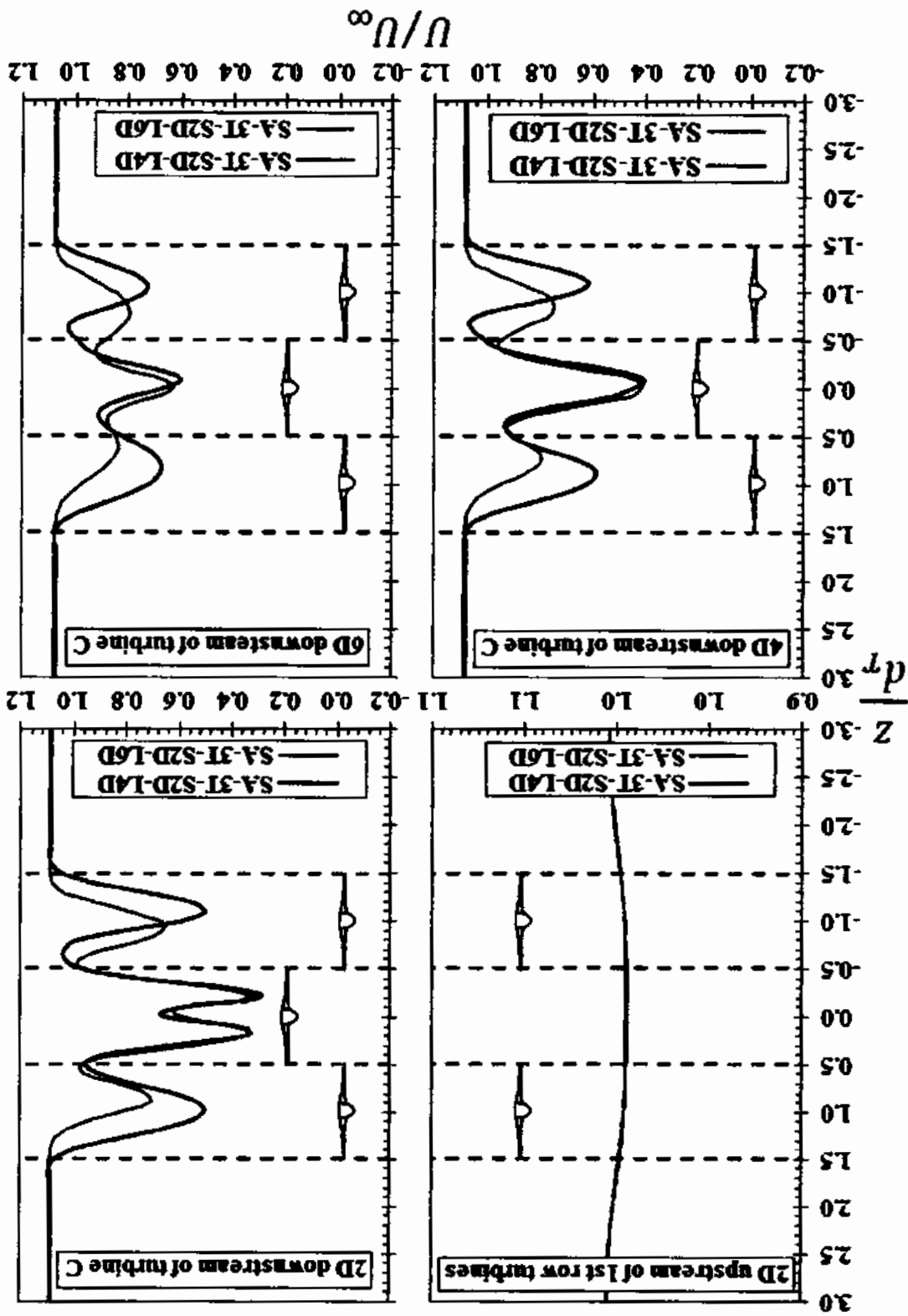


Figure 6.33 Vertical profiles of normalized velocity for the three turbine 1.5D staggered arrays (Red dash dotted lines represent the span of turbine blades)

At 2D downstream of turbine C, the extents of lower and upper by flows is also almost similar (about 0.5D) from the channel boundaries in both the cases. The velocity in the lower by pass region is about 4-6% lower than the undisturbed free stream velocity for both the array configurations. Whereas, the velocity in the upper bypass region is about 10% greater than the undisturbed free stream velocity. The velocity difference in the upper and lower bypass regions indicate that the tower effect in both these cases is significant at 2D downstream of turbine C. The velocity starts gradually decreasing at the extents of bypass regions in almost a linear manner. The wake region of turbine C in the vertical plan extends

upto about $0.6-0.8D$ from the center of the channel on each side. Within the wake region of turbine C the effect of upstream devices is clearly evident and the velocity profile is not uniform. The velocity increases as we move from the edges of the wake region to center of the channel. However, the velocity once again decreases at the central core of the wake that is clearly shifted towards the upper bypass region for both the cases. The velocity within the wake region continuously changes in the vertical direction within the range of 34-72% of the undisturbed free stream velocity. At $4D$ downstream the wake region is expanded showing the mixing of wake flow with the surrounding flow. Additionally, the effect of upstream device on the wake of turbine C has become less pronounced and the vertical velocity profile within the wake region is transforming into a more uniform single device like profile. The wake gradually expands further downstream to cover almost the entire depth of the channel at about $12D$. At $1D$ upstream of the channel exit the velocity along the entire depth of the channel ranges from about 80-94% of the undisturbed free stream velocity.

The transverse profiles for the 2D staggered arrays is shown in Figure 6.34. In this case the wake of each turbine is clearly distinguishable unlike in the 1.5D staggered arrays. Velocity in the upper and lower bypass region 2D downstream of turbine C is about 8-9% greater than the undisturbed free stream velocity. The velocity deficit in the wake behind the 1st row turbines is more for the case of turbine C placed longitudinally at $4D$ compared to $6D$. The velocity at 2D downstream of turbine C along the hub center line of the 1st row turbines is about 50-55% of the undisturbed free stream velocity for the case of turbine C longitudinally placed at $4D$. Whereas, for the case of turbine C longitudinally placed at $6D$ this velocity is about 70-80% of the undisturbed free stream velocity. The velocity profile in the transverse direction within the wake region of turbine C is similar for both the array configurations. However, the velocity at the hub centerline of turbine C is about 67% and 61% of the undisturbed free stream velocity for the case of turbine C placed longitudinally at $4D$ and $6D$ respectively. Two areas of extreme velocity drop are clearly evident within the wake region of turbine C downstream of each blade. These apex of these velocity zones is at $0.2D$ (4m) from the channel centerline towards both the side boundaries. The velocity at the upper apex point is about 33% of the undisturbed free stream velocity and similar for both the array configurations. Whereas, for the lower apex point the velocity is about 28%



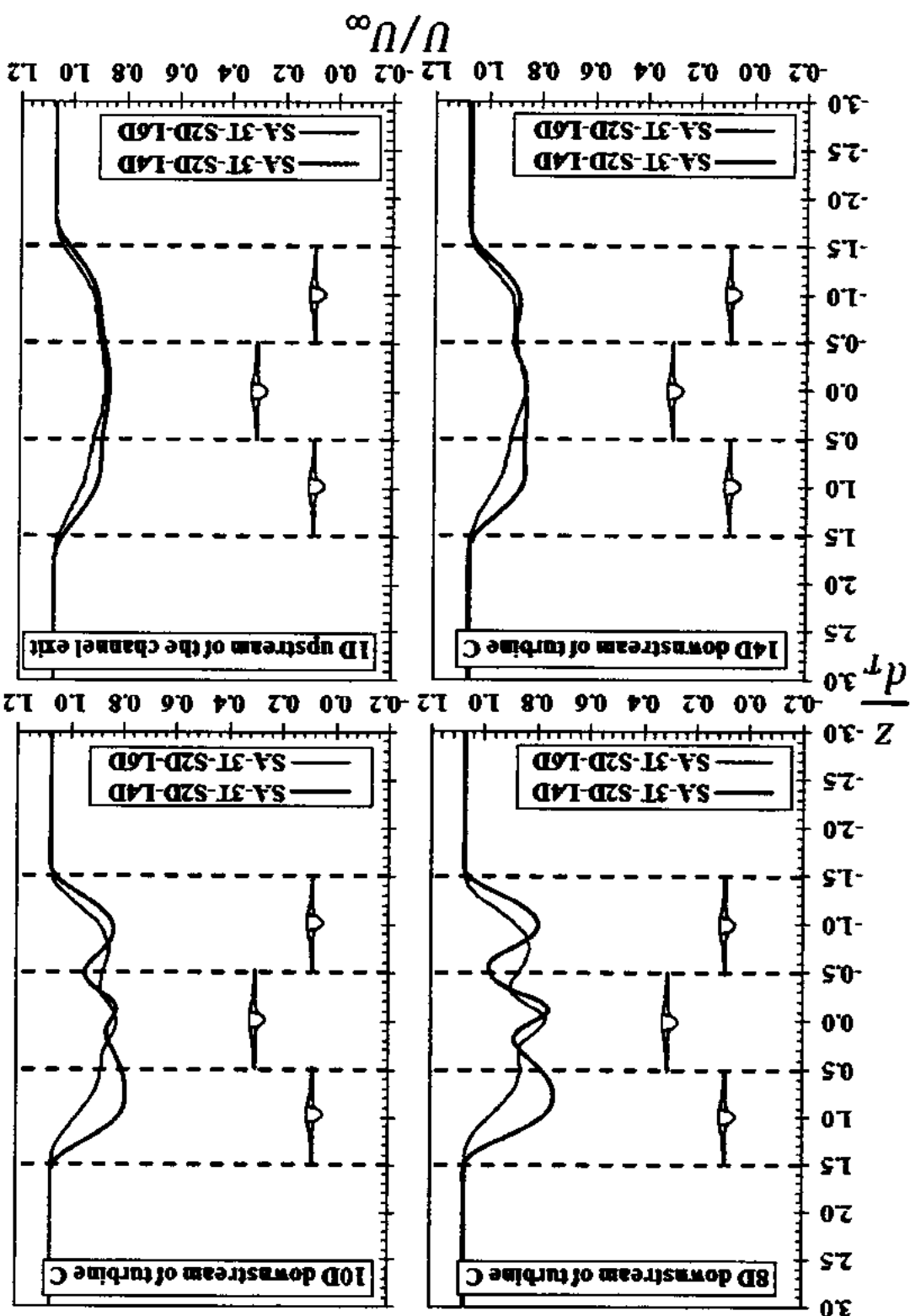
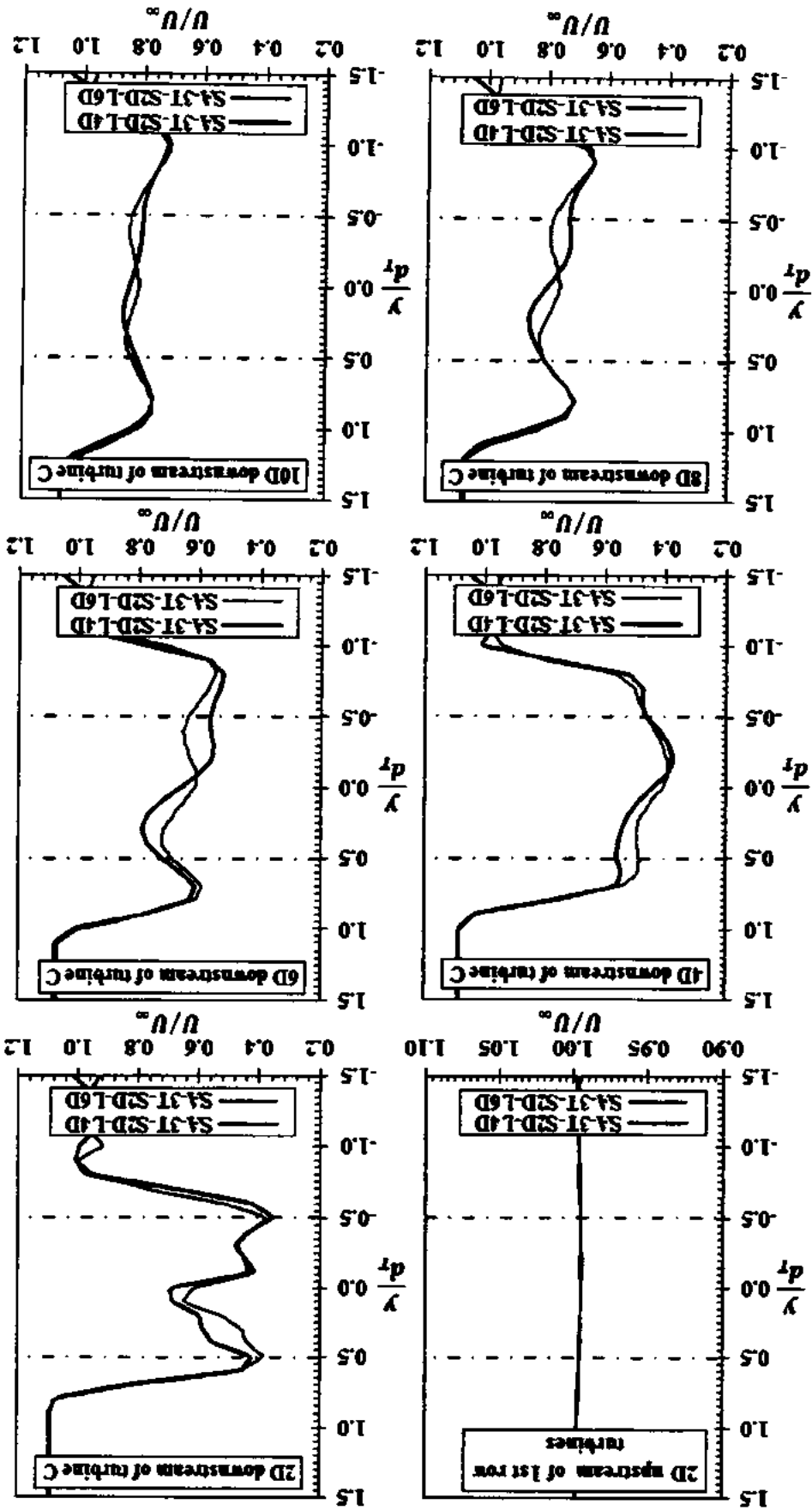


Figure 6.34 Transverse profiles of normalized velocity for the three turbine S1.5D staggered arrays (dashed lines represent the span turbine blades)

and 32% of the undisturbed free stream velocity for the case of turbine C longitudinally placed at 4D and 6D respectively. Further downstream of turbine C at 4D, the velocity profile in the transverse direction within the wake region of turbine C is almost identical. However, the difference between the profiles of the two array configurations with in the wake regions of 1st row turbines is now more prominent. The wakes of individual turbines mixes with each other and surrounding by pass flows along the length of the channel and at 14D the wake of all the array devices merges completely to form a single uniform wake. At 1D upstream of the channel exit the velocity in bypass regions has decreased by about 2% and 1% for the case of turbine C longitudinally placed at 4D and 6D respectively due to the wake mixing. It is therefore established that the wake mixing between the devices is more significant compared to the wake mixing with the surrounding flow. It is quite understandable because the flow turbulence in the wake regions is more and known to enhance the wake mixing compared to the surrounding flow. At 1D upstream of the channel exit the velocity recovery at the channel centerline is about 87-88% for both the 2D staggered array configurations.

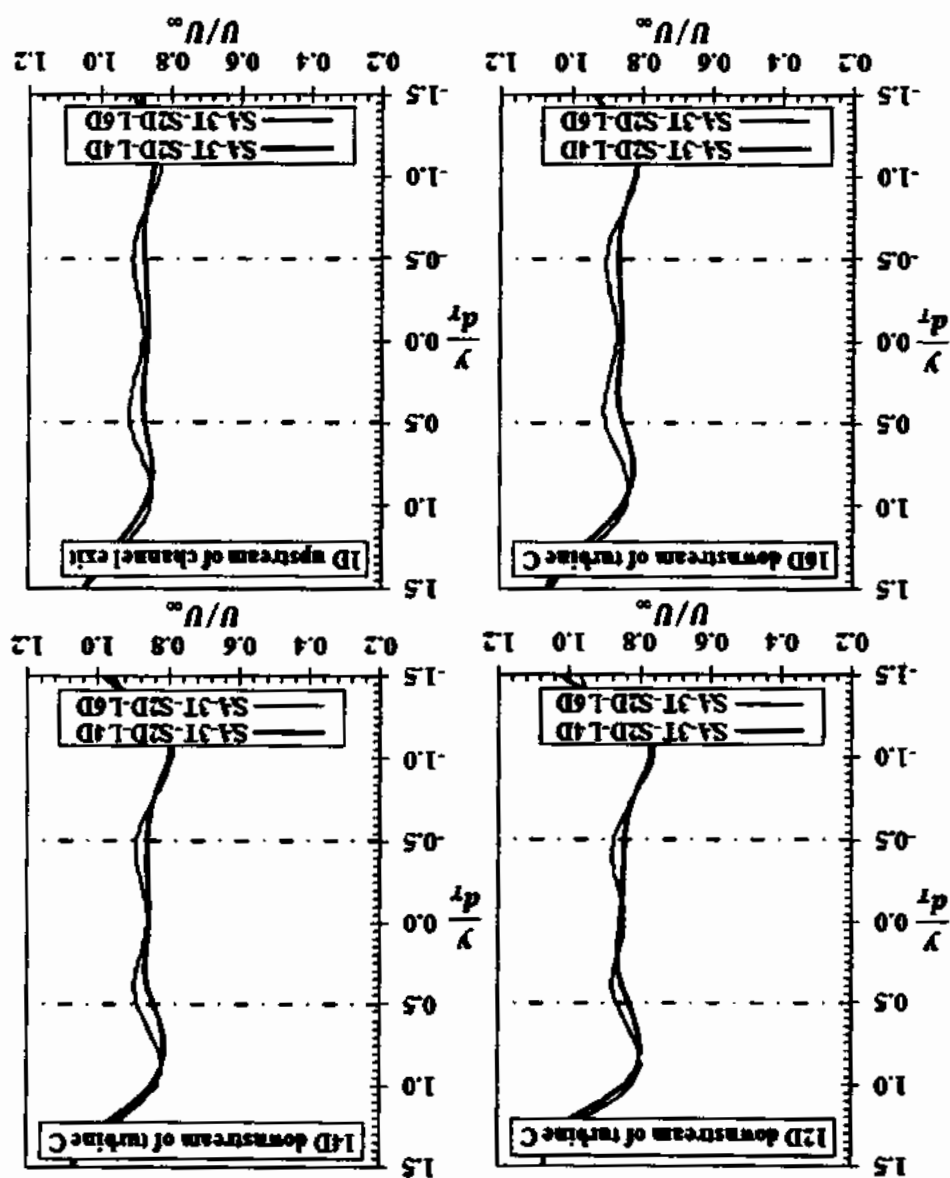
The velocity profiles along the depth of the channel at mid width for the 2D staggered array configurations is given in Figure 6.35. The flow behavior in the vertical direction at mid width is essentially similar to that already explained in Figure 6.33 for the 1.5D staggered arrays. This discussion is not provided here to avoid repetition.



The definition of blade loads for tidal current turbine in this thesis is shown in Figure 6.36.

6.2.2.3 Structural loads on turbine blades

Figure 6.35 Vertical profiles of normalized velocity for the three turbine 2D staggered arrays (Red dash dotted lines represent the span of turbine blades)

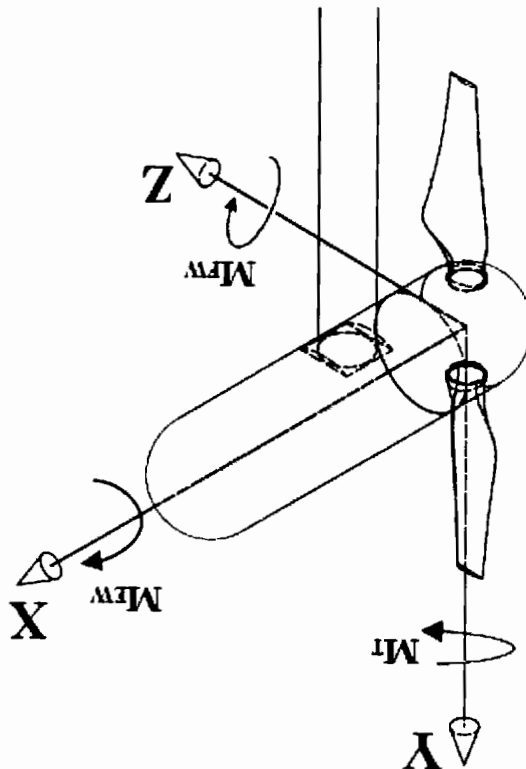


where, M is the bending moment, C_M the bending moment co-efficient either flap-wise $C_{M,FW}$ or edge-wise $C_{M,EW}$ or torsional $C_{M,T}$ and R is the blade tip radius.

$$M = \frac{1}{2} \rho A U_\infty^2 R C_M \quad (6.1)$$

Three type of moment loads are the flap-wise bending moment (M_{FW}), edge-wise bending moment (M_{EW}) and torsional bending moment (M_T). The flap-wise bending moment load is caused by thrust force acting in the direction of flow. This is the most critical load component and most likely to cause structural failures of turbine blades [48, 49]. The edge-wise bending moment load acts along the blade chord line and causes the blade to rotate along shaft axis. The torsional bending moment causes the blade to pitch around the blade root to hub junction. The flap-wise and edge-wise bending moments are the two significant structural load components for a tidal current turbine blade due to their ability to cause structural failures. Whereas, the torsional bending moment is not much critical as a blade structural load component and therefore would not be analyzed in this thesis. The mathematical expression for blade bending moment is as in equation (6.1).

Figure 6.36 Definition of blade loads for tidal current turbine



In the CFD simulations, the moments are calculated by the projection of net force moment about a reference point onto a unit vector along the respective axis as in equation (6.2).

$$M_{axis} = e_{axis} \cdot \sum (r - r_{ref}) \wedge F \quad (6.2)$$

where, e_{axis} represent the relevant axis, r_{ref} the reference point and F the net surface force on a blade surface cell face and the summation is over surface cell faces at a greater radius than the reference point. For the net force the ANSYS CFX solver computes the pressure and viscous components of forces on blades specified as walls boundaries as shown in

Figure 6.37.

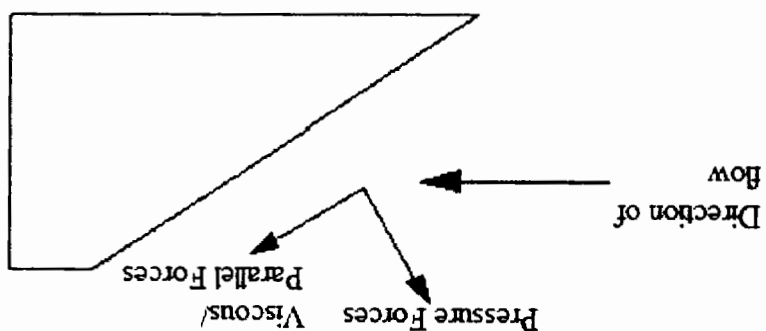


Figure 6.37 Pressure and viscous forces on wall boundaries in ANSYS CFX

The viscous forces are parallel and the pressure forces are normal to the wall surface. The net force in equation (6.2) includes both the pressure and viscous force components. The axis system for turbines in array is as shown in Figure 6.36. The bending moments results are computed at the respective axis system for each turbine constructed such that axis system and its location relative to the respective turbine is similar for all the array devices.

6.2.2.4 Variation of structural loads on turbine blades in co-axial turbine arrays

The time histories of moment load coefficients and moment load normalized with respect to cycle mean during a single turbine rotation for the blade of upstream turbine A operating in the co-axial array configuration is shown in Figure 6.38.

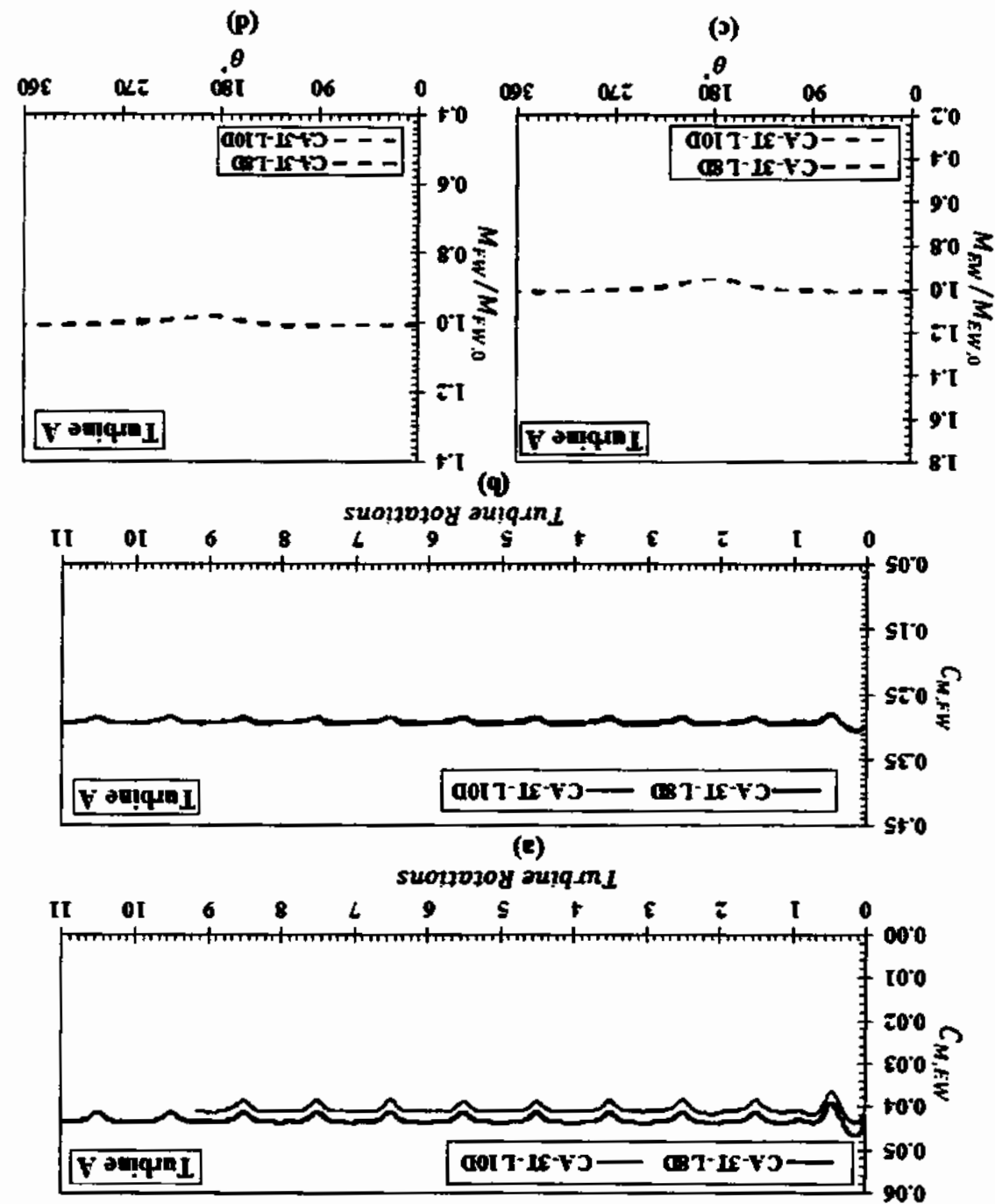


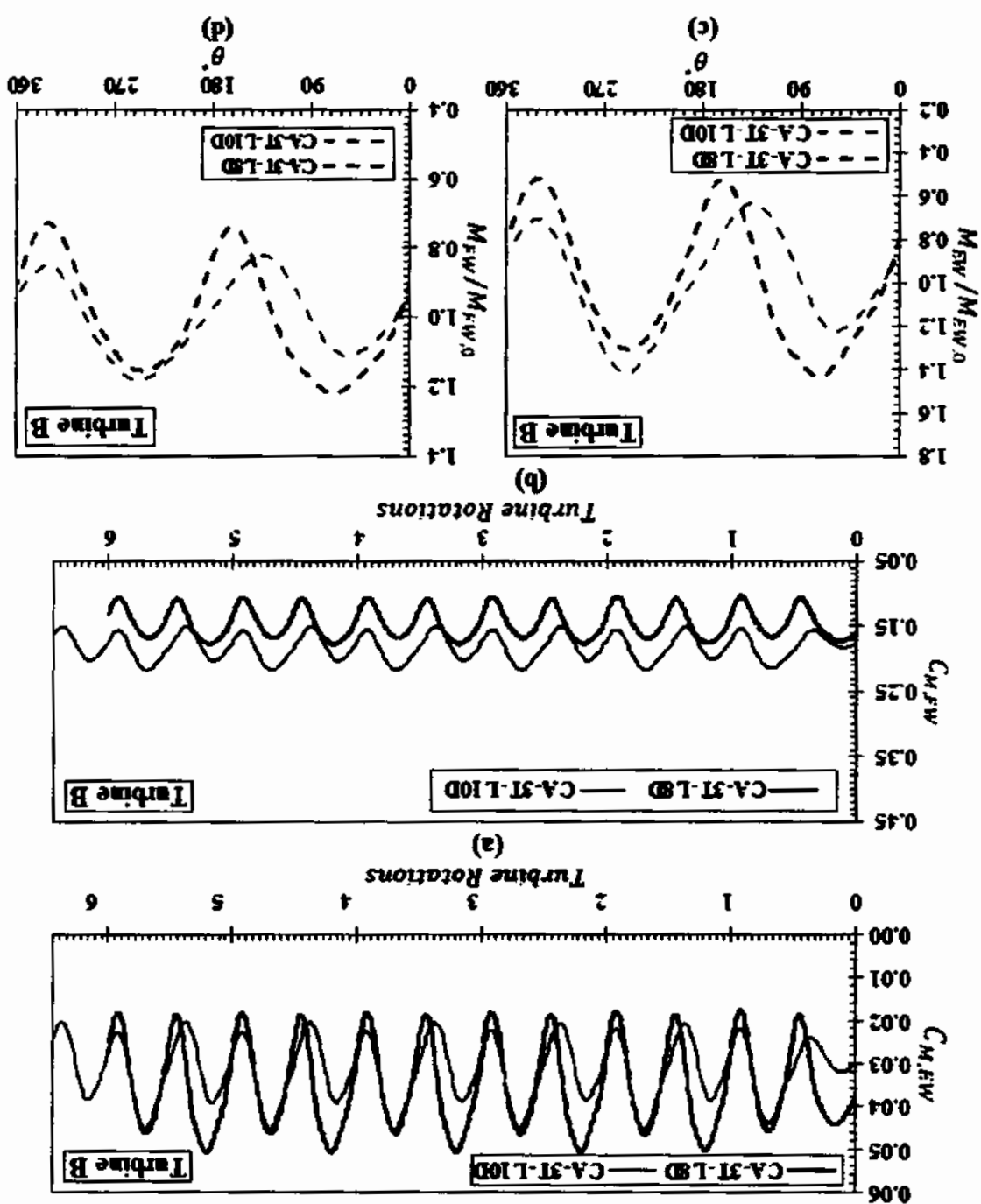
Figure 6.38 Moment loads on the blade of turbine A operating in co-axial array. Time history of moment loads (a) edge-wise (b) flap-wise and moment load normalized with respect to cycle mean during a single turbine rotation (c) edge-wise (d) flap-wise

Figure 6.38 shows that the behavior of edge-wise and flap-wise moment loads for turbine A is similar in essence although their magnitudes are quite different. The time series of moment load coefficients for the upstream turbine A are very similar to that of a standalone turbine reported in Yahagi et al. [157]. The moment loads time series for turbine A shows

obvious troughs due to passing of the turbine blade in front of tower once during each turbine rotation. The drop in moment loads is for a short span and the curve quickly recovers to almost a flat shape for most part of the turbine rotation. For the upstream turbine A, it is clearly evident that moment loads are almost similar for both co-axial arrays. The variation in a single turbine rotation is minimal with a single drop in one rotation near $(\theta = 180^\circ)$ representing the effect of tower shadow. This observation is very similar to that reported for a standalone turbine by Ahmed et al. [47]. The moment loads time series curve for the 1st downstream device turbine B (Figure 6.39) is entirely different due to the effect of upstream turbine operation.

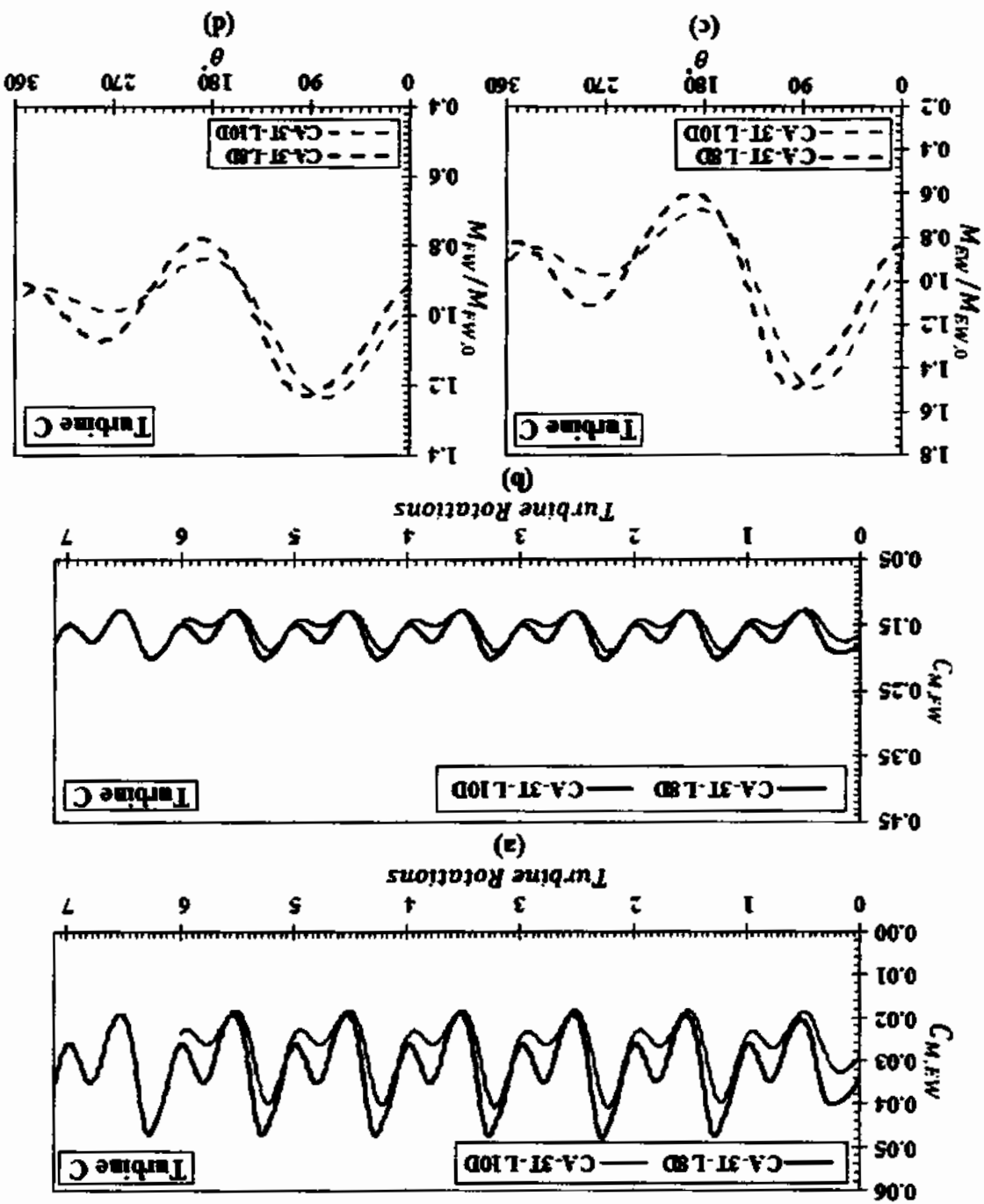
The time series of moment loads exhibit almost a sinusoidal behavior with two peaks and troughs during one turbine rotation. The drop in moment loads is also exaggerated and the frequency of variation is twice that of turbine A. The drop in moment loads does not occur exactly at the position ($\theta = 180^\circ$) and there is a lag which is similar to the findings of

Figure 6.39 Moment loads on the blade of turbine B operating in co-axial array. Time history of moment loads (a) edge-wise (b) flap-wise and moment load normalized with respect to cycle mean during a single turbine rotation (c) edge-wise (d) flap-wise



other CFD studies Mason-Jones et al. [79], Badshah et al. [159] and from the experimental test of full scale turbine Ahmed et al. [47]. The pairs of peaks during a single rotation are not similar and one of the two consecutive peaks is slightly higher than the other one. Unlike turbine A, the moment loads are changing significantly at each degree of rotation and the flat portion of curve has disappeared. The slope of turbine B moment loads curve is steeper for the 8D spaced array compared to the case of 10D spaced configuration. This time series also indicates that for the 10D spaced array the effect of upstream device on moment loads of downstream device is comparatively less prominent. Additionally, the edge-wise moment load for turbine B is greater for the case of 8D spaced array compared to the case of 10D spacing. Contrarily, the flap-wise moment load is more in the case of turbine B placed at 10D compared to the 8D spaced array. The behavior of moment loads time series curve for turbine C (Figure 6.40) is similar in essence to turbine B. However, the difference between the higher and lower peak is further exaggerated and it seems that the lower peak is diminishing to return the curve to its shape like that in the case of turbine A. From this time series it can be suggested that a part of the load fluctuations originated due to the operation of turbine A are suppressed by the operation of turbine B before reaching turbine C. This behavior is somewhat similar to the case of increasing wake mixing as the flow passes through more and more devices. This is an encouraging sign for multi device co-axial arrays to suggest that the effect on load fluctuations due to the imprints of upstream turbine operation will diminish as the flow passes through more and more devices. However, to further ascertain this conclusion, multi device co-axial arrays with relatively larger number of devices may be investigated. The difference between load variation for 8D and 10D spaced arrays decreases in the case of turbine C. However, for turbine B and C it is clearly evident that the effect of load fluctuations is more in the case of 8D spacing compared to 10D spacing to suggest the obvious that increasing the interdevice longitudinal spacing in co-axial array would also reduce the effect of upstream turbine on the load fluctuation of downstream devices.

Figure 6.40 Moment loads on the blade of turbine C operating in co-axial array. Time history of moment loads (a) edge-wise (b) flap-wise and moment normalized with respect to cycle mean during a single turbine rotation (c) edge-wise (d) flap-wise



To further quantify the effect of upstream turbine operation on the load variation of downstream turbine blades the loads variation statistics for all devices in both co-axial array configurations is given in Table 6.9.

Table 6.9 Load variation statistics for the blade of turbines operating in co-axial arrays

Moment Load	Turbine A		Turbine B		Turbine C		
	CA-3T-L8D	CA-3T-L10D	CA-3T-L8D	CA-3T-L10D	CA-3T-L8D	CA-3T-L10D	
Flap-wise Moment Load Coefficient ($C_{M,FW}$)	Mean	0.291	0.293	0.145	0.183	0.164	0.153
	Peak	0.292	0.296	0.177	0.217	0.202	0.189
	Range	0.008	0.008	0.071	0.067	0.074	0.061
	% Variation	3	3	49	36	45	40
Edge-wise Moment Load Coefficient ($C_{M,EW}$)	Mean	0.043	0.040	0.035	0.032	0.032	0.027
	Peak	0.044	0.041	0.051	0.046	0.047	0.040
	Range	0.002	0.003	0.032	0.025	0.028	0.022
	% Variation	6	7	91	78	89	82

The variation over mean cycle value for flap-wise moment load on the blade of turbine A is about 3% for both co-axial array configurations. For the 1st downstream turbine (turbine B) the variation from mean cycle value in flap-wise moment loads increases to about 49 and 36% for the case of turbine B placed at 8D and 10D respectively. Compared to the upstream turbine A, the mean of flap-wise moment load coefficient for the blade of turbine B has decreased from 0.29 to 0.145 and 0.183 for the case of 8D and 10D spaced co-axial arrays respectively. Contrarily, the range has increased by an order of magnitude from 0.008 to 0.071 and 0.067 for the case of 8D and 10D spaced co-axial arrays respectively. The range calculated as the difference between the peak and minimum value during a single rotation cycle is a key parameter for the prediction of fatigue loads on tidal turbine blade [160]. Similarly, the mean cycle value of moment loads on the turbine blade is another key parameter that would significantly influence the fatigue life. The fatigue life of turbine blade would decrease with increase in the mean stress and or stress range and vice versa. This quantitative comparison along with change in behavior of flap-wise moment loads already depicted in Figure 6.39 indicate that blades of the 1st downstream device (turbine B) are more susceptible to fatigue failure compared to the upstream device and this change is solely due to the operation of upstream turbine. Additionally, the flap-wise moment loads on the blades also vary with changing the inter device spacing between the upstream and downstream device. The mean of flap-wise moment load on the blade increases from 0.145 to 0.183, the range decreases from 0.071 to 0.067 and the percentage variation decreasing from 49 to 36% in the case of turbine B placed at 8D compared to the case of 10D. These statistics suggest that load variations for turbine B at 10D spacing are comparatively less pronounced compared to the case of 8D placement. Although, these differences are marginal except the percentage variation but still gives an indication that the effect of upstream device on the load variation of downstream device would increase with decreasing interdevice spacing between the upstream and downstream device. For turbine C in the case of 8D array, the flap-wise moment load variation statistics does not vary significantly compared to turbine B with variation decreasing from 49 to 45%, the mean increases from 0.145 to 0.164 and the range increases from 0.071 to 0.074. Again these changes in variation statistics between turbine B and C for the case of 8D spaced co-axial array are marginal. For turbine C in the 10D spaced co-axial array the mean and range of

flap-wise moment load decreases, the percentage variation marginally increases compared to turbine B of the same array. The turbine C for the case of 10D spaced array very clearly indicate that it is placed in a much better location compared to turbine B of the same array as well as turbine C of the 8D spaced array in terms of blade load fluctuations and fatigue life. The flap-wise moment load variation statistics for both co-axial arrays suggest that blades of the 1st downstream turbine (turbine B) would be more susceptible to load fluctuations and fatigue failure compared to the 2nd downstream device (turbine C). It would however be very interesting to investigate the imprints of upstream turbine operation for the load fluctuations on downstream turbine blade further downstream by adding more turbines to the co-axial arrays investigated in this thesis.

Table 6.9 shows that the edge-wise moment load variation from mean cycle value during a single rotation on the blade of upstream turbine (turbine A) is almost similar for both the co-axial arrays with values of about 6-7%. The variation over mean cycle value in blade edge-wise moment load is almost twice that of the flap-wise moment load which is similar to the observation of Blackmore et al. [63] in the experimental trials of a standalone turbine. For the 1st downstream device (turbine B), the mean value of edge-wise moment load during a single rotation decreases to 0.035. However, the range and variation increases to 0.032 and 91% respectively for the case of 8D spaced array. Similarly, for the case of 10D spaced array, the mean edge-wise moment load for this turbine is 0.032 with a range of 0.025 and variation of 78%. These variation statistics suggest that just like the flap-wise moment loads, turbine B is clearly more vulnerable to blade load variations and fatigue failure due to edge-wise moment loads compared to turbine A for both the co-axial arrays. Additionally, these statistics very clearly indicate that for the case 8D spaced array the blades of turbine B will experience more load fluctuations and would be more susceptible to fatigue failure compared to the case of 10D spaced array. The variation in edge-wise moment loads from mean cycle value is not only significant from the perspective of load variations and life fatigue on turbine blades but also significant from the perspective of quality of power output. The FSI simulations of Badshah et al. [159] suggest that the fluctuations in total turbine power output during a single rotation would be half the variation in edge-wise bending moment of a single blade. These results suggest that the placement location of turbine B for both the evaluated co-axial array cases in not only

vulnerable to excessive load fluctuations and chances of fatigue failure but also severe power fluctuations. Blades of the downstream turbine (turbine B) are severely affected by the operation of upstream turbine in terms of load fluctuations and fatigue failure and these adverse effects would decrease with increasing inter device spacing between the upstream and downstream devices operating in co-axial arrays. For turbine C the range and variation of edge-wise moment loads during a single rotation are lower than turbine B for the case of 8D spaced array indicating that the 2nd downstream device (turbine C) operating under the combined effect of two upstream devices is comparatively less affected in terms of blade load variations. This finding suggest that the effect of operation of upstream device on the load fluctuations of downstream turbine blades would not increase with increasing number of devices operating in the upstream. The current study suggest that these effect may successively reduce further downstream with additional devices operating in the upstream. However, to ascertain this conclusion further investigations would be required with co-axial arrays consisting of more than three devices. Additionally, for the case of 10D spaced array, the mean, range and variation of edge-wise moment loads on the blade of turbine C are lower than the 8D spaced array to suggest that increasing interdevice spacing between the 2nd and 3rd downstream device would be beneficial for the reduction of blade load variations and associated chances of fatigue failure.

6.2.2.5 Variation of structural loads on turbine blades in staggered turbine arrays

The time histories of moment load coefficients and moment load normalized with respect to cycle mean during a single turbine rotation for the blade of 1st row upstream devices (Turbine A and B) in the staggered array with 1.5D transverse spacing is shown in Figures 6.41-6.42.

Figure 6.41 Moment loads on the blade of turbine A operating in staggered array with transverse spacing of 1.5D. Time history of moment loads (a) edge-wise (b) flap-wise and moment load normalized with respect to cycle mean during a single turbine rotation (c) edge-wise (d) flap-wise

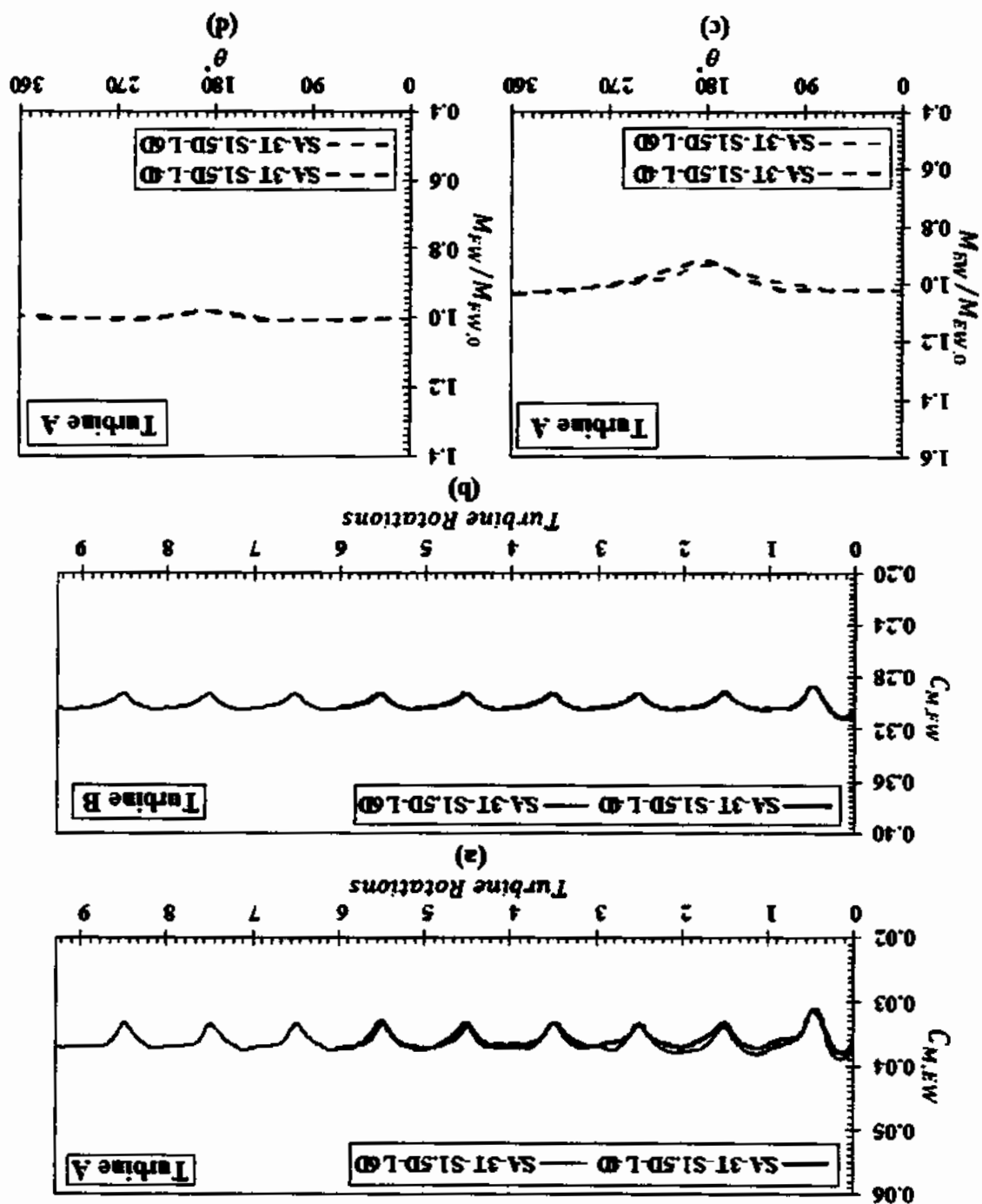
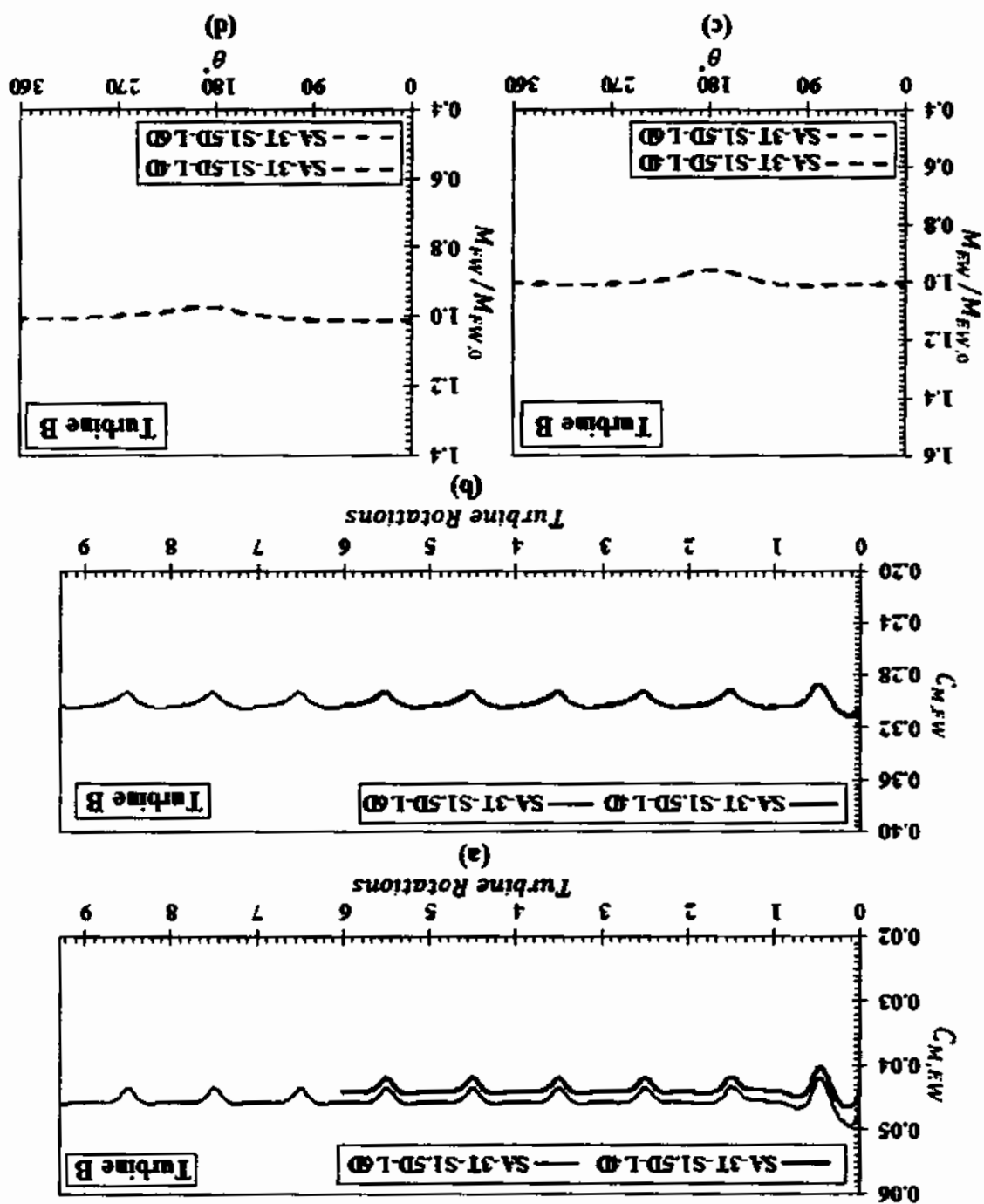


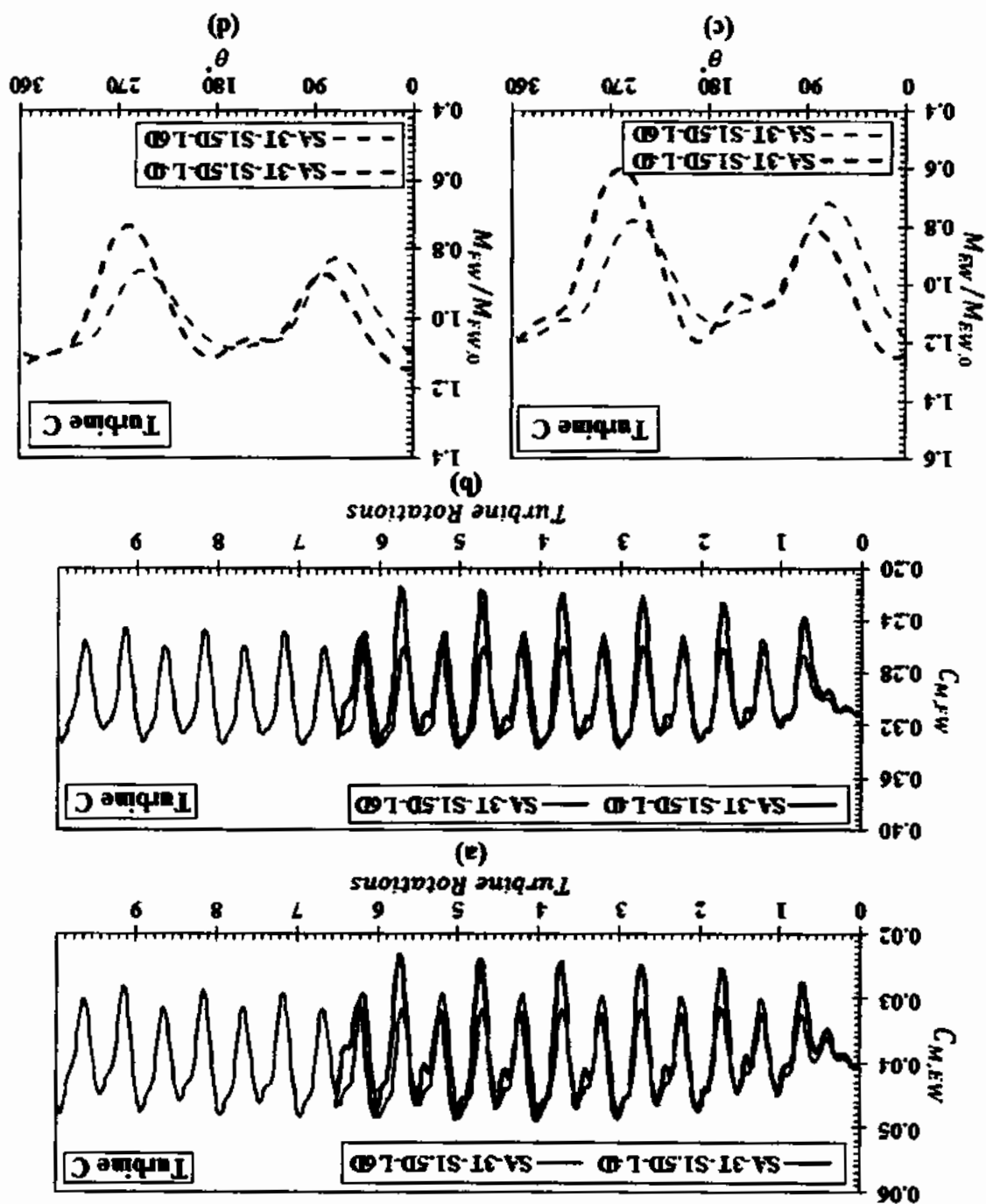
Figure 6.42 Moment loads on the blade of turbine B operating in staggered array with transverse spacing of 1.5D. Time history of moment loads (a) edge-wise (b) flap-wise and moment load normalized with respect to cycle mean during a single turbine rotation (c) edge-wise (d) flap-wise



These moment loads coefficients time histories are similar in essence to any standalone turbine and for that matter turbine A in the already presented co-axial arrays. The 1st row upstream devices are receiving the undisturbed free stream flow as they are not operating in the wake of any upstream device. All these curves exhibit a single drop during a single rotation cycle due to the tower shadow effect. The moment load curves normalized with respect to cycle mean highlights that the drop in moment loads is not significant and the span of the drop is very short. The curves very quickly recover to a flat shape and almost stay unchanged for most part of the cycle. The general behavior of edge-wise and flap-wise moment loads for the 1st row devices (turbine A and B) is almost similar. However, the edge-wise moment load seems to have relatively greater variation compared to the flap-wise moment load which is in accordance to the observation of Blackmore et al. [63]. Additionally, these figures further gives the obvious indication that load behavior of the 1st row devices would not change with the downstream device location whether located at 4D or 6D.

The time histories of moment load coefficients and moment load normalized with respect to cycle mean during a single turbine rotation for the blade of turbine C in the staggered array with 1.5D transverse spacing is shown in Figure 6.43. Turbine C is operating in the downstream between the gap of 1st row devices and its moment load behavior is

Figure 6.43 Moment loads on the blade of turbine C operating in staggered array with transverse spacing of 1.5D. Time history of moment loads (a) edge-wise (b) flap-wise and moment load normalized with respect to cycle mean during a single turbine rotation (c) edge-wise (d) flap-wise



significantly influenced by the 1st row upstream devices. For turbine C the edge-wise and flap-wise moment loads behavior on the turbine blade is almost similar. These moment curves exhibit two peaks and troughs during a single turbine rotation with significant variation in the magnitude of loads and the variation covering every degree of rotation. The normalized bending moment curve (Figures 6.43c and d) clearly shows that the drop at $(\theta = 180^\circ)$ representing the tower shadow effect has vanished. The two troughs are now near $(\theta = 90^\circ \text{ and } 270^\circ)$. This is because the gap between the upstream devices is only 0.5D which means that almost half of the blade length penetrates with in the wake of each upstream device when the turbine blade is at the position $(\theta = 90^\circ \text{ or } 270^\circ)$. Since, the flow velocity within the wake is significantly lower therefore at both these positions the moment loads of the blade are lower. Contrarily, when the blade is vertically aligned with the tower either at the top or bottom at the position $(\theta = 0^\circ \text{ or } 180^\circ)$, the blade is operating in the accelerated flow region between the gaps of upstream turbine. The normalized flap and edge-wise moment loads curve for turbine C placed at 6D exhibits a comparatively stable behavior with smaller variation compared to the case of 4D placement.

The variation of moment loads on the blade of turbines operating in the 1.5D staggered arrays are further quantified in Table 6.10. The mean, range and variation of flap-wise moment load coefficient for the blade of 1st row upstream device (turbine A and B) during a single turbine rotation is similar which is very obvious. However, it is interesting to note that the mean value of flap-wise moment load coefficient for turbine C is also almost similar to the 1st row upstream devices. Whereas, the range and variation are considerably higher due to drop in the value of minimum flap-wise moment load in a single rotation cycle. As already discussed in the preceding paragraph this is due to the operation of almost half the length of turbine blade in the wake of upstream devices at the positions $(\theta = 90^\circ \text{ and } 270^\circ)$. The percentage variation in flap-wise moment load for turbine C located longitudinally at 4D is about 41%. Whereas, this variation decreases to 28% for the case when turbine C is located downstream longitudinally at 6D. Because, at this downstream distance (6D) the wake of upstream devices has recovered relatively more velocity compared to the case of downstream distance of 4D. The considerable increase in the range

Table 6.10 Load variation statistics for the blade of turbines operating in the 1.5D staggered arrays

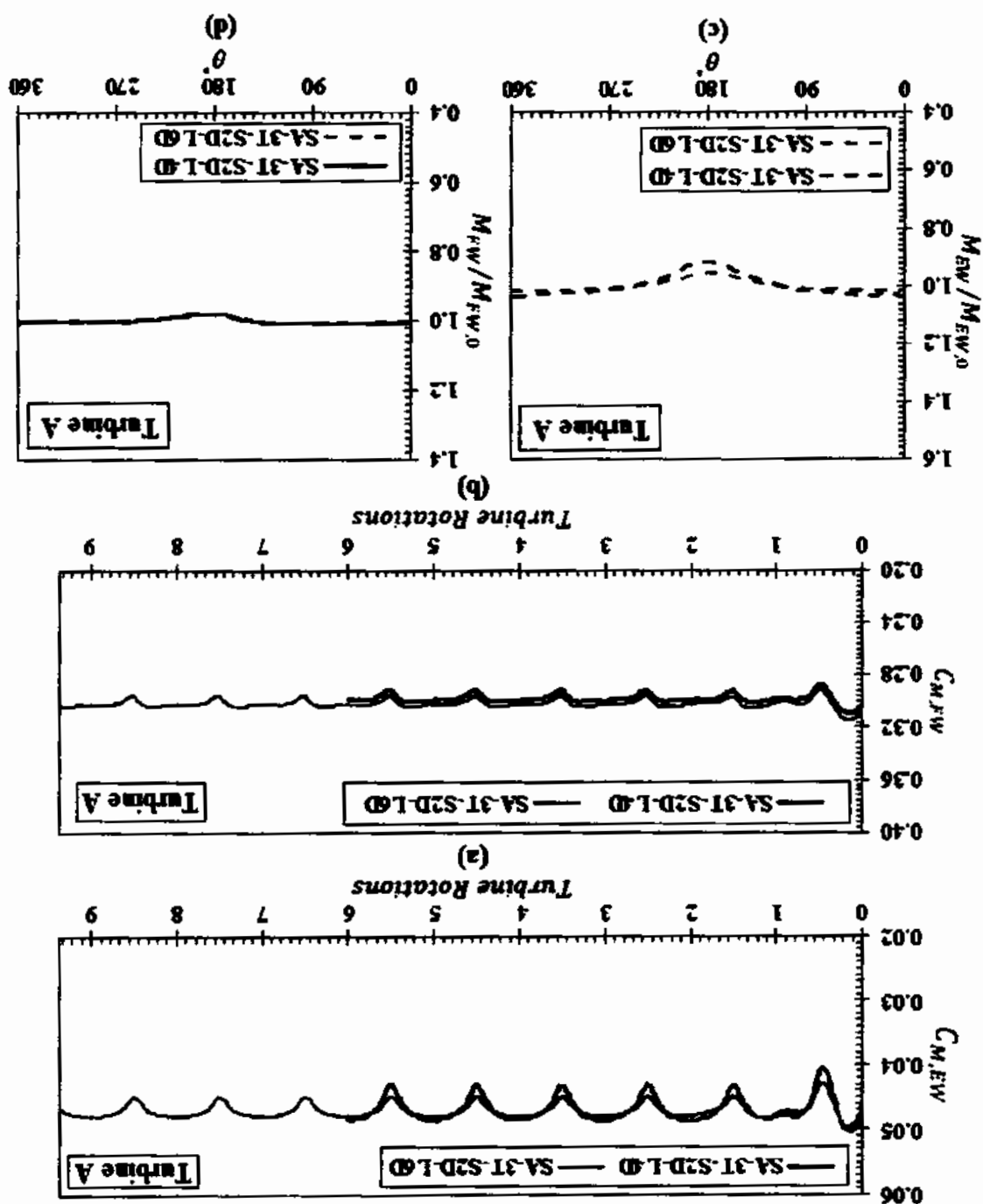
Moment Load		Turbine A		Turbine B		Turbine C	
Flap-wise Moment	Mean	0.30	0.30	0.30	0.30	0.29	0.30
	Peak	0.30	0.30	0.30	0.30	0.34	0.34
	(C _{M,Fw})	Range	0.012	0.012	0.012	0.012	0.121
% Variation		4	4	4	4	41	28
Edge-wise Moment	Mean	0.044	0.044	0.044	0.044	0.039	0.041
	Peak	0.044	0.044	0.044	0.044	0.049	0.049
	(C _{M,Ew})	Range	0.002	0.002	0.002	0.002	0.025
% Variation		6	6	6	6	65	47

and variation of flap-wise moment load coefficient during a single rotation on the blades of turbine C clearly indicate that blades of this turbine are by far more susceptible to load variations and fatigue failure compared to the upstream devices. Therefore, the structural design criteria for the blade of turbine C would need to be different than any of the standalone turbine or the 1st row upstream devices. In these situations if the structural design of blade is same for all the array devices the blade would not be able to sustain these significantly higher load variations and would not be reliable from the perspective of fatigue failure. Additionally, for the blade of turbine C located at a comparatively larger downstream distance of 6D with in the same array, the variation in flap-wise moment load decreases to about 28% to indicate that even a small increase in the downstream distance would substantially reduce the structural design requirements of the blade against load variations and fatigue failure. Similar to case of flap-wise moment load coefficient, the edge-wise moment load coefficient on the blades of 1st row upstream devices (turbine A and B) are almost similar and exhibits a behavior similar to a standalone turbine. For the downstream turbine C the mean cycle value of edge-wise moment load coefficient on the blade decreases compared to the upstream devices for both the cases of 4D and 6D longitudinal placement. However, the peak and minimum value decreases to cause a considerable increase in the range and variation during a single turbine rotation. These

variations in the edge-wise moment load would not also contribute to increasing the overall load variations but would also deteriorate the quality of power output from the turbine. Additionally, it is also evident that the variations in edge-wise moment load coefficients during a single rotation are considerably greater than the flap-wise moment load coefficients. The variation in edge-wise moment coefficient considerable decreases with increasing the downstream distance between the 1st row upstream devices and downstream device.

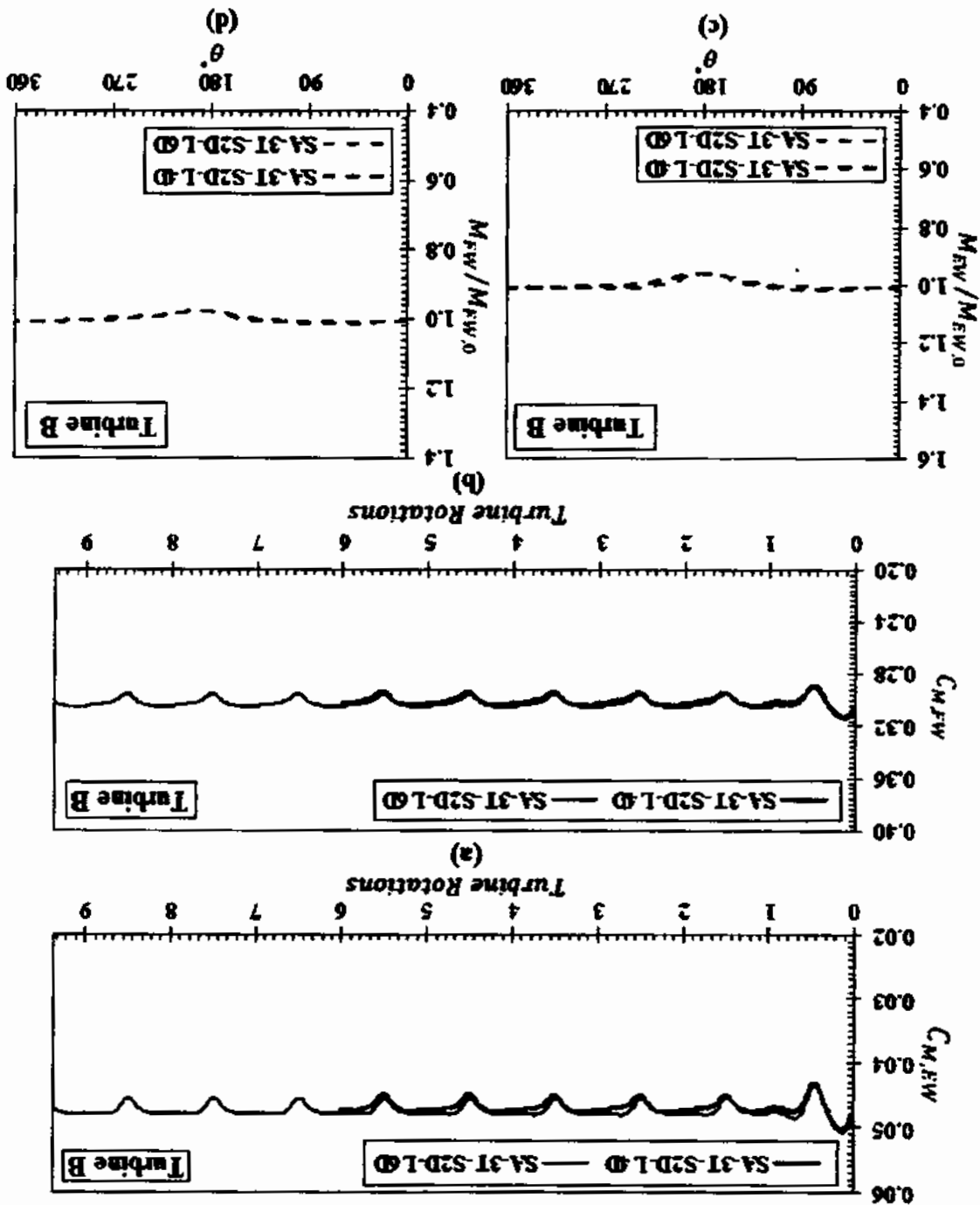
The time histories of moment load coefficients and moment load normalized with respect to cycle mean during a single turbine rotation for the blade of 1st row devices operating in the staggered arrays with transverse spacing of 2D between the 1st row devices is shown in Figures 6.44-6.45. These moment curves are similar to any upstream turbine operating in undisturbed free stream flow. The moment loads curve details for the upstream devices has already been discussed in the case of co-axial arrays and staggered arrays with transverse spacing of 1.5D and is not provide here once again to avoid repetition. The figures are only provided here to establish that the performance of 1st row upstream devices would not change between the various array configurations and location of the downstream devices for the evaluated downstream spacing.

Figure 6.44 Moment loads on the blade of turbine A operating in staggered array with transverse spacing of 2D. Time history of moment loads (a) edge-wise (b) flap-wise and moment load normalized with respect to cycle mean during a single turbine rotation (c) edge-wise (d) flap-wise



For the 2D staggered array the transverse spacing is such that tip to tip clearance between the 1st row upstream devices (turbine A and B) is 1D. In this array configuration the downstream turbine C operating between the gap of 1st row upstream devices with in the

Figure 6.45 Moment loads on the blade of turbine B operating in staggered array with transverse spacing of 2D. Time history of moment loads (a) edge-wise (b) flap-wise and moment normalized with respect to cycle mean during a single turbine rotation (c) edge-wise (d) flap-wise



accelerated flow region is minimally interacting with the downstream wake of the upstream devices compared to the case of 1.5D staggered arrays. The moment load time histories curves (Figures 6.46a and b) shows some fluctuations other than the major troughs of tower shadow effect which are relatively more visible in the flap-wise moment loads compared to the edge-wise moment load. However, these fluctuations are by no means comparable to the scales of load fluctuations of turbine C operating in the 1.5D staggered arrays. The normalized flap and edge-wise moment load curves (Figures 6.46c and d) for turbine C indicate that the curve is not completely flat on either side of the tower shadow drop. However, these fluctuations can be in no means termed as significant even on the scales of normalized moment curves for the blade in a single turbine rotation. Which indicate that the downstream turbine C is interacting with the wake of 1st row upstream devices but this interaction is not significant to create a substantial impact on the moment load behavior of the blade of downstream turbine C.

Figure 6.46 Moment loads on the blade of turbine C operating in staggered array with transverse spacing of 2D. Time history of moment loads (a) edge-wise (b) flap-wise and moment load normalized with respect to cycle mean during a single turbine rotation (c) edge-wise (d) flap-wise

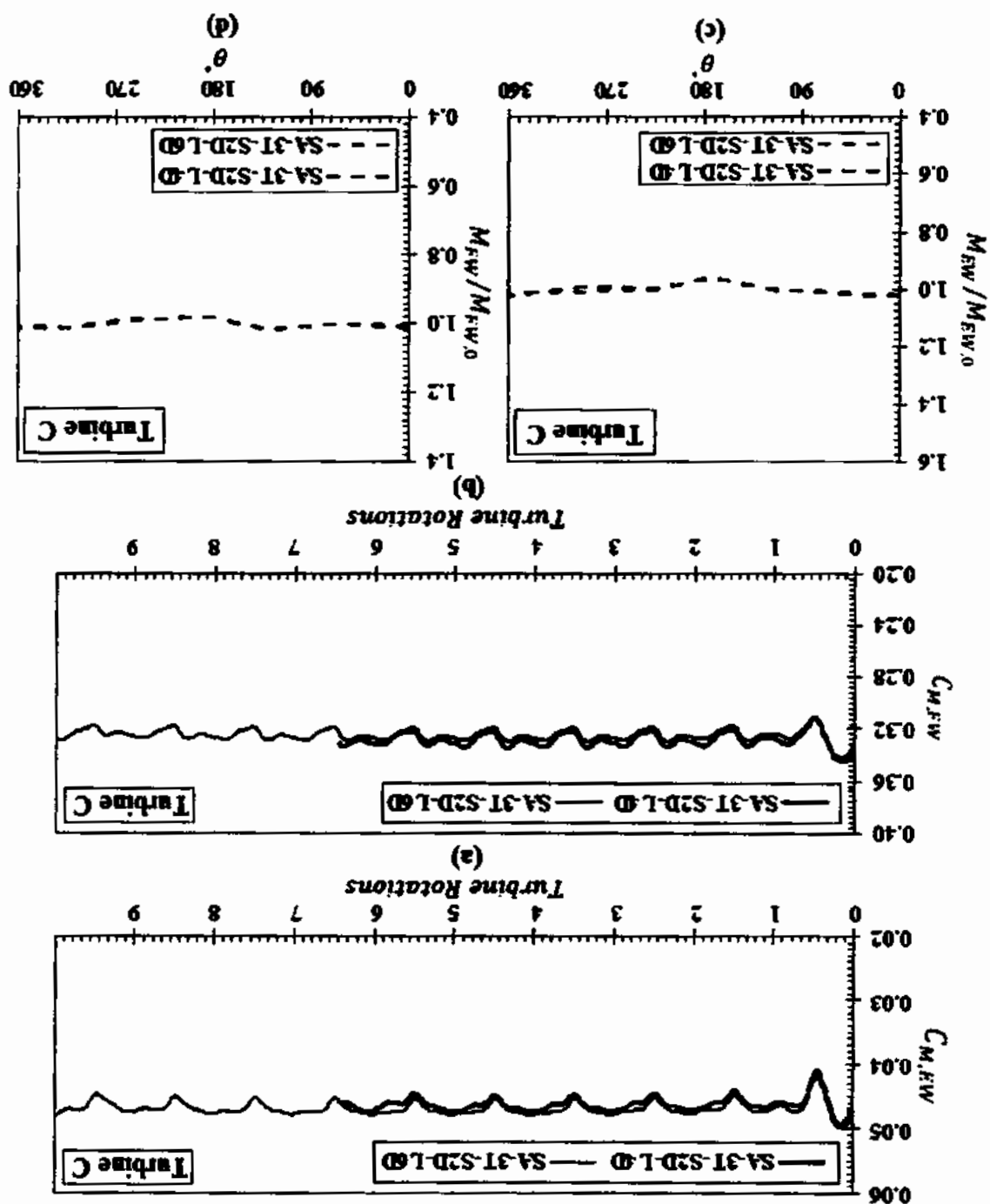


Table 6.11 Load variation statistics for the blade of turbines operating in the 2D

Moment Loads		staggered arrays											
		Turbine A			Turbine B			Turbine C					
		SA-3T-S2D			SA-3T-S2D			SA-3T-S2D					
		-L4D			-L6D			-L4D			-L6D		
Flap-wise Moment		0.30	0.30	0.30	0.30	0.30	0.30	0.30	0.30	0.33	0.33	0.33	
Load Coefficient		0.30	0.30	0.30	0.30	0.29	0.29	0.30	0.30	0.33	0.33	0.33	
(C _{M,Fw})		Min	0.29	0.29	0.29	0.29	0.29	0.29	0.29	0.32	0.32	0.32	
		Range	0.013	0.013	0.013	0.013	0.013	0.013	0.013	0.011	0.010	0.010	
% Variation			4	4	4	4	4	4	3	3	3		
Edge-wise Moment		Mean	0.044	0.044	0.044	0.044	0.044	0.044	0.044	0.046	0.047	0.047	
Load Coefficient		Peak	0.044	0.044	0.044	0.044	0.044	0.044	0.044	0.047	0.048	0.048	
(C _{M,Ew})		Min	0.042	0.042	0.042	0.042	0.042	0.042	0.042	0.045	0.045	0.045	
		Range	0.002	0.002	0.002	0.002	0.002	0.002	0.002	0.003	0.003	0.003	
% Variation			6	6	6	6	6	6	6	6	5		

turbine. Additionally, for the case of downstream turbine C placed at the longitudinal distance of 6D the variation in edge-wise moment loads on turbine blade is marginally less than the upstream turbines and turbine C placed at 4D. This finding again suggest the obvious that increasing the inter device distance between the upstream and downstream devices would decrease the variation in edge-wise moment loads on the turbine blade.

6.3 Summary

This chapter presents the development of RANS CFD methodology for simulating tidal turbine arrays to investigate the influence of array layout and interdevice spacing on the performance and structural loads on the blade of TCT. This simulation methodology is successively evolved from RANS CFD methodology of full scale SAFL RMI turbine earlier developed in this thesis and described in chapter 4. The investigations are accomplished through a series of simulations for two and three turbine co-axial and staggered arrays with different interdevice spacing. The performance for all turbines in all array configurations is evaluated in terms of power coefficient and total array power output. Additionally, the influence of operation of upstream device on the performance of downstream devices in the evaluated array layouts is described. The wake of all devices operating in all array configurations with different interdevice spacing is also characterized with velocity contours and velocity deficit plotted along the channel centerline. Additionally, vertical and horizontal velocity profiles at different upstream and downstream distances along the channel length for all array layouts is provided to describe the flow field of entire computational domain. Finally, the structural load behavior of turbine blade and its variations for all turbines in all array layouts is evaluated through plots of moment loads coefficients time histories and normalized moment loads during a turbine rotation cycle. The behavior and variations of moment loads and its influence on the reliability and fatigue life of turbine blade is further substantiated by presenting the mean, range and variation of moment loads during a single turbine rotation for all array layouts.

Chapter 7

Conclusions and

Recommendation for Future Work

The work carried out throughout the course of this research have led to some important conclusions. Although, most of these conclusions have been already mentioned in the respective chapters. This chapter will outline some of the major conclusions and provide recommendation for future research in this area.

7.1 Conclusions

- The power output of downstream devices operating in the co-axial array is significantly lower due to the effect of upstream device operation. This effects may be somewhat reduced by manipulating the interdevice spacing between the array devices. The power output of 1st downstream device would increase with increasing interdevice spacing between the upstream and downstream device. However, further downstream behind the 1st downstream device, the higher interdevice spacing is counterproductive in terms of power output from the individual turbine. Therefore, it would be useful to successively reduce the interdevice spacing between the downstream devices along the channel length.

- The power output of a downstream device operating in staggered arrays between the gap of 1st row devices would depend on the transverse spacing between the upstream devices. This spacing should be large enough so that the blades of the downstream turbine may not interact with the wake of upstream turbines. From the results of the evaluated array cases in this research, it is suggested that the transverse spacing between the 1st row devices should not be less than the diameter of downstream device for closely spaced downstream devices. The power output of the downstream device would be less than the upstream devices for staggered arrays having transverse spacing

of less than the diameter of the downstream device between the 1st row devices. However, the power output of the downstream device can be significantly improved with an optimal transverse spacing between the 1st row upstream devices. Additionally, the power output of downstream device would decrease with increasing interdevice spacing between the 1st row upstream devices and downstream device for staggered arrays with optimal spacing between the 1st row upstream devices. The total array power output of the staggered arrays would be substantially greater than an equivalent coaxial array with similar number of devices of similar design. The relative disadvantage of co-axial array in terms of power output can be better represented by the case of two turbines placed side by side in a single row producing more power than three turbines co-axial arrays even with a considerably larger interdevice spacing.

- The behavior of edge-wise and flap-wise moment loads is similar in essence for each turbine operating in array although their magnitudes are quite different. However, the behavior changes from turbine to turbine depending upon its location within the array. For the upstream device operating in an idealized uniform flow environment, the moment loads curve of a blade during the turbine rotation would exhibit only a single drop due to the tower shadow effect. This drop in moment loads would be for a short span and the curve will quickly recover to almost a flat shape for most part of the turbine rotation.

- The moment loads curve of a blade during the turbine rotation for the 1st downstream device operating in co-axial array would be entirely different due to the effect of upstream turbine operation. The curve would almost be like a sinusoidal curve with two peaks and troughs during one turbine rotation. The drop in moment loads would also be exaggerated and the moment loads would be changing significantly at every degree of turbine rotation. However, this behavior of moment loads would not be similar for all the downstream devices and it would change between the 1st downstream and 2nd downstream device. The variations in moment loads on the blade would successively decrease for the 2nd downstream operating within the combined wake of two upstream devices in the co-axial arrays. For the evaluated co-axial array cases in this research it seems that the 2nd device would somewhat suppress the imprints of the effect of upstream device operation on the moment loads variation of the blade for the

third turbine. However, it would be interesting to investigate this phenomenon further with the addition of more devices in the co-axial arrays. Additionally, the effect of upstream turbine operation on the variation of moment loads behavior of the downstream device would decrease with increasing inter device spacing.

- The mean cycle value of moment loads on the blade of downstream devices would be lower compared to the upstream device for turbines operating in co-axial arrays. However, the range of moment loads would be significantly higher. The fatigue life of turbine blade would decrease with increase in the mean cycle value of moment loads and or range and vice versa. The co-axial array cases evaluated in this research lead to the conclusion that blades of the downstream devices would experience more variation in the moment loads and may be more susceptible to fatigue failure compared to the upstream device and this change is solely due to the operation of upstream turbine. Additionally, the variation in edge-wise moment loads on the blades of downstream devices for the evaluated co-axial array cases clearly indicate that the quality of power output from the downstream devices would be highly deteriorated in terms of power fluctuations compared to the upstream device. The adverse effects on the moment loads variation and power fluctuation can be somewhat reduced by increasing the interdevice spacing between devices in the co-axial arrays.

- The behavior of moment loads on the blades of 1st row turbines would not depend on the transverse spacing between the 1st row devices in the staggered arrays. However, the moment loads behavior on the blades of downstream devices would be significantly influenced by this spacing. For the case of very closed transverse spacing between the upstream devices some part of the blade of downstream device would penetrate into the wake of upstream devices and as a result the moment loads would vary significantly twice during a rotation cycle. These variation in moment loads on the blade of downstream devices would decrease with increasing spacing between the 1st row and downstream device. The mean value of moment loads on the blades of downstream turbine would be almost similar to the 1st row devices. However, the range and variation would be considerably higher due to drop in the value of minimum cycle value of moment load. The blades of the downstream turbine in this case would be far more susceptible to load variations and fatigue failure compared to the upstream

devices. Therefore, the structural design criteria for the blade of downstream turbine should be different than a standalone turbine or the 1st row upstream devices to sustain these significantly higher load variations and be reliable from the perspective of fatigue failure.

- The downstream turbine operating in the flow accelerated within the gap of 1st row devices in staggered arrays with transverse spacing (i.e., tip to tip clearance) between the 1st row upstream devices equal to the diameter of the downstream device would minimally interact with the wake of upstream devices. The moment loads on the blade of downstream device in this case would not exhibit any significant variations other than the tower shadow effect.

- The mean cycle value of moment loads on the turbine blade would be comparatively higher than the 1st row upstream devices due to operation in the accelerated flow region. However, the range of moment loads during a rotation cycle would be similar to the upstream devices. Therefore, the blades of this turbine would be more susceptible to fatigue failure due to increased mean cycle value of moment loads despite no significant change in the variation of moment loads compared to the upstream device. Additionally, the increased interdevice spacing between the 1st row and downstream devices would not be desirable in this case. As this would not further improve the moment loads behavior of the turbine blade and may result in the loss of power output.

- The work carried out during this research employed the RANS CFD models for simulating the performance and coupled FSI models for simulating the performance and structural response of a standalone tidal current turbine. The CFD and FSI modelling approaches have their distinct features and use. Both these techniques have their unique positions as research tools in the modern day research and may never be considered as a replacement of one another. The RANS CFD models treat the turbine blades to be non-deformable (rigid) against the incident flow. Whereas, the FSI models are capable to model the turbine performance while taking into account the deformation of turbine blades due to the onset flow. Therefore, both these models would predict almost a similar turbine performance for cases involving smaller blade deformations. However, for cases involving larger blade deformations the prediction of turbine

performance between both the models would be significantly different. The CFD models are less complicated, computationally efficient and require less computational resources. Therefore, they should generally be preferred for investigating the turbine performance. Alternatively, the FSI models may be preferred for modeling the turbine performance in cases involving larger blade deformations or when the focus of investigation is to determine the structural response in terms of stresses, deformation or fatigue evaluation. Additionally, the coupled FSI simulation capabilities of the ANSYS workbench software could not be readily utilized for simulating tidal turbine arrays due to the associated computational cost.

- The RANS CFD simulation of the standalone SAFL RM-1 scaled model rotor leading to the development of RANS CFD model for simulating tidal turbine arrays have shown that at lower TSRs, the variation of blockage ratio had almost no effect on turbine performance. However, at higher TSRs, a positive correlation exist between blockage ratio and turbine performance. The effect of blockage on performance is less pronounced at blockage ratios below 10%, but increases rapidly for blockage ratios above 10%. Similarly, proximity to the channel boundaries also affects the turbine performance in terms of power and thrust. These findings have led to the conclusion that the effect of blockage ratio and boundary proximity may be duly accounted for while investigating the performance of tidal turbines and the structural loads behavior of the turbine blade operating as a standalone device as well as in tidal arrays.

7.2 Recommendations for future work

The following are recommendations by the author to be considered for future research:

- For the research in this thesis, a standalone turbine operating in the array domain at optimum TSR was simulated to determine the onset velocity for the second turbine. This velocity was required to compute the angular speed of the second turbine that is input to simulation. Similarly, for determining the angular speed of third turbine a two turbine array was first simulated. This approach is very time consuming and is limited in that it cannot be directly applied for the simulation of multi device arrays. An alternate approach could be to input the angular speed of each turbine as a function of the average velocity in an area equal to the diameter of the turbine at 2D upstream of

each turbine. Thus the angular speed of the turbine will be determined by the solver itself based on some expression or subroutine. Additionally, this alternate methodology would be more suited to further extend this research for evaluating the behavior of structural loads on turbine blades in tidal turbine arrays with more realistic flow conditions closely resembling a real tidal flow.

- The coupled FSI simulation methodology adopted in this thesis has been observed to be computationally very expensive requiring large computational resource and time consuming. In its current form it could not be utilized for the simulation of multi device tidal arrays with the CFD based on blade resolved turbine models. However, an alternate method would be to employ an uncoupled FSI simulation methodology where the CFD and FEA solution should be run independent of each other with no communication between the two solvers. The time histories for the blade structural loads for each array device may be obtained from the CFD simulation and then these load time histories may be input to the FEA solver for transient structural simulations to obtain the structural response in terms of stresses, deformation and fatigue evaluation.

- The co-axial array cases evaluated in this research have indicated that the power output and moment loads on the blade of each downstream device would not be identically influenced by the effect of upstream devices operation. However, the evaluated array cases consisted of only three turbines which were not sufficient to fully ascertain this finding. Therefore, it is recommended that co-axial arrays with greater number of devices may be investigated to explain this phenomenon with greater details and higher degrees of confidence.

- The variation of moment loads on the blades of downstream devices operating in tidal arrays have been quantified under the assumption of uniform inflow velocity in this thesis. Whereas, Hydrodynamic conditions in actual marine environments are site-specific and vary considerably from site to site. Every hydrodynamic condition has different effects on the performance and structural loads of a tidal turbine blade. Amongst the various hydrodynamic conditions, the wave-current interaction, turbulence and velocity shear could substantially influence the structural loads on the

blade and turbine performance. Results from the FSI simulations of full scale standalone device reported in this thesis have shown that the effect of velocity shear and tower on the blade load variation are augmenting effects. Similarly, in tidal turbine arrays the hydrodynamic conditions like wave current interaction and velocity shear may either exaggerate or suppress the adverse effects of the upstream turbine operation on the moment loads of downstream turbine blades. Therefore, it is recommended that tidal turbine arrays may be investigated with realistic tidal flows for quantifying the moment loads behavior of downstream turbine blade and how these variations would impact the fatigue life. So that the reliability of future turbine blades against fatigue failure may be improved.

- Staggered array configurations with tip to tip clearance of 0.5D and 1D between the 1st row upstream devices have been investigated in this research. However, both the 1st row device were rotating in the same direction. It is recommended that further investigations may be performed with counter rotating 1st row devices to study the effect of turbine direction of rotation on the performance and blade loads of upstream devices with different transverse interdevice spacing. Additionally, the downstream wake of staggered arrays with counter rotating 1st row devices may be simulated to study the effects of turbine direction of rotation on the downstream wake expansion and symmetry and how this would affect the downstream turbine performance and blade loads.

References

- [1] A. Bahaj, The status of tidal stream energy conversion. In *Global Status and Critical Developments in Ocean Energy*. Ocean Energy Systems (OES) 2008. p. 23.
- [2] A. Raftiee, K.R. Khalilipour. Renewable Hybridization of Oil and Gas Supply Chains. In *Polygeneration with Polystorage for Chemical and Energy Hubs*. Academic Press 2019. pp. 331-72. <https://doi.org/10.1016/B978-0-12-813330-6-4.00011-2>.
- [3] IRENA. *Global Energy Transformation: A roadmap to 2050*. International Renewable Energy Agency, Abu Dhabi, 2018. p. 3.
- [4] IRENA. *Renewable Capacity Statistics 2018*. International Renewable Energy Agency, Abu Dhabi, 2018.
- [5] P. Fraenkel. Marine current turbines: pioneering the development of marine kinetic energy converters. *Proceedings of the Institution of Mechanical Engineers, Part A: Journal of Power and Energy*. 221 (2007) 159-69. <https://doi.org/10.1243/09576509JPE307>.
- [6] IRENA. *Tidal Energy Technology Brief*. International Renewable Energy Agency, Abu Dhabi, 2014. p. 21.
- [7] F.O. Rourke, F. Boyle, A. Reynolds. Tidal energy update 2009. *Applied Energy*. 87 (2010) 398-409. <https://doi.org/10.1016/j.apenergy.2009.08.014>.
- [8] W. Batten, A. Bahaj, A. Molland, J. Chaplin. Experimentally validated numerical method for the hydrodynamic design of horizontal axis tidal turbines. *Ocean Eng*. 34 (2007) 1013-20. <https://doi.org/10.1016/j.oceaneng.2006.04.008>.
- [9] I. Galarrraga, M. Gonzalez-Eguino, A. Markandya. *Handbook of sustainable energy*. Edward Elgar Publishing 2011. pp. 264-265.
- [10] N.D. Laws, B.P. Epps. Hydrokinetic energy conversion: Technology, research, and outlook. *Renewable and Sustainable Energy Reviews*. 57 (2016) 1245-59. <https://doi.org/10.1016/j.rser.2015.12.189>.
- [11] G.L. Alistair, Borthwick. *Marine Renewable Energy Seascape*. Engineering. 2 (2016) 69-78. <https://doi.org/10.1016/j.eng.2016.01.011>.
- [12] M.F. Rod, P. Robin. Renewable Energy from the Ocean. *Marine Policy*. 26 (2002) 471-9. [https://doi.org/10.1016/S0308-597X\(02\)00045-3](https://doi.org/10.1016/S0308-597X(02)00045-3).

- [13] M. Davide, U. Andreas. 2014 JRC ocean energy status report. EUR 26983 EN. Publications Office of the European Union, Luxembourg, 2015. p. 15. <https://doi.org/10.2790/866387>.
- [14] S.P. Neill, A. Vögler, A.J. Goward-Brown, S. Baston, M.J. Lewis, P.A. Gillibrand, et al. The wave and tidal resource of Scotland. *Renewable energy*. 114 (2017) 3-17. <https://doi.org/10.1016/j.renene.2017.03.027>.
- [15] T. Blackmore, W. Batten, A. Bahaj. Influence of turbulence on the wake of a marine current turbine simulator. *Proceedings of the Royal Society A: Mathematical, Physical and Engineering Sciences*. 470 (2014) 20140331. <https://doi.org/10.1098/rspa.2014.0331>.
- [16] A. Bahaj, L. Myers, M. Thomson, N. Jorge. Characterising the wake of horizontal axis marine current turbines. In *proceedings of the 7th European wave and tidal energy conference*, Porto, Portugal, 2007.
- [17] R. Vennell, S.W. Funke, S. Draper, C. Stevens, T. Divett. Designing large arrays of tidal turbines: A synthesis and review. *Renewable and Sustainable Energy Reviews*. 41 (2015) 454-72. <https://doi.org/10.1016/j.rser.2014.08.022>.
- [18] A. MacLeod, S. Barnes, K. Rados, I. Bryden. Wake effects in tidal current turbine farms. In *proceedings of the international conference on marine renewable energy*, Newcastle, UK, Sep 11, 2002. pp. 49-53.
- [19] T. Daly, L. Myers, A. Bahaj. Experimental analysis of the local flow effects around single row tidal turbine arrays. In *proceed of the Third International Conference and Exhibition on Ocean Energy*, Bilbao, Spain 05 - 07 Oct 2010.
- [20] P. Mycek, B. Gaurier, G. Germain, G. Pinon, E. Rivoalen. Experimental study of the turbulence intensity effects on marine current turbines behaviour. Part I: One single turbine. *Renewable Energy*. 66 (2014) 729-46. <https://doi.org/10.1016/j.renene.2013.12.036>.
- [21] T.J. Stallard, T. Feng, P.K. Stansby. Experimental study of the mean wake of a tidal stream rotor in a shallow turbulent flow. *Journal of Fluids and Structures*. 54 (2015) 235-46. <https://doi.org/10.1016/j.jfluidstructs.2014.10.017>.
- [22] R. Vennell. Exceeding the Betz limit with tidal turbines. *Renewable Energy*. 55 (2013) 277-85. <https://doi.org/10.1016/j.renene.2012.12.016>.
- [23] S.R. Turnock, A.B. Phillips, J. Banks, R. Nicholls-Lee. Modelling tidal current turbine wakes using a coupled RANS-BEMT approach as a tool for analysing power capture of arrays of turbines. *Ocean Engineering*. 38 (2011) 1300-7. <https://doi.org/10.1016/j.oceaneng.2011.05.018>.
- [24] R. Malki, I. Masters, A.J. Williams, T.N. Croft. Planning tidal stream turbine array layouts using a coupled blade element momentum-computational fluid dynamics

- model. Renewable Energy. 63 (2014) 46-54.
<https://doi.org/10.1016/j.renene.2013.08.039>.
- [25] A. Bahaj, L.E. Myers. Shaping array design of marine current energy converters through scaled experimental analysis. Energy. 59 (2013) 83-94.
<https://doi.org/10.1016/j.energy.2013.07.023>.
- [26] C. Hill, V.S. Neary, B. Gunawan, M. Guala, F. Sotiropoulos. US Department of Energy Reference Model Program RM1: Experimental Results. Technical Report 2014. <https://doi.org/10.2172/1172793>. Available online: <https://www.osti.gov/biblio/1172793-department-energy-reference-model-program-rm1-experimental-results> (accessed on 21 July 2019).
- [27] Roger H. Charlier, Loic Menanteau, M.-C.P. Chainoux. The rise and fall of the tide mill. Ocean sciences bridging the millennia - A spectrum of historical accounts 315-38.
- [28] R.H. Charlier. Re-invention or aggrorniamiento? Tidal power at 30 years. Renewable and Sustainable Energy Reviews. 1 (1997) 271-89.
- [29] P.L. Fraenkel. Development and testing of Marine Current Turbine's SeaGen 1.2 MW tidal stream turbine. In the proceedings of 3rd International Conference on Ocean Energy, 2010.
- [30] J.P. Frau, 1993. Tidal energy: promising projects: La Rance, a successful industrial-scale experiment IEEE Transactions on Energy Conversion 3.
- [31] P.L. Fraenkel. Marine current turbines: pioneering the development of marine kinetic energy converters. Proceedings of the Institution of Mechanical Engineers, Part A: Journal of Power and Energy. 221 (2007) 159-69.
[10.1243/09576509jpe307](https://doi.org/10.1243/09576509jpe307).
- [32] J. Thake. Development, installation and testing of a large-scale tidal current turbine Technical report No. T-06/00210/00/REP; URN-05/1698, IT Power, U.K, 2005.
- [33] A. Bahaj, A. Molland, J. Chaplin, W. Batten. Power and thrust measurements of marine current turbines under various hydrodynamic flow conditions in a cavitation tunnel and a towing tank. Renewable energy. 32 (2007) 407-26.
- [34] S. Bal, M. Atlar, D. Usar. Performance prediction of horizontal axis marine current turbines. Ocean Systems Engineering. 5 (2015) 125-38.
[10.12989/ose.2015.5.2.125](https://doi.org/10.12989/ose.2015.5.2.125).
- [35] S.C. Tedds, I. Owen, R.J. Poole. Near-wake characteristics of a model horizontal axis tidal stream turbine. Renewable Energy. 63 (2014) 222-35.
[10.1016/j.renene.2013.09.011](https://doi.org/10.1016/j.renene.2013.09.011).

- [36] T.A. De Jesus Henriques, T.S. Hedges, I. Owen, R.J. Poole. The influence of blade pitch angle on the performance of a model horizontal axis tidal stream turbine operating under wave-current interaction. *Energy*. 102 (2016) 166-75.
- [37] F.M. Jing, W.J. Ma, L. Zhang, S.Q. Wang, X.H. Wang. Experimental study of hydrodynamic performance of full-scale horizontal axis tidal current turbine. *Journal of Hydrodynamics*, Ser B. 29 (2017) 109-17. 10.1016/s1001-6058(16)60722-9.
- [38] H.W. Liu, H.B. Zhou, Y.G. Lin, W. Li, H.G. Gu. Design and test of 1/5th scale horizontal axis tidal current turbine. *China Ocean Engineering*. 30 (2016) 407-20. 10.1007/s13344-016-0027-5.
- [39] E. Kulunk. Aerodynamics of wind turbines. Fundamental and advanced topics in wind power. IntechOpen, 2011.
- [40] W. Batten, A. Bahaj, A. Molland, J. Chaplin. The prediction of the hydrodynamic performance of marine current turbines. *Renewable energy*. 33 (2008) 1085-96.
- [41] B. Mujahid, B. Saeed, J. Sakhi. Hydrodynamic Design of Tidal Current Turbine and the Effect of Solidity on Performance. *Journal of Engineering and Applied Sciences*. 36 (2017). <https://doi.org/10.25211/jeas.v36i2.2068>
- [42] F. O'Rourke, F. Boyle, A. Reynolds, D.M. Kennedy. Hydrodynamic performance prediction of a tidal current turbine operating in non-uniform inflow conditions. *Energy*. 93 (2015) 2483-96.
- [43] John D Anderson, Jr. Computational Fluid Dynamics- The basics with application., In. McGraw-Hill, Inc 1995. pp. 23-5.
- [44] H.K. Versteeg, W. Malalasekera. An introduction to computational fluid dynamics: the finite volume method. Pearson education 2007.
- [45] S. Tedds, I. Owen, R. Poole. Near-wake characteristics of a model horizontal axis tidal stream turbine. *Renewable Energy*. 63 (2014) 222-35.
- [46] I.A. Milne, R.N. Sharma, R.G. Flay, S. Bickerton. Characteristics of the turbulence in the flow at a tidal stream power site. *Phil Trans R Soc A*. 371 (2013) 20120196.
- [47] U. Ahmed, D. Apsley, I. Afgan, T.J. Stallard, P.K. Stansby. Fluctuating loads on a tidal turbine due to velocity shear and turbulence: Comparison of CFD with field data. *Renewable Energy*. 112 (2017) 235-46.
- [48] P. Ouro, M. Harrold, T. Stoesser, P. Bromley. Hydrodynamic loadings on a horizontal axis tidal turbine prototype. *Journal of Fluids and Structures*. 71 (2017) 78-95.

- [49] P. Ouro, T. Stoesser. Impact of Environmental Turbulence on the Performance and Loadings of a Tidal Stream Turbine. Flow, Turbulence and Combustion. (2018) 1-27.
- [50] M. Badshah, J. VanZwieten, S. Badshah, S. Jan. CFD study of blockage ratio and boundary proximity effects on the performance of a tidal turbine. IET Renewable Power Generation. 13 (2019) 744-9. DOI: 10.1049/iet-rpg.2018.5134
- [51] K. Nitin, B. Arindam. Performance characterization and placement of a marine hydrokinetic turbine in a tidal channel under boundary proximity and blockage effects. Applied Energy. 148 (2015) 121-33. doi:10.1016/j.apenergy.2015.03.052.
- [52] S. Tatum, M. Allmark, C. Frost, D. O'Doherty, A. Mason-Jones, T. O'Doherty. CFD modelling of a tidal stream turbine subjected to profiled flow and surface gravity waves. International Journal of Marine Energy. 15 (2016) 156-74.
- [53] W. Tian, J.H. VanZwieten, P. Pyakurel, Y. Li. Influences of yaw angle and turbulence intensity on the performance of a 20 kW in-stream hydrokinetic turbine. Energy. 111 (2016) 104-16. doi:https://doi.org/10.1016/j.energy.2016.05.012.
- [54] J. Liu, H. Lin, S.R. Purmilita, M.D. ET. The effects of blade twist and nacelle shape on the performance of horizontal axis tidal current turbines. Applied Ocean Research. 64 (2017) 58-69.
- [55] G.S. Bir, M.J. Lawson, Y. Li. Structural design of a horizontal-axis tidal current turbine composite blade. In proceedings of the ASME 2011 30th International Conference on Ocean, Offshore and Arctic Engineering. pp. 797-808.
- [56] M.O.L. Hansen. Aerodynamics of Wind Turbines. Second ed. Earthscan in the UK and USA2008.
- [57] J. Jones, A. Davies. Influence of wave-current interaction, and high frequency forcing upon storm induced currents and elevations. Estuarine, Coastal and Shelf Science. 53 (2001) 397-413.
- [58] L. Myers, A. Bahaj. An experimental investigation simulating flow effects in first generation marine current energy converter arrays. Renewable Energy. 37 (2012) 28-36.
- [59] D.H. Zeiner-Gundersen. Turbine design and field development concepts for tidal, ocean, and river applications. Energy Science & Engineering. 3 (2015) 27-42.
- [60] F. Maganga, G. Germain, J. King, G. Pinon, E. Rivoalen. Experimental characterisation of flow effects on marine current turbine behaviour and on its wake properties. IET Renewable Power Generation. 4 (2010) 498-509.

- [61] N. Bartrop, K. Varyani, A. Grant, D. Clelland, X. Pham. Investigation into wave—current interactions in marine current turbines. *Proceedings of the Institution of Mechanical Engineers, Part A: Journal of Power and Energy*. 221 (2007) 233-42.
- [62] L. Luznik, K.A. Flack, E.E. Lust, K. Taylor. The effect of surface waves on the performance characteristics of a model tidal turbine. *Renewable energy*. 58 (2013) 108-14.
- [63] T. Blackmore, L.E. Myers, A.S. Bahaj. Effects of turbulence on tidal turbines: Implications to performance, blade loads, and condition monitoring. *International Journal of Marine Energy*. 14 (2016) 1-26.
- [64] A. Mason-Jones, D. O'doherty, C. Morris, T. O'doherty, C. Byrne, P. Prickett, et al. Non-dimensional scaling of tidal stream turbines. *Energy*. 44 (2012) 820-9.
- [65] S. Draper, T. Nishino, T. Adcock, P. Taylor. Performance of an ideal turbine in an inviscid shear flow. *Journal of Fluid Mechanics*. 796 (2016) 86-112.
- [66] H. Li, Z. Hu, K. Chandrashekhara, X. Du, R. Mishra. Reliability-based fatigue life investigation for a medium-scale composite hydrokinetic turbine blade. *Ocean Eng.* 89 (2014) 230-42.
- [67] G. McCann. Tidal current turbine fatigue loading sensitivity to waves and turbulence—a parametric study. In *proceedings of the 7th European Wave and Tidal Energy Conference*, 2007.
- [68] E.E. Lust, L. Luznik, K.A. Flack, J.M. Walker, M.C. Van Benthem. The influence of surface gravity waves on marine current turbine performance. *International Journal of Marine Energy*. 3 (2013) 27-40.
- [69] P.R. Pinet. *Invitation to Oceanography*. fifth ed. Jones & Bartlett Publishers 2009. pp. 237.
- [70] P. Galloway, L. Myers, A. Bahaj. Studies of a scale tidal turbine in close proximity to waves. In *proceedings of the Third International Conference and Exhibition on Ocean Energy*, Bilbao, 2010.
- [71] B. Gaurier, P. Davies, A. Deuff, G. Germain. Flume tank characterization of marine current turbine blade behaviour under current and wave loading. *Renewable Energy*. 59 (2013) 1-12.
- [72] J. Senat. *Numerical simulation and prediction of loads in marine current turbine full-scale rotor blades*. Doctoral dissertation, Florida Atlantic University 2011.
- [73] I. Milne, A. Day, R. Sharma, R. Flay. Blade loading on tidal turbines for uniform unsteady flow. *Renewable Energy*. 77 (2015) 338-50.

- [74] I. Milne, A. Day, R. Sharma, R. Flay. The characterisation of the hydrodynamic loads on tidal turbines due to turbulence. *Renewable and Sustainable Energy Reviews*. 56 (2016) 851-64.
- [75] G.S. Payne, T. Stallard, R. Martinez, T. Bruce. Variation of loads on a three-bladed horizontal axis tidal turbine with frequency and blade position. *Journal of Fluids and Structures*. 83 (2018) 156-70.
- [76] G. McCann. Tidal current turbine fatigue loading sensitivity to waves and turbulence—a parametric study. In *proceedings of the 7th European Wave and Tidal Energy Conference*, 2007.
- [77] M. Lewis, S. Neill, P. Robins, M. Hashemi. Resource assessment for future generations of tidal-stream energy arrays. *Energy*. 83 (2015) 403-15.
- [78] L. Blunden, A. Bahaj. Tidal energy resource assessment for tidal stream generators. *Proceedings of the Institution of Mechanical Engineers, Part A: Journal of Power and Energy*. 221 (2007) 137-46.
- [79] A. Mason-Jones, D. O'doherty, C. Morris, T. O'doherty. Influence of a velocity profile & support structure on tidal stream turbine performance. *Renewable Energy*. 52 (2013) 23-30.
- [80] N. Hafeez, S. Badshah, M. Badshah, S.J. Khalil. Effect of velocity shear on the performance and structural response of a small-scale horizontal axis tidal turbine. *Marine Systems & Ocean Technology*. (2019) 1-8. <https://doi.org/10.1007/s40868-019-00057-0>.
- [81] G. Larsen, H. Madsen, F. Bingöl, K. Hansen, T. Larsen. Dynamic wake meandering modeling. Technical Report R-1607. Technical University of Denmark, Risø National Laboratory, 2007.
- [82] A. Bahaj, L. Myers, M. Thomson, N. Jorge. Characterising the wake of horizontal axis marine current turbines. In *proceedings of the 7th European wave and tidal energy conference*, Porto, Portugal, 2007. p. 9.
- [83] L. Myers, A.S. Bahaj. Wake studies of a 1/30th scale horizontal axis marine current turbine. *Ocean Engineering*. 34 (2007) 758-62. <http://dx.doi.org/10.1016/j.oceaneng.2006.04.013>.
- [84] M.E. Harrison, W.M.J. Batten, L.E. Myers, A.S. Bahaj. Comparison between CFD simulations and experiments for predicting the far wake of horizontal axis tidal turbines. *IEE Renewable Power Generation*. 4 (2010) 613. 10.1049/iet-rpg.2009.0193.
- [85] L. Myers, A. Bahaj. Experimental analysis of the flow field around horizontal axis tidal turbines by use of scale mesh disk rotor simulators. *Ocean Engineering*. 37 (2010) 218-27.

- [86] T. Blackmore, W. Batten, A. Bahaj. Influence of turbulence on the wake of a marine current turbine simulator. In proceedings of the Proc R Soc A, 2014. p. 20140331.
- [87] A. MacLeod, S. Barnes, K. Rados, I. Bryden. Wake effects in tidal current turbine farms. In proceedings of the International conference on marine renewable energy, 2002. pp. 49-53.
- [88] L. Myers, A. Bahaj, G. Germain, J. Gilles. Flow boundary interaction effects for marine current energy conversion devices. In proceedings of the World Renewable Energy Congress X, Glasgow, Juillet 2008.
- [89] L. Myers, A. Bahaj. Near wake properties of horizontal axis marine current turbines. In proceedings of the 8th European Wave and Tidal Energy Conference, 2009. pp. 558-65.
- [90] R. Vennell. The energetics of large tidal turbine arrays. Renewable Energy. 48 (2012) 210-9.
- [91] G. Corten. Heat generation by a wind turbine. In proceedings of the 14th IEA symposium on the aerodynamics of wind turbines, 2000. pp. 1-8.
- [92] C. Garrett, P. Cummins. Limits to tidal current power. Renewable Energy. 33 (2008) 2485-90.
- [93] R. Vennell. Realizing the potential of tidal currents and the efficiency of turbine farms in a channel. Renewable Energy. 47 (2012) 95-102.
- [94] N.K. Steijzenmuller. Marine hydrokinetic turbine array performance and wake characteristics. Master's thesis, Department of Mechanical Engineering, University of Washington, 2013.
- [95] T. Javaherchi, N. Steijzenmuller, A. Aliseda, 2015. Experimental and numerical analysis of a small array of 45:1 scale horizontal axis hydrokinetic turbines based on the DOE reference model. In proceedings of the 3rd Marine Energy Technology Symposium.
- [96] C.-H. Jo, K.-H. Lee, J.-Y. Yim. A study on the interference effects for tidal current power rotors. Science China Technological Sciences. 53 (2010) 3094-101.
- [97] S.H. Lee, S.H. Lee, K. Jang, J. Lee, N. Hur. A numerical study for the optimal arrangement of ocean current turbine generators in the ocean current power parks. Current Applied Physics. 10 (2010) S137-S41. <http://dx.doi.org/10.1016/j.cap.2009.11.018>.
- [98] D.M. O'Doherty, A. Mason-Jones, C. Morris, T. O'Doherty, C. Byrne, P.W. Prickett, et al. Interaction of marine turbines in close proximity. In proceedings of the 9th European Wave and Tidal Energy Conference (EWTEC) Southampton, UK, 2011. pp. 10-4.

- [99] M. Nuernberg, L. Tao. Three dimensional tidal turbine array simulations using OpenFOAM with dynamic mesh. *Ocean Engineering*. 147 (2018) 629-46.
- [100] M. Nuernberg, L. Tao. Experimental study of wake characteristics in tidal turbine arrays. *Renewable energy*. 127 (2018) 168-81.
- [101] P. Mycek, B. Gaurier, G. Germain, G. Pinon, E. Rivoalen. Experimental study of the turbulence intensity effects on marine current turbines behaviour. Part II: Two interacting turbines. *Renewable Energy*. 68 (2014) 876-92.
- [102] M. Nuernberg, L. Tao. Experimental study of flow field characteristics in tidal stream turbine arrays. In *proceedings of the ASME 35th International Conference on Ocean, Offshore and Arctic Engineering 2016*, American Society of Mechanical Engineers Digital Collection.
- [103] V.T. Nguyen, A. Santa Cruz, S.S. Guillou, S. Elsouk, N. Mohamad, J. Thiébot. Effects of the Current Direction on the Energy Production of a Tidal Farm: The Case of Raz Blanchard (France). *Energies*. 12 (2019) 2478.
- [104] M.J. Churchfield, Y. Li, P.J. Moriarty. A large-eddy simulation study of wake propagation and power production in an array of tidal-current turbines. *Philosophical Transactions of the Royal Society A: Mathematical, Physical and Engineering Sciences*. 371 (2013) 20120421.
- [105] W. Hunter, T. Nishino, R.H. Willden. Investigation of tidal turbine array tuning using 3D Reynolds-averaged Navier–Stokes simulations. *International Journal of Marine Energy*. 10 (2015) 39-51.
- [106] C. Vogel, R. Willden, G. Houlisby. Tidal stream turbine power capping in a head-driven tidal channel. *Renewable energy*. 136 (2019) 491-9.
- [107] M.G. Gebreslassie, G.R. Tabor, M.R. Belmont. Investigation of the performance of a staggered configuration of tidal turbines using CFD. *Renewable Energy*. 80 (2015) 690-8.
- [108] Y. Chen, B. Lin, J. Lin, S. Wang. Effects of stream turbine array configuration on tidal current energy extraction near an island. *Computers & geosciences*. 77 (2015) 20-8.
- [109] M. Davide, M. Riccardo, U. Andreas. JRC ocean energy status report: 2016 Edition. EUR 28407 EN. Publications Office of the European Union, Luxembourg, 2016. p. 4. <https://doi:10.2760/509876>.
- [110] T.D. Corsatea, D. Magagna. Overview of European innovation activities in marine energy technology. EUR 26342 EN. Publications Office of the European Union, Luxembourg, 2013. p. 34. <https://doi:10.2790/99213>.

- [111] J.N. Goundar, M.R. Ahmed. Design of a horizontal axis tidal current turbine. *Applied energy*. 111 (2013) 161-74.
- [112] P.M. Singh, Y.-D. Choi. Shape design and numerical analysis on a 1 MW tidal current turbine for the south-western coast of Korea. *Renewable energy*. 68 (2014) 485-93.
- [113] C. Hee Jo, J. young Yim, K. hee Lee, Y. ho Rho. Performance of horizontal axis tidal current turbine by blade configuration. *Renewable Energy*. 42 (2012) 195-206.
- [114] J. McCosker. Design and optimization of a small wind turbine. M.S. Thesis, Rensselaer Polytechnic Institute, Troy, NY, 2012.
- [115] C. Jo, S. Hwang, J. Lee, K. Lee. Design Procedure and Performance Estimation of Tidal Current Power System. In proceedings of the 7th International Conference on Asian and Pacific Coasts (APAC 2013). pp. 873-6.
- [116] H.J. Vermaak, K. Kusakana, S.P. Koko. Status of micro-hydrokinetic river technology in rural applications: A review of literature. *Renewable and Sustainable Energy Reviews*. 29 (2014) 625-33.
- [117] Z.L. Nasir Mehmood, J. Khan. Diffuser augmented horizontal axis tidal current turbines. *Research Journal of Applied Sciences, Engineering and Technology*. 4 (2012) 3522-32.
- [118] C. Morris. Influence of solidity on the performance, swirl characteristics, wake recovery and blade deflection of a horizontal axis tidal turbine. Doctoral dissertation, Cardiff University. Wales, UK, 2014.
- [119] V.S. Neary, M. Lawson, M. Previsic, A. Copping, K.C. Hallett, A. LaBonte, et al. Methodology for Design and Economic Analysis of Marine Energy Conversion (MEC) Technologies. In proceedings of the 2nd Marine Energy Technology Symposium, Seattle, WA, April 15-18, 2014.
- [120] M.J. Lawson, Y. Li, D.C. Sale, 2011. Development and verification of a computational fluid dynamics model of a horizontal-axis tidal current turbine. ASME 2011 30th International Conference on Ocean, Offshore and Arctic Engineering.
- [121] T. Javaherchi, N. Stelzenmuller, A. Aliseda, 2013. Experimental and numerical analysis of the DOE reference model 1 horizontal axis hydrokinetic turbine. In proceedings of the 1st Marine Energy Technology Symposium.
- [122] P. Lissaman. Low-Reynolds-number airfoils. *Annual review of fluid mechanics*. 15 (1983) 223-39. <https://doi.org/10.1146/annurev.fl.15.010183.001255>.

- [123] T. Javaherchi, J. Seydel, N. Stelzenmüller, A. Aliseda, 2014. Experimental and numerical analysis of a scale model horizontal axis hydrokinetic turbine. In proceedings of the 2nd Marine Energy Technology Symposium.
- [124] ANSYS Inc. ANSYS CFX Solver Theory Guide.
- [125] U. Ahmed, D. Apsley, I. Afgan, T. Stallard, P. Stansby. Fluctuating loads on a tidal turbine due to velocity shear and turbulence: Comparison of CFD with field data. *Renewable Energy*. 112 (2017) 235-46.
- [126] B. Sanderse, S. Van der Pijl, B. Koren. Review of computational fluid dynamics for wind turbine wake aerodynamics. *Wind energy*. 14 (2011) 799-819.
- [127] S.F. Suftan, M. Li, B.A. O'Connor. 3D modelling of impacts from waves on tidal turbine wake characteristics and energy output. *Renewable Energy*. 114 (2017) 308-22. 10.1016/j.renene.2017.04.030.
- [128] A.H. Martin, D. Ole Gunnar, F. Céline. CFD Analysis of Wave-Induced Loads on Tidal turbine blades. *Journal of oceanic engineering*. 40 (2015).
- [129] X. Li, M. Li, S.J. McLelland, L.B. Jordan, S.M. Simmons, L.O. Amoudry, et al. Modelling tidal stream turbines in a three-dimensional wave-current fully coupled oceanographic model. *Renewable Energy*. 114 (2017) 297-307. 10.1016/j.renene.2017.02.033.
- [130] R. Noruzi, M. Vahidzadeh, A. Riasi. Design, analysis and predicting hydrokinetic performance of a horizontal marine current axial turbine by consideration of turbine installation depth. *Ocean Engineering*. 108 (2015) 789-98. 10.1016/j.oceaneng.2015.08.056.
- [131] ANSYS Inc. ANSYS CFX Solver Modelling Guide.
- [132] J. Mozafari, A. Teymour. Numerical investigation of Marine Hydrokinetic Turbines: methodology development for single turbine and small array simulation, and application to flume and full-scale reference models. Doctoral Dissertation, University of Washington, 2015.
- [133] H.J. Chul, Y.Y. Jin, H.L. Kang, H.R. Yu. Performance of horizontal axis tidal current turbine by blade configuration. *Renewable Energy*. 42 (2011) 195-206. 10.1016/j.renene.2011.08.017.
- [134] S.C. Tatum, C.H. Frost, M. Allmark, D.M. O'Doherty, A. Mason-Jones, P.W. Prickett, et al. Wave-current interaction effects on tidal stream turbine performance and loading characteristics. *Int J Mar Energy*. 14 (2016) 161-79. 10.1016/j.ijome.2015.09.002.
- [135] J. Liu, H. Lin, S.R. Purmilita. Wake field studies of tidal current turbines with different numerical methods. *Ocean Engineering*. 117 (2016) 383-97.

- [136] T. Kinsey, G. Dumas. Impact of channel blockage on the performance of axial and cross-flow hydrokinetic turbines. *Renewable Energy*. 103 (2017) 239-54.
- [137] T. Nishino, R.H.J. Willden. Effects of 3-D channel blockage and turbulent wake mixing on the limit of power extraction by tidal turbines. *International Journal of Heat and Fluid Flow*. 37 (2012) 123-35. [10.1016/j.ijheatfluidflow.2012.05.002](https://doi.org/10.1016/j.ijheatfluidflow.2012.05.002).
- [138] W.X.M. Koh, E.Y.K. Ng. A CFD study on the performance of a tidal turbine under various flow and blockage conditions. *Renewable Energy*. 107 (2017) 124-37. [10.1016/j.renene.2017.01.052](https://doi.org/10.1016/j.renene.2017.01.052).
- [139] C.A. Consul, R.H. Willden, S.C. McIntosh. Blockage effects on the hydrodynamic performance of a marine cross-flow turbine. *Phil Trans R Soc A*. 371 (2013) 20120299.
- [140] T. Chen, L. Liou. Blockage corrections in wind tunnel tests of small horizontal-axis wind turbines. *Experimental Thermal and Fluid Science*. 35 (2011) 565-9.
- [141] M.R.I. Network. Tidal Measurement Best Practice Manual.
- [142] S. Tedds, R. Poole, I. Owen, G. Najafian, A. Mason-Jones, C.E. Morris, et al., 2011. Experimental investigation of horizontal axis tidal stream turbines. In *proceedings of the 9th European Wave and Tidal Energy Conference (EWTEC)*.
- [143] ITTC, 2014. Practical Guidelines for RANS Calculation of Nominal Wakes, The Specialist Committee on CFD in Marine Hydrodynamics of the 27th ITTC. No. 7.5-03-03-02.
- [144] T. O'Doherty, A. Mason-Jones, D. O'Doherty, C. Byrne, I. Owen, Y. Wang. Experimental and computational analysis of a model horizontal axis tidal turbine. In *proceedings of the 8th European Wave and Tidal Energy Conference (EWTEC)*, Uppsala, Sweden, 2009.
- [145] D.M. Grogan, S.B. Leen, C. Kennedy, C.O. Brádaigh. Design of composite tidal turbine blades. *Renewable Energy*. 57 (2013) 151-62.
- [146] B. Kim, S. Bae, W. Kim, S. Lee, M. Kim. A study on the design assessment of 50kW ocean current turbine using fluid structure interaction analysis. In *proceedings of the IOP Conference Series: Earth and Environmental Science*, 2012. p. 042037.
- [147] C.-H. Jo, D.-Y. Kim, Y.-H. Rho, K.-H. Lee, C. Johnstone. FSI analysis of deformation along offshore pile structure for tidal current power. *Renewable energy*. 54 (2013) 248-52. [doi:https://doi.org/10.1016/j.renene.2012.07.018](https://doi.org/10.1016/j.renene.2012.07.018).
- [148] U. Habib, M. Hussain, N. Abbas, H. Ahmad, M. Amer, M. Noman. Numerical investigation of modal and fatigue performance of a horizontal axis tidal current

- turbine using fluid-structure interaction. *Journal of Ocean Engineering and Science*. (2019).
- [149] N. Hafeez, S. Badshah, M. Badshah, S.J. Khalil. Effect of velocity shear on the performance and structural response of a small-scale horizontal axis tidal turbine. *Marine Systems & Ocean Technology*. 14 (2019) 51-8.
- [150] R. Nicholls-Lee, S. Turnock, S. Boyd. Application of bend-twist coupled blades for horizontal axis tidal turbines. *Renewable Energy*. 50 (2013) 541-50. doi:<https://doi.org/10.1016/j.renene.2012.06.043>.
- [151] T. Suzuki, H. Mahfuz. Analysis of large-scale ocean current turbine blades using Fluid-Structure Interaction and blade element momentum theory. *Ships and Offshore Structures*. 13 (2018) 451-8.
- [152] M. Davide, U. Andreas. 2014 JRC ocean energy status report. 2015. 10.2790/866387.
- [153] G. Hagerman, G. Fader, R. Bedard. New Brunswick tidal in-stream energy conversion (TISEC): Survey and characterisation of potential project sites. *EPRI North American tidal flow power feasibility demonstration project*. EPRI TP-003 NB Rev 1. 2006.
- [154] M. Badshah, S. Badshah, K. Kadir. Fluid Structure Interaction Modelling of Tidal Turbine Performance and Structural Loads in a Velocity Shear Environment. *Energies*. 11 (2018) 1-13.
- [155] F. Zahle, N. Sørensen. Overset grid flow simulation on a modern wind turbine. In proceedings of the 26th AIAA Applied Aerodynamics Conference, 2008. p. 6727.
- [156] F. Zahle, N.N. Sørensen, J. Johansen. Wind turbine rotor-tower interaction using an incompressible overset grid method. *Wind Energy: An International Journal for Progress and Applications in Wind Power Conversion Technology*. 12 (2009) 594-619.
- [157] K. Yahagi, K. Takagi. Moment loads acting on a blade of an ocean current turbine in shear flow. *Ocean Engineering*. 172 (2019) 446-55.
- [158] P. Mycek, B. Gaurier, G. Germain, G. Pinon, E. Rivoalen. Numerical and experimental study of the interaction between two marine current turbines. *International Journal of Marine Energy*. 1 (2013) 70-83.
- [159] M. Badshah, S. Badshah, J. VanZwieten, S. Jan, M. Amir, S.A. Malik. Coupled Fluid-Structure Interaction Modelling of Loads Variation and Fatigue Life of a Full-Scale Tidal Turbine under the Effect of Velocity Profile. *Energies*. 12 (2019) 2217. <https://doi.org/10.3390/en12112217>.

- [160] P.W. Harper, S.R. Hallett. Advanced numerical modelling techniques for the structural design of composite tidal turbine blades. Ocean Engineering. 96 (2015) 272-83.

